Preparation, Characterisation, and Modelling of Graphene-based Polymer Nanocomposites with Enhanced Mechanical and Electrical Properties

Giovanni Santagiuliana

Submitted in partial fulfilment of the requirements of the Degree of Doctor of Philosophy

Supervisors: Dr Emiliano Bilotti
Prof Nicola Pugno

School of Engineering and Materials Science
Queen Mary, University of London

In loving memory of my dear mother, Bertilla “Betty” Fanton

I, Giovanni Santagiuliana, confirm that the research included within this thesis is my own work or that where it has been carried out in collaboration with, or supported by others, that this is duly acknowledged below, and my contribution indicated. Previously published material is also acknowledged below.

I attest that I have exercised reasonable care to ensure that the work is original, and does not to the best of my knowledge break any UK law, infringe any third party's copyright or other Intellectual Property Right, or contain any confidential material.

I accept that the College has the right to use plagiarism detection software to check the electronic version of the thesis.

I confirm that this thesis has not been previously submitted for the award of a degree by this or any other university.

Signature:

Date:

Details of collaboration and publications:

- Data presented in this work from self-heating measurements, and impedance spectroscopy were collected by colleagues Harshit Porwal and Maria Crespo Ribadeneyra, respectively. Maria Crespo also collected the rheology data. Thermal diffusivity tests were performed by Politecnico di Torino (Samuele Colonna, Alberto Fina). HDPE + 2 wt.% xGnP750 masterbatch was kindly provided by colleague Olivier Picot. Samples of LLDPE + 4.8 vol.% GNP were prepared in collaboration with Luca Rubini. Micromechanical investigation of the P&F process was conducted by Lorenzo Botto.

- "Pressing-and-Folding for the preparation of efficient and highly loaded 2D materials-based polymer nanocomposites"
  Oral presentation given at the 17th European Conference on Composite Materials (ECCM17), Munich, Germany, June 2016.

- "Graphene-based polymer nanocomposites: the effect of filler orientation and distribution on the electrical and mechanical properties"
  Oral presentation given at the 9th European Solid Mechanics Conference (ESMC 2015), Madrid, Spain, July 2015.

- "How to effectively disperse graphene into polymers?"
  Poster presentation for the 1st London Polymer Group Symposium, UCL, March 2015; and for the Industrial Liaison Forum (ILF), QMUL, October 2015.

- Santagiuliana, G.; Picot, O. T.; Crespo, M.; Porwal, H.; Zhang, H.; Li, Y.; Rubini, L.; Colonna, S.; Fina, A.; Barbieri, E.; Spoelstra, A. B.; Mirabello, G.; Patterson, J. P.; Botto, L.; Pugno, N. M.; Peijs, T.; Bilotti, E. Breaking the Nanoparticle Loading–Dispersion Dichotomy in Polymer Nanocomposites with the Art of Croissant-Making. *ACS Nano* **2018**, *12*, 9040–9050, doi:10.1021/acsnano.8b02877.

- Taroni, P. J.; Santagiuliana, G.; Wan, K.; Calado, P.; Qiu, M.; Zhang, H.; Pugno, N. M.; Palma, M.; Stingelin-Stutzman, N.; Heeney, M.; Fenwick, O.; Baxendale, M.; Bilotti, E. Toward Stretchable Self-Powered Sensors Based on the Thermoelectric Response of PEDOT:PSS/Polyurethane Blends. *Adv. Funct. Mater*. **2018**, 1704285 (1-7), doi:10.1002/adfm.201704285.

- Li, Y.; Zhang, H.; Crespo, M.; Porwal, H.; Picot, O.; Santagiuliana, G.; Huang, Z.; Barbieri, E.; Pugno, N. M.; Peijs, T.; Bilotti, E. In Situ Exfoliation of Graphene in Epoxy Resins: A Facile Strategy to Efficient and Large Scale Graphene Nanocomposites. *ACS Appl. Mater. Interfaces* **2016**, 8, 24112–24122, doi:10.1021/acsami.6b07492.

Abstract

Despite the exceptional properties of graphene and graphite nanoplatelets (GNP), the performance of their polymer nanocomposites is often disappointing. Nanofiller agglomeration is one among many other reasons for this failure in performance, but it is still poorly investigated. In this project, I have systematically studied how the mechanical and electrical properties of nanocomposites are influenced by the nanofiller's agglomeration and distribution inside the polymer matrix. I have also investigated viable routes able to take advantage of nanofiller agglomeration for the preparation of nanocomposites with enhanced multifunctionalities.

A theoretical framework has been proposed to explain how a nanocomposite microstructure influences the macroscopic properties of nanocomposites. This theory well explains the loss of nanocomposite performance reported in the literature and has been further validated by experimental data obtained from model nanocomposites.

These graphene- and GNP-based model nanocomposites were prepared using three different techniques. The first one, "spray-assisted layer-by-layer", followed a bottom-up approach. This method allowed tailoring the spatial distribution of graphene within the polymer matrix. Thus, the effect of nanofiller distribution on the nanocomposite electrical properties was determined. The second technique was an alternative top-down approach inspired by the preparation of puff pastry for croissants and called "pressing-and-folding" (P&F). This iterative technique was developed to prepare samples containing well-defined, increased dispersion/distribution levels of nanofiller. Consequently, it was possible to study how the nanocomposite mechanical properties improve with nanofiller dispersion, and to demonstrate how the electrical conductivity can reach a maximum value for non-perfect nanofiller dispersion/distribution states. Thirdly, nanocomposites prepared by traditional melt-blending techniques (twin-screw extrusion and multi-layer coextrusion) were used to compare and assess the properties of P&F nanocomposites and highlight the differences between P&F and melt-blending techniques.

Finally, these theoretical and experimental findings illustrate how tailoring the microstructures could enhance desired technological functionalities of nanocomposites, such as mechanical reinforcement, health-monitoring, self-heating, and energy management.

Acknowledgments

This work could not have been done without the invaluable opportunity offered me by Professor Nicola Pugno, to whom goes my special thanks! I also acknowledge the scholarship received from the School of Engineering and Materials Science, Queen Mary, University of London.

I am grateful to the priceless guidance of Dr Emiliano Bilotti throughout my PhD. I also acknowledge Professor Ton Peijs and Dr Lorenzo Botto for their precious collaboration.

A special thank goes to Dr Olivier Picot for being my lab mentor and for his vital, competent support! I also thank Prospero Taroni and Dr Maria Crespo Ribadeneyra for their incredible help and for making the lab life more enjoyable!

I acknowledge the teamwork with Wei Tu, Maurizio Leo, Harshit Porwal, Yi Liu, Yan Li, Han Zhang, and the master and undergraduate students that I supervised.

I would like to express a special thought for my family that has always supported and encouraged me in this PhD. I am forever grateful to my mother, Betty, for her model life and unconditional love. Even in her last days she never stopped taking care of us, always putting our family before herself. Her loss was and will always be an unbridgeable abyss. Thus, I thank my father, Giuseppe, and my brother, Mario, for giving me the motivation to carry on with this PhD despite this pain.

A lovely thank goes to my partner, Shirleny Romualdo Cardoso, for showing me that there is always a sunflower in any dark land. Thank you very much for your help and love!

I also thank all my beloved relatives and friends for making my life happier!

I acknowledge the lab instrument failures, the difficult people to deal with in the lab, and the endless formal procedures to gain access to lab facilities. They gave me the right motivation and several good reasons for leaving the labs, sit down on a chair, and start working on the theoretical models of this thesis.

Lastly, I thank those few scientists that with their ingenious minds managed to explain difficult concepts with easy-to-understand and even enjoyable texts and speeches, demonstrating that scientific papers and conference talks can be as appealing and inspiring as bestseller books and movies.

Table of Contents

List of figures

List of tables

List of symbols

E_c = Young's modulus of a (nano)composite

Y_c = yield stress of a (nano)composite

E_f = Young's modulus of the (nano)filler

E_m = Young's moduli of the matrix

G_m = shear modulus of the matrix

Y_m = yield stress of the matrix

v_m = Poisson's ratio of the matrix

V_f = volume fraction of the (nano)filler

V_m = volume fraction of the matrix

η_L = length efficiency factor

η_o = orientation factor

ξ_f = aspect-ratio of nanofiller

B = Pukanszky's interaction parameter

σ_c = nanocomposite electrical conductivity

σ_f = nanofiller electrical conductivity

V_c = nanofiller volume fraction at the electrical percolation threshold

V_f^{eff} = effective reinforcing volume fraction of the nanofiller

V_f^c = critical volume fraction of nanofiller at which agglomeration occurs

A_f = specific surface area of the nanofiller

A_p = total nanofiller surface area

A_c = nanofiller-matrix contact area

A_g = inter-particle agglomeration contact area

D = nanofiller dispersion factor

s = nanofiller agglomeration rate

I = distribution rate

t = processing time

A_0 = initial nanofiller-matrix contact area at $t = 0$

V_g = volume fraction of the graphene-rich zone

g = fraction of the graphene sheets inside the graphene-rich zone out of the total number of graphene sheets

V_{fg} = concentration of graphene inside the graphene-rich zone

V_{fp} = concentration of graphene inside the graphene-poor zone

ξ_g = average aspect-ratio of the graphene-rich zones

β_g = rate of increment of V_g with V_f

σ_m = polymer matrix conductivity

σ_h = polymer matrix conductivity due to electron tunnelling

h = rate of increment of σ_h with V_f

h_p = hopping rate between the graphene sheets inside the graphene-poor region

h_g = hopping rate between the agglomerates

Chapter 1.

Overview

1.1 Graphene-based polymer nanocomposites: a brief introduction

A graphene-based polymer nanocomposite is a polymer containing a nano-metric filler (thus the “nanocomposite” term) made of graphene platelets or one of the graphene derivatives, such as graphene oxide. Graphene is one of the constitutive atomic layers of graphite, thus it is a two-dimensional atomic crystal made of carbon atoms arranged in a hexagonal lattice. Since graphene is 1-atom-thick layer of graphite, it has at least one dimension in the nano-meter scale. In the scientific literature, many papers improperly refer to the word “graphene”, while frequently employing fillers consisting of graphite nanoparticles (GNP) made of many atomic layers, but still with a thickness lower than 100 nm.

Graphene can be obtained in different ways, such as mechanical exfoliation of graphite, and chemical synthesis by chemical vapour deposition (CVD). The synthesis methods differ in amount of graphene that can be produced, efficiency of the procedure, and quality (in terms of absence of defects and lateral dimensions) of graphene. A parameter used to describe graphene particles is the aspect-ratio, which is the length to thickness average ratio of the platelets. The high aspect-ratio, combined with high intrinsic physical properties, makes graphene a very promising nanofiller for polymer nanocomposites.

1.2 Technological advantages of using nanocomposites and graphene

By introducing long, strong and stiff reinforcement phases (e.g. continuous fibres like carbon fibres) into a polymer, high performance composites can be made, for instance with mechanical properties close to those of metals. The low density and the high strength and stiffness of polymer composites make them ideal for demanding applications, like aircraft or sports utilities. Unfortunately, their high costs and labour intensive and batch-like production process severely limit their use. Short fibres or micro-metric fillers have been introduced to simplify and speed up the production process, despite the performance of the resulting composites can result reduced.

Compared to traditional composites made of long fibres or micro-metric fillers, nanocomposites have the advantage of showing high physical properties increase (e.g. mechanical properties, electrical and thermal properties, flame retardant, resistance to

gas permeation, etc.) at much lower filler's volume fraction, which can result in a weight saving.

Nanocomposites have been already widely studied by the scientific community, as they were introduced more than two decades ago with polymer-clay nanocomposites. It is well known that the properties of nanocomposites originate from the nano-metric dimensions (that corresponds to high surface areas) and high aspect-ratios of the nanofillers, combined with high physical properties. A good comparison between the properties of nano-composites and common micro-composites can be achieved by using analytical composite models. According to these theories, graphene is expected to be the filler of choice over conventional clays and micro-fillers because of its high specific surface area, potentially high values of aspect-ratio, and exceptional physical properties, as well as for its superior thermal, electrical and gas barrier properties. The resulting nanocomposites are expected to show enhanced multifunctionalities, together with an easier processability due to low amounts of graphene needed.

Another aspect related to nanofillers is the toughness of the resulting composites: because of the high interfacial area between filler and matrix, it is possible to efficiently dissipate a big impact energy, which can translate into toughness that is much higher than those of the individual materials that constitute the composite.

1.3 Issues with graphene-based nanocomposites

Despite graphene was isolated more than ten years ago, and a lot of research has been conducted to find an efficient method to obtain graphene in high quantities and good quality, as well as techniques to produce performing nanocomposites, some problems have still to be addressed or at least overcame for graphene-based nanocomposites to reach their full potential.

- Independently from the synthesis technique, the yield of production of graphene of sufficient quality is still too low to allow the commercialisation of products;
- The addition of functional groups to graphene platelets is useful for a good linkage with the matrix, which results in nanocomposites with optimised properties. However, certain functionalization routs may not result to be very effective, or could introduce damages and defects to the structure of graphene, thus deteriorating the properties of the nanocomposites;

- Lastly, it has been proven to be difficult to control the spatial organisation of graphene and its planarity during the preparation of nanocomposites; which means the capability of maintaining graphene in a planar configuration and in a well-dispersed, ordered arrangement inside the matrix.

Because of these issues, obtaining nanocomposites with properties close to the one theoretically predicted by composite models is a challenge, especially for high volume fractions of graphene.

1.4 Objectives of this research

In reference to the above, this thesis will address the latter point, namely the spatial organisation and dispersion of graphene in particular in a polymer matrix. The aims of this research are an attempt to provide further progress or clarifications to the following aspects:

1. To understand the effect of graphene agglomeration and distribution on the mechanical and electrical properties of nanocomposites, both theoretically and experimentally;
2. To develop some processing techniques for graphene-based nanocomposites with a well-ordered micro-structure and a good dispersion of graphene platelets;
3. To validate the common mechanical models of composites with the experimental results from the nanocomposites here synthesised, or to formulate new theoretical models able to consider the spatial organization of the nanofiller;
4. To understand how to achieve high filler content in polymer/graphene nanocomposites in order to enhance the reinforcement effect;
5. Eventually, to explore potential applications of graphene-based nanocomposites obtained by the research methods here introduced, such as strain-sensing, or energy-management.

1.5 Project description

This project has investigated the techniques that allow the preparation of nanocomposites with well-defined spatial distributions and dispersions of graphene and GNP, and how they relate to nanocomposite physical properties. Two different preparation approaches have been employed in this project:

1. Bottom-up, with the “spray-assisted layer-by-layer” (sa-LbL) technique. With sa-LbL, it is possible to create nanocomposites by combining the nanofiller with the matrix step-by-step from the nanoscale up to the macroscale. The advantage of this technique is that it allows tailoring the concentration of the nanofiller in each layer that has being created in each step, thus tuning the global nanofiller spatial distribution in the nanocomposite microstructure.

   The materials used in this part of the project were poly-vinyl-alcohol (PVA) and graphene oxide (GO). As PVA and GO are both water soluble, they are easily processable by sa-LbL with no health hazards. Moreover, the good interactions between the chemical groups of PVA and GO guarantee a good compatibility between these two materials. As the main objective of this project unit is to determine the effect of nanofiller distribution on the electrical properties, the samples have been annealed to reduce GO and recover the defect-free basal plane of graphene, thus its conductivity. Then, the samples were characterised with a 2-point-probe setup.

   In comparison with other LbL and solution processing techniques, sa-LbL is quite fast, with a good potential for scaling-up. From this perspective, the sa-LbL apparatus has been recently automatized. However, some technical issues (e.g. effectiveness of the airbrush) must be resolved before it can be used reliably.
2. Top-down, with the “pressing and folding” (P&F) technique. In this method, nanofiller and matrix are joined at the macroscale and, by iterating cycles of pressing and folding, they are mixed down to the nanoscale. At each cycle, the P&F performs an erosion of the nanofiller agglomerates and allows increasing the control over alignment and spatial organisation of GNP, obtaining nanocomposites with a well-oriented micro-structure. By collecting samples at different P&F cycles, it is then possible to study the effect of nanofiller dispersion and distribution on the mechanical and electrical properties of the nanocomposites.

   The materials used in this project unit were GNP obtained from exfoliation of expanded graphite, and linear low-density polyethylene (LLDPE). LLDPE was

chosen because of its low melting point (116 °C). The nanocomposites obtained have been characterised by scanning electron microscopy (SEM), X-ray diffraction (XRD), tensile and electrical tests in addition to rheology analysis.

Other types of nanofiller and polymer matrices have also been used to validate the dispersion mechanism of the P&F technique. Moreover, samples prepared by traditional melt-blending techniques, such as twin-extrusion and multi-layer coextrusion, have been prepared to evaluate the differences between P&F and melt-blending techniques.

Both the experimental data collected in this project and data reported in the literature have been examined and explained by classical composite theories that have been properly modified with new parameters able to define the nanofiller dispersion and distribution states.

Finally, based on these theoretical and experimental findings, it has been demonstrated that nanocomposites with tailored microstructures are able to enhance some desired technological functionalities, such as high mechanical reinforcement due to a nacre-like 2-level hierarchical microstructure; health-monitoring and self-heating functionalities increased by a diffused and interconnected nanofiller agglomeration; and energy management activated by an optimised nanofiller dispersion state and alignment.

Chapter 2.

Literature review

2.1 Potentialities and challenges of graphene-based nanocomposites

Nowadays, the development of technological commercial products (such as sporting goods, parts of cars, and aircrafts components) benefits from the recent nano-technology (the manipulation of matter at the nano-scale), as it provides new materials with exceptional properties. Indeed, when materials have at least one dimension lower than 100 nano-meters, they show properties that can be highly different from those commonly observed when all dimensions are in the macro-scale (i.e. when materials are in their "bulk phase"). For example, nanomaterials can possess altered melting temperatures and glass transition temperatures [1], higher hardness [2], mechanical characteristics (like strength and stiffness) close to the theoretical limits of their constituent materials [3–8], and unique optical behaviours (i.e. interaction with light or other electromagnetic waves) [9–13].

These properties are a consequence of two main phenomena that occur when materials are reduced to the nano-scale: the number of atoms on the surfaces becomes greater than the number of atoms inside the materials; and the number of defects inside the crystal lattices reduces dramatically. For instance, graphene [7], a one-atom-thick layer of graphite (Figure 2.1), is made only of superficial atoms, and has been proven to possess the following properties:

- exceptional mechanical performances [8], with Young's modulus of 1 TPa and strength of 130 GPa, which corresponds to five times the stiffness and more than 200 times the strength of steel A36, a common structural material. However, it must be noted that the mechanical properties of steel must be higher if it was confined in the nanoscale because there would be less defects;
- barrier to gas molecules [14];
- high charge carrier mobility [15], and a thermal conductivity of ~5000 $Wm^{-1}K^{-1}$ [16], which is about three times the conductivity of diamond, the best bulk crystalline thermal conductor.

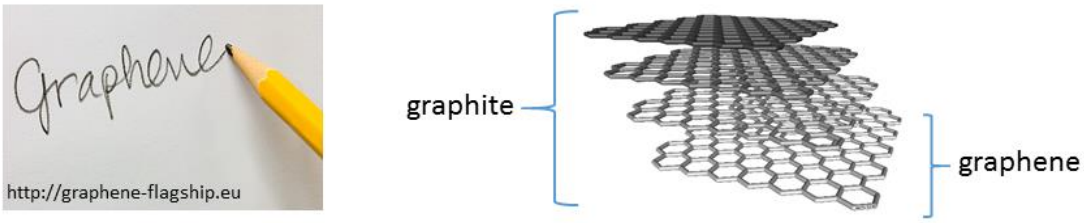

Figure 2.1 Illustration of graphene. Graphene is made of carbon atoms organised in a honeycomb structure, and is the building block of graphite, a common material used, for example, in pencil leads.

The advantage of using graphene and other nanomaterials as nano-fillers is that they can improve the properties of those materials already employed for common products. Indeed, the mixing of nanomaterials with polymers (commonly called “plastics”) result in nano-composite materials with enhanced performances otherwise impossible to achieve with traditional fillers like carbon or glass fibres. The reason of this enhancement lies not only on the exceptional properties of these nanofillers, but also on the large interfaces between nanofillers and hosting polymers [17].

Considering the above mentioned properties of graphene and its large specific surface area of 2630 m^2/g [18], polymer nanocomposites based on graphene are promising candidates for increasing the properties of common polymers. They are potentially able to simultaneously perform different functions, such as mechanical support [19], sensing of deformation [20,21], barrier to gases [22–24], electrical conduction and thermal management [25], bringing significant improvements in several potential applications. Nevertheless, these materials have not fulfilled their potential yet (Figure 2.2), and many issues still need to be overcame before large industrial applications can be achieved, as explained by this study.

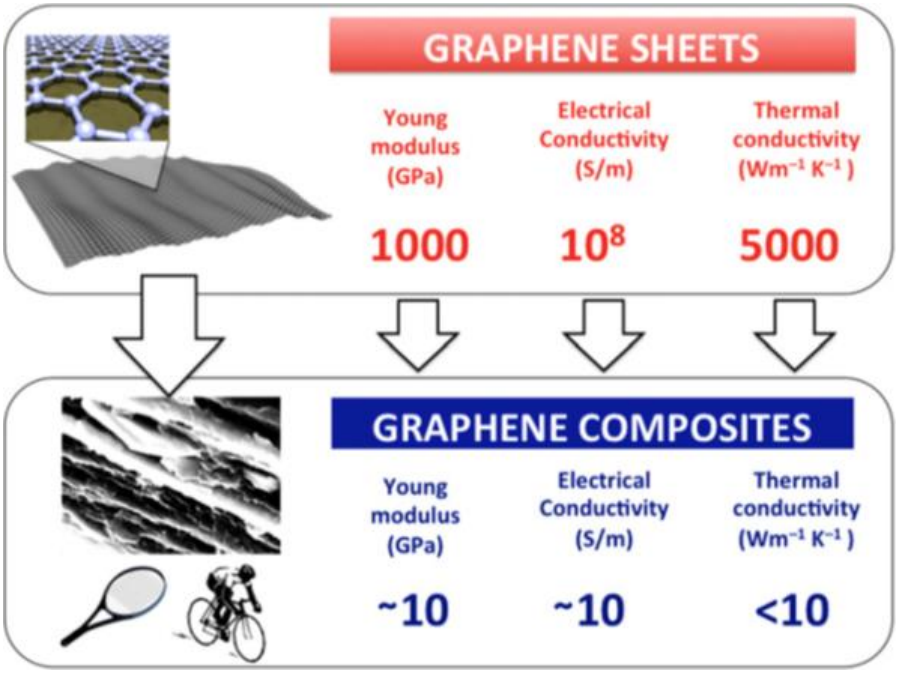

Figure 2.2 Representation of the difference in performance between ideal graphene and graphene-based nanocomposites. Figure from ref. [26].

2.1.1 Mechanical performances

2.1.1.1 Expectations for stiffness and strength of graphene nanocomposites

The first obvious application of graphene is that of mechanical reinforcement for polymers, creating structural materials with enhanced stiffness, strength (the maximum tensile stress that a material can withstand), and toughness (the energy needed to break a material) [27]. Therefore, it is important to analyse the potentials and limits of graphene nanocomposites in terms of mechanical properties.

What are the best mechanical properties achievable by traditional composite materials?

Carbon, glass, and aramid fibres traditionally act as the reinforcement phase in polymer composites. Can graphene nanocomposites outperform traditional composites (provided they have the same matrices) and even replace them? In order to assess this, we need to find out and compare the maximum theoretical mechanical performances achievable by traditional composites and by graphene nanocomposites.

An easy way to calculate the stiffness of fibre-reinforced composites is to use the rule of mixture (RoM):

$$E_c = E_f V_f + E_m V_m \qquad \textit{Equation 2.1}$$

where E_c is the Young's modulus of the composite, E_f and E_m the Young's moduli of fibres and matrix, and V_f and V_m the volume fractions of fibres and matrix, respectively. However, Equation 2.1 is valid only for the prediction of the composite stiffness along the fibres direction. Along the direction perpendicular to the fibres, the inverse rule of mixture applies (IRoM):

$$E_c = \left(\frac{V_f}{E_f} + \frac{V_m}{E_m}\right)^{-1} \qquad \textit{Equation 2.2}$$

From these equations, it is clear that the RoM is used as an upper bound for the estimation of a composite stiffness, while the IRoM as a lower bound.

Considering a composite made by 74 vol.% (which is the maximum volume fraction that can be reached by circular cross-section fibres) of the stiffest carbon fibres [28,29] commonly used by the industry (Toray M60J, with a tensile modulus of ~600 GPa) and by 26 vol.% of epoxy resin matrix (typically ~3.5 GPa stiff), the benchmark appears to be 445 GPa. Note that this benchmark represents only the stiffest composite that could

realistically be prepared. However, common composites are made with different types of fabrics with fibres oriented along defined directions, so they have much lower values of stiffness.
The RoM can also predict the strength of a material. In this case, the benchmark results 4.8 GPa, considering a composite with 74 vol.% of the most used strongest fibres (Toray T1000G, with a tensile strength of ~6.5 GPa), and an epoxy resin matrix with a strength of ~0.08 GPa.

Could graphene-based nanocomposites realistically reach and outperform these benchmarks of strength and stiffness?

One of the earliest concerns among researchers was whether traditional composite theories could also be applied to the properties of nanocomposites based on graphene. Interestingly, they experimentally found that continuum mechanics is still valid at the nanoscale, and able to describe the mechanical reinforcement by graphene [30]. However, the maximum values of stiffness and strength that can be calculated by the RoM for graphene nanocomposites would depend on the maximum achievable graphene volume fraction, which is where the first limitation comes from.
If the thickness of a graphene sheet is 0.34 nm, and the thinnest achievable layer of polymer is ~5 nm (this value actually depends on the size of the polymer chain in consideration), then the maximum volume fraction of graphene is only 6.4%. Therefore, the maximum stiffness and strength of graphene-epoxy resin nanocomposites are 67 GPa and 8.4 GPa, respectively.
Clearly, graphene nanocomposites could potentially outperform traditional carbon fibre-reinforced composites only in strength. The Young's modulus of graphene nanocomposites is relatively low, as low as that of aluminium alloys.

Would it be reasonable to replace traditional composites with graphene nanocomposites then?

Supposing that we can produce these nanocomposites with composition, structure, and properties as described before, then it might be worthy using them as replacement of traditional composites. Indeed, they could be 20% less dense than the benchmark composites, and possess good stiffness and high strength not only along one direction, but also in all directions contained in their basal plane.

Unfortunately, it is still not possible to prepare large amounts of such continuous graphene nanocomposites, i.e. containing graphene sheets as wide as the

nanocomposites (Figure 2.3). The reason for this is that only large-area graphene sheets synthesised by chemical vapour deposition are suitable for preparing continuous nanocomposites, but they are quite expensive sheets and suffer from defects that decrease their intrinsic properties. Moreover, it is not easy to create polymer layers with a thickness of few nanometres. Indeed, only few reports are available in the scientific literature regarding continuous graphene nanocomposites [31,32]. The reported materials are only lab-scale samples prepared by specific methods that limit the choice of polymers to thermoplastics, and the amount of graphene to volume fractions lower than 0.2%. An overview of the preparation methods for graphene and nanocomposites with their pros and cons is provided in the next section.

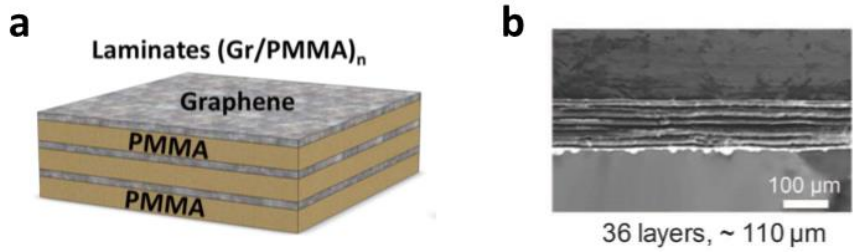

*Figure 2.3 Continuous graphene nanocomposites. (**a**) Illustration of laminates of graphene and poly-methyl methacrylate (PMMA); figure from reference [31]. (**b**) Scanning electron microscopy (SEM) picture of graphene-polycarbonate laminates, taken from ref. [32].*

As the preparation of continuous graphene nanocomposites may not be practical for real mechanical applications, most of the technological research has been devoted to the synthesis of nanocomposites containing small graphene sheets rather than continuous sheets. In this case, the generalised rule of mixtures (GRoM) is more suitable for the calculation of the stiffness of these discontinuous nanocomposites:

$$E_c = \eta_L \eta_o E_f V_f + E_m V_m \qquad \textit{Equation 2.3}$$

with

$$\eta_L = 1 - \frac{tanh(a\,L/t)}{a\,L/t} \qquad \textit{Equation 2.4}$$

and

$$a = \sqrt{\frac{G_m V_f}{E_f V_m}} \approx \sqrt{\frac{E_m V_f}{2(1+\nu_m) E_f V_m}} \qquad \textit{Equation 2.5}$$

In the above equations, G_m is the shear modulus of the matrix; ν_m is the matrix Poisson ratio (usually ~0.5); L is the lateral size and t the thickness of the graphene sheets. In Equation 2.3, η_L and η_o are the length efficiency and orientation factors, respectively.

These factors serve to quantify the effect of the aspect-ratio (i.e. the *L/t* ratio; the higher the better) and spatial orientation of the graphene sheets inside the nanocomposites. It is important to note that the η_L factor comes from the shear-lag theory of Cox [33], which explains how the filler can reinforce the matrix. According to this theory, the filler must be a mechanical continuum, perfectly aligned and completely surrounded by and bonded to the matrix. It is assumed that the matrix as a whole is strained homogeneously under an externally applied load, but that locally the strain is perturbed by the transfer of load to the filler, which happens by shear forces. Hence, the local displacement of the matrix is the same as that of the filler. It is also assumed that the stress transfer gradient along the filler is proportional to the difference between the displacement in the filler and the matrix if the filler was absent. Consequently, the higher the shear modulus G_m of the matrix, the better the transfer of load to the filler and the closer the strain of the filler to the strain of the whole matrix. As the filler as a higher elastic modulus, then its stress must be much higher than the stress of the matrix, and this explains why the filler acts as a mechanical reinforcement.

Both the length efficiency and orientation factors could range from 0 to 1, so we would expect the theoretical maximum properties of discontinuous graphene nanocomposites to be even lower than those of nanocomposites containing continuous graphene sheets. Definitely, graphene nanocomposites do not have the potential to replace traditional composites for mechanical applications. The real target is thus to use graphene nanocomposites as matrices for traditional fibres and fillers. This means that graphene (usually in a powder form or suspended in particular solvents) is at first mixed with desired polymers (such as epoxy resins, or polyamides). Subsequently, these nanocomposites are used to impregnate fabrics employed for the layup of composite laminates, or blended with short fibres to create materials that will be chopped in pellets suitable for the production of objects by injection moulding.

2.1.1.2 Actual reinforcement limits of graphene nanocomposites

There is a number of practical issues limiting the performances of these materials. In fact, real graphene nanocomposites cannot withstand the predictions of the GRoM when containing graphene volume fractions higher than only 1%, with experimental properties much lower than what expected. Figure 2.4 contains representative data of the Young's modulus of graphene nanocomposites relative to their matrices (that is the E_c/E_m ratio), as a function of graphene concentration. The figure contains also the prediction lines from the RoM, IRoM, and GRoM at different aspect-ratios (ξ) of graphene sheets.

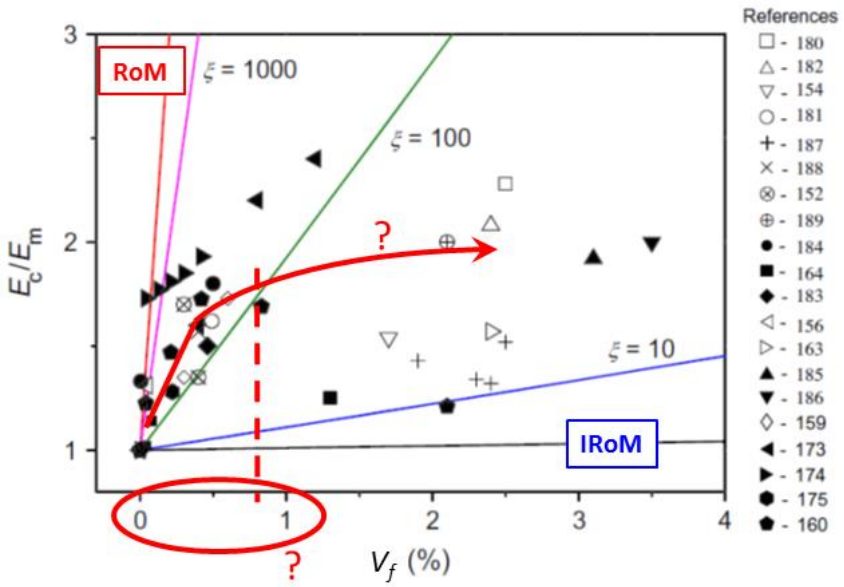

Figure 2.4 Assessment of the relative stiffness of graphene nanocomposites with rigid polymer matrices (i.e. with $E_f/E_m \approx 1.000$) from different scientific reports. This figure has been adapted from ref. [19].

As graphene is commonly prepared with lateral dimensions of 0.1 – 1 μm, we would expect to find nanocomposites in the region delimited by the GRoM prediction lines corresponding to graphene sheets with aspect-ratios of 100 – 1000. Most of the literature data lay within this region only when the volume fraction of graphene is lower than 1%. For higher graphene contents, the data fall inside a lower reinforcement region corresponding to nanocomposites with graphene aspect-ratios of 10 – 100.

This drawback applies also to the strength [34], and limits the actual performances of graphene nanocomposites to values of stiffness and strength that in the best-case scenario are generally only two or three times higher than those of pure polymer matrices. (However, the performances of graphene-elastomers nanocomposites appear greatly improved compared to those of pure elastomers, but they are still too low for structural applications).

2.1.1.3 Main causes for the loss of mechanical reinforcement

Many reasons can explain the discrepancy between theoretical predictions and actual performances of graphene nanocomposites:

1. Graphene sheets agglomerate more and more as their concentration increases, so it becomes even more difficult to efficiently transfer stress from matrix to graphene [34]. Moreover, the higher the aspect-ratio of graphene, the higher the tendency to agglomeration is, or more difficult the dispersion of graphene is [35];

2. Composite theories, like the GRoM, are based on the ideal case of a perfect contact between matrix and filler, thus an efficient stress transfer. Unfortunately, this is not always the case, as the interfacial interaction between graphene and hosting polymer could be rather weak. A way to increase the interfacial strength is to functionalise graphene so that on its surface there are particular chemical groups that can interact with the chemical groups of the polymer matrix (Figure 2.5a). Functionalisation also helps to improve the dispersion of graphene during the preparation of nanocomposites and increase the final mechanical properties. However, it can impart basal defects to the crystal lattice of graphene (Figure 2.5b), deteriorating its mechanical properties significantly. Therefore, functionalisation can help to improve a nanocomposite performance up to a certain limit. A more detailed overview of functionalisation is provided in the next section;

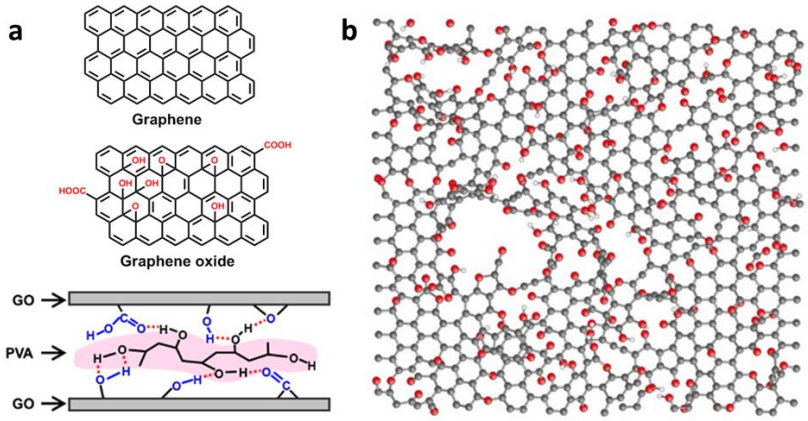

*Figure 2.5 Effects of graphene functionalisation. (**a**) Interactions through strong hydrogen bonds between graphene oxide and polyvinyl alcohol; the figure has been arranged from ref. [36]. (**b**) Defects on the crystal lattice of functionalised graphene; figure taken from ref. [37].*

3. What we commonly consider as “graphene” is actually a mixture of particles with different thicknesses (Figure 2.6), ranging from graphene to graphite nanoplatelets (GNP). Typical synthesis technique produce particles with thicknesses following a log-normal distribution [38]. Thus, the fraction of actual graphene is always quite small. In addition, the aspect-ratio of these particles is also described by a log-normal distribution, and its average might be smaller than expected, as thick particles of GNP are present too. Consequently, the fraction of particles with low aspect-ratios provide very limited reinforcements (the factor η_L becomes closer to zero), skewing the overall performance.

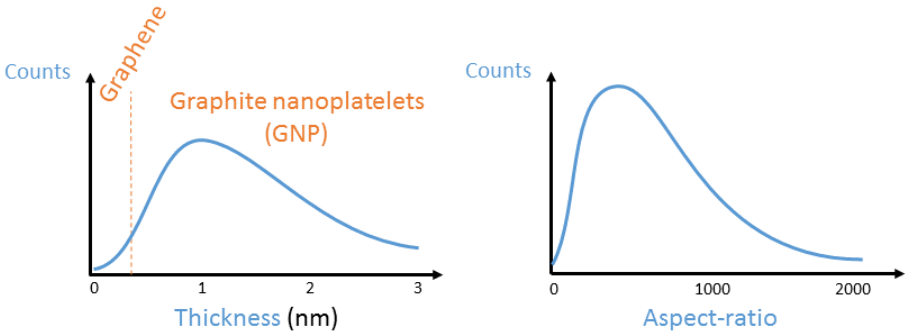

Figure 2.6 *Thickness and aspect-ratio distributions of typical "graphene" powders.*

There is another implication of this distribution of the particle thickness. The shear stress transferred between the graphene layers contained in one graphite particle might be not efficient, as there are weak interaction bonds among the layers. Consequently, the effective Young's modulus of GNP might be smaller than that of pristine graphene [39]:

$$E_{GNP}^{eff} = \frac{E_{graphene}}{\frac{n_l}{2} - k_i\left(\frac{n_l}{2} - 1\right)}, \quad \text{with} \quad n_l > 2 \qquad \textit{Equation 2.6}$$

where n_l is the average number of graphene layers stacked inside the GNP, and k_i is a stress transfer efficiency factor between the layers (≈ 0.7). A graphite nanoparticle with only seven layers has already half the elastic modulus of graphene! This drawback affects also multi-walled carbon nanotubes (CNT) [40]. However, thick GNP allow to reach higher volume fractions [39], thus they could be beneficial for the mechanical properties of nanocomposites, regardless their intrinsic lower elastic modulus;

4. Both graphene and GNP can assume different crumpled configurations (Figure 2.7), such as scrolls, folds, and wrinkles [41]. This problem decreases the stiffness of a composite, as crumpled platelets would unfold under a tensile or shear stress, rather than bear the load by stretching in-plane [42];

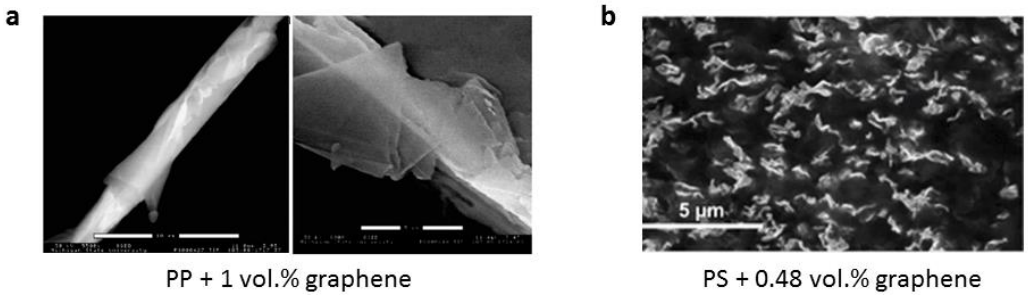

Figure 2.7 *SEM pictures of different morphologies adopted by graphene and GNP inside nanocomposites. (**a**) Scrolls (left), folds (right); figures from ref. [35]. (**b**) Wrinkles; figure from ref. [43].*

5. Last aspect that can explain why the experimental data are lower than expected is the orientation of the particles inside the nanocomposites. The prediction lines in Figure 2.4 are for nanocomposites with aligned graphene sheets, so the parameter η_o of Equation 2.3 has the maximum value: 1. Unfortunately, when the concentration of nanofiller increases, the control over nanofiller orientation decreases [44], so the real value of η_o becomes smaller than 1. When a nanocomposite contains nanoplatelets randomly oriented in all 3D directions, η_o acquires the minimum value of 8/15 [44]. In this last situation, we lose one of the advantages of composite materials: anisotropy, which allows designing the required strength and stiffness only in the direction in which these properties are desired. Therefore, researchers are developing new techniques that have better control over nanofiller orientation, allowing the preparation of highly loaded anisotropic nanocomposites, as it has also been done in this research project and shown in Figure 2.8.

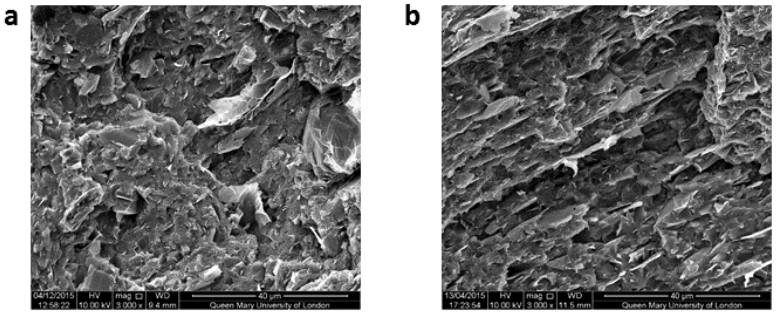

*Figure 2.8 SEM pictures of nanocomposites with same composition but different orientation of graphene caused by different preparation techniques: (**a**) 3D random orientation, and (**b**) in-plane random orientation. These data are discussed in detail in the next chapters.*

It is important to note that the orientation factor depends also on the shape of nanofiller, not only on nanofiller orientation. From this point of view, carbon nanotubes might be a better choice than graphene/GNP for preparing nanocomposites with good mechanical properties. Indeed, in the case of CNT, the orientation factor has values of 1 when all CNT are aligned along one direction, 3/8 when CNT are in-plane randomly oriented, and 1/5 when CNT are 3D oriented [45]. This factor must be combined with a length efficiency factor specific for CNT, which is Equation 2.4 with the following parameter *a* [45]:

$$a_{CNT} = \sqrt{\frac{-3}{2\ln V_f}\frac{E_m}{E_f}} \approx 2a_{graphene} \qquad \textit{Equation 2.7}$$

Consequently, the final effect of CNT on the elastic properties of nanocomposites could be even higher than that of graphene (assuming the same nanofiller aspect-ratio, volume fraction, and type of matrix).

A comparison between graphene-based and CNT-based nanocomposites (Figure 2.9) clearly shows how CNT with small (<<1000) aspect-ratios give always a better mechanical reinforcement effect than graphene for any nanofiller orientation. The only advantage of using graphene would be a really high reinforcement in both cases of 2D and 3D orientation, provided it has a really high (>1000) aspect-ratio. Unfortunately, it is still unrealistic to prepare graphene or GNP with such large aspect-ratios.

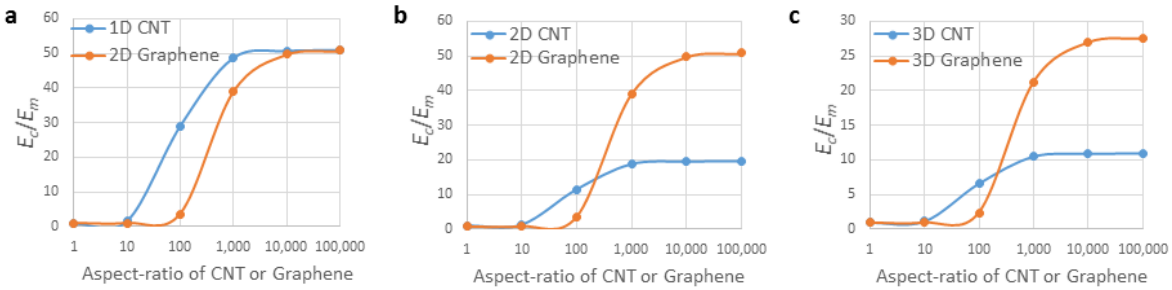

Figure 2.9 Mechanical reinforcement of graphene- and CNT-based nanocomposites as a function of nanofiller aspect-ratio and for different nanofiller orientations. The curves were simulated considering a nanofiller volume fraction of 5%, a nanofiller elastic modulus of 1000 GPa, and a matrix with an elastic modulus (E_m) of 1 GPa.

2.1.1.4 Other mechanical improvements that graphene nanocomposites could bring

Despite all these hurdles that researchers are still trying to address, graphene nanocomposites could bring other mechanical benefits other than high stiffness and strength, such as improved yield stress and toughness [46]. These properties depend on the specific surface area of the nanofiller (hence on the contact area between nanofiller and matrix) and are a more direct indication of the interfacial interaction between nanofiller and polymer.

The yield stress is closely related to the amount of energy that can elastically deform a material (i.e. without permanent deformation). Therefore, the yield stress of a material is an important engineering parameter for calculating the maximum stress that a structure can withstand without being permanently deformed or damaged. From this point of view, graphene could induce high increments of yield stress, Y_c, because of its large specific surface area [17,47]:

$$Y_c = Y_m \frac{1 - V_f}{1 + 2.5V_f} e^{BV_f}$$ *Equation 2.8*

with

$$B = \left(1 + A_f \rho_f l\right) \ln \frac{Y_i}{Y_m}$$ *Equation 2.9*

where Y_m is the polymer matrix yield stress. B is an interaction parameter that estimates the interfacial strength and size of the nanofiller-matrix contact area, and it depends on the nanofiller specific surface area (contact area) A_f, nanofiller density ρ_f, thickness l and yield stress Y_i of the interphase.

In addition to the yield stress, the amount of nanofiller-matrix contact area and the magnitude of the interfacial interaction are important factors for the total energy required to brake a material, that is, the toughness. In fact, nanocomposites made by nature are much more efficient than man-made composites, because the interface between nanoparticles and proteins (the biological equivalent of synthetic polymers) is maximised. From this perspective, nacre is considered as a reference structure for composite materials because it is made of calcium carbonate (the same material of chalk, which is well known to be brittle, Figure 2.10) finely divided in nano-grains kept together by proteins in platelet-like "bricks". It is exactly because of this "brick-and-mortar" microstructure that nacre shows a very high toughness [48,49].

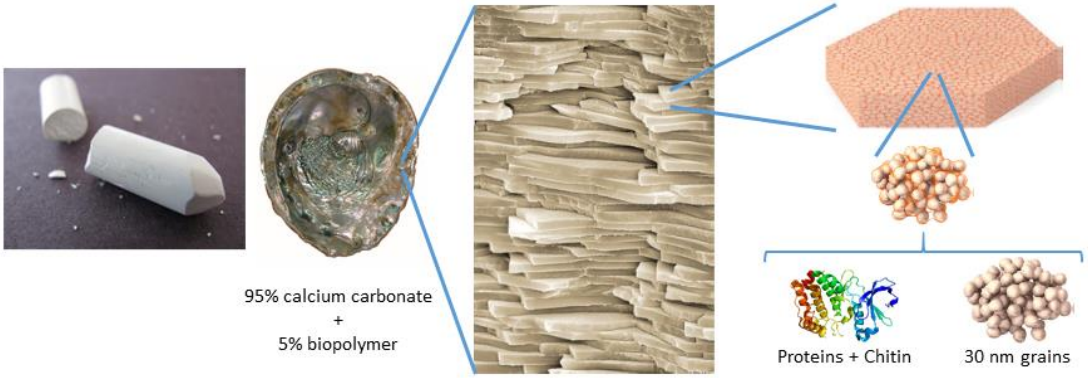

Figure 2.10 Chalk and nacre: two materials similar in composition (mainly calcium carbonate), but with very different microstructures, and thus toughness. Figure adapted from ref. [49].

In light of this, researchers have tried to prepare graphene nanocomposites with a microstructure similar to that of nacre [50] and with a content of "mortar" much lower than that of "bricks" (Figure 2.11). These nanocomposites exhibit a toughness even higher than that of nacre [51–55]. However, their stiffness is not much improved compared to the stiffness of their polymer matrices. Moreover, they are usually in forms of thin films

or fibres, as they are not easy to be prepared in amounts large enough for massive and thick materials.

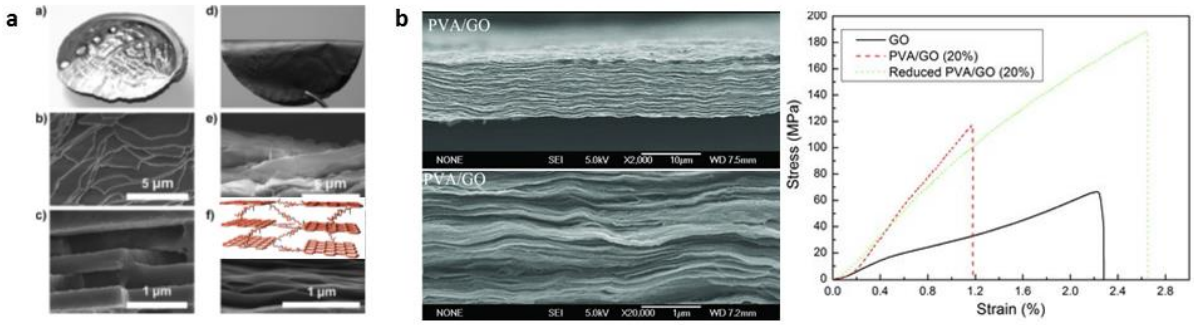

*Figure 2.11 Nacre-inspired nanocomposites: (**a**) reduced graphene oxide – 10,12-pentacosadiyn-1-ol (PCDO) nanocomposites (pictures from ref. [53]); and (**b**) 80 vol.% graphene oxide – polyvinyl-alcohol (PVA) nanocomposites (figures from ref. [51]).*

In conclusion, the beneficial effects of graphene and GNP on the yield stress and toughness of nanocomposites are fundamental when these materials are combined with traditional fibres, and in those situations where the matrix behaviour is dominant over the fibres behaviour. From this point of view, graphene-based nanocomposites can be promising matrices for classical fillers, as they prevent fibres from buckling when they are under compression, because of the nanocomposite enhanced yield stress (and elastic modulus). Nanocomposites can also reduce the propagation of inter-fibres cracks thanks to bridging effects of graphene/GNP, which results in composites with increased interlaminar fracture toughness [46,56].

Graphene-based nanocomposites could bring other mechanical advantages, such as improved impact and puncture resistance, but these aspects are not well understood. Surely, the dispersion level of graphene plays an important role for the effectiveness of these properties. Therefore, until an efficient dispersion method is not found, graphene-based nanocomposites cannot meet these promises.

There are other physical properties and functions that graphene can impart besides mechanical properties, as illustrated below.

2.1.2 Gas-barrier effect

A useful consequence of adding graphene/GNP to polymers is the dramatic decrease of the permeability to gases because of the formation of a tortuous path for the diffusing gas molecules (Figure 2.12a,b) [57]. This tortuous path results to be longer and longer

as the graphene sheets have higher aspect-ratios and better dispersions (Figure 2.12c) [22,58]. The permeability, P_c, of nanocomposites can be predicted using different models (ref. [59] contains a comprehensive list of permeability models), like the modified-Nielsen model (Figure 2.12a) [60]:

$$P_c = P_m \frac{1 - V_f}{1 + (1/6)\xi V_f}$$ *Equation 2.10*

or the Cussler model (Figure 2.12b) [61]:

$$P_c = P_m \left(1 + \frac{\xi^2 V_f^2}{1 - V_f}\right)^{-1}$$ *Equation 2.11*

In both equations, P_m is the permeability of the neat polymer matrix, and ξ is the nanofiller aspect-ratio. The nanocomposite permeability reduces already at extremely low concentrations of nanofiller, provided the nanofiller is well aligned and its aspect-ratio is high enough. However, it was found that at very low loadings of graphene (below 0.05 vol.%), the decrease in gas permeability is largely caused by a reduction in gas solubility in the nanocomposite, rather than a barrier effect [43].

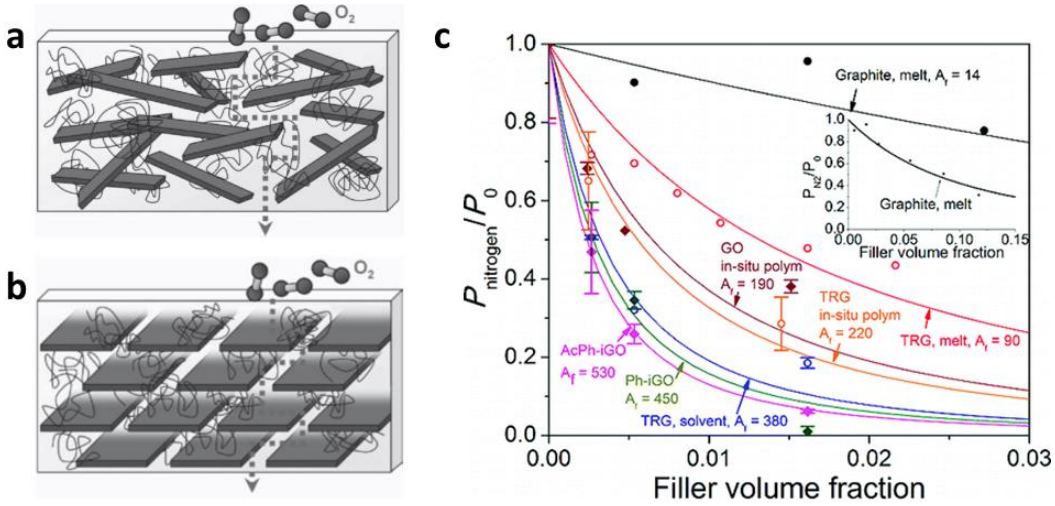

*Figure 2.12 Gas-barrier effect in graphene-based nanocomposites. (**a** - **b**) Representations of the tortuous path for gas molecules as described by the modified-Nielsen and Cussler models, respectively; images from ref. [43]. (**c**) Relative permeability at 35°C to nitrogen molecules (gas that forms 78% the atmosphere of Earth) of thermoplastic polyurethane (TPU) nanocomposites with different graphene aspect-ratios (represented as A_f) and types of graphene (GO = graphene oxide; TRG = thermally-reduced GO; Ph-iGO = phenyl isocyanate-treated GO; AcPh-iGO = acetyl phenyl isocyanate-treated GO), together with prediction lines of Equation 2.11; figure from ref. [58].*

2.1.3 Thermal management

Another advantage of introducing graphene in traditional composites is to enhance the thermal conductivity. Consequently, composites can dissipate heat more easily. This is fundamental for several applications. For example, bicycle calliper brakes work by transforming kinetic energy into heat when applying friction forces on the surfaces of the rims. Therefore, rims heat up very quickly during braking, and if they are made of carbon composites, they can reach a certain temperature (the “glass temperature” of the epoxy resin) and degrade irredeemably (Figure 2.13a). If this happens, it might not be possible to brake properly anymore, or not brake enough at all, causing dangerous accidents.

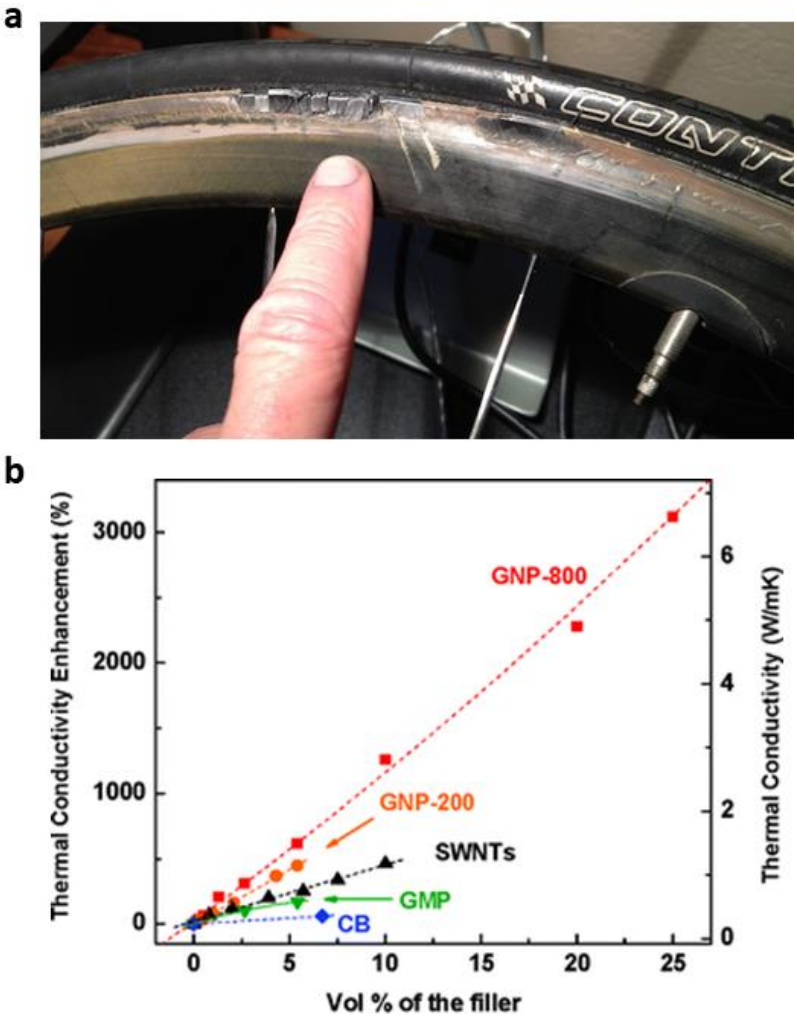

*Figure 2.13 Thermal behaviour of epoxy-based composites. (**a**) Carbon rim thermally degraded after serious braking; picture taken from ref. [62]. (**b**) Thermal conductivity of epoxy-based composites at 30 °C (GNP-800 = GNP exfoliated at 800 °C; GNP-200 = GNP exfoliated at 200 °C; SWNTs = single-walled carbon nanotubes; GMP = graphitic micro-particles; CB = carbon black); figure from ref. [63].*

The scientific literature reports several improvements in the thermal conductivity of polymers containing graphene [64], with values ranging between 3 and 6 W m^{-1} K^{-1} for

graphene-epoxy nanocomposites, as compared with ~0.2 W m^{-1} K^{-1} for neat epoxy [42]. As shown in Figure 2.13b, the thermal conductivity reached by nanocomposites with 25 vol.% of well exfoliated graphene (that is supposed to have high aspect-ratios) surpasses the performances of composites with ~70 vol.% of conventional fillers [63]. CNT possess similar thermal conductivities of graphene, but the 2D geometry of graphene may provide lower interfacial thermal resistance, thus producing higher thermal conductivities in the nanocomposites [42]. Moreover, since the thermal conduction in polymers is mainly caused by the mobility of phonons, strong covalent bonds between graphene and polymers can reduce the phonon scattering at the interfaces, hence promoting high thermal conductivities even further [65].

Besides enhanced thermal conductivities, graphene nanocomposites show improved degradation temperatures (even dozens of degrees higher than neat polymers), as the kinetics of thermal decomposition is reduced by the presence of graphene [22]. One of the mechanisms is the interaction between polymers and graphene, "which would decrease the mobility of the polymer chains near the interface and increase the thermal stability of the nanocomposites" [64]. This thermal degradation resistance is often companied by altered glass temperatures (T_g). Only little amounts of graphene in epoxy resins are enough to change both the T_g and the degradation temperature of several Celsius degrees [56,66].

The enhanced thermal properties of graphene nanocomposites include also their thermal expansion behaviour. Graphene-epoxy nanocomposites show a reduced coefficient of thermal expansion below their glass temperature as compared to their neat epoxy resin matrices. This can be explained by the negative thermal expansion coefficient of graphene [22,42]. Composites with small coefficients of thermal expansion may be important for maintaining the dimensional stability of structural components when they are subjected to high temperatures and also in reducing thermal shrinkage upon cooling in moulded parts.

Lastly, graphene can improve not only the thermal properties of its nanocomposites, but also help their preparation. Because of its good thermal conductivity, graphene can aid curing of thick composite parts (Figure 2.14) by reducing those overheat phenomena that induce thermal stresses in the final composites, negatively affecting their performances [67]. As a consequence, composite parts could be produced more successfully and quickly, as there is no need to wait for overheat dispersion during production.

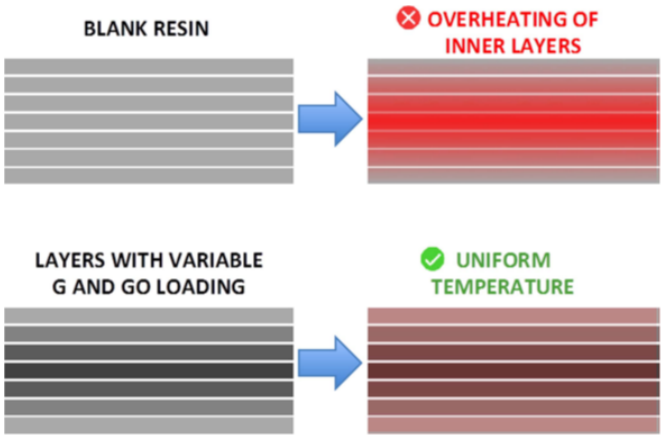

Figure 2.14 Schematic representation of the use of differently G and GO layers to promote heat control during thick composite curing. Figure and caption from ref. [67].

2.1.4 Electrical conductivity

Another property that can be enhanced in graphene nanocomposites is electrical conduction. The conductivity of these nanocomposites is based on electrical percolation, which brings different advantages over traditional conductive materials. Thanks to this percolation characteristic, it is not only possible to conduct electricity, but also to detect the deformation of the material itself under an external load, or to monitor the curing process of composite materials [20].

When a conductive nanofiller is mixed with an insulating material, the overall electrical conductivity of the resulting nanocomposite can dramatically change, depending on the amount of nanofiller added. We can identify three different situations based on the nanofiller volume fraction (Figure 2.15a): 1) the nanofiller concentration is so small that each nanoparticle is well-isolated from each other, thus the nanocomposite is overall electrically non-conductive; 2) above a critical volume fraction (V_c), the inter-particle distance becomes small enough for electrons to “jump” from one nanoparticle to another, creating conductive percolation paths throughout the nanocomposite and a huge electrical conductivity enhancement over several orders of magnitude; 3) for high nanofiller volume fractions, we observe much smaller increments, as the nanocomposite conductivity (σ_c) approaches that of nanofiller (σ_f).

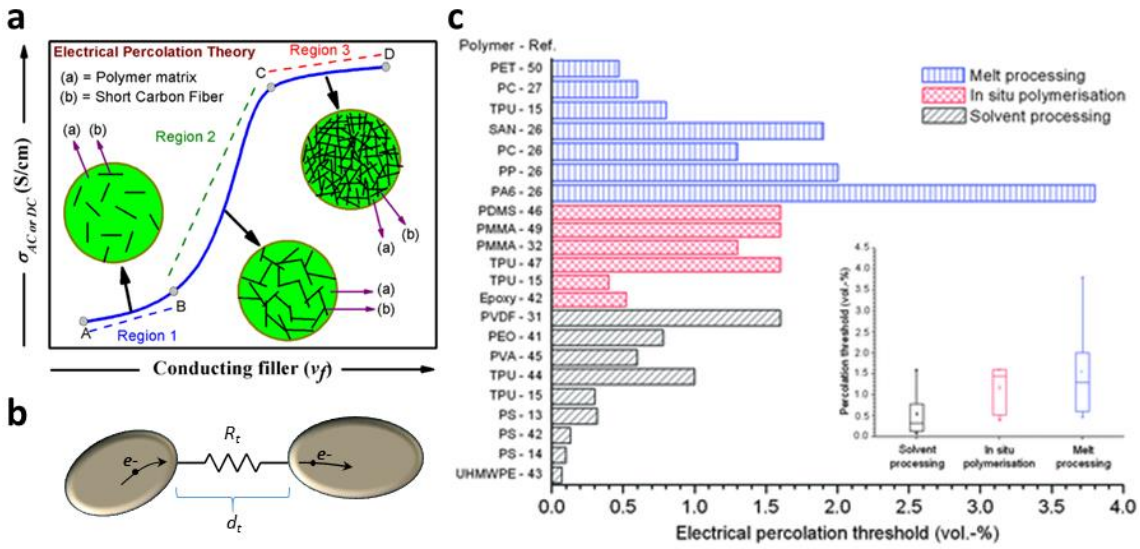

*Figure 2.15 Electrical percolation in nanocomposites and its applications. (**a**) Schematic representation of the percolation behaviour of in polymer/conductive filler composites; picture from ref. [68]. (**b**) Sketch of electron tunnelling between two graphene platelets placed at a distance d_t from each other, which is the dominant mechanism in the electric behaviour of conductive nanocomposites. (**c**) Electrical percolation thresholds of graphene-polymer nanocomposites according to processing strategy; figure from ref. [69].*

This electrical behaviour near and above the percolation threshold is commonly described by the percolation theory:

$$\sigma_c = \sigma_f \left(\frac{V_f - V_c}{1 - V_c}\right)^s \qquad \textit{Equation 2.12}$$

where *s* is a conductivity exponent that depends on the dimensionality of the conductive network inside the nanocomposite (usually, values <2 are found for 2D networks, and values >2 for 3D networks). The percolation threshold, V_c, depends on the type of nanofiller employed, and its orientation inside the nanocomposite. For the case of nanocomposites containing well-aligned (2D randomly oriented) graphene sheets, the percolation threshold can be theoretically expected as follow [70]:

$$V_{c,2D} = 2\pi \frac{\xi^2 t^3}{(\xi t + d_t)^3} \qquad \textit{Equation 2.13}$$

where *t* is the mean thickness of the GNP, and d_t is the maximum "tunnelling distance" (usually ~10 nm for polymers), that is the maximum inter-particle distance that allows electrons to jump from one graphene sheet to another one (Figure 2.15b). If a nanocomposite contains 3D randomly oriented graphene sheets, the minimum amount of graphene needed for transforming the material from insulator to conductor results to be about three times higher than the previous case [70]:

$$V_{c,3D} = \frac{27\pi}{4}\frac{\xi^2 t^3}{(\xi t + d_t)^3}$$ *Equation 2.14*

From Equation 2.13 and Equation 2.14, it is clear that the percolation threshold depends both on aspect-ratio (ξ) and thickness of graphene. This is the reason why the percolation thresholds found for graphene nanocomposites are generally much lower than those of traditional composites containing carbon fibres or carbon black, as these common fillers have a high thickness (carbon fibres possess high aspect-ratios, but are few micrometres thick).

Additionally, the electrical conductivity of graphene nanocomposites does not seem to suffer the problems affecting the mechanical properties. On the contrary, the big issue of graphene agglomeration that dramatically reduces the mechanical performances is actually beneficial for the electrical conductivity, as it can decrease the percolation threshold [71,72].

Small percolation thresholds are a big advantage, as less conductive filler is needed to make a polymer conductive. For the case of graphene nanocomposites, the percolation threshold is usually below 2 vol.%, and is influenced not only by the quality of graphene, but also by the technique used to prepare the nanocomposites (Figure 2.15c). Depending on the level of conductivity reached, graphene nanocomposites can be used for electrostatic dissipation (when $\sigma < 10^{-4}$ S/m), electrostatic painting ($10^{-4} < \sigma < 10$ S/m), or electromagnetic (EMI) shielding ($\sigma > 10$ S/m). In addition, the conductivity of graphene nanocomposites can be useful also for strain-sensing purposes.

The advantage of strain sensors based on polymers containing graphene is that these materials can be much more sensitive than traditional strain gauges made of metal. Both types of sensors transmit the variation in their electrical resistance (ΔR) caused by an external force that has deformed them of a certain strain (ε). The resistance variation of metal strain gauges is caused only by dimensional changes (ε), as their electrical conductivity (σ) remains unaffected. On the contrary, graphene nanocomposites modify also their conductivity with the strain. This is because, during deformation, the distance between graphene sheets increases more and more, so the tunnelling resistance intensifies (R_t, Figure 2.15b), acquiring even more relevance on the overall nanocomposite conductivity. In general, the relative resistance variation of a strain gauge (at low strain) can be represented as follow [73]:

$$\frac{\Delta R}{R_0} = (1 + 2\nu)\varepsilon + \frac{\Delta\sigma(\varepsilon)}{\sigma_0}$$ *Equation 2.15*

where R_0 and σ_0 are the resistance and conductivity of the material without any deformation, and v is the Poisson's ratio. The first term of Equation 2.15 accounts for the resistance variation due to dimensional changes only, whereas the second term for the strain-dependent conductivity (which is negligible for metal strain gauges). The sensitivity of a strain sensor is commonly valuated by the "gauge factor", which describes how the relative resistance variation depends on strain:

$$\mathrm{GF} = \frac{d(\Delta R/R_0)}{d\varepsilon} = \frac{1}{R_0}\frac{dR}{d\varepsilon} \qquad \textit{Equation 2.16}$$

This means that, for metal-based strain sensors at low strain, GF is equal to about two. Differently, graphene nanocomposites possess GF up to 50 [73], thus they are much more effective to detect strain than traditional gauges. Potentially, graphene nanocomposites can show even higher GF if their content of graphene is around the percolation threshold (region 2 in Figure 2.15a): the effect of a deformation is similar to decreasing the concentration of graphene because the inter-particle distance increases. Therefore, as in this percolation region the conductivity changes several orders of magnitude, the GF could result as high as 1000, or even more.

It is now clear how graphene nanocomposites can be used both to create structural components and, at the same time, to sense their deformation or monitor their integrity, alerting the presence of eventual damages. Besides structural materials, graphene nanocomposites can also monitor the body motion of people. Wearable and stretchable sensors based on graphene nanocomposites are promising allies for athletes, as they could monitor heartbeat, blood pressure, and other vital functions. Traditional silicon/metal-based electronics, instead, are not suitable for sensing devices able to deform, stretch, fold or twist in response of the body motion of athletes, so they can hardly be mounted directly to the skin or integrated inside the sporting cloths.

From this perspective, the scientific literature has already reported stretchable, easy-to-prepare, and highly sensitive graphene-based strain-sensors. For example, the group of Prof. Coleman, Trinity College Dublin, has demonstrated a strain sensor with a GF of 35 based on commercial elastic bands infiltrated with graphene (Figure 2.16a) that is able to detect huge strains >800%, and suitable for kinaesthetic purposes, detecting motions as subtle as those associated with breathing and pulse [73].

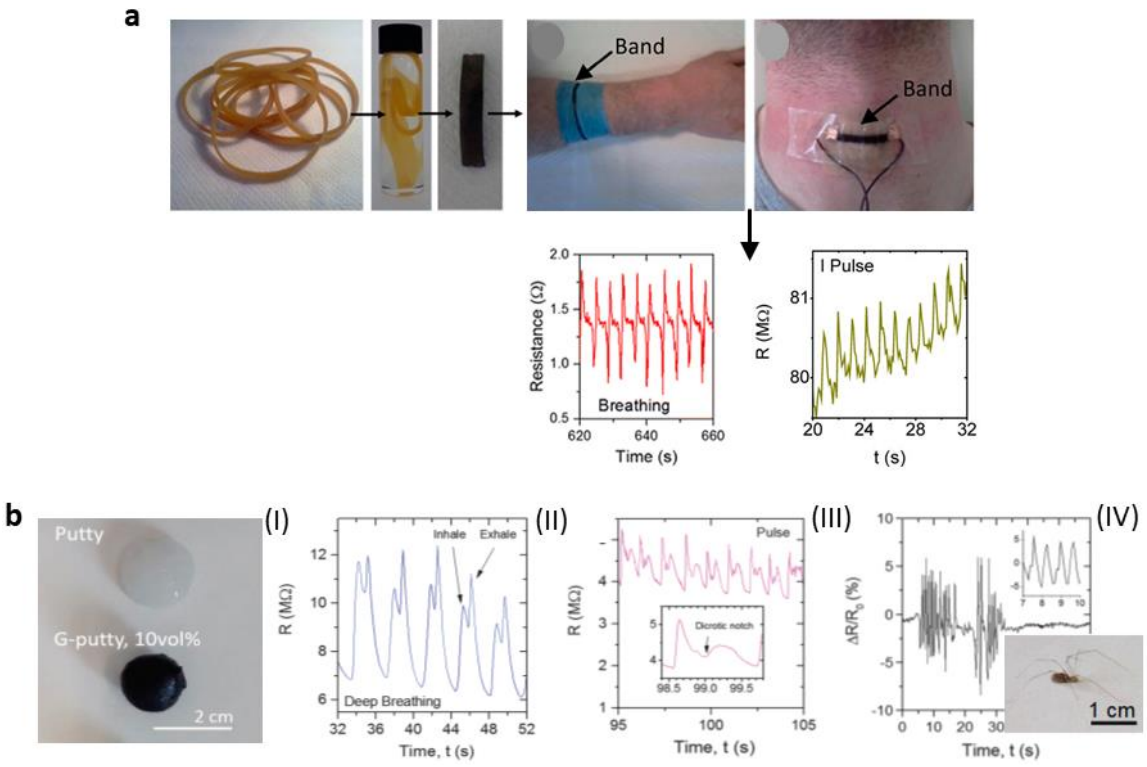

*Figure 2.16 Sensing abilities of graphene nanocomposites. (**a**) Elastic bends swelled in toluene and then soaked inside a graphene suspension in order to obtain an elastic strain-sensor band, able to monitor breathing and pulsing; pictures from ref. [73]. (**b**) Photograph of hand-rolled spheres of neat Silly Putty and graphene filled putty, also called G-putty (I); resistance waveforms measured while using G-putty to sense breathing (II), and pulse (III, the inset shows a single period with the characteristic dichroitic notch); relative resistance variation associated with a spider walking across a thin circular sheet of G-putty (IV, the inset shows individual footsteps). All pictures of part (b) are from ref. [74].*

The same group has also infused graphene to “silly putty”, a silicon-based rubber (Figure 2.16b-I), obtaining a strain sensor with a GF >500 that can measure breathing (Figure 2.16b-II), pulse (Figure 2.16b-III), blood pressure, and so sensitive than can even detect the footsteps of a walking spider (Figure 2.16b-IV) [74].

Lastly, it has been shown that graphene can be a good coating material for glass fibres (Figure 2.17a), so they can become strain sensors with GF ~17, able to detect the deformation of the host composite(Figure 2.17b), and also to provide local resin curing information during the composite manufacturing process (Figure 2.17c) [20]. This approach is a valuable alternative to graphene nanocomposites, as graphene-fibres sensors do not necessarily make the hosting composite overall electrically conductive (thus avoiding the problem of galvanic corrosion of metal parts in contact with the composite), but still providing sensing functionalities to the final products.

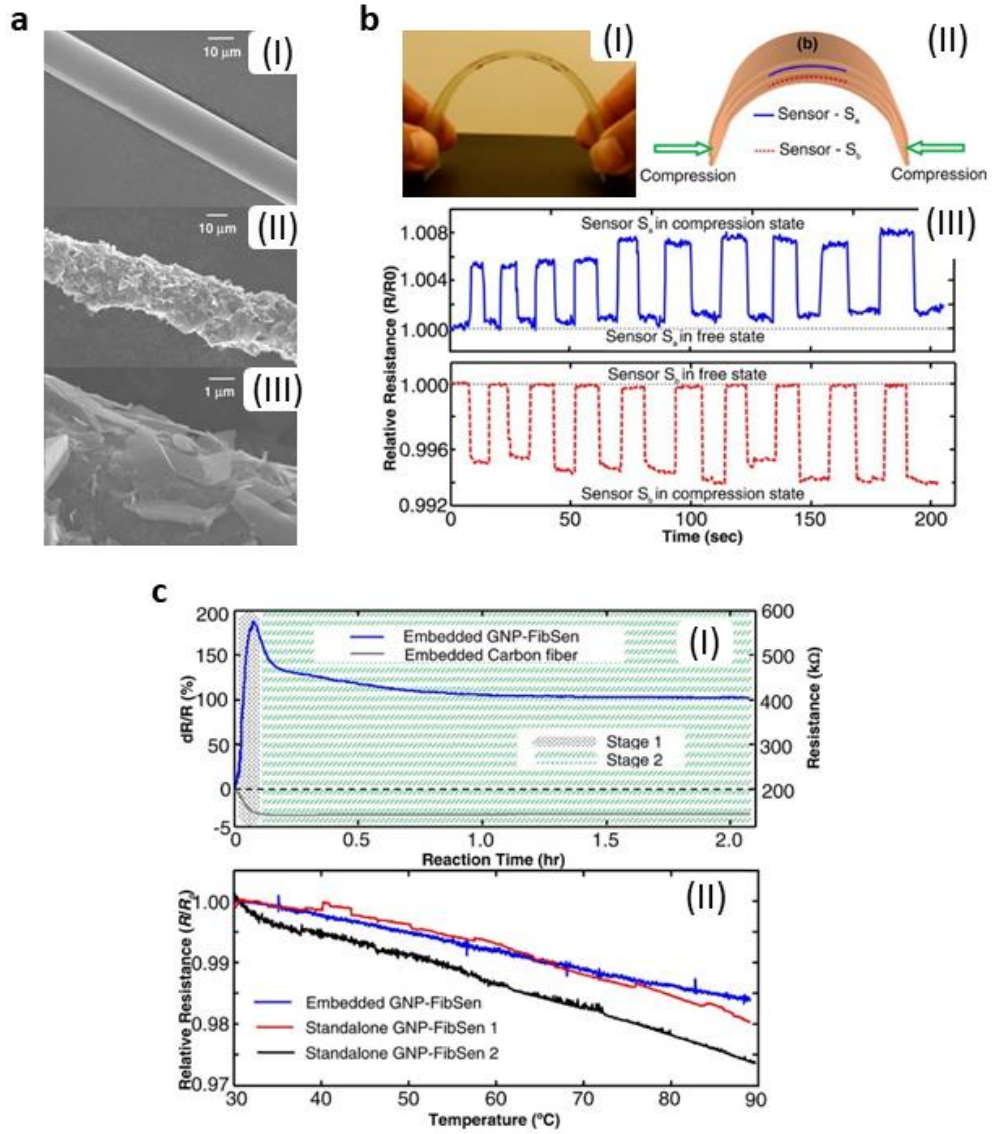

*Figure 2.17 Sensing abilities of smart fibres based on graphene. (**a**) SEM images of a neat glass fibre (I), of a glass fibre coated with graphene (II), and of the graphene packing structure on top of the graphene-coated fibre (III). (**b**) Strain sensing of a composite containing two graphene-glass fibre sensors: photo image of the bended composite (I); schematics of the composite containing fibre sensor S_a (blue) above, and sensor S_b (red) below the neutral surface (II); resistance response of the fibres sensors when the composite is subjected to repeating bending deformation. (**c - I**) Two-stage curing process of the composite (stage 1: temperature ramping from 25 to 143 °C; stage 2: isothermal at 143 °C for 2 h) monitored by the resistance change of the embedded graphene-glass fibre sensor, as compared with a composite containing only a carbon fibre. The resistance change of the embedded graphene-fibre sensor is not only due to a temperature effect, but also to the physical/chemical changes of the resin matrix, as proved with the next graph. (**c - II**) Comparison of the temperature-dependent electrical resistance for the standalone graphene-glass fibre sensors and the one embedded in the fully cured epoxy/glass fibre composite: in all cases, the sensors show a negative temperature coefficient of resistance. However, the embedded graphene-fibre sensor during the stage 1 curing process (in graph c-I) had a positive temperature coefficient of resistance that must have been caused by the progressive changes of viscosity and cross-link density of the epoxy resin during the curing process. All images are from ref. [20].*

2.2 Production techniques

This section introduces the main routes to produce and characterise graphene and its nanocomposites. Most of the techniques developed so far is suitable only for lab-scale productions, and only few can produce materials on a scale large enough for the preparation of real products.

2.2.1 Synthesis of graphene

The synthesis methods for the production of graphene can be divided in two categories: “top-down” and “bottom-up” approaches. The first type of techniques starts with a bulk material (usually graphite) that is gradually reduced in size down to the nanoscale, until graphene is obtained. The second type employs carbon atoms (obtained from specific precursors, like hydrocarbon gases or solid carbides) to build up graphene from scratch.

2.2.1.1 Top-down approaches.

These methods can potentially satisfy large-scale production of graphene. The most important, or promising, techniques are the following:

1. Micromechanical cleavage. This approach is also known as the “scotch tape” method, because the group of Prof. Geim at Manchester University used it in 2004 to exfoliate graphene for the first time [15]. It consists in repeated peeling of highly oriented pyrolytic graphite particles using a scotch tape (Figure 2.18a). The graphene sheets obtained in this way are of extremely high quality in terms of crystallinity (absence of defects), lateral size (>10 μm), and thickness (<10 nm), thus with aspect-ratios >>1000. Unfortunately, this method is slow and can produce only small amounts of graphene (low yield). Consequently, several studies have focused on scaling-up this system (see example in Figure 2.18b) [75,76].

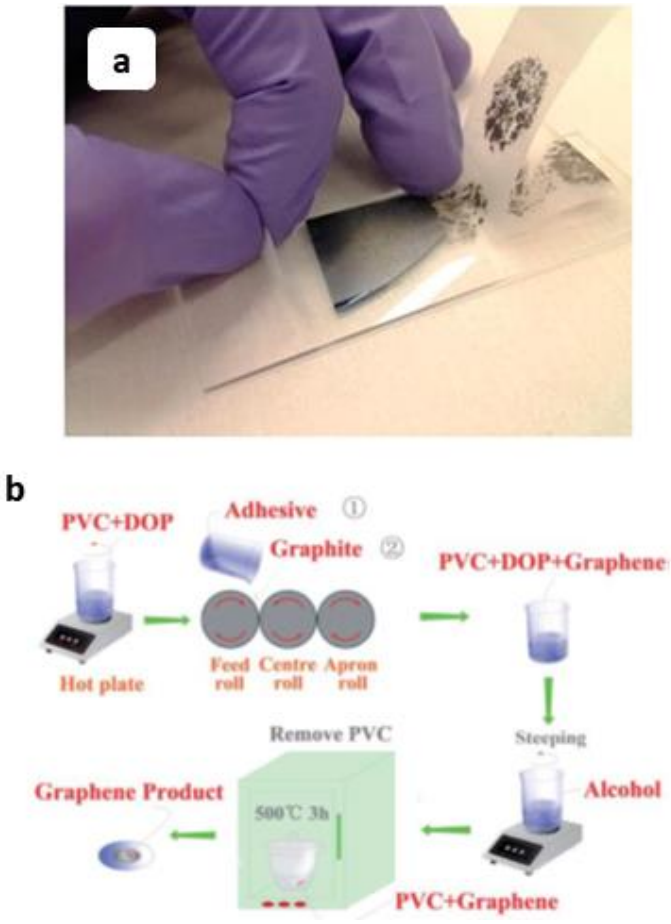

*Figure 2.18 Micromechanical cleavage of graphene. (**a**) Scotch-tape method; image from ref. [75]. (**b**) Continuous production of graphene by mechanical cleavage with a three-roll-mill; figure from ref. [76].*

2. Exfoliation of graphite intercalation compounds (GICs) and graphite oxide. GICs are compounds of graphite with atoms or molecules (such as alkali metals or mineral acids) intercalated between the graphene layers (Figure 2.19). These compounds can be exfoliated more easily than pure graphite. This can be done by rapid heating or by a microwave treatment, obtaining expanded graphite (EG), which is made of thick graphite nanoparticles, generally with specific surface areas <40 m^2/g. EG can be further exfoliated by other techniques, such as sonication in liquid media, to produce GNP <5 nm thick. A similar approach employs graphite oxide, which is obtained when graphite is treated with strong mineral acids and oxidizing agents (Hummers method and its modifications). Then, solvent-based exfoliation, or thermal exfoliation, is finally used to produce individual sheets of graphene oxide (GO), which can be chemically or thermally reduced to restore the basal structure of pristine graphene. Many graphene suppliers base their productions on this type of approach.

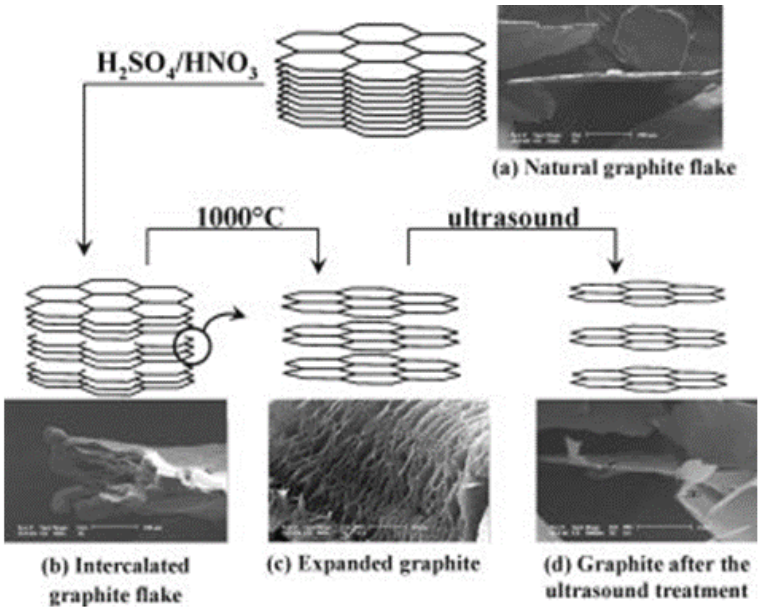

Figure 2.19 Exfoliation of GICs compounds. Illustration of the process for obtaining intercalated graphite, expanded graphite, and graphite nanoplatelets, together with SEM pictures of each product; figure from ref. [77].

3. Liquid exfoliation. These approaches exfoliate graphene sheets from a graphite (or graphite oxide of GICs) powder dispersed in appropriate solvents that guarantee stable graphene solutions, avoiding agglomeration, besides facilitating the energy required to exfoliate. They can employ cavitation energy from a strong sonication treatment (Figure 2.20a) to break down the graphite particles [78]; or shear forces (Figure 2.20b) generated by shear mixers in the liquid media to peel off or slide away the graphene sheets from the graphite particles [79]. This last method has been proved to be efficient even when kitchen blenders are used, and can easily produce large amounts of graphene with industrial shear mixers [79].

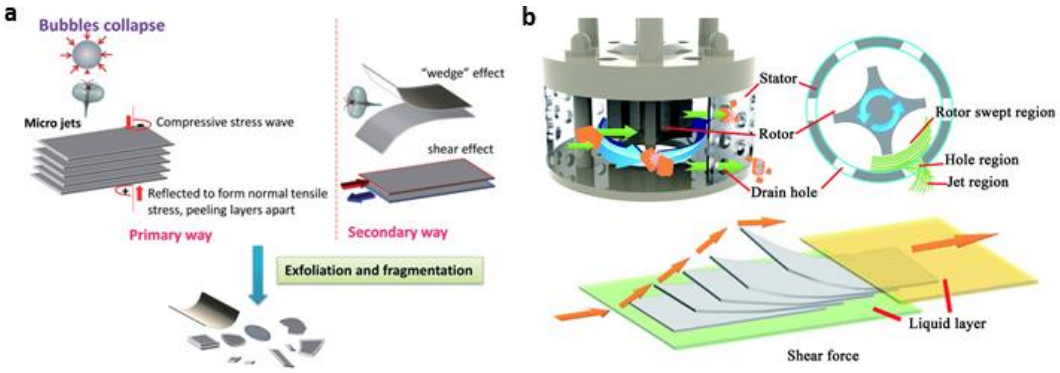

*Figure 2.20 Liquid-phase exfoliation of graphene. (**a**) Representation of the effects of cavitation bubbles on graphite nanoparticles, leading to the exfoliation of graphene; image from ref. [80]. (**b**) Drawing of a shear mixer, which allows liquid-phase shear exfoliation; image from ref. [81].*

4. Electrochemical exfoliation. This approach involves the electrochemical oxidation (or reduction) of a graphite host due to an applied voltage, leading to intercalation of ions from an electrolyte (which may be aqueous, organic or an ionic liquid) followed by exfoliation (Figure 2.21) [82,83]. The production rate of this method can be really high, and the graphene sheets of good quality.

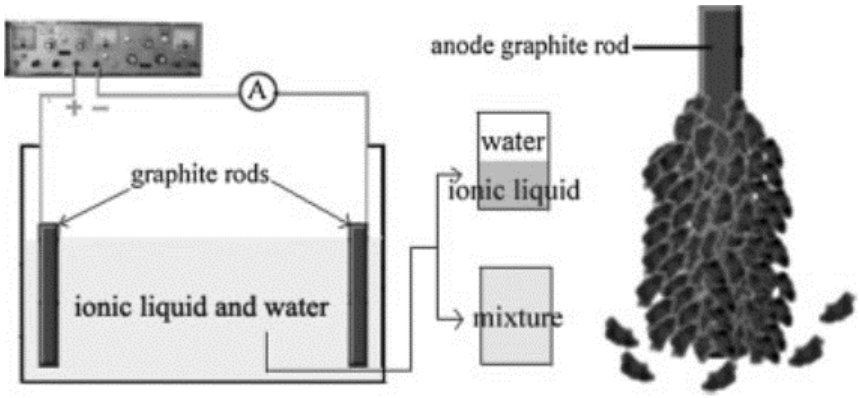

Figure 2.21 Electrochemical exfoliation of graphene. Diagram of an experimental set-up for the exfoliation of a graphite electrode, image from ref. [84].

2.2.1.2 Bottom-up approaches.

The techniques in this category can prepare wide-area (>100 cm^2) graphene sheets, but do not seem to produce high amounts and cheap enough for the purposes of polymer nanocomposites. The graphene sheets obtained with such approaches are mainly used in electronic applications. In general, we can divide the bottom-up methods in two approaches:

1. Chemical vapour deposition (CVD, see Figure 2.22a): graphene is synthesised by thermally degrading (thermal CVD) an organic precursor in vapour state over a heated metallic substrate (usually nickel or copper), or by the action of a plasma in the reaction chamber (plasma enhanced CVD) [22,85]. Plasma-based process are promising techniques able to scale up the production of graphene [86].
2. Epitaxial growth: graphene forms after the surface thermal degradation of a ceramic substrate, such as silicon carbide (Figure 2.22b) [22].

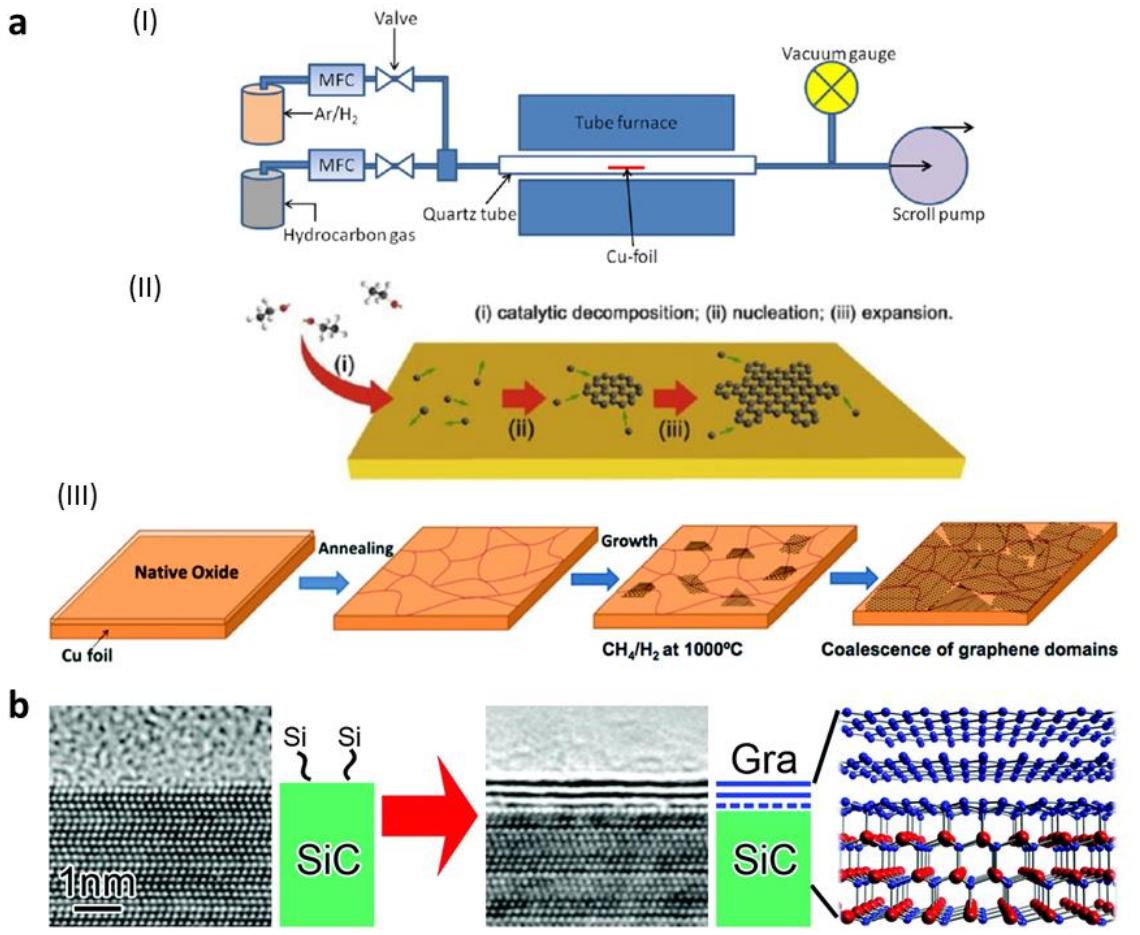

*Figure 2.22 Bottom-up techniques for the preparation of graphene. (**a**) Chemical vapour deposition: schematic diagram of a typical CVD setup (I, image from ref. [87]); simple representation of the steps involved in the formation of graphene (II, image from ref. [85]); another representation of the growth of a graphene sheet with the coalescence of single domains (III, image from ref. [88]). (b) Epitaxial growth of graphene by thermal decomposition of SiC; figure from ref. [89].*

2.2.2 Graphene characterisation

It is worth noting that what is commonly called “graphene” comprises both pristine graphene and GNP in a powder state or suspended inside an appropriate liquid solvent. The quality of this “particle collection” is crucial for the final performances of any composite and device. But how can we evaluate the quality of a produced graphene?

Graphene products are often characterised with methods that are inappropriate for the measurement of platelet-like particles. For example, an important parameter is the average lateral size of the graphene platelets. Unfortunately, methods such as D10, D50, D90 are based on laser diffraction or dynamic light scattering [90] that are relatively straight-forward only for spherical particles. A realistic estimation of the lateral size distribution of the graphene particles can be done only by time-consuming techniques,

for instance scanning electron microscopy (SEM), transmission electron microscopy (TEM), and atomic force microscopy (AFM). Yet, some concerns rise from the number of particles analysed (the reported lateral size is statistically representative of the overall product only if hundreds of particles have been measured) and the method used to prepare the samples for such analysis (for example, the common method of spin-coating a solution of graphene could get rid of the biggest particles that make up most of the particle collection, while a spray deposition can keep all the particles, and homogeneously distribute them on top of the substrate).

Another important characteristic of a produced graphene particle collection is the statistical distribution of the particle thickness. The only ways to get such a distribution is by AFM and TEM. However, good quality graphene collections in terms of thickness are commonly claimed by showing the X-ray diffraction (XRD) spectra, highlighting the small (002) peak around 26° 2θ, or even its absence. This peak is caused by the diffraction of the X-rays through the stacking of the graphene layers in a graphite particle. The higher the number of stacked graphene sheets, the stronger, more intense, and narrower the diffraction peak. This characterisation method can indeed prove the exfoliated state of the particle collection and give an estimation of the average particle thickness. Yet, XRD cannot provide any information about the wideness of the thickness distribution. Therefore, an analysed particle collection could still contain few thick and poor-performing graphite particles that are not “seen” by the XRD [17]. Nonetheless, if only a rough idea of the mean particle thickness is needed, then a quicker way is to look at the BET specific surface area (*S*) of the particle collection, which is a value reported quite often. The mean thickness can be approximately calculated as follow: $t = 2/(d \cdot S)$, where *d* is the density of graphite (2.2 g/cm^3). Thus, graphene powders with a BET >100 m^2/g contain reasonably thin (<10 nm) GNP.

Another important aspect that defines the quality of a particle collection is the presence of defects on the graphene basal plane (also called topological defects). Such defects can be caused, for instance, by the synthesis method that damage the as-produced graphene sheets, or by the functionalisation process. A way to detect these defects is by X-ray photoelectron spectroscopy (XPS), as it quantitatively measures the elemental composition of graphene-like products. XPS is particularly useful, for example, to find the ratio between carbon and oxygen atoms in graphene oxide. The lower the C/O ratio, the higher the functionalisation (oxidation) and the better the interaction with some polymers like epoxy resins (thus the better the dispersions and nanocomposite performances) [91], but also the higher the number of defects, so the lower the intrinsic mechanical and

electrical properties of graphene oxide [92,93]. Another way to characterise the defects is by Raman spectroscopy. Raman spectra of graphene can show three peaks (Figure 2.23a and d): the G-peak at ~1580 cm^{-1} Raman shifts, the 2D-peak at ~2700 cm^{-1}, and a small D-peak at ~1350 cm^{-1}. The intensity of the latter peak is directly related to the presence of both edge and basal defects, and a way to assess the overall amount of these defects is to calculate the ratio between the intensities of the D-peak and G-peak: I_D/I_G, the closer to zero, the better. In case of graphene sheets without basal defects, it has been shown the I_D/I_G ratio can be inversely proportional to the mean length (L) and width (W) of the particles: $I_D/I_G \propto (L^{-1} + W^{-1})$, as the total number of edge defects increases when the lateral sizes decrease [94]. Raman spectra (especially the 2D-peak) can also give information about the thickness of the graphene sheets (Figure 2.23b and c) [78,95], but to be representative of the mean graphene thickness of a particle collection, hundreds of graphene platelets should be analysed.

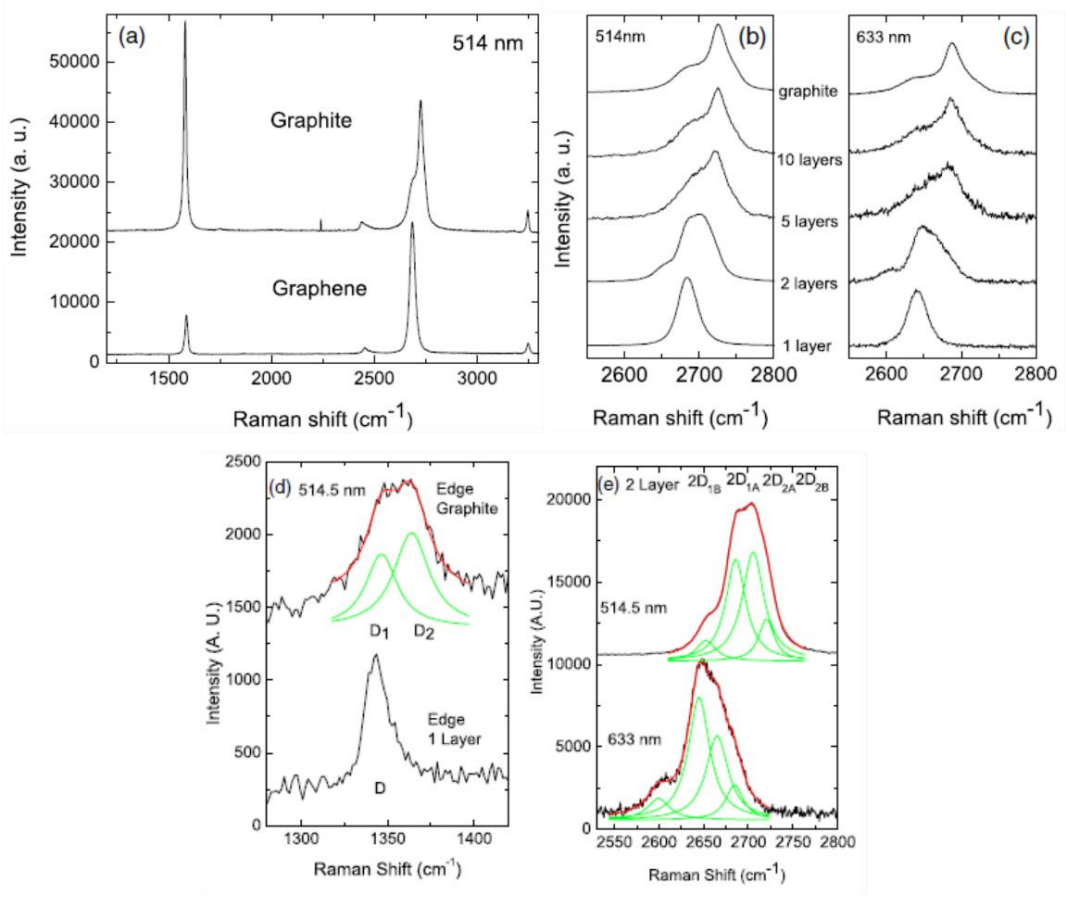

*Figure 2.23 Raman spectra of graphite, graphene and few-layer graphene. (**a**) Comparison of Raman spectra at 514 nm for graphite and single layer graphene. (**b** and **c**) Evolution in 2D band as a function of graphene layers at 514 and 633 nm excitations. (**d**) Comparison of the D band at the edge of bulk graphite and single layer graphene. The fit of the D1 and D2 components of the D band of bulk graphite is shown. (**e**) The four components of the 2D band in 2-layer graphene at 514 and 633 nm. Figure and caption from ref. [95].*

2.2.3 Graphene functionalisation

To improve the dispersion of graphene and increase its interactions with polymers, graphene can be functionalised, i.e. modified with some chemical groups. Many scientific reviews [64,96–100] describe in detail these chemical modifications that we can divide in three different types (Figure 2.24):

1. Covalent functionalisation. The chemical groups are strongly bonded to graphene, and can provide strong interactions with hosting polymers, thus increasing the mechanical and thermal performances of the final nanocomposites. This type of functionalisation is particularly useful if only the edges of graphene are modified [101]. Functionalisation of the basal plane of graphene, such the case of graphene oxide, can introduce too many defects that decrease the mechanical properties and deteriorate the electrical conductivity.

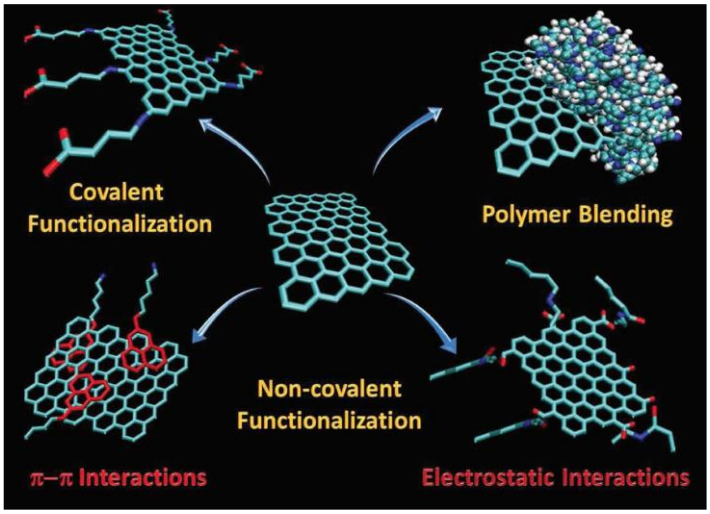

Figure 2.24 Types of graphene functionalisation. Figure from ref. [102].

2. Non-covalent functionalisation by π-π interactions. Aromatic molecules and other compounds (including some types of matrix polymers) can interact with the π orbitals of graphene. These interactions are similar to the bonds between the graphene layers in graphite particles. They are generally weaker than covalent functionalisation, but at least can preserve the integrity of graphene basal plane. Liquid suspensions containing this type of functionalised graphene can give good performing nanocomposites, after a solution mixing process with a desired polymer followed by solvent evaporation.
3. Adsorption. Some molecules (small molecules, like monomers, or long polymer chains) can adsorb on top of the surface of graphene through weak electrostatic

interactions. This approach is useful to prevent the agglomeration of graphene sheets after being exfoliated in liquid media. As in the previous approach, this method can help the preparation of nanocomposites by solution mixing.

2.2.4 Preparation of graphene-based nanocomposites

The preparation of nanocomposites can be grouped in two main categories depending on whether solvents are used or not. In solution-based processes, polymers and nanofillers are initially dispersed in a solvent, so the interactions between polymeric chains and between platelets are minimised, and nanocomposites start building up upon solvent removal. In melt-blending techniques, polymers and nanofillers are two distinct, separated phases that are gradually mixed down to the nanoscale. Lastly, there is a new category that includes processes that differ from solution-mixing and melt-blending techniques, like foam infiltration.

2.2.4.1 Solution-based techniques.

This type of techniques is useful to obtain highly loaded nanocomposites with good anisotropic microstructures. The most common nanocomposites produced by these methods are those with epoxy matrices, or with polymers that are soluble in solvents and/or cannot be processed in melt otherwise can thermally degrade. Unfortunately, the production rates of bottom-up techniques are still quite low (mainly limited by solvent evaporation kinetics), and the amount of nanocomposite obtained is generally so little that these approaches make sense only for thin films/membranes or coating materials, rather than for massive production of structural composites.

Solution-based techniques are based on two different approaches:

1. Solution processing (solution mixing/casting). A solution of graphene and one of polymer are mixed together using several strategies like stirring, tip sonication, bath sonication, mechanical mixing, and shear mixing; and then left the solvent to evaporate or filtrate (Figure 2.25a). During the removal of the solvent, graphene and polymer deposit on the bottom of the solution container (or on top of the filter), building up the final nanocomposite that contains highly aligned graphene sheets. In some cases, the starting solution contains graphene and monomers that, after solvent evaporation, polymerise. Graphene-epoxy nanocomposites are usually prepared in this way [66]. Before the cross-linking

step, the graphene-epoxy mixture can be used for coating or to impregnate fabrics of carbon/glass fibres.

A particular solution processing method consists in solution spinning (Figure 2.25b), which allows to obtain graphene-based nanocomposite in fibres rather than in films [103]. The nanocomposite fibres can be prepared in several ways: by ejecting the starting solution through a nozzle, then coagulating the forming filament in a particular bath, and collecting it with a spinning drum; or by applying an electrical potential between the nozzle and a collecting plate (also called "electrospinning"); or by rotating the nozzle at high speeds ("force-spinning"). In all cases, the forces that pull the forming filaments allow to align the graphene sheets along the fibre axis. These fibres may be interesting not only as mechanical reinforcements, but also for sensing applications once embedded in traditional composites or in garments.

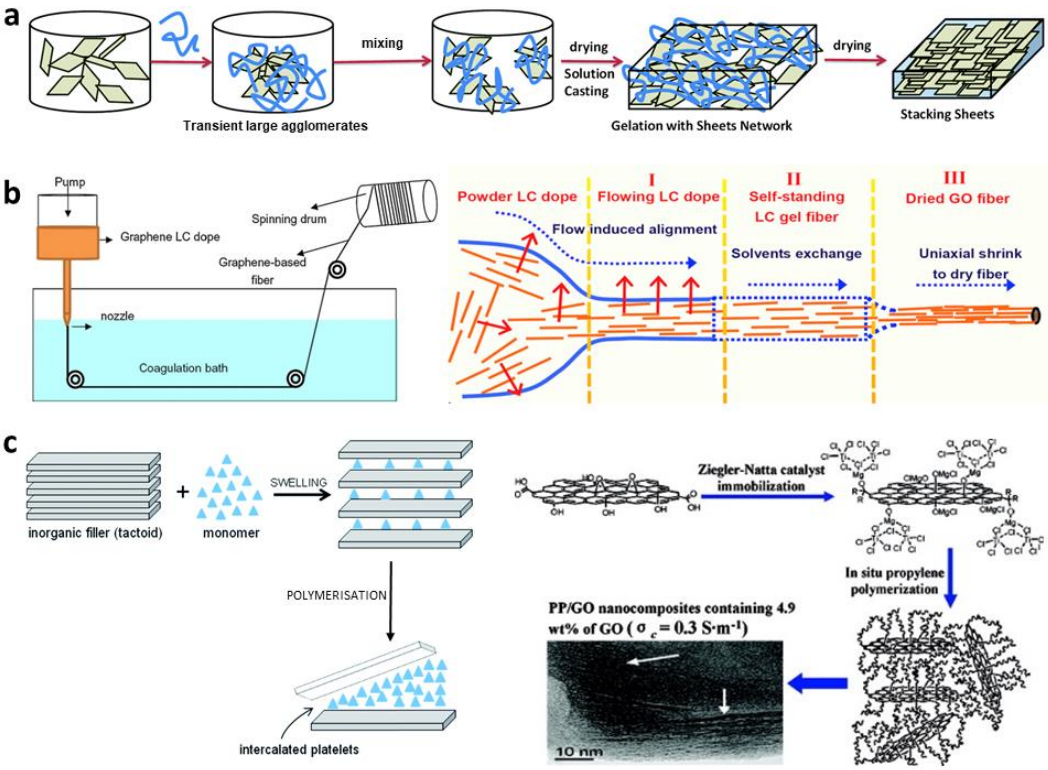

*Figure 2.25 Solution processing techniques for the preparation of graphene-based nanocomposites. (**a**) Solution mixing of polymer (or monomers), with graphene (or functionalised graphene), followed by solution casting; image from ref [104]. (**b**) Illustration of a "wet-spinning" process, together with a representation of the steps involved in the formation of fibres containing aligned graphene sheets; figure from ref. [103]. (**c**) Illustration of in-situ polymerisation with monomers exfoliating thick particles (image from ref. [105]), and an example of in-situ polymerised polypropylene-graphene oxide nanocomposite (figure from ref. [106]).*

Solution processing techniques may suffer from graphene agglomeration at volume fractions >1 vol.% [34]. However, some methods can avoid this problem.

One of them involves the precipitation of the graphene/polymer suspension using a non-solvent for the polymer, causing the polymer chains to encapsulate graphene upon precipitation. In this way, graphene results well disperse in the final nanocomposite, without any chance of agglomeration during the process.
In other situations, liquid monomers (or a solution of monomers) are mixed with functionalised graphene (or graphite nanoplatelets intercalated by monomers). The polymerisation process starts directly inside the solution and may lead to the exfoliation of GNP. Also this approach, called “in-situ polymerisation” (Figure 2.25c) [107], has the advantage of avoiding graphene agglomeration, as the graphene sheets are chemically bonded to the growing polymer chains. The resulting nanocomposites have potentially perfect graphene dispersions, though the graphene sheets are more likely to be 3D randomly oriented.

2. Layer-by-Layer (LbL). These methods are based on the alternated deposition of one-molecule-thick layer of polymer and one of graphene step-by-step on a substrate (Figure 2.26a). The substrate is typically repetitively immersed in a polymer solution, washed to get rid of excess material depositions, immersed in a graphene solution, and washed again [108]. The solutions of polymer and graphene are usually oppositely charged, so that the new depositing material is electrostatically attracted to the previously deposited layer, while electrostatic repulsion provides self-limitation of the absorption of the same material in each layer [109–111]. This type of LbL is called “dip-coating” because the substrate is immersed inside the polymer and graphene solutions, but there are other types of LbL, for example spin-coating, and spray-coating. All LbL methods can potentially give highly loaded nanocomposites with minor agglomerations problems, maintaining the graphene sheets always well aligned along the substrate. However, LbL methods are generally time consuming. The method that can potentially be scaled up more easily and increase the nanocomposites production rate is the spray-assisted LbL [112]. This method can also employ just one solution containing both polymer and graphene (Figure 2.26b), joining the advantages of LbL (high loadings without agglomerations) and solution mixing/casting approaches (higher amounts of nanocomposites in a faster time).

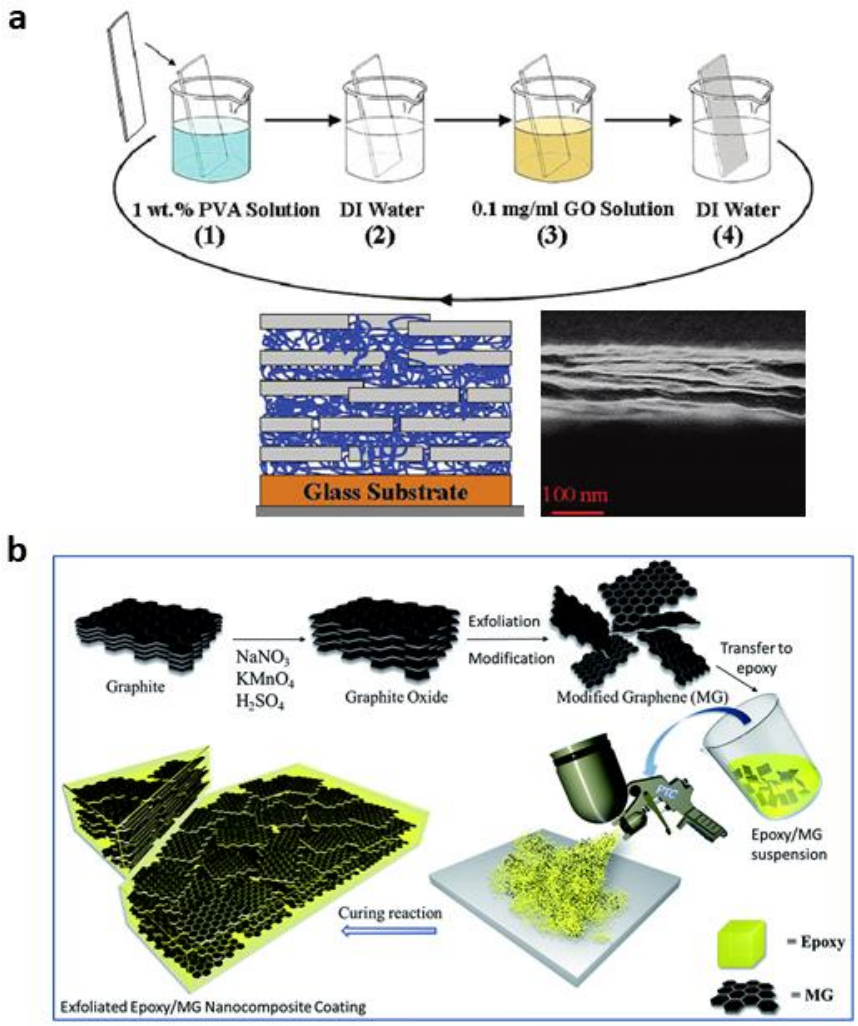

*Figure 2.26 LbL techniques for the preparation of graphene-based nanocomposites. (**a**) Illustration of the Layer-by-Layer assembly, together with a SEM picture of the cross-section of a layered polyvinyl alcohol-graphene oxide nanocomposite; figure from ref. [108]. (**b**) Spray deposition of graphene-epoxy solutions for coating applications; figure from ref. [113].*

2.2.4.2 Melt-based techniques.

Generally, these methods do not involve any solvent during processing and allow fast production rates. Therefore, they are ideal for relatively cheap, industrial preparation of graphene nanocomposites. However, they are not as efficient as solution-mixing techniques in obtaining well aligned microstructures, and highly loaded materials.

Melt-based techniques belong to three main categories:

1. Melt blending/compression moulding. This type of approaches is suitable for the production of thermoplastic polymer nanocomposites. They involve the melting of a polymer and the blending with a graphene powder by using a twin-screw extruder (Figure 2.27a). After these steps, the resulting nanocomposite is cut in

pellets and injection moulded or compression moulded to obtain the final objects. As the industry widely employs these techniques for the production of thermoplastic goods, the final price of nanocomposites produced in this way should be low. Unluckily, it is tricky to compound graphene with polymers, because the graphene powders usually have bulk densities <0.05 g/cm^3. This means that they are extremely airborne, thus also dangerous for the health of people working with the compounding process. A way to make graphene powders less dusty and easier to be introduced inside the extruders is to compress them so that they increase their bulk density [114], or to pre-disperse them in a liquid.

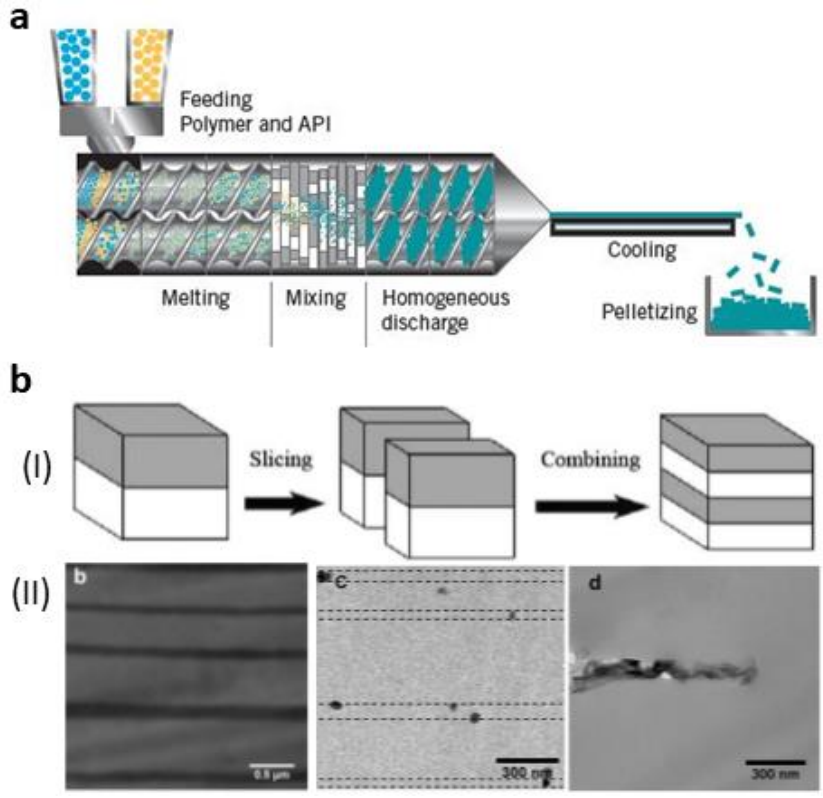

*Figure 2.27 Melt-blending techniques for the preparation of graphene-based nanocomposite. (**a**) Melt-blending of polymers with graphene powders; image from ref. [115]. (**b**) Multilayer coextrusion: sketch of the multilayer formation (I, from ref. [116]), and cross-sections of layered graphene-thermoplastics nanocomposites (II, from ref. [117]).*

Nanocomposites prepared by melt-blending are generally less performing than those produced by solution-mixing. There are many reasons causing this issue: solution-mixing involves already well dispersed graphene suspensions, while melt-blending distribute little-by-little graphene sheets from the initial powder (which can be seen as a huge agglomerate) throughout the melted polymer. The final nanocomposites, though, may still contain regions with graphene

agglomerates. Consequently, higher temperatures, longer blending times, or higher shear rates are used to improve the dispersion. Yet, these approaches may degrade the polymers and the graphene sheets, so the final nanocomposites could show properties even worse than those of neat polymers. The best way to aid dispersion is the functionalisation of graphene, so that it increases its compatibility with the melted polymer. Moreover, after the final compression moulding step, the nanocomposites may not show a completely aligned microstructure, with graphene sheets 3D randomly oriented, especially deep inside the samples.

A way to improve the alignment of nanocomposites prepared by melt-blending is the introduction of some static mixers in the extrusion line. Static mixers are elements that, differently from the screws of extruders, do not move [118]. They change the structure of the composite melt by cutting its flow in two parts, then overlapping these two parts together, and squeezing them, so that the final cross-section of the melt has the same size and shape of the initial one (Figure 2.27b-I). This mechanism is mathematically described by the baker's transformation [119]. As the P&F technique used in this thesis is also based on the baker's transformation, it is worth investigating the effect of static mixers on nanocomposites. By adding several cutting-and-combining static elements (also called multiplying elements or stages) to the extrusion line, the structure of a composite melt becomes organised in 2^n layers, where n is the number of multiplying static elements. This method is commonly called multi-layer co-extrusion, and it has been used to prepare nanocomposites containing well aligned graphene sheets (Figure 2.27b-II) with good in-plane mechanical properties [117], or nanocomposites containing GNP nanoparticles that can be exfoliated during the process, resulting in high effective mechanical reinforcements and improved water barrier properties [120]. Static mixers have been used also to prepare talc and carbon black composites with mechanical and gas barrier properties improving with the number of multiplying stages, but with deteriorating electrical properties because of a more even distribution of the carbon black particles [121]. However, other studies have shown a different electrical behaviour of carbon black/polypropylene nanocomposites, with the percolation threshold and electrical resistivity decreasing with the number of static elements, despite the agglomeration of carbon black decreased with the number of layers [116]. Other electrically conductive multi-layered nanocomposites have been prepared using carbon nanotubes, showing decreasing percolation thresholds and better aligned nanotubes with the number

of layers [122], and improved mechanical properties [123]. Multi-layered nanoclay/polyethylene nanocomposites have been prepared with improved gas barrier properties, and the permeability could be further decreased with an annealing treatment that allowed the interdiffusion of the polymer layers and the confinement/densification of the nanoclays in thinner hosting layers [124]. In any case, melt-blending/multi-layer co-extrusion techniques do not allow reaching high nanofiller contents, otherwise the polymer melts become too viscous and difficult to process because of large nanofiller agglomerates. Besides in multi-layer co-extrusion, static mixers are also used for other applications in the pharmaceutical, petrochemical, water treatment, food, paper and paint industries [118]. Another mixing technique based on the baker's transformation was studied decades ago to blend immiscible polymers together [125], and it involved a press and the manual folding of the samples (in a very similar way in which the P&F samples were prepared in this thesis). This technique requires that the two immiscible polymers must have similar flow behaviours, so that they can be blended down to the nanoscale with a few repetitions of the baker's transformation. The same concept was used later to prepare layered polymer blends with static mixers [126,127].

2. Three-roll mill. A way to prepare graphene-epoxy nanocomposites is to use a three-roll mill (Figure 2.28), which creates high shear forces in the gaps between the rolls, as these rotate in opposite directions.

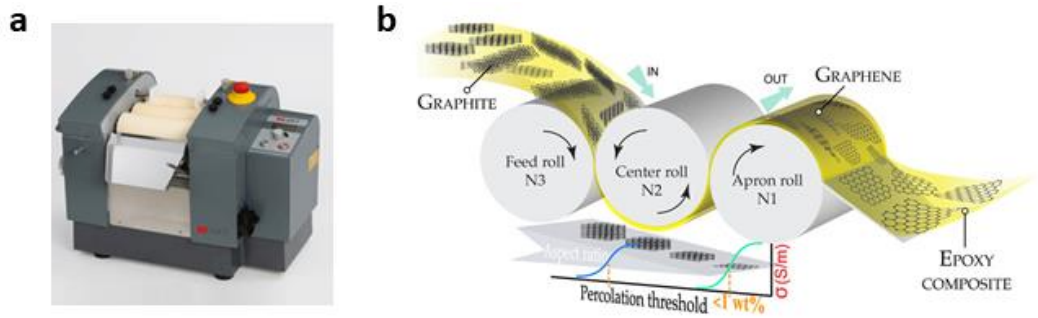

*Figure 2.28 Three-roll mill for the in-situ exfoliation and dispersion of graphene inside epoxy resins. (**a**) Picture of a typical three-roll mill (from ref. [130]), and (**b**) illustration of the process (from ref. [129]).*

Epoxy resins and graphene (that can be pre-mixed together by solution-mixing) are repeatedly introduced inside the gap between the first two rolls, collected from the third roll, and added again to the mill. The high shear forces guarantee a good dispersion of the graphene sheets throughout the epoxy resins, and, under certain conditions, can even exfoliate thick graphite particles [128,129].

This in-situ exfoliation of graphene directly inside the epoxy resins during the dispersion process is a huge advantage, as two steps are executed at once, and the production rate can be much faster than exfoliation/solution-mixing techniques. However, the resulting nanocomposites could present disordered microstructures.

3. Calendering (two-roll mill). Graphene-elastomers nanocomposites can be prepared by solution-mixing, but also by the traditional techniques used to process rubbers. Indeed, two-roll milling can produce well aligned graphene-rubber nanocomposites (Figure 2.29). As graphene powders are airborne and can fly away from the mill rather than be mixed with the rubbers, some tricks must be adopted to avoid this issue, such as pre-compression of the powder in pellets, or pre-blending of graphene with rubber by solution-mixing, or by preparing a slurry of graphene with volatile solvents [131,132].

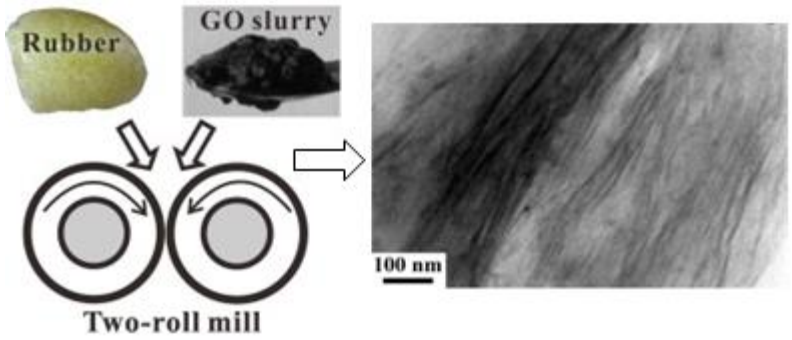

Figure 2.29 Calendering for the preparation of graphene-rubber nanocomposites. Figure from ref. [131].

2.2.4.3 New techniques: foam infiltrations.

New approaches for the preparation of structured graphene nanocomposites have been developed based on the concept of graphene foams infiltration by low viscous polymers, epoxy resins or monomers (Figure 2.30). The graphene foams can be obtained in several ways, for example by sublimating the solvent from a graphene aerogel (Figure 2.30a) [133,137], by CVD synthesis of graphene on a metallic foam template followed by etching of the metal (Figure 2.30b) [134], or by freeze-drying a graphene water solution (Figure 2.30c) [135,138]. The latter approach prepares highly oriented graphene scaffolds thanks to the templating effect of growing ice crystals [139]. The mono-directional freezing of the solution can be induced by placing the bottom of the solution container in contact with liquid nitrogen. The ice crystals are then removed by sublimation. With this method, a graphene scaffold infiltrated with a silicon-based rubber (Figure 2.30d) has

shown self-healing and sensing capabilities [136]. Despite the limited amount of materials processable in such a way, foam infiltration approaches are promising for the preparation of multifunctional devices.

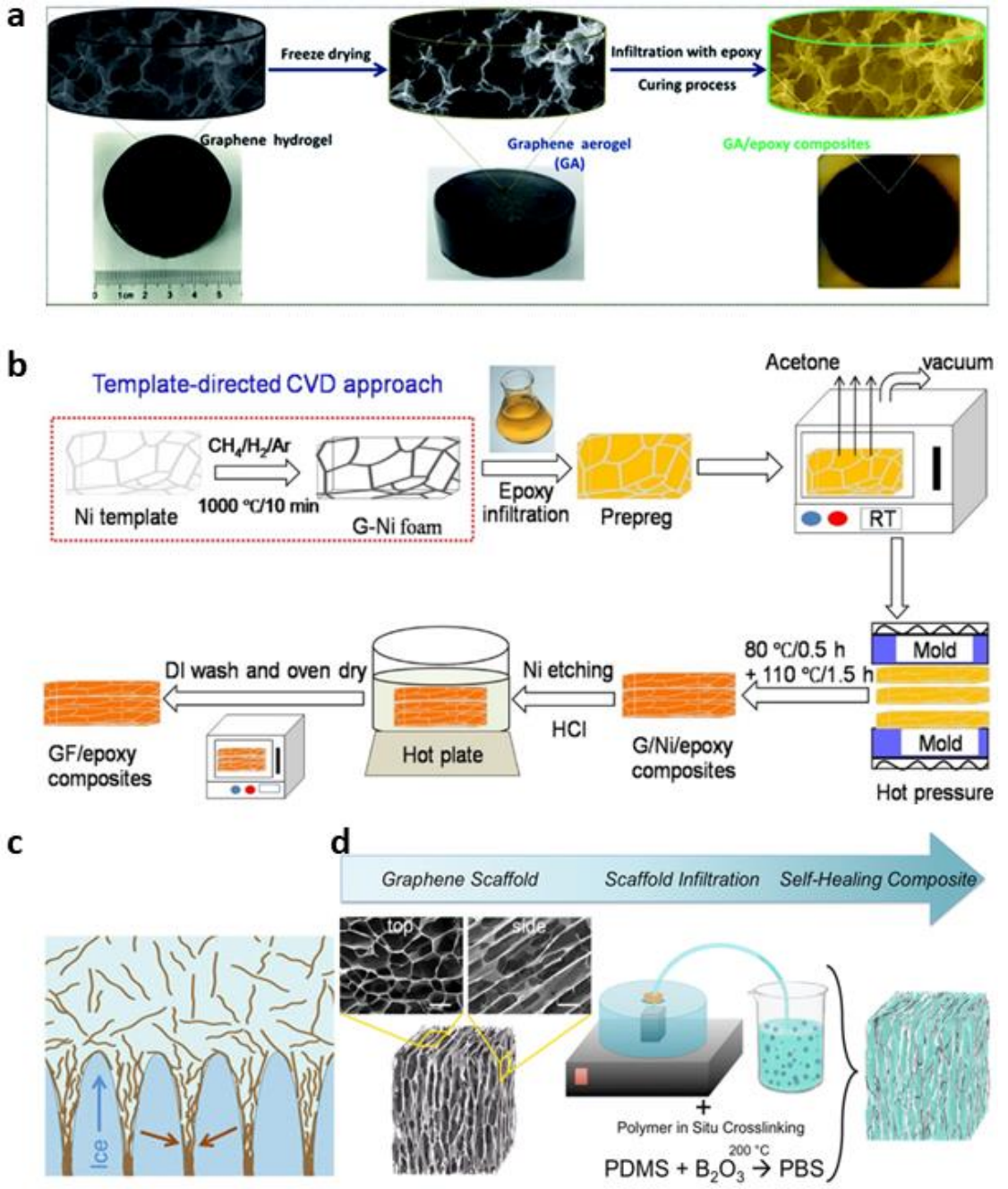

*Figure 2.30 Graphene foams infiltration. (**a**) Epoxy-infiltrated graphene aerogels (from ref. [133]). (**b**) Epoxy-infiltrated CVD-grown graphene foam (from ref. [134]). (**c**) Illustration of graphene scaffold formation by ice growth-templating (from ref. [135]). (**d**) Graphene scaffold-PBS multifunctional nanocomposites (from ref. [136]).*

2.3 Conclusive remarks

Graphene presents huge potentials for the development of technological materials with multifunctional properties. The mechanical reinforcement effect has proven to be effective mainly when little amounts of graphene are contained in the nanocomposites. The control over graphene spatial distribution, orientation and dispersion during the preparation of nanocomposites plays an important role for the achievement of good microstructures that can guarantee high mechanical, electrical, and thermal properties. However, the relationship between the organisation and dispersion of graphene within the polymer matrix and the mechanical and electrical properties of nanocomposites must be further investigated.

In this study, new bottom-up and top-down approaches have been advanced to prepare model nanocomposites with well-defined microstructures to clarify this relationship. The next chapters show how these results have been explained by new theoretical models that consider the nanofiller dispersion and distribution states. They also demonstrate how to take advantage of this ability to control the microstructures to prepare nanocomposites with enhanced multifunctional properties.

Chapter 3.

Materials and methods

3.1 Materials

3.1.1 Materials used for sa-LbL

Poly-vinyl alcohol (PVA) 99+% hydrolyzed (Mw 89000-98000) was purchased from Sigma Aldrich (product number 341584-25G). PVA was dissolved in deionized water by mixing at 200 rpm and 95 °C for 4 h to obtain a solution with a final concentration of 1 wt.%. A 4 mg/mL graphene oxide (GO) water suspension was purchased from Graphenea (Spain).

PVA and GO were chosen because both of them form suspensions in water, so they can be mixed together in the same solution. Moreover, water is not a dangerous solvent.

Poly-styrene (PS) was dissolved in toluene by continuous stirring at 90 °C for 3 h to obtain a 5 wt.% solution, and was spin-coated on glass slides to form a sacrificial layer.

3.1.2 Materials used for melt-processing

Linear low-density polyethylene (LLDPE, density 0.921 g/cm^3, melting point 116 °C, MFI 26 at 190 °C) Flexirene MS20A (Versalis S.p.A., Italy), and expanded graphite (EG, bulk density 0.04 g/cm^3, BET specific surface area 25 m^2/g) Timrex C-Therm 002 (Timcal Ltd, Switzerland) were the most used materials for preparing samples with P&F technique and a twin-screw extruder. LLDPE was chosen because of its low melting point, which would help to speed up the P&F process as it would cool down/melt in a relatively short time (few seconds). EG was selected because we thought that it could be exfoliated in thinner particles down to mono-layer graphene sheets during the P&F process (however, this did not happen, as shown later in the thesis).

Other fillers employed were graphene powder xGnP750 (bulk density 0.2-0.4 g/cm^3, BET specific surface area 750 m^2/g, XG Sciences) and montmorillonite nanoclay (MMT) Cloisite 20A (natural montmorillonite modified by dimethyl, dihydrogenated tallow, quaternary ammonium, with a modifier concentration of 95 meq/ 100 g nanoclay; density 1.77 g/cm^3; bulk density 0.12 g/cm^3; Southern Clay Products).

Other polymers were high-density polyethylene (HDPE, density 0.967 g/cm^3, MFI 1.2 at 190 °C) Surpass HPs 167-AB (Nova Chemicals); polyhydroxy ether bisphenol A

(phenoxy, T_g 92 °C, Mw 52000) PKHH (InChem); polycarbonate (PC, density 1.19 g/cm^3, T_g 145 °C, MFI 17 at 250 °C) Makrolon OD2015 (Covestro); polyamide 6 (PA6, density 1.14 g/cm^3, melting point 222 °C, MFI 25 at 235 °C) Durethan B31F (Lanxess); thermoplastic polyurethane (TPU, density 1.19 g/cm^3, melting point 167 °C) Estane 58437 (Lubrizol); polydimethylsiloxane (PDMS) Silopren C350 (Momentive) that was cross-linked using ketoxime (1.6 mL for 10 g of PDMS).

3.2 Preparation techniques

3.2.1 Sa-LbL

Spray-assisted Layer-by-Layer (sa-LbL) for the preparation of nanocomposites consists in spraying PVA/GO water dispersions with an airbrush. The solutions were sprayed on a glass slide that was previously cleaned with acetone, and corona treated for about 30 s. The glass slide was kept vertically in front of a hot-plate, which was heated up to 80 °C (Figure 3.1). The airbrush was an Iwata HP-C Plus and was kept 30 cm far from the glass slide. The flux of the airbrush was set to 2 mL/min, and the compressed air to 0.3 mPa. The air compressor had an electro-valve connected to a time switcher, that was set in a way to allow the valve to be cyclically open for 60 s and then close for 30 s. In this way, during the OFF time of the valve, the compressed air was not supplied to the airbrush, hence the sprayed material on top of the glass slide could dry properly before new material was added during the next ON time of the compressor valve.

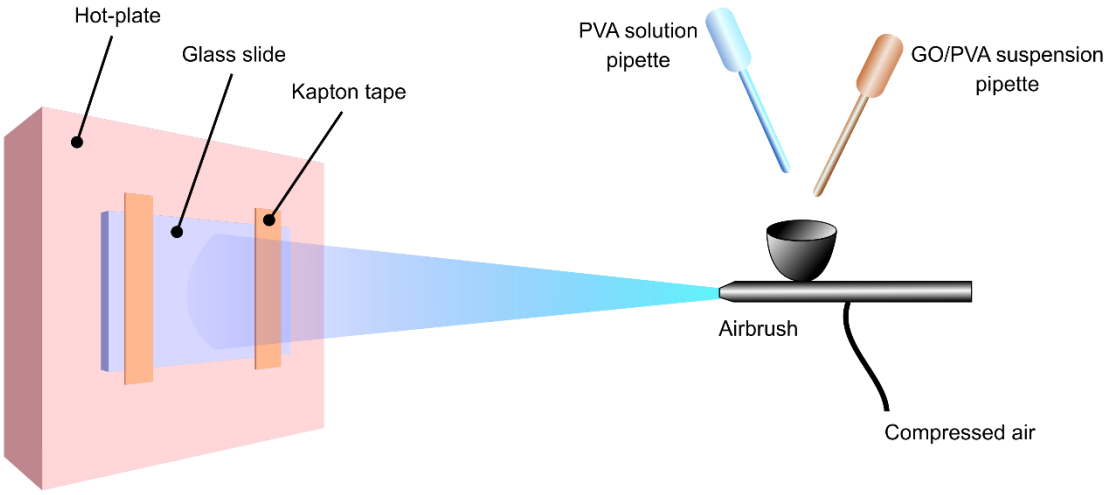

Figure 3.1 *Schematic representation of the sa-LbL technique.*

To create samples with different distributions of GO, two pipettes were used to add materials to the airbrush reservoir. One pipette contained only PVA solution (material “A”), while the other contained a suspension of GO/PVA in different proportions (material “B”). The solutions of these pipettes were added alternatively to the airbrush, creating nanocomposites with a layered structure of $(A/B)_n$ materials, where *n* is the number of layers. In this way it was possible to control the overall concentration of GO in the nanocomposite, the absolute thickness of each layer, the relative thickness of layers B to layers A, and the confinement of GO in layers B (by changing the concentration of GO in the GO/PVA suspension). Because of this deposition approach, this sa-LbL technique should not be strictly considered as a LbL technique, but a variation of solution casting. In fact, the term “layer” used in LbL usually refers to materials thick only one molecule, while in this sa-LbL study, the deposited layers may be much thicker than one polymer chain or than individual GO sheets.

The samples were then thermal treated at 160 °C for 1 hour on top of a horizontal hot-plate, as it has been shown that this treatment is good enough to reduce GO into well conductive reduced graphene oxide [140]. The electrical conductivity of the samples was then measured following the procedure described in the next session.

3.2.2 P&F

The pressing-and-folding (P&F) technique is similar to the process of making the puff pastry for croissants (Figure 3.2a), consisting of repetitive folding and pressing of alternating layers of dough and butter. It is based on the baker’s transformation [119], which is a mechanism already employed by chaotic mixing approaches [141,142] or static mixers used for industrial multilayer co-extrusion of polymers and nanocomposites [143]. Indeed, by iterating the baker’s transformation (Figure 3.2b), two materials can, in principle, be blended down to the nanoscale after only a few cycles.

The P&F technique can be divided in three steps. First, two polymer films are prepared by hot-pressing polymer pellets inside a hot-press (Collin P 300 E). Subsequently, a nanofiller powder is introduced between these films (Figure 3.2c) and hot-pressed at 40 bar at a temperature slightly above the polymer melting point (for LLDPE based nanocomposites, the temperature was 120 °C) for 30 s to join the two materials. In the final processing step, polymer and filler are gradually dispersed by repetitive folding and hot-pressing the film (Figure 3.2d). At each P&F cycle, the sample is manually folded twice in a symmetric manner and pressed at 40 bar and above the melting point of the

polymer for 30 s inside an aluminium frame in order to maintain the resulting thickness at ~300 µm after each pressing. The nanofiller weight concentration inside each sample can be calculated by measuring the weight of the initial polymer films, before and after adding the nanofiller.

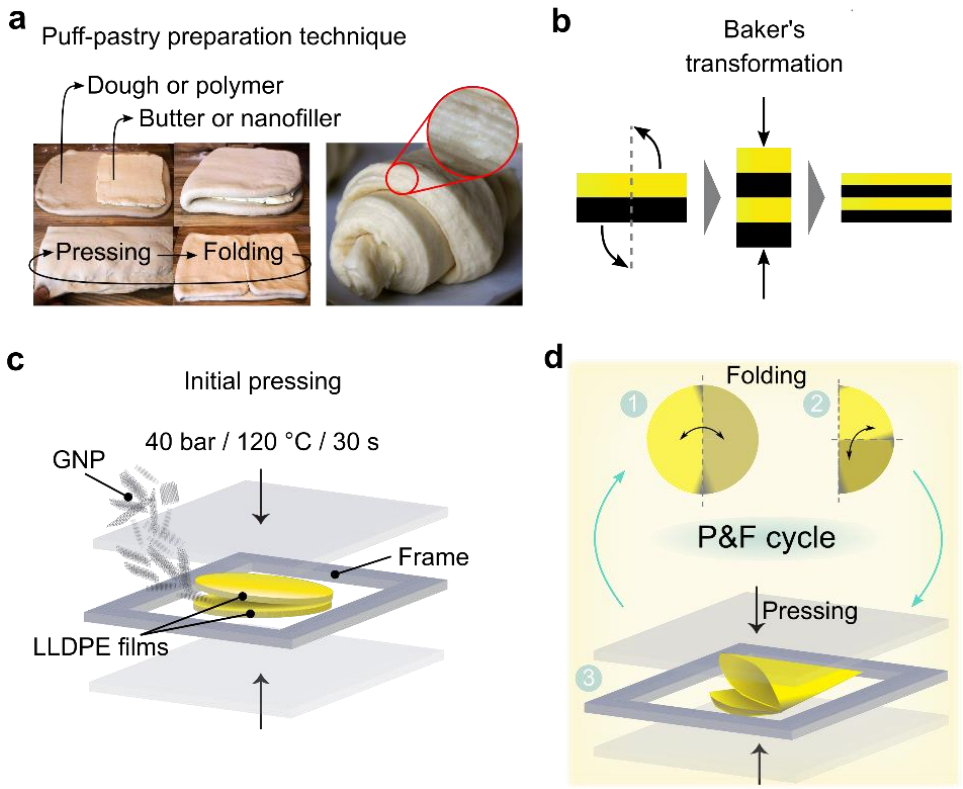

*Figure 3.2 Representation of the P&F technique. (**a** – **b**) Methods that inspired the P&F: puff-pastry preparation process (a), and baker's transformation (b). (**c**) Initial combination of nanofiller and polymer. (**d**) P&F cycle.*

Differently from melt-blending/multi-layer co-extrusion (i.e. techniques also based on the baker's transformation), the P&F allows to prepare samples with a wide range of nanofiller dispersion and distribution states, which is the main reason why it has been used in this study. From this perspective, it is important to note that the possibility of nanofiller re-agglomeration is minimised during the P&F process because the samples are solidified after each pressing step, hence their microstructures are "frozen" (this mechanism is explained in more detailed in chapter 6). Moreover, with the P&F process, it is possible to process high nanofiller loadings in highly viscous blends. This cannot be done with traditional melt blending techniques, as too high viscosities would require too high screw torques, and the blends may not flow. Similarly, the P&F allows to blend materials at temperatures relatively low and close to the melting point of the polymers used, i.e. where their viscosities are high and the possibility to face thermal degradation

is minimised (besides limiting the possibility of nanofiller re-agglomeration, as explained later).

In order to study the properties of the nanocomposites as a function of P&F cycles – corresponding to GNP dispersion and distribution throughout the matrix – samples of LLDPE containing 10.7 wt.% (4.8 vol.%) of GNP were prepared at different P&F cycles. Moreover, a series of samples containing several GNP loadings were prepared at 200 P&F cycles to prove the ability of the technique to disperse high nanofiller amounts with the same efficiency.

3.2.3 Twin-screw extrusion

A reference sample of LLDPE + 10.7 wt.% of GNP was prepared by traditional melt-blending followed by a compression moulding technique. Here LLDPE pellets and GNP were used without drying. The composite was prepared by melt-blending at 120 °C under nitrogen atmosphere using a DSM X'plore 15cc micro compounder. The compounder has a vertically positioned, abrasion and chemical resistant barrel with two detachable, conical mixing screws. In the front and at the back of the barrel there are three separate heating zones to control the process temperature. The compounding materials can be inserted from an aperture located at the top of the screws, and can be brought on top again from the bottom of the screws through a recirculating channel, which allows to blend the materials through the screw for a desired number of times. Compounding was performed for 9 min at a screw speed of 180 rpm. The resulting compound was collected by opening a valve at the bottom of the screws, which closes the recirculating channel. The compound was then hot-pressed at 40 bar and 120 °C for 30 s inside an aluminium frame ~300 µm thick.

3.2.4 Multi-layer co-extrusion

Two single-screw extruders TeachLine E16/E20 (Collin) were connected to a coextrusion adaptor. Pellets of HDPE containing 2 wt.% xGnP750 were introduced to both extruders, which were running at 20 rpm. The temperature profile for both extruders was 190 °C, 210 °C, 220 °C. The melt tubes connecting the extruders with the coextrusion adaptor were kept at 225 °C, and the adaptor at 200 °C. The samples were prepared by changing the number of splitting and recombining multi-layer elements: 1

splitting/recombining pair (corresponding to a composite made of 2 layers), 6 pairs (composite with 64 layers), and 8 pairs (256 layers). The multi-layer elements were set to 175 °C. The die at the end of the multi-layer elements was heated up to 140 °C, and its gap adjusted to 350 µm. The composite films were collected by a flat film line (TeahLine CR72, Collin), with its two clamping rolls kept at a distance of 9.5 cm from the extrusion die. The clamping rolls were heated up to 95 °C and set to a clamping pressure of 2 bar. The speed and torque of the clamping rolls and collector roll of the flat film line were adjusted accordingly to the extrusion speed, without any film stretching to avoid excessive polymer chain orientation along the machine extrusion direction that would impair the comparison of nanocomposites prepared with this technique and P&F nanocomposites.

3.3 Characterisation techniques

3.3.1 Lateral size of particles

The lateral size of the EG powder particles was characterised by scanning electron microscopy (SEM, FEI Inspect-F). One hundred particles were measured for statistical determination of the particles' length and width. The length was considered as the longest side, whereas the width was measured along the normal of the length.

3.3.2 Particle thickness

The thickness of EG powder particles and GO sheets was characterised by atomic force microscopy (AFM, NT-MDT Ntegra) in semi-contact mode. The thickness of a particle was calculated by averaging the height profile. At least twenty particles were measured for statistical determination of particles' thickness.

3.3.3 X-ray diffraction

X-ray diffraction (XRD) studies were carried out at room temperature on a Panalytical X'Pert Pro diffractometer in reflection mode between 5°-70° 2θ and 2.5°-35° Ω, moving

the samples with a spinner revolution time of 4 s. The X-ray tube used a tension of 45 kV, and 40 mA of current. The incident beam employed the k-alpha1 radiation (0.154 nm) of the cupper anode. A filter made of nickel selected the diffracted beam. The crystalline interlayer spacing of GNP was determined by using Bragg's law:

$$d = \frac{\lambda}{2\sin(\theta)} \qquad \textit{Equation 3.1}$$

where λ is the incident wavelength, and θ is the Bragg's angle of the (002) reflection around 26.6° 2θ.

The mean thickness of GNP, and the mean sizes of the LLDPE crystallites were calculated with the Debye-Scherrer's formula [144,145]:

$$T = \frac{0.9\,\lambda}{\beta\cos(\theta)} \qquad \textit{Equation 3.2}$$

where β is the full-width at half-maximum (FWHM) in radians of graphite (002) peak, or LLDPE (110) and (200) peaks around 21.6° 2θ and 23.8° 2θ, obtained from a single Gaussian peak fit between 20°-35° 2θ for EG or xGnP750 powder, and from a multiple Gaussian peaks fit between 10°-35° 2θ for pure LLDPE and nanocomposites samples.

The degree of LLDPE crystallinity (X_c) was calculated from the integrated intensities of the (110) and (200) peaks, and from the area of the amorphous halo on which the crystalline peaks are superimposed, as described by the Hermans-Weidinger method [145,146]:

$$X_c = \frac{I_c^{110} + I_c^{200}}{I_a + I_c^{110} + I_c^{200}} \cdot 100 \qquad \textit{Equation 3.3}$$

3.3.4 Scanning electron microscopy

The microstructures of the nanocomposites were studied by analysing the cross-sections of cryogenically broken samples by scanning electron microscopy (SEM, FEI Inspect-F). The specimens were previously gold-sputtered to cover them with a conductive film 6-8 nm thick. For statistical determination of filler agglomerates contained in nanocomposites of LLDPE + 4.8 vol.% GNP as a function of P&F cycles, diameter (the longest side) and thickness (segment along the normal of diameter) of each filler agglomerate was measured from at least three different specimens for each P&F sample, in order to have at least 100 measured agglomerates per sample. The aspect-ratio of each agglomerate was calculated by dividing its diameter by its thickness. The histograms of agglomerates'

diameter, thickness, and aspect-ratio were fitted with a log-normal function to find out the geometrical mean values as a function of P&F cycles.

3.3.5 Electrical conductivity tests

Electrical conductivity measurements were performed in-plane and out-of-plane of the samples by a 2-points probe connected to a DC system power supply (Agilent 6614c, 0-100V/0-0.5A), and a picoammeter (Keithely 6485, 2nA–20mA). A low electric field from 0 to 1.5 V/mm was applied in both cases in order to avoid a non-linear current-voltage relationship [147], and 20 voltage-current data points were measured and recorded after waiting 100 ms at each 0.075 V/mm interval. For P&F samples, five specimens per sample were tested both for in-plane and out-of-plane conductivity. Length (*L*), width (*W*), and thickness (*T*) of each specimen were measured and recorded before testing (in particular, specimen of 15×8×0.3 mm^3 nominal size were used for in-plane, and 10×10×0.3 mm^3 for out-of-plane measurements). The sa-LbL samples were prepared for electrical measurements by peeling off the two Kapton tapes from the glass substrates (see Figure 3.1) and covering with silver paint the resulting two exposed edges of the nanocomposite coatings. Two copper tapes were then stuck on the glass substrates and put in contact with the silver painted edges of the nanocomposites. These connections were further covered by silver paint. The electrodes of the measuring system described above were clamped to the copper tapes. The electrical conductivity of each specimen, σ, was calculated after a linear fit of the current-voltage data:

$$\sigma = \frac{BL}{WT} \qquad \textit{Equation 3.4}$$

where *B* is the slope of the fitting equation ($y = A + Bx$, with *y* = current, and *x* = voltage).

3.3.6 Tensile tests

Tensile tests were executed following the ASTM D 638-02a standard method with specimen type V, performing five specimens per sample in a universal testing machine (Instron 5566), equipped with a 1 kN load cell. The experimental data points were collected every 10 ms. Width and thickness of each specimen were measured before testing. LLDPE samples were tested at 1 mm/min until a strain of 10% was reached, then the tests continued at 30 mm/min until failure. Nanocomposites and a reference sample of pure LLDPE were tested at 1 mm/min until breakage. The stress-strain curves were

reconstructed using the collected load-extension data points and the specimens' sizes. The elastic modulus of each specimen was determined from the slope of a linear fit of the stress-strain curve over a strain range of 0.25% after the toe's region. The yield point was considered as the first zero-slope point on the stress-strain curve.

Tensile tests of nacre-like PDMS/TPU/MMT nanocomposites were performed on 15×2.5 mm^2 stripes. The initial separation of the clamps was 10 mm, and the cross-head speed 1 mm/min. The testing machine was equipped with a 2.5 N load cell.

3.3.7 Thermal diffusivity tests

Thermal diffusivity measurements were carried out using an incident laser pulse on the sample and recording temperature signal versus time with an IR detector. The thermal conductivity of the samples was calculated by multiplying the recorded thermal diffusivity with the samples' density and heat capacity (the latter was estimated by rule of mixture using a heat capacity of 1.555 J g^{-1} K^{-1} for LLDPE, and one of 0.709 J g^{-1} K^{-1} for GNP).

3.3.8 Self-heating tests

Joule/self-heating experiments were performed by applying a voltage using an AC power source from 0 to 240 V in steps. Current was recorded using a Tenma 72-7765 digital multimeter. Change in temperature on the sample surface was recorded with time by applying thermocouples to at least 3 different points. Thermal images of the samples were taken using a FLIR E40 thermal camera. The samples were placed in between insulating glass fibre mats to avoid heat loss.

3.3.9 Strain-sensing tests

Strain-sensing tests were performed using samples with nominal size of 50×0.3×15 mm^3 in a universal testing machine (Instron 5566), equipped with a 1 kN load cell. The grips were 20 mm far from each other at the beginning of each test. The extremities of the samples were previously coated with silver paint in order to assure a good electrical contact with a 2-points probe setup connected to a DC system power supply (Agilent 6614c, 0-100V/0-0.5A), and a picoammeter (Keithely 6485, 2nA–20mA). Two types of

strain-sensing tests were conducted: cyclic tests consisting of stretching the samples between 0.5 and 3% of nominal strain for five times at a speed of 1 mm/min, and recording the resistance every second; and tensile tests at a speed of 1 mm/min until failure, recording the resistance every second.

3.3.10 Impedance spectroscopy

Impedance spectroscopy measurements were performed between 100 mHz and 1 MHz using a SP-300 (SN 0623) Bio-Logic impedance analyser controlled by the EC-lab software. An AC-potential perturbation of 100 mV was used for all experiments. Nanocomposite films of ~300 µm in thickness were cut with a 1 cm diameter hole puncher. Round samples were placed between two full metallic electrodes that were tightened together with a screw press (*aka.* supercapacitor energy storage module). The permittivity of composites was determined from the impedance data according to the following equations [148]: $\varepsilon' \approx Z''/(Z''^2 + Z''^2)$ and $\varepsilon'' \approx Z'/(Z''^2 + Z''^2)$. As the shape factor (thickness/area) of all samples is equivalent, permittivity magnitudes were compared excluding this value.

3.3.11 Rheology tests

Rheological measurements were performed on a hybrid DHR-3 rheometer (TA instruments) in a parallel plate configuration with a 20 mm geometry. Flow sweeps within shear rates of $1.0 \cdot 10^{-3}$ and 100 s^{-1} were carried out consecutively at 120, 140 and 180 °C with a soak time of 20 minutes between temperatures.

Chapter 4.

Modelling of nanofiller dispersion and distribution effects on nanocomposite mechanical properties

4.1 Introduction

As illustrated in the literature review chapter, it is usually observed that the mechanical reinforcement of graphene nanocomposite becomes smaller than expect with increasing amounts of graphene. In other words, the reinforcement efficiency decreases with nanofiller content. This problem is commonly attributed to graphene agglomeration. It is also noted that nanocomposites containing graphene agglomerates distributed in certain ways within the matrix can decrease the electrical percolation, resulting in nanocomposites with enhanced conductivities.

To describe these effects, we define what dispersion and distribution mean in this study. Dispersion is here intended as the contact area between graphene and matrix. Therefore, saying that graphene is well dispersed means that its surface area is completely in contact with the matrix. Likewise, when graphene is agglomerated means that its surface area is not entirely in contact with the matrix because the platelets are touching each other. This means that graphene is badly dispersed. With the term distribution we intend the spatial position of graphene throughout the matrix. A good distribution indicates that the distance between the centre of mass of one platelet and the centre of mass of its near neighbours is constant for each platelet, and that every platelet has the same coordination number (excluding the platelets on the sample surface). In this situation, the volume fraction occupied by each platelet inside the volume delimited by its near neighbours is the same as the overall volume fraction of graphene contained in the nanocomposite. When graphene is agglomerated, the distribution of the platelets loses its homogeneity within the matrix, and some platelets may occupy a higher or lower local volume fraction than the overall graphene volume fraction.

Using this approach, the term dispersion describes the surface contact of graphene, whereas the term distribution describes the location of the platelets in the 3D space. Dispersion and distribution are not two states always independent from each other, as when the dispersion is bad there must also be a certain degree of bad distribution too, and vice versa. However, we simplify our following discussion by considering the effects of dispersion and distribution separately on the mechanical and electrical properties of nanocomposites.

If we focus on the dispersion state of graphene, we can infer that its effect on the mechanical properties must be decisive. Indeed, the shear-lag theory of Cox is based on the ideal case where there is a perfect contact between nanofiller and matrix [33]. As explained in the literature review chapter, the shear-lag theory describes how efficient is

the shear stress transfer from the matrix to the nanofiller and is used to derive the efficiency length parameter η_L (Equation 2.4). Therefore, the lower the matrix-nanofiller contact, the lower the stress transfer and the lower the mechanical reinforcement effect observed in the nanocomposite. On the other hand, the nanocomposite electrical conductivity is governed by electron tunnelling from one platelet to another one, so if graphene is badly dispersed because the platelets are touching each other, the electrical conductivity may be improved. However, if the graphene agglomerates are localised only in certain zones of the matrix and not widespread and interconnected throughout the composite, the electrical conduction is hampered. In other words, the distribution state of graphene plays a major role on the electrical conduction than the dispersion state does. Therefore, we can make an initial approximation by stating that the dispersion state of graphene has an effect only on the nanocomposite mechanical properties.

If now we consider the distribution state of graphene, we already know that it is fundamental for determining the nanocomposite electrical conductivity. However, what about the effect of graphene distribution on the mechanical properties? To answer this question, we can ideally divide a nanocomposite with a bad graphene distribution in two zones: one graphene-rich zone, and one graphene-poor zone. If the graphene-rich zone is split in many small sphere-like volumes distributed throughout the graphene-poor zone, then the nanocomposite mechanical reinforcement can be roughly calculated using the IRoM (Equation 2.2) after substituting E_f and E_m with the moduli of the graphene-rich and graphene-poor zones, and V_f and V_m with the volume fractions of the graphene-rich and graphene-poor zones. This means that the distribution state of graphene could have bad effects on the nanocomposite mechanical properties.

This current chapter attempts to describe and predict the effects of graphene dispersion and distribution on the nanocomposite mechanical properties. The next chapter is instead focused on the effect of graphene agglomeration on the electrical properties of nanocomposites.

4.2 Effect of nanofiller dispersion on mechanical properties

As mentioned previously, when there is no perfect contact between nanofiller and matrix due to a bad dispersion, there cannot be a good stress transfer from matrix to nanofiller, and the platelets inside the agglomerates cannot give their contribution to the

nanocomposite mechanical properties. Thus, only one portion of the nanofiller volume fraction effectively reinforce the matrix:

$$V_f^{eff} \equiv D \cdot V_f \qquad \textit{Equation 4.1}$$

V_f^{eff} is the effective reinforcing volume fraction, V_f is the nominal volume fraction, and D is a dispersion factor, which ranges from 0 (nanofiller and matrix completely not in contact) to 1 (nanofiller perfectly dispersed and completely in contact with the matrix). It is important to note that the D factor is valid only for those nanofillers that, when perfectly distributed in a nanocomposite, can form perfect contacts with the matrix, as assumed by the shear-lag theory of Cox. Thanks to the D factor, we have now a parameter that can quantify the dispersion level of graphene or GNP inside nanocomposites. V_f^{eff} can then be used instead of V_f inside any composite theory to predict the properties of any nanocomposite if its nanofiller dispersion level is known, or, contrariwise, to back-calculate an unknown D-factor.

As we have defined the dispersion as the nanofiller-matrix contact area, then the D factor must depend on the contact area too. However, defining *a priori* how the D factor varies with the overall nanofiller-matrix contact area, A_c, is challenging. In first approximation and to avoid to over-parameterise the model, we could define the following relation:

$$D \approx \frac{A_c}{A_p} \qquad \textit{Equation 4.2}$$

where A_p is the nanofiller surface area that can be easily calculated by multiplying the nanofiller specific surface area by the amount of nanofiller introduced in the nanocomposite. In this way, when $A_c = 0$ (no contact between nanofiller and matrix), then also D is zero, and when $A_c = A_p$ (nanofiller perfectly in contact with the matrix), then $D = 1$. According to Equation 4.2, the D factor could indirectly be measured by estimating the local nanofiller-matrix contact area from a nanocomposite microstructure, which could potentially be done, for example, from SEM and TEM observations [149], although these methods reveal local information only [150], and might not be representative of the overall nanofiller dispersion state. Note that the local D factor calculated from SEM/TEM observations may not be valid to correlate the local reinforcement of a nanoparticle (Equation 4.1) with its dispersion state (Equation 4.2). For example, we can consider two cases where a disc-like nanoparticle has D = 50%, i.e. half of its surface is in contact with the matrix. In the first case, the nanoplatelet is located at the edge of an agglomerate, with half of its diameter trapped inside the agglomerate and the other half embedded in the matrix. In the second case, the nanoplatelet is located at the surface of

the agglomerate, and has one face toward the agglomerate and the other face in perfect contact with the matrix. For simplicity, we do not consider any stress concentration effect inside the matrix caused by the presence of the agglomerate. In the first case, it is straightforward to consider only half of the nanoparticle volume as the responsible for the local mechanical reinforcement. In the second case, it is not very clear the amount of stress that can be transferred from the matrix to the nanoparticle, so Equation 4.2 should not be used inside Equation 4.1. In other words, the approximation of Equation 4.2 is not reliable at the nanoscale.

Moreover, the dispersion state of each individual nanoparticle could be different, depending on whether the nanoparticles are located on the surface of an agglomerate or deep inside the agglomerate. This heterogeneity of the dispersion states of the nanoparticles poses a challenge on what value should be used to represent the overall dispersion state of the nanoparticles and, ultimately, to describe the mechanical properties of a nanocomposite affected by nanofiller agglomeration.

For all these reasons, we can consider the *D* factor only as a global parameter to describe the stress-transfer efficiency of nanocomposites containing agglomerates, and it may not correspond to a mean dispersion value calculated using the individual dispersion states of each nanoparticle observed under SEM and TEM. From this perspective, a better way to represent the *D* factor is by considering the overall nanofiller-matrix contact area, A_c, rather than the local nanoparticles-matrix contact area. We can indirectly evaluate how A_c varies during the synthesis of a nanocomposite, and how it changes when nanocomposites contain increasing amounts of nanofiller. As these aspects depend on the nanocomposite preparation technique, we show below how A_c can be estimated for the two most commonly employed processes of melt-blending and solution mixing/casting. Consequently, we can investigate how the *D* factor changes for these techniques, how it is influenced by the nanofiller volume fraction and, ultimately, how the mechanical properties are affected by the nanofiller agglomeration.

4.2.1 Dispersion-factor for solution-mixing/casting processes

Solution-mixing followed by solution casting is a technique where nanocomposites are formed by the assembly of nanoparticles with polymers at the nanoscale level when solvent is started being removed (solution casting). During this process, nanocomposites grow up in volume with solvent evaporation, but nanofiller agglomeration may happen when the nanofiller concentration is higher than the critical volume fraction at which

rigidity percolation occurs. Rheological studies of viscoelastic properties of graphene suspensions reported in literature [151] suggest that this critical volume fraction, V_f^c, is proportional to the nanofiller aspect-ratio, ξ:

$$V_f^c \approx \frac{1.5}{\xi} \qquad \textit{Equation 4.3}$$

Above V_f^c, the nanoparticles may start touching each other, forming an interparticle agglomeration contact area, A_g. The variation of A_g may depend on the following factors:

- Variation in nanofiller volume fraction, ΔV_f;
- Difference between V_f and V_f^c because nanofiller agglomeration when V_f is lower than V_f^c is unlikely to occur;
- Difference between the total surface area of the nanoparticles, A_p, and the actual agglomeration contact area: $A_p - A_g$. In fact, when all nanoparticles are completely agglomerated, it is impossible to further increase the agglomeration contact area;
- s, which is a parameter that describes how fast the nanoparticles agglomerate. This parameter may be influenced by different aspects such as the nature of the nanoparticles (if nanoparticles interact with one another with strong Van der Waals forces, they are likely to agglomerate quickly); functionalisation of nanoparticles or polymers (if nanoparticles are bonded to the polymer matrix, it will be less likely that they agglomerate); and nanoparticle aspect-ratio (the higher the aspect-ratio, the more difficult is to control the configuration of the nanoparticles, and the more likely the nanoparticles crumple or fold).

These aspects can be translated into the following equation:

$$\Delta A_g(V_f) = \Delta V_f \cdot \left(V_f - V_f^c\right) \cdot s \cdot \left(A_p - A_g(V_f)\right) \qquad \textit{Equation 4.4}$$

When $\Delta V_f \rightarrow 0$, Equation 4.4 becomes a differential equation. We can find the following solution to this differential equation knowing that when $V_f = V_f^c$, A_g is zero:

$$A_g\left(V_f\right) = A_p - A_p e^{-s\left(V_f - V_f^c\right)^2} \qquad \textit{Equation 4.5}$$

Eventually, considering that the nanofiller-polymer contact area A_c is given by the difference $A_p - A_g$, we can derive the dispersion factor for a solution-mixing/casting process:

$$D_{s-m/c}(V_f) = \begin{cases} 1 & \text{for } V_f \leq V_f^c \\ e^{-s\left(V_f - V_f^c\right)^2} & \text{for } V_f > V_f^c \end{cases}$$

Equation 4.6

By introducing $D_{s\text{-}m/c}$ inside V_f^{eff} (Equation 4.1), and substituting V_f with V_f^{eff} in any classical composite theories such as the GRoM (Equation 2.3) or the Halpin-Tsai equations [152–154], we can predict or describe the mechanical behaviour of casted nanocomposites affected by nanofiller agglomeration.

For example, we can select some literature data for graphene and another 2D material like boron nitride (BN) that have a narrow and well-defined distribution of nanoparticle aspect-ratios [34,155], and fit these data using the Halpin-Tsai model modified by V_f^{eff}, leaving *s* as the only fitting parameter. Figure 4.1 shows that the data can be well fitted indeed, proving that V_f^{eff} and $D_{s\text{-}m/c}$ are able to describe the loss of reinforcing efficiency always observed in nanocomposites with the increase of V_f (see section 2.1.1.2). A powerful feature of our method is that ξ is used both to determine the slope of the reinforcement and the volume fraction at which agglomeration begins.

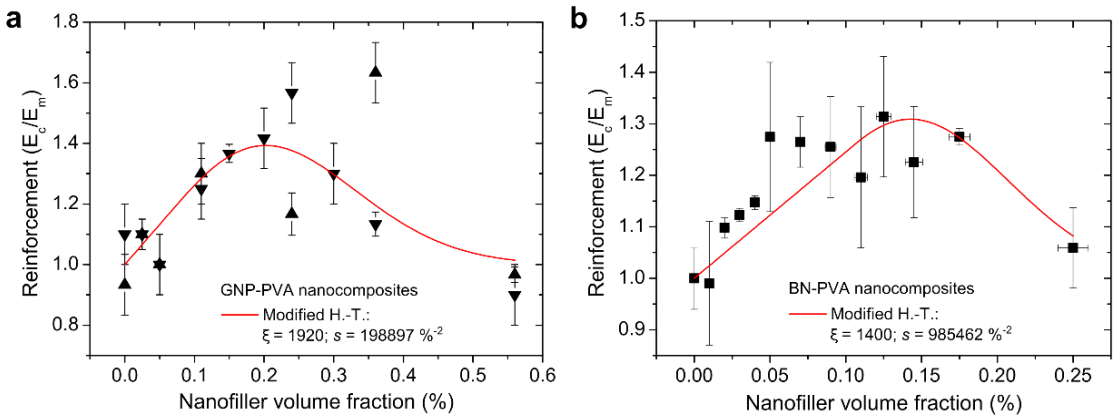

*Figure 4.1 Mechanical reinforcement of nanocomposites prepared by solution-mixing/casting. (**a**) Graphene/polyvinyl alcohol (PVA) nanocomposites literature data [34]. Note that two independent sets of samples are reported as indicated by the different symbols. These sets of data were simultaneously fitted using the modified Halpin-Tsai model with E_f = 1 TPa, E_m = 3 GPa and ξ = 1920 [34], leaving "s" as the only adjustable parameter. (**b**) BN/PVA nanocomposites literature data [155], with a fitting line using the modified Halpin-Tsai model with E_f = 850 GPa [156], E_m = 2.55 GPa and ξ = 1400 [155], leaving "s" as the only adjustable parameter.*

In Figure 4.1, we observe that BN nanocomposites start losing reinforcement efficiency at a volume fraction lower than that of GNP nanocomposites (~0.15 vol.% vs. ~0.2 vol.%), despite BN platelets have a lower ξ so their V_f^c = 0.11 vol.% is higher than V_f^c = 0.08 vol.% of GNP. This is because *s* (which describes how fast the agglomeration occurs) results 5 times higher for BN than GNP. To explain this higher agglomeration rate, we may infer that BN has a lower compatibility with PVA, but we also note that BN has a broader ξ distribution containing platelets with ξ up to 3000 [155], so agglomeration

could be facilitated by these platelets. Therefore, even if nanoplatelets with high aspect-ratios give the highest mechanical reinforcements, they can also be responsible for agglomeration to occur at quicker rates. This is a dramatic drawback if highly loaded nanocomposites are need by demanding mechanical applications.

Lastly, we remark that the fitting curves in Figure 4.1 are based on the assumptions that the loss of reinforcing efficiency with increasing V_f is only due to worsening nanofiller dispersion states and that the approximation made by Equation 4.2 is valid. Hence, the fitted values of *s* must be taken with caution. Indeed, these assumptions may not be always true, and other factors could explain the decrease of reinforcing efficiency with increasing V_f, like the deterioration of nanofiller distribution, as explained afterwards.

4.2.2 Dispersion-factor for melt-blending processes

The increase of contact area, $A_c(t)$, between graphene and polymer during a melt-blending process may depend on the following aspects:

- Extent of the processing time interval, Δt;
- Distribution rate, *I*, which is a constant that describes how fast the nanofiller is being distributed and dispersed during the process. This factor *I* depends on the type of nanofiller and polymer used, but also on the shear rate and stress applied by the blending instrument, nanofiller or matrix functionalisation and polymer viscosity;
- Difference between the total surface area of the nanofiller particles, A_p, and the actual interfacial area with the matrix: $A_p - A_c(t)$. In fact, when all particles are in contact with the matrix ($A_c(t) = A_p$, i.e. perfect nanofiller dispersion) it is impossible to further increase the nanofiller-matrix interface, and distribution is the only phenomena left to occur in the process.

These considerations can be expressed by the following differential equation:

$$\partial A_c(t) = \partial t \cdot I \cdot \left(A_p - A_c(t)\right) \qquad \textit{Equation 4.7}$$

Supposing that A_0 is the initial interfacial area at $t = 0$, then a solution of Equation 4.7 may be the following:

$$A_c(t) = A_p - (A_p - A_0)e^{-I \cdot t} \qquad \textit{Equation 4.8}$$

By introducing $A_c(t)$ into Equation 4.2, we can find how the dispersion state of graphene evolves during a melt-blending process:

$$D_{m-b}(t) = 1 - \frac{(A_p - A_0)}{A_p} e^{-I \cdot t} \qquad \textit{Equation 4.9}$$

Note that that the *I*-factor, hence $D_{m\text{-}b}$, may be influenced by some aspects that can deteriorate both the polymer and the nanofiller, such as the delivered extrusion power, high processing temperatures and a prolonged processing time.

It is interesting to investigate the effect of the pre-exponential term, $(A_p\text{-}A_0)/A_p$, on $D_{m\text{-}b}$ at the beginning of the process, i.e. for t → 0. Depending on the amount of nanofiller introduced in the blending instrument, $(A_p\text{-}A_0)/A_p$ ranges from 0 to 1. Figure 4.2a shows how $D_{m\text{-}b}$ decreases for increasing A_0/A_p ratios. For extremely low amounts of nanofiller or for nanofillers with very low specific surface areas ($A_0/A_p \rightarrow 1$) the dispersion state could be optimum already at the very beginning of the melt-blending process. Moreover, Figure 4.2a shows that high amounts of nanofiller or nanofillers with high specific surface areas ($A_0/A_p \rightarrow 0$) require longer times to reach an optimal dispersion during processing.

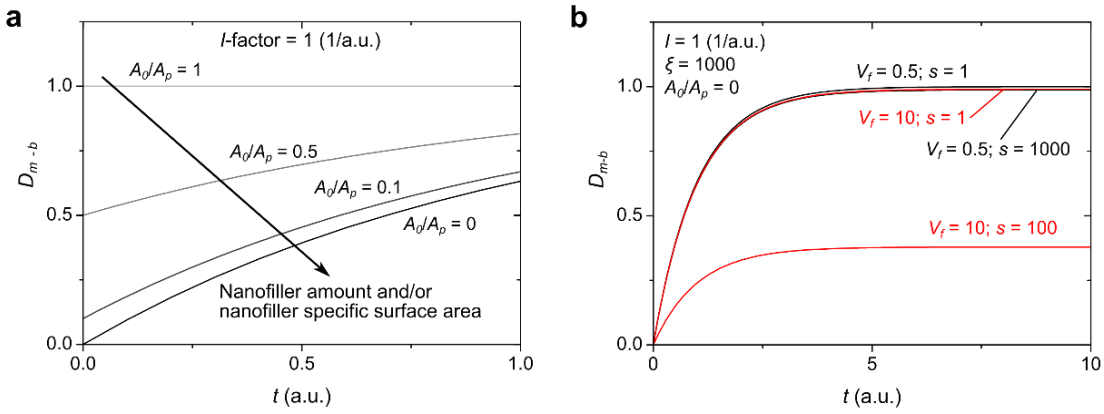

*Figure 4.2 Nanofiller dispersion state in nanocomposites prepared by melt-blending as a function of processing time. (**a**) $D_{m\text{-}b}$ predicted by Equation 4.9 and for increasing nanofiller amounts or specific surface areas (A_0/A_p ratios). (**b**) $D_{m\text{-}b}$ predicted by Equation 4.10 for two different volume fractions and agglomeration rates.*

When $A_0/A_p \rightarrow 0$, $D_{m\text{-}b}$ seems to be independent from the nanofiller amount and initial contact area. If this is true, then any amount of nanofiller could potentially be perfectly dispersed, and the reinforcing efficiency should not decrease with V_f. Unfortunately, this is never observed in nanocomposites. The rigidity percolation of the platelets is responsible again for the nanofiller agglomeration. Thus, it does not matter how long the blending process last, or how much power the process delivers: the interactions between platelets will form again in the polymer melt when the nanofiller concentration is above

V_f^c. This situation is even worsened by the fact that the platelets are initially all agglomerated ($A_0/A_p \rightarrow 0$).

Therefore, we need to correct our assumption relative to the highest reachable nanofiller-matrix interface: in Equation 4.7, we cannot use the difference ($A_p - A_c(t)$), but ($A_{max} - A_c(t)$), where A_{max} is the maximum nanofiller-matrix contact area allowed by a certain nanofiller volume fraction above V_f^c. We can find an expression for A_{max} as a function of V_f in the same way we did it for the nanofiller-matrix contact area in a solution-mixing process: $A_p e^{-s\left(V_f - V_f^c\right)^2}$, so $D_{m\text{-}b}$ becomes the following:

$$D_{m-b}\left(t, V_f\right) = \begin{cases} 1 - \left(1 - \dfrac{A_0}{A_p}\right) e^{-I \cdot t} & \text{for } V_f \leq V_f^c \\ e^{-s\left(V_f - V_f^c\right)^2} - \left(e^{-s\left(V_f - V_f^c\right)^2} - \dfrac{A_0}{A_p}\right) e^{-I \cdot t} & \text{for } V_f > V_f^c \end{cases} \qquad \textit{Equation 4.10}$$

Consequently, the best dispersion level obtainable in melt blended nanocomposites processed for a time $t \rightarrow \infty$ is also defined by Equation 4.6. Figure 4.2b shows the effect of V_f and s on $D_{m\text{-}b}$ as a function of processing time. When V_f is close to V_f^c, it does not matter how fast the nanofiller could agglomerate (parameter s), the dispersion level always reaches a plateau close to 1 during processing. But when $V_f >> V_f^c$, then s plays a crucial role, and the plateau of $D_{m\text{-}b}$ results much smaller than 1. Again, this means that nanofillers with high ξ give the highest reinforcements, but also the smallest V_f^c, so it is impossible to well disperse them in high concentrations.

4.3 Representation of a graphene distribution state

To understand how the distribution of graphene affects the microstructure, hence the properties of nanocomposites, we need to introduce some parameters able to describe the distribution state of graphene. First, we divide the volume of a nanocomposite into two zones: a graphene-rich zone and a graphene-poor zone, with the latter one surrounding the first one (Figure 4.3b). Then, we denote the volume fraction of the graphene-rich zone as V_g (so the volume fraction of the graphene-poor zone is 1-V_g) and the fraction of the graphene sheets inside the graphene-rich zone out of the total number of graphene sheets as g (so the fraction of platelets in the graphene-poor zone is 1-g). Consequently, the concentration of graphene inside the graphene-rich zone is the following:

$$V_{fg} = \frac{g}{V_g} V_f$$ *Equation 4.11*

and the graphene concentration inside the graphene-poor zone:

$$V_{fp} = \frac{(1-g)}{(1-V_g)} V_f$$ *Equation 4.12*

From these equations, it follows that the volume fraction of the graphene-rich zone varies within the range $gV_f \leq V_g \leq g$, and the fraction of graphene inside the graphene-rich zone within $V_g \leq g \leq 1$. Figure 4.3c shows the effect of the parameter g on a nanocomposite microstructure, whereas Figure 4.3d the effect of V_g. When $V_g = g$, the distribution results homogeneous.

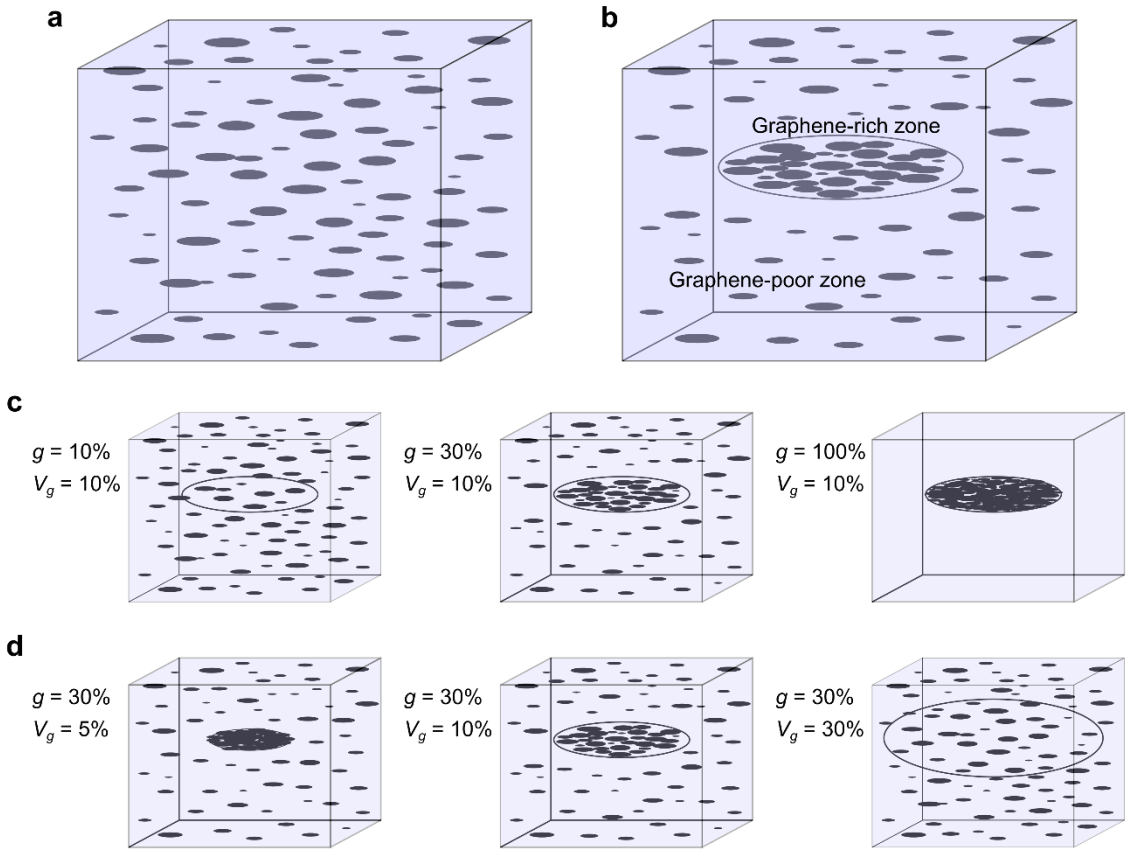

*Figure 4.3 Representation of different graphene distribution states inside nanocomposites. (**a**) Homogeneous distribution. (**b**) Inhomogeneous distribution, and partition of a nanocomposite volume into one graphene-rich zone, and one graphene-poor zone. (**c**) Effect on the microstructure of the percentage of graphene sheets distributed inside the graphene-rich zone (parameter g). (**d**) Effect on the microstructure of the volume fraction of the graphene-rich zone (parameter V_g).*

Note that when $V_g > g$, we have an inverted microstructure: the graphene-poor zone is surrounded by the graphene-rich zone, thus V_g will denote the volume fraction of the graphene-poor zone and g the percentage of graphene sheets inside the graphene-poor zone. We will not consider such situation.

The graphene-rich zone is not just one ellipsoidal volume as one may think by looking at Figure 4.3, but it consists of many graphene-rich volumes distributed all over the nanocomposite with an average aspect-ratio ξ_g, average lateral size l_g, average thickness t_g, and average orientation η_{og}. Therefore, a distribution can result homogeneous not only when $g/V_g = 1$, but also when $g/V_g = 1/V_f$ if $l_g \rightarrow L$ (average graphene sheets lateral size) and $t_g \rightarrow t$ (average graphene thickness). In this case, the graphene-rich volumes are exactly the graphene platelets themselves. If a system approaches this situation where $V_g \rightarrow gV_f$, we can represent the degree of inhomogeneity of its graphene distribution with the ratios l_g/L, t_g/t and ξ_f/ξ_g. The l_g/L and t_g/t ratios should always have values ≥ 1, unless the platelets are buckled or rolled up.

To understand how a graphene distribution changes with the amount of graphene, we need to find some expressions for g and V_g as a function of V_f. We can suppose that the variation of g with V_f is influenced by the following aspects:

- Variation of graphene amount ΔV_f;
- A proportional factor α_g that describes how fast g increases with V_f;
- Difference $V_f^{max} - V_f$, as when graphene reaches the maximum volume that can physically occupy, g becomes 1 and cannot further increase (when graphene is 2D randomly oriented, $V_f^{max} = \pi/4$);
- Actual value of g, because if two systems have the same α_g but different g_i at a certain V_{fi}, then, once a nanofiller amount of ΔV_f has been added to them, the observed increment of g will result higher for the system that had a higher g_i.

This means that we need to solve the equation $\partial g = \partial V_f \cdot \alpha_g \cdot \left(V_f^{max} - V_f\right) \cdot g$. As we know that when $V_f = V_f^{max}$, g becomes 1, and supposing to know the value g_0 when $V_f \rightarrow 0$, we can find the following expression:

$$g\left(V_f\right) = g_0^{\left(1-\frac{V_f}{V_f^{max}}\right)^2} \qquad \textit{Equation 4.13}$$

Regarding V_g, we could assume that its variation with V_f depends on these factors:

- Variation of graphene amount ΔV_f;
- A proportional factor β_g that describes how fast V_g increases with V_f;
- Difference $V_g - gV_f$, as V_g cannot be smaller than gV_f. We could call the product gV_f as V_g^{min};
- Difference $g - V_g$, as V_g cannot be higher than g.

Again, we need to solve a differential equation: $\partial V_g = \partial V_f \cdot \beta_g \cdot (V_g - V_g^{min}) \cdot (g - V_g)$. Supposing to know the value V_{g0} when $V_f \rightarrow 0$, we obtain the following expression:

$$V_g(V_f) = g(V_f) \cdot \frac{V_f + exp\left(g(V_f) \cdot (1 - V_f) \cdot \left(\beta_g V_f + \frac{1}{g_o} \ln \frac{1}{\frac{g_0}{V_{g0}} - 1}\right)\right)}{1 + exp\left(g(V_f) \cdot (1 - V_f) \cdot \left(\beta_g V_f + \frac{1}{g_o} \ln \frac{1}{\frac{g_0}{V_{g0}} - 1}\right)\right)}$$

Equation 4.14

Figure 4.4a shows an example of how g and V_g increases with the overall graphene concentration. In general, when the V_g curve is close to the g curve, the compactness of graphene inside the agglomerates is the most loose and the overall graphene distribution results always homogeneous; whereas when the V_g curve is close to the V_g^{min} curve, the tightness of graphene inside the agglomerates is the densest and the graphene distribution becomes homogeneous only if $l_g/L = t_g/t = \xi_f/\xi_g = 1$.

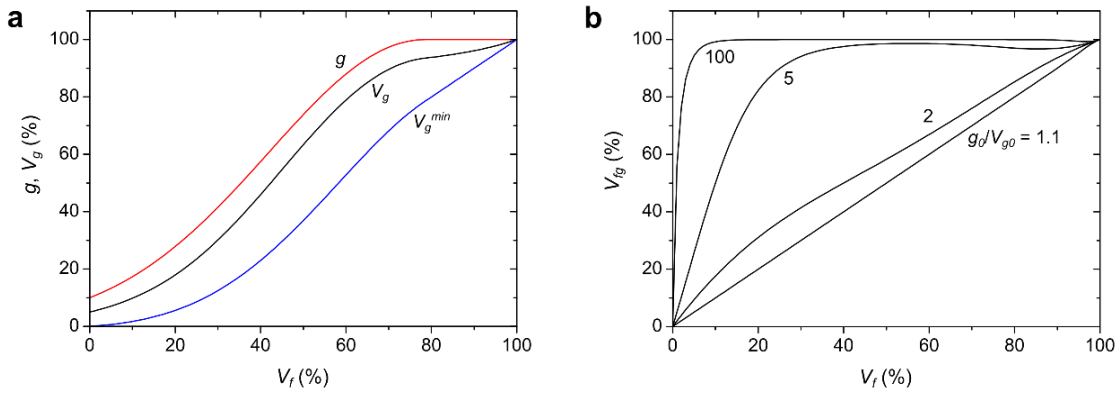

*Figure 4.4 Distribution parameters as a function of the overall graphene concentration in the nanocomposite V_f. (**a**) g, V_g and V_g^{min}(=gV_f) as a function of V_f. (**b**) Graphene concentration inside the graphene-rich zone as a function of V_f.*

The g_0/V_{g0} ratio seems to have a big influence on V_g: if it is close to 1, it does not matter how small β_g (the increasing rate of V_g with V_f) is, the V_g curve will always result close to g for any V_f. Figure 4.4b shows that g_0/V_{g0} has also an effect on the concentration of graphene inside the graphene-rich zone: when g_0/V_{g0} is low (i.e. very loose platelets inside the graphene-rich zone), V_{fg} increases almost linearly with the overall graphene

concentration. On the contrary, when g_0/V_{g0} is very high (dense number of platelets inside the graphene-rich zone), V_{fg} increases rapidly with V_f until reaches a plateau.

Using this graphene distribution model and the GRoM (or the Halpin-Tsai model), we can then describe any mechanical property P_c of a nanocomposite affected by inhomogeneous graphene distribution:

$$P_c = \eta_{og}\eta_{Lg}P_gV_g + P_p(1-V_g) \quad \text{with} \quad \begin{cases} P_g = \eta_o\eta_L P_f V_{fg} + P_m(1-V_{fg}) \\ P_p = \eta_o\eta_{Lp}P_f V_{fp} + P_m(1-V_{fp}) \end{cases} \qquad \textit{Equation 4.15}$$

where P_g and P_p are the properties of the graphene-rich and graphene-poor zones, respectively. P_f and P_m are the properties of graphene and polymer matrix.

In the following sections we will see in detail the cases of mechanical reinforcement and electrical conductivity affected by different graphene distribution states.

4.3.1 Graphene distribution effect on nanocomposite mechanical properties

When $P = E$ (elastic modulus), we can use Equation 4.15 to describe the mechanical properties of nanocomposites affected by inhomogeneous nanofiller distributions. Note that the absolute dimensions of the graphene-rich volumes and those of GNP are not important for the mechanical properties: what really matter is their aspect-ratios.

Kalaitzidou *et al.* prepared by melt-mixing nanocomposites of polypropylene (PP) and GNP using high and low aspect-ratio GNP [35]. Unexpectedly, they found that the reinforcement of high aspect-ratio GNP was much lower than that of low aspect-ratio GNP. Indeed, the nanocomposites with high aspect-ratio GNP had more agglomerates and contained more buckled and rolled up platelets. The left panels of Figure 4.5a,b present the reinforcement found in these two types of nanocomposites together with fitting lines (in red) of Equation 4.15. In both cases, the data are fitted keeping g fixed at 100% to find the best fitting values for the other parameters of the distribution model. Interestingly, both fittings give low values of V_{g0}, meaning that the agglomerates (i.e. the graphene-rich volumes) are dense. Thus ξ_f/ξ_g ratio can be used to indicate the degree of inhomogeneity of the graphene distributions. It results higher for the nanocomposites with high aspect-ratio graphene (175 vs. 4), meaning that there is a larger number of platelets per aggregate. Moreover, V_{g0} and β_g are greater for nanocomposites containing high aspect-ratio GNP (Figure 4.5a), denoting looser agglomerates occupying bigger spaces, probably because high aspect-ratio GNP are more prone to fold and roll.

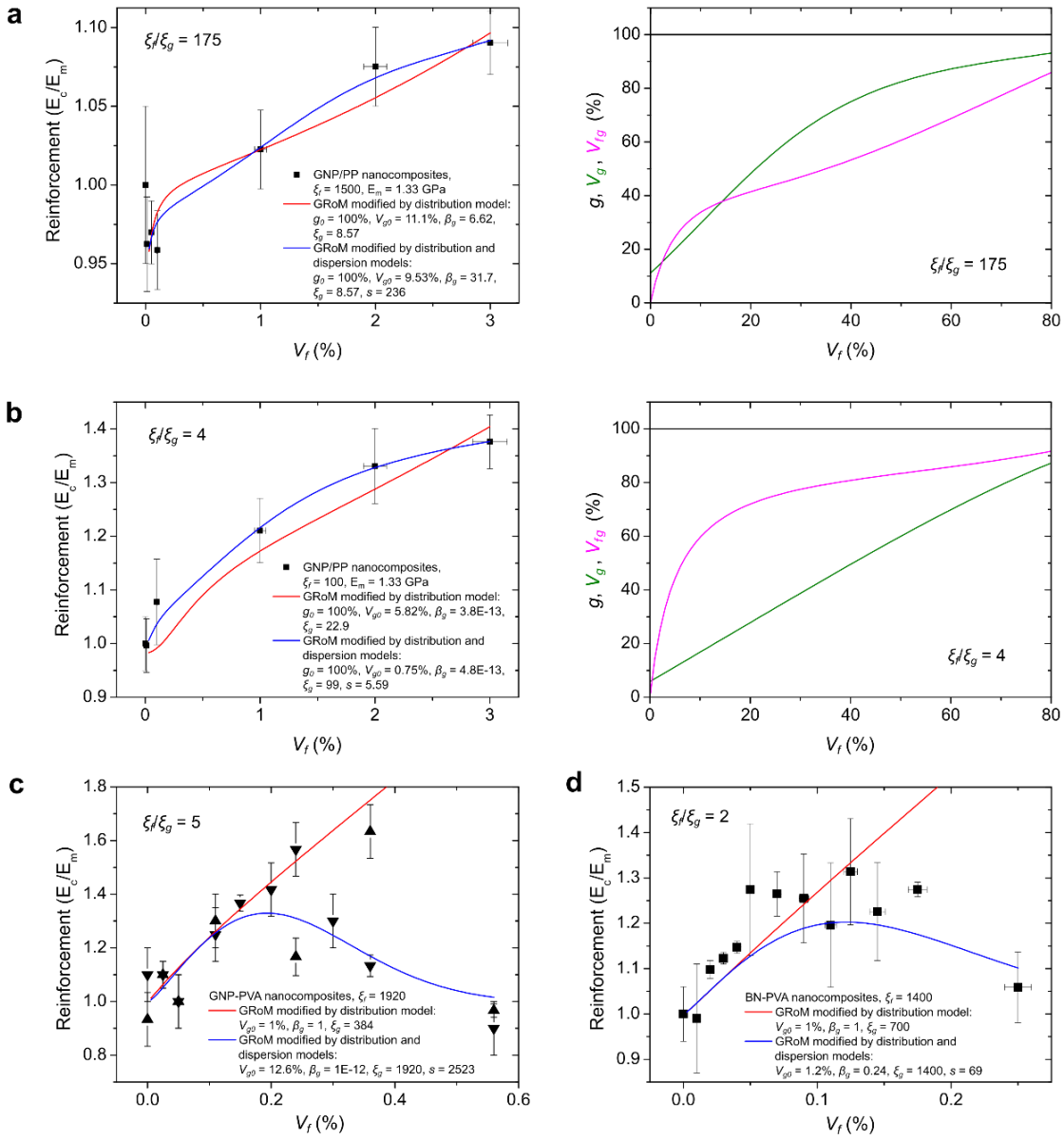

*Figure 4.5 Effect of nanofiller distribution and dispersion on nanocomposite mechanical properties. (**a**) Mechanical properties of GNP/PP nanocomposites containing high aspect-ratio GNP (left panel); evaluation of the distribution parameters as a function of V_f (right panel). (**b**) Mechanical properties of GNP/PP nanocomposites containing low aspect-ratio GNP (left panel); evaluation of the distribution parameters as a function of V_f (right panel). (**c** - **d**) Mechanical properties of GNP/PVA and BN/PVA nanocomposites.*

The green lines in the right graphs in Figure 4.5a,b simulate how the volume of the graphene agglomerates increases with the overall graphene concentration inside these nanocomposites. Note that the V_g curve for nanocomposites with low aspect-ratio GNP increases linearly with V_f (i.e. $V_g \rightarrow gV_f = V_f$), meaning that each agglomerate tends to be made of only few (ξ_f/ξ_g is close to 1) compacted platelets. This feature is also confirmed by the simulation curves of the local graphene concentration inside the aggregates (magenta curves in the right graphs of Figure 4.5a,b). Indeed, V_{fg} increases rapidly inside the agglomerates of low aspect-ratio graphene nanocomposites, while V_{fg}

of high aspect-ratio graphene increases slower because the volume of the aggregates is bigger. These observations are in good agreement with the microstructural analysis of ref. [35]. Eventually, the agglomerates of low aspect-ratio graphene have a bigger aspect-ratio than the agglomerates of high aspect-ratio graphene (22.9 vs. 8.57), which gives a better reinforcement effect.

It is important to note that the red fitting curves in Figure 4.5a,b are based on the assumption that there is a perfect stress-transfer from polymer to GNP even inside the agglomerates. However, this might not be true, and the platelets deep inside the agglomerates may not be able to bear the external load. Therefore, we used the effective volume fraction (Equation 4.1, with D defined by Equation 4.6) only for the graphene-rich zone and fitted the data again (blue curves of Figure 4.5a,b). The data are even better explained by this combined dispersion and distribution model, and we observe that the high aspect-ratio platelets inside the agglomerates are affected by a worse stress-transfer from the matrix (parameter s = 236, vs 5.59 for low aspect-ratio graphene). We point out that these data cannot be fit by the dispersion model alone, so the effect of graphene distribution is dominant for these nanocomposites.

Lastly, we can fit again the reinforcement data of GNP/PVA [34] and BN/PVA nanocomposites [155] prepared by solution-mixing presented before, this time using the distribution model. The red lines of Figure 4.5c,d show that Equation 4.15 can interpret the data well only before the drop of the reinforcing efficiency observed for nanocomposites with $V_f \geq V_f^c$. From these fitting lines we find that the microstructures of these nanocomposites must have an almost homogeneous nanofiller distribution with a very few and compacted platelets per aggregate, as indicated by the ξ_f/ξ_g ratios close to 1 and low values of V_{g0}. These observations are again in agreement with what reported by the authors. When we combine the distribution model with the dispersion model, we can finally explain the experimental data. The blue fitting lines in Figure 4.5c,d reveal that there is a poor stress-transfer to the platelets when their concentration is above V_f^c inside very small agglomerates. Once again, the nanocomposites with high aspect-ratios have the lowest stress-transfer efficiency inside the agglomerates: s = 2523 for GNP (ξ_f = 1920), while for BN (ξ_f = 1400) s = 69.

In conclusion, our distribution model has been proven to be a powerful tool to understand how the microstructure of nanocomposites affect the mechanical properties. It can describe the observed experimental data from nanocomposites with different nanofiller distribution states and prepared with different techniques. Combined with the dispersion

model, the distribution model is able to explain the mechanical data of a variety of nanocomposites affected by nanofiller agglomeration.

4.4 Conclusion

The dispersion of graphene, here defined as the percentage of graphene surface area in contact with the polymer matrix, is the major challenge for obtaining mechanically performing nanocomposites. Unfortunately, the dispersion worsens with the concentration and aspect-ratio of graphene, resulting in nanocomposites with poor stress-transfer from matrix to nanofiller especially when the nanofiller concentration is higher than the critical volume fraction at which rigidity percolation occurs.

The distribution of graphene, here defined as the spatial organisation of graphene in terms of percentage of graphene sheets that are agglomerated and how dense they are packed inside the agglomerates, is detrimental to the nanocomposite mechanical properties as well.

The analytical expressions of the models here developed to treat the dispersion (Equation 4.1) and distribution of graphene (Equation 4.11 and Equation 4.12) are simple and could be used by a broad scientific community to describe the mechanical properties of nanocomposites affected by nanofiller agglomeration.

Chapter 5.

Effect of nanofiller distribution on the electrical properties of nanocomposites

5.1 Introduction

In the previous chapter, the mechanical properties of nanocomposites affected by nanofiller agglomeration have been predicted using the dispersion and the distribution models. It has also been explained why the electrical conductivity of these nanocomposites is mainly affected by the nanofiller distribution, rather than the nanofiller dispersion state. In this chapter, the same model used previously to describe the nanofiller distribution is used to study the effect of nanofiller agglomeration on the electrical conductivity of nanocomposites. The conductivity model here developed shows how the percolation threshold depends on the aspect-ratio of the agglomerates. The second part of this chapter presents some nanocomposites prepared by spray-assisted Layer-by-Layer (sa-LbL) with tailored levels of graphene distributions. The experimental results validate the developed conductivity model and indicate the way toward nanocomposites with ultra-low electrical percolation thresholds.

5.2 Modelling of graphene distribution effect on nanocomposite electrical conductivity

If we want to use Equation 4.15 to model the effect of graphene distribution on the electrical properties of nanocomposites, ones may argue that this is not possible because the electrical conductivity does not follow the rule of mixtures, but the percolation theory (Equation 2.12). Indeed, electrical conduction in graphene nanocomposites is based on electron hopping from one platelet to another when the platelets are close enough to each other, i.e. when the graphene volume fraction is higher than a critical value.

Some studies [70] suggest that this critical volume fraction may be slightly higher than V_f^c that we have used previously (Equation 4.3) and dependent on the orientation of the graphene sheets (see Equation 2.13 and Equation 2.14). Li *et al.* [157] explained how the percolation threshold of CNT nanocomposites is also affected by the degree of CNT entanglement. They demonstrated that when the aspect-ratio of CNT increases, the percolation threshold decreases rapidly, as we would expect. But they also found that there is a critical CNT aspect ratio above which the degree of CNT entanglement becomes crucial, so the percolation threshold reaches a plateau for higher CNT aspect-ratios (Figure 5.1a). The only way to further reduce the percolation threshold would be

to disentangle the CNT. To model the effect of CNT entanglement on the percolation threshold, they introduced two parameters: one that describes how tight the entanglement is (which could be done also by the g/V_g and ξ_f/ξ_g ratios of our distribution model), and another one that represents the fraction of CNT that are entangled (which could also be represented by the parameter g of our distribution model). The smaller these parameters, the more disentangled the CNT are, and the smaller the percolation threshold results. However, their model accounts for the effect of CNT entanglement only on the percolation threshold, and not on the overall conductivity of nanocomposites at different V_f.

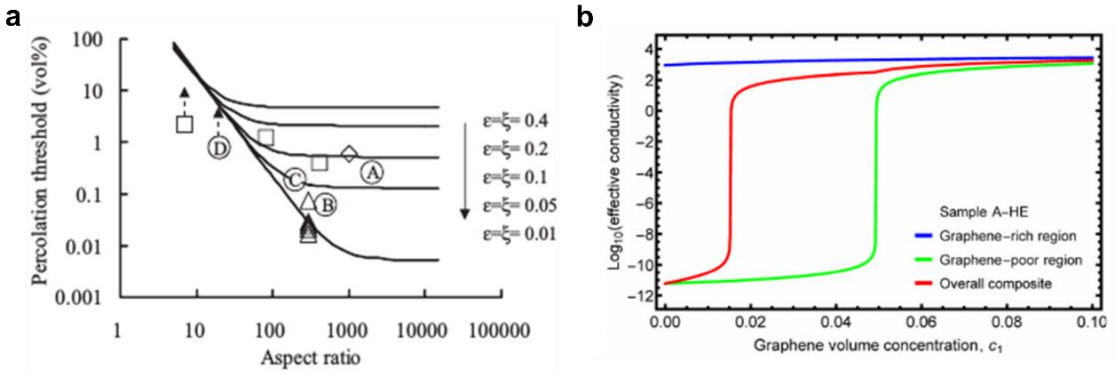

*Figure 5.1 Literature models for the effect of nanofiller distribution on nanocomposite electrical properties. (**a**) Effect of aspect-ratio on the percolation threshold of CNT-reinforced polymer nanocomposites with varying distribution states [157]. Parameter ε describes how tight the CNT entanglements are, while ξ the fraction of CNT that are entangled. (**b**) Contributions of the conductivity of the graphene-rich region (blue line) and graphene-poor region (green line) on the overall nanocomposite conductivity (red line) based on the model of ref. [72].*

Wang *et al.* [72] presented an electrical conductivity model based on the continuum theory that takes into account the effects of nanofiller agglomeration, imperfect nanofiller/matrix interface, and electron tunnelling. In their model, the nanofiller agglomeration was described using an approach really similar to the one introduced within this thesis. They used three parameters to identify the percentage of nanofiller that is agglomerated, the density of the agglomerates and their aspect-ratio. Their model proved that graphene must be completely agglomerated into elongated agglomerates to decrease the percolation threshold. However, it is more difficult to visualise the effects of their distribution parameters on a nanocomposite conductivity. Moreover, the conductivity curves that they obtain are somehow unrealistic around the percolation threshold (Figure 5.1b) as they appear to be perfectly vertical when $V_f = V_f^c$. However, the biggest concern about their model is that the formula for the nanocomposite electrical conductivity is implicit, which is difficult to be handled by a broad scientific community.

Here we show that the rule of mixtures (or the Halpin-Tsai model), if properly modified to consider the electron hopping effect, can describe also the electrical conductivity of nanocomposites. In this way, we can use our distribution model to explain the effect of graphene agglomerates on the electrical conductivity, and how to take advantage of them.

5.2.1 Modelling the electron tunnelling phenomenon in nanocomposite electrical conductivity

We consider the electron hopping effect as a factor that changes the conductivity of the polymer matrix σ_m. This means that when electron hopping occurs, the polymer matrix conductivity results increased up to a value σ_h. We can assume that the variation of the polymer conductivity with the nanofiller concentration (i.e. with the electron hopping effect) depends on these aspects:

- Variation of graphene amount ΔV_f;
- A proportional factor h that describes how fast σ_h increases with V_f;
- Difference $V_f - V_f^c$, as when the concentration of graphene is below V_f^c, the matrix conductivity remains constant and equal to σ_m;
- Difference $\sigma_f - \sigma_h$, because the matrix conductivity cannot increase to values greater than then nanofiller conductivity.

These assumptions are represented by the differential equation $\partial\sigma_h = \partial V_f \cdot h \cdot \left(V_f - V_f^c\right) \cdot \left(\sigma_f - \sigma_h\right)$. As we know that $\sigma_h = \sigma_m$ when $V_f = V_f^c$, we obtain the following expression:

$$\sigma_h\left(V_f\right) = \begin{cases} \sigma_m & \text{for } V_f \le V_f^c \\ \sigma_f - \left(\sigma_f - \sigma_m\right)e^{-h\left(V_f - V_f^c\right)^2} & \text{for } V_f > V_f^c \end{cases} \qquad \textit{Equation 5.1}$$

Figure 5.2a depicts the matrix conductivity as a function of V_f for different hopping rates (parameter h).

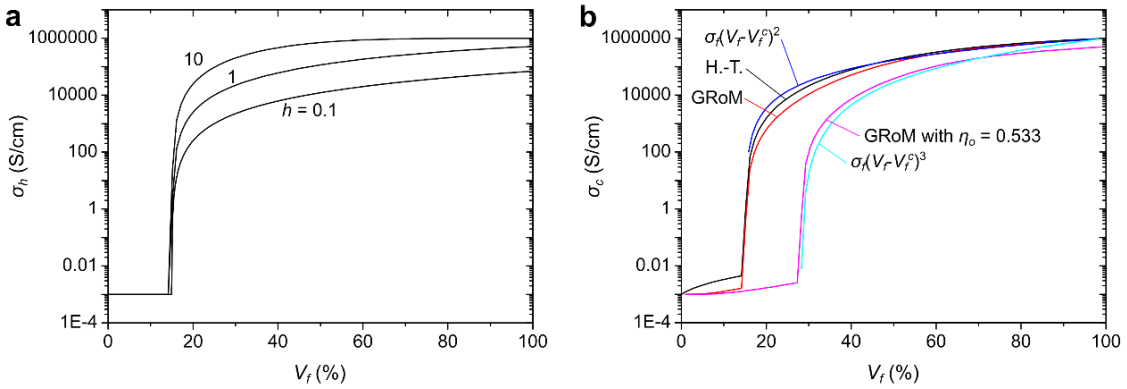

*Figure 5.2 Predictions of electrical conductivities affected by electron hopping. (**a**) Electrical conductivity of polymer matrix as a function of V_f. (**b**) Comparison between nanocomposite electrical conductivities predicted by the percolation theory and by our model.*

Now if we replace σ_m with $\sigma_h(V_f)$ inside the GRoM or the Halpin-Tsai model, we can predict the nanocomposite electrical conductivity. The black and red lines in Figure 5.2b simulate the conductivity of nanocomposites containing homogeneously and 2D-randomly distributed graphene platelets with an aspect-ratio ξ_f = 10, using the Halpin-Tsai and the GRoM models. For consistency, V_f^c was calculated using Equation 4.3. The blue line of the same graph represents the conductivity based on the percolation theory for the same type of nanocomposites. The similarity of these three curves is impressive, but there are some differences. First, the percolation theory cannot describe the nanocomposite conductivity when $V_f \leq V_f^c$. This can be done by the GRoM and the H.-T., despite these two models do not have exactly the same trend within this region. Second, when V_f is slightly above V_f^c, the H.-T. prediction is closer to the percolation theory. This is due to fact that the GRoM considers the Poisson's ratio (Equation 2.5), while the H.-T. does not. The physical meaning of the Poisson's ratio in terms of electrical properties is unclear, however, if we use different values for this coefficient, then the GRoM predictions can result much closer to those of the H.-T or percolation theory.

In Figure 5.2b we have also simulated the conductivity of the same nanocomposites when the graphene platelets are 3D-randomly oriented (curve in magenta colour), using the GRoM with an orientation parameter η_o = 0.533. In this case, the value used for the percolation threshold was V_f^c/η_o. Once again, the GRoM predictions are close to those of the percolation theory for 3D randomly oriented platelets (curve in light blue colour).

Since our conductivity model seems to be reliable as it gives similar predictions of the well-established percolation theory, we can use it in combination with our distribution model (Equation 4.15) to describe the electrical properties of nanocomposites containing graphene agglomerates.

5.2.2 Nanocomposite electrical conductivity affected by graphene agglomeration

Tkalya *et al.* [71] prepared by solution mixing/compression moulding four types of polystyrene nanocomposites containing graphene with different polydispersity (i.e. the distribution of thickness and diameter, Figure 5.3a) and arranged in different spatial distributions caused by thermodynamic instabilities. They used a model based on a connectivity percolation theory [158] able to consider the effect of graphene polydispersity to calculate theoretical percolation thresholds and compare these values with the experimental results. Despite the trend of the theoretical model seems to follow the experimental one, the values do not match very well, probably because the effect of graphene agglomeration is not considered by the model.

To see the effect of graphene agglomeration on the electrical conductivity of their nanocomposites (Figure 5.3b), the average aspect-ratio ξ_f of each type of graphene that they used must be identified first, as it was not reported. They prepared three types of aqueous graphene dispersions using sonication: dispersions A, A-LC (lower concentration of graphene inside the solution), and A-HE (solution sonicated with higher energy). The fourth graphene dispersion, dispersion B, was obtained by liquid-phase exfoliation. From the TEM observations, the graphene sheets from dispersions A and A-LC have the widest lateral size: 0.25 – 1 µm. Graphene A-HC has a slightly smaller lateral size in the range 0.2 – 0.5 µm, whereas graphene B contains the smallest platelets: 0.1 – 0.2 µm. The average thickness of the platelets could be guessed by spectroscopy data. Raman and UV-Vis spectroscopies revealed that graphene B is the most exfoliated, defect-free, and stable inside the solution. Thus, we could assign an average thickness within the range 1 – 2 nm. Taking this range as reference and looking at the UV-vis spectra recorded over time, we could guess a thickness of 1.5 – 3 nm for both graphene A and A-LC (with the thickness of A-LC close to the upper limit of this range), and 1.3 – 2.5 nm for graphene A-HC. From these considerations, we can establish the following average aspect-ratios: 375 for graphene A, 300 for graphene A-LC, 230 for graphene A-HC, and 125 for graphene B. Plohen and Liu [159] have proved a linear correlation between the mean aspect ratio measured by AFM and the effective particle diameter measured by dynamic light scattering. As our estimations of ξ_f are in good agreements with the average effective hydrodynamic diameters obtained from dynamic light scattering (Figure 5.3a), we can conclude that our calculated values are about right.

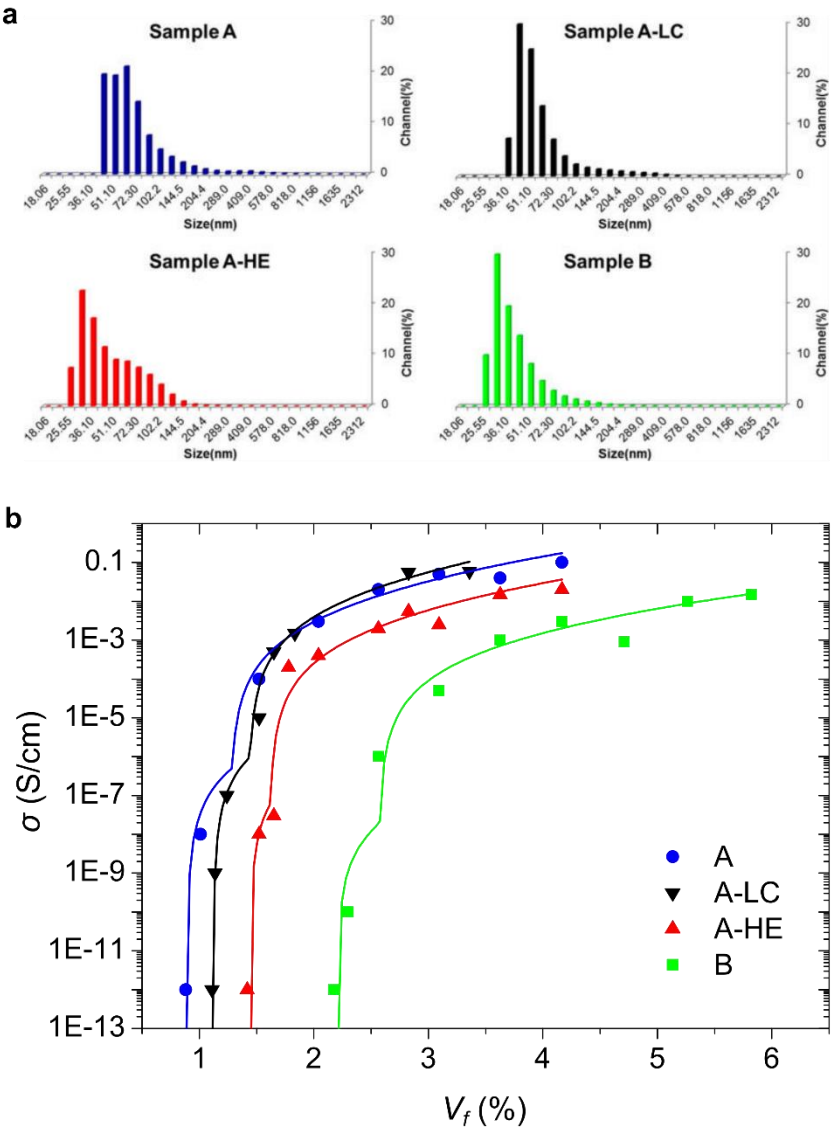

*Figure 5.3 Electrical conductivity of nanocomposites containing graphene agglomerates; data from ref. [71]. (**a**) Dynamic light scattering data of the size distributions of aqueous graphene dispersions A, A-LC, A-HE, and B used to prepare the nanocomposites. (**b**) Electrical conductivity of the nanocomposites together with fitting lines of our conductivity model that considers the effect of graphene agglomeration.*

Using these ξ_f inside Equation 4.3, we find that the theoretical percolation thresholds for these nanocomposites are < 0.4 vol.%, much lower than the experimental ones. This discrepancy might be due to graphene agglomeration, which was proved in ref. [71] to be a very likely phenomenon especially for graphene A and A-LC. We can fit the electrical conductivities of these nanocomposites (Figure 5.3b) using our distribution model (Equation 4.15) with the hopping conductivities (Equation 5.1). Note that we have three possible electron tunnelling phenomena: one inside the graphene agglomerates, one among the graphene sheets in the graphene-poor region, and one between the agglomerates. Therefore, the percolation threshold of a nanocomposite is due either to electron tunnelling between the graphene sheets in the graphene-poor region, or to

electron tunnelling between the agglomerates. If graphene is highly agglomerated already at really low volume fractions ($g_0 \rightarrow 100\%$) or if the aspect-ratio of the agglomerates is higher than ξ_f (which is quite unlikely for compression moulded samples like these), then the percolation threshold is due to electron tunnelling between the agglomerates, and vice-versa. To avoid to over-parameterise the fittings, we fix the conductivities of graphene and matrix to $1 \cdot 10^{6}$ S/cm and $1 \cdot 10^{-14}$ S/cm respectively. We also assume that the hopping rate is relatively high inside the agglomerates ($h = 1$) because the graphene sheets must be highly dense inside them ($V_{g0} = 0.001\%$) and they will always be ($\beta_g = 0$), and both the orientations of graphene and agglomerates remain planar ($\eta_o = 1$). In this way, we can change four parameters to fit the data of Figure 5.3b: the aspect-ratio of the agglomerates (ξ_g), the initial percentage of graphene sheets that are agglomerated (g_0), the hopping rate between the graphene sheets inside the graphene-poor region (h_p), and the hopping rate between the agglomerates (h_g).

Table 5.1 *Fitting parameters used in Figure 5.3b.*

	ξ_f	ξ_g	g_0 (%)	h_p ($\times 10^{-7}$)	h_g ($\times 10^{-5}$)
A	375	208	55	1	6
A-LC	300	185	55	3	15
A-HE	230	167	54.1	0.6	2.5
B	125	125	44.2	0.03	3

Table 5.1 reports the values used in each fitting line of Figure 5.3b. The parameters g_0 and the ratios ξ_f/ξ_g tell us that the most homogeneous microstructure is the one of nanocomposites with graphene B, in agreement with the findings of Tkalya *et al.* [71]. Interestingly, the hopping rate between the agglomerates is similar for all types of nanocomposites ($h_g \approx 6 \cdot 10^{-5}$) and the hopping rate between the non-agglomerated graphene sheets is not only much smaller than h_g but it also seems to strongly depend on the aspect-ratio of graphene. Note that the kink of the fitting lines is due the percolation of the agglomerates that happens after the percolation of non-agglomerated graphene sheets.

In conclusion, the distribution model modified to consider the hopping-effect can well describe the electrical conductivity of nanocomposites affected by graphene agglomeration. This model is also a powerful tool for materials design because it can show that nanocomposites containing agglomerates could present higher conductivities and lower percolation thresholds than homogeneous nanocomposites if $\xi_f/\xi_g < 1$ because

h_g is generally > h_p. Such microstructures could be prepared by particular preparation techniques such as the Layer-by-Layer, or by heat treatments of nanocomposites because this will lead to ξ_f/ξ_g ratios to become smaller and smaller over time, as already demonstrated by our group [160–162].

5.3 Toward nanocomposites with ultra-low electrical percolation thresholds: PVA/RGO nanocomposites prepared by sa-LbL

Based on our conductivity model of nanocomposites affected by graphene agglomeration (Equation 4.15 with Equation 5.1), it is desirable to introduce graphene agglomerates with aspect-ratios higher than that of individual graphene sheets, so to decrease the electrical percolation threshold and enhance the conductivity. When $\xi_g \rightarrow \infty$, the enhancement should be the highest. Freeze-casting graphene suspensions and infiltration of the resulting foams with polymers may produce such "infinitely" long agglomerates. Using this approach, D'Elia *et al.* [136] have prepared nanocomposites of PDMS and reduced graphene oxide (RGO) with conductivities as high as 0.9 S/cm at RGO loadings <1 wt.%, whereas the same starting materials gave insulating nanocomposites when blended by traditional solution mixing even when the RGO concentration was as high as 10 wt.%. Wang *et al.* [163] have demonstrated that with the same method it is possible to obtain nanocomposites of RGO and epoxy resin with an incredibly low electrical percolation threshold of 0.007 vol.%.

We wonder whether it is possible to control the shapes of the agglomerates and the concentration of the graphene sheets inside them to experimentally prove our conductivity model and pave the way toward ultra-low electrical percolated nanocomposites.

5.3.1 Electrical conductivity of PVA/RGO nanocomposites

A range of reference PVA/RGO nanocomposites (Figure 5.4) have been prepared by solution mixing followed by spraying deposition and thermal treatment to reduce GO into RGO.

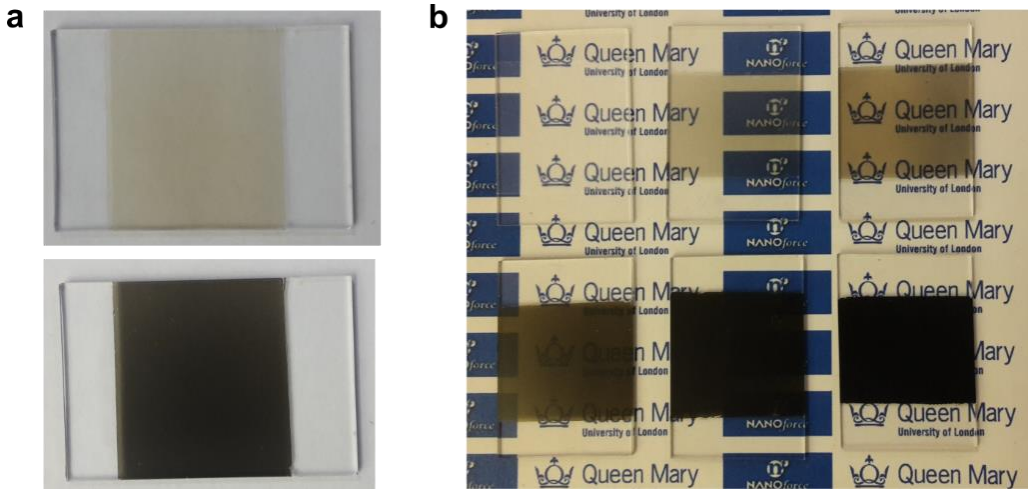

*Figure 5.4 PVA/RGO nanocomposite films. (**a**) Optical pictures of a film before (picture on top) and after (bottom picture) thermal treatment. (**b**) Series of films containing 0, 0.008, 0.04, 0.2, 1 and 5.3 vol.% RGO. The films are ~ 20 µm thick.*

A way to induce agglomerates is by diluting the initial GO suspension in tap water instead of deionised water, as depicted in Figure 5.5. Therefore, when the PVA/GO solutions are sprayed on top of the glass substrates, the agglomerates should have an unfolded morphology within the forming nanocomposites.

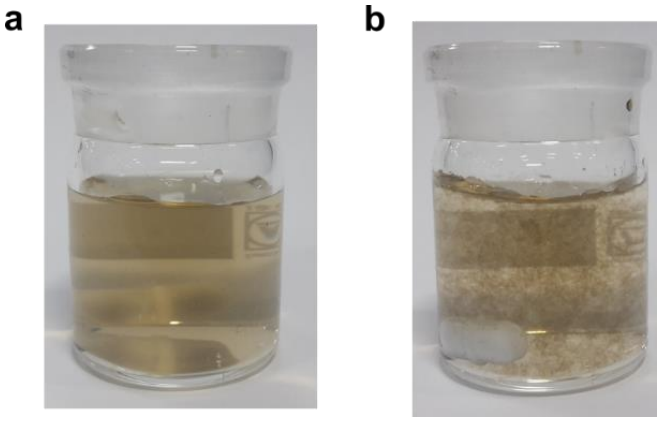

*Figure 5.5 Pictures of GO suspensions. (**a**) Clear suspension in deionised water. (**b**) Suspension with GO agglomerates in tap water.*

Figure 5.6 presents the electrical conductivities of these nanocomposites as a function of RGO loading. As the initial GO has an aspect-ratio of ~ 1000 (obtained from AFM measurements), we expect to find a percolation threshold close to 0.15 vol.% if the RGO was homogeneously distributed and well dispersed inside the matrix. However, the range of reference PVA/RGO samples has a percolation threshold around 0.3 vol.%, meaning that a slight agglomeration happens in these samples. Fitting these data with our conductivity model in a similar way as done in Figure 5.3, we find an initial percentage of agglomerated RGO g_0 = 47%, a ξ_f/ξ_g ratio of 9.05, a hopping rate between the

dispersed RGO sheets h_p = 8.2·10^{-7}, and a much lower hopping rate between the agglomerates h_g = 1.4·10^{-46}. This means that these agglomerates do not bring any contribution to the conductivity of the nanocomposite.

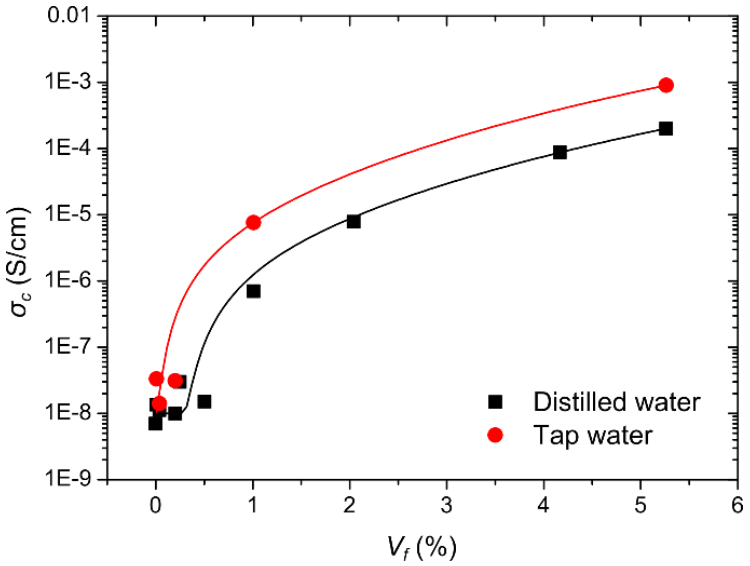

Figure 5.6 Electrical conductivities of PVA/RGO nanocomposites prepared in distilled water and in tap water (i.e. with induced agglomerates) together with fitting lines of Equation 4.15 with Equation 5.1.

The nanocomposites with induced agglomerates, instead, present a lower percolation threshold that is close to 0.1 vol.%. In this case, the agglomerates have a beneficial effect on the nanocomposite conductivity. From the data fitting, we find g_0 = 98%, ξ_f/ξ_g = 0.22, h_p = 7.5·10^{-13}, and h_g = 1.4·10^{-10}. This proves the fact that agglomerates with an aspect-ratio larger than that of individual nanoparticles can induce lower percolation thresholds and higher conductivities.

With sa-LbL technique we can further investigate the effects of the agglomerates.

5.3.2 Electrical conductivity of PVA/RGO nanocomposites with tailor induced RGO agglomerates

The advantage of the sa-LbL is that we can prepare layered nanocomposites with tailored microstructures. To investigate the effects of parameters g, V_g and ξ_g (see section 4.3) on the electrical conductivity, we have prepared nanocomposites with graphene-poor and graphene-rich layers.

5.3.2.1 *Conductivity of PVA + 1 vol.% RGO nanocomposites with variable density of RGO inside layered agglomerates*

The effect of decreasing V_g when g = 100 % and V_f = 1 vol.% has been obtained with a series of nanocomposites containing 10 graphene-rich layers embedded inside 11 polymer layers. The graphene-rich layers represent the agglomerates, and their volume fraction V_g has been changed from 100 to 21, 5, 2, 1 vol.%. Consequently, the density of RGO inside the agglomerates, V_{fg}, ranges from 1 to 100 vol.%. The aspect-ratio of the agglomerates should tend to ∞ because the agglomerates are represented by continuous layers. However, some local defects always occur during the deposition of the layers, and more the thickness of the layers reduces, the more the defects play a crucial role. Therefore, we have also prepared a series of samples with the same range of V_g and V_{fg} with only one graphene-rich layer embedded within two polymer films.

Figure 5.7 shows the conductivities of the samples. The series prepared with one graphene-rich layer presents higher values because $\xi_g \rightarrow \infty$ as the probability of containing defects is lower. When the volume fraction of the agglomerates is 100 %, the distribution of RGO is actually homogeneous and there are no polymer layers. When $V_g \rightarrow 0$, the density of RGO inside the agglomerates is maximum, so $V_{fg} \rightarrow$ 100 vol.% (as indicated on the top axis in Figure 5.7) and the RGO distribution is the most inhomogeneous, which reflects in a conductivity enhancement.

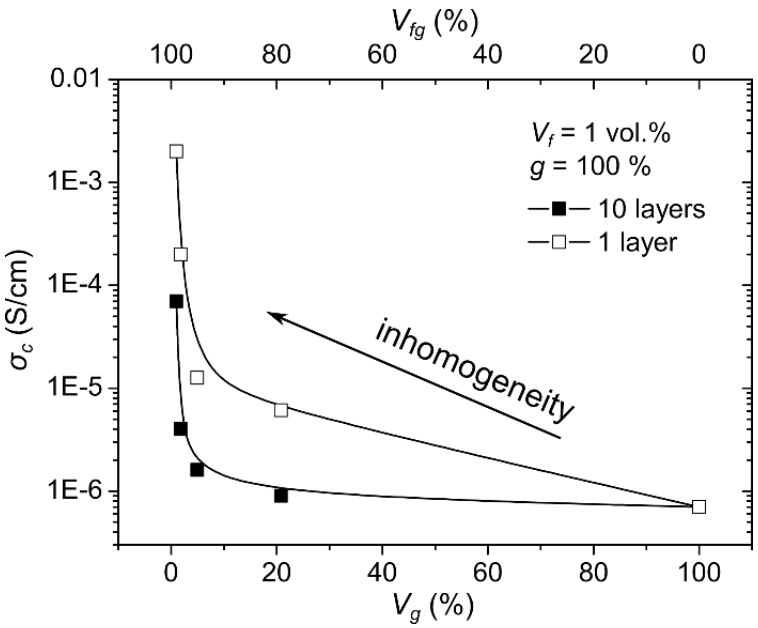

Figure 5.7 Conductivity of PVA + 1 vol.% RGO nanocomposites as a function of agglomerate volume fraction or RGO density inside the agglomerates.

5.3.2.2 *Conductivity of PVA + 1 vol.% RGO nanocomposites with variable aspect-ratios of agglomerates*

The effect of increasing ξ_g from ξ_f to ∞ for microstructures with g = 100 %, V_{fg} = 100 vol.% and V_f = 1 vol.% has been obtained with a series of nanocomposites containing 100, 10 and 1 RGO layers interspersed with PVA layers. As pointed out earlier, the thickness of the graphene-rich layers is affected by defects. The thinner the layers are and the more influence the defects have, so the smaller ξ_g appears to be. When the number of RGO layers increases, the thickness of each layer and ξ_g decrease. The extreme case is represented by an infinite number of layers, where the thickness of each layer must be equal to the thickness of individual RGO sheets, and also $\xi_g \rightarrow \xi_f$. Summarising, when the number of RGO layers → ∞ then $\xi_f/\xi_g \rightarrow 1$, and when the layers number decreases to 1 then $\xi_f/\xi_g \rightarrow 0$.

Figure 5.8 shows how the conductivity of these samples increases linearly with the decrease of number of layers (in a log-log scale), i.e. with the inhomogeneity of RGO distribution. When the number of RGO layers → ∞, the conductivity of this series of nanocomposites must approach that of homogeneous nanocomposites ($7 \cdot 10^{-7}$ S/cm), which is indicated by the dashed lined. The transition between homogeneous and inhomogeneous distribution seems to start between 200 and 400 RGO layers.

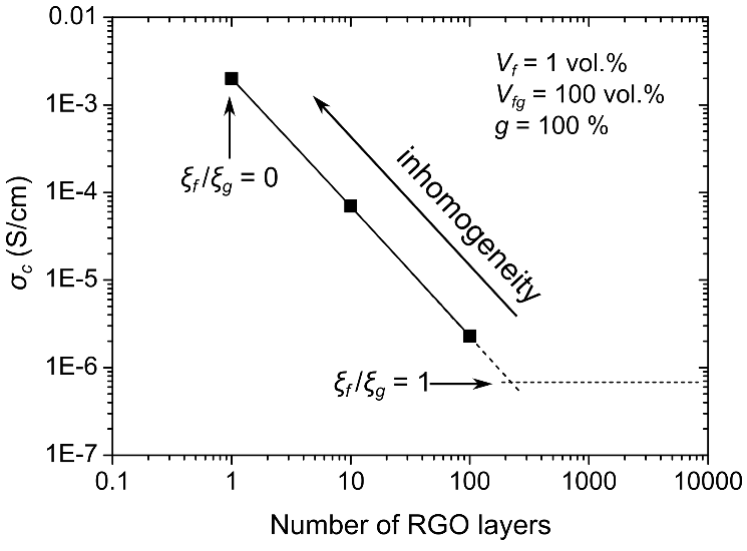

Figure 5.8 Conductivity of PVA + 1 vol.% RGO nanocomposites as a function of agglomerates' aspect-ratio, represented as number of RGO layers.

5.3.2.3 *Conductivity of PVA/RGO nanocomposites with RGO highly packed inside agglomerates of infinite aspect-ratios*

The control of RGO distribution allowed by sa-LbL can be exploited for nanocomposites with high density RGO sheets (V_{fg} = 100 vol.%) inside infinite aspect-ratio agglomerates (i.e. one layer of RGO inside the film). Figure 5.9 reports the conductivity of these nanocomposites (blue coloured data), together with the conductivities of the samples presented initially. Note that despite the new nanocomposites contain highly packed agglomerates, they do not delaminate, and the films remain always consistent before and after the thermal treatment.

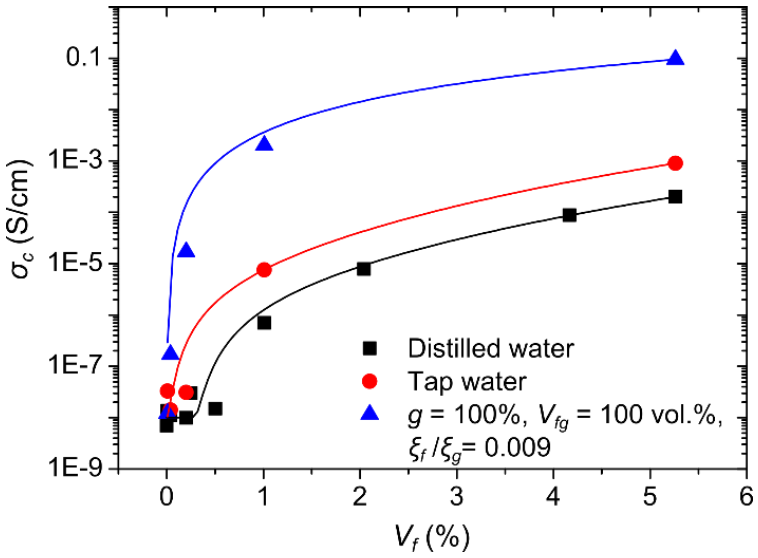

Figure 5.9 Electrical conductivities of PVA/RGO nanocomposites with different types of RGO agglomerates, together with fitting lines of Equation 4.15 with Equation 5.1.

The new data can be fitted by our conductivity model, with g_0 = 100%, ξ_f/ξ_g = 0.009, h_p = 0 (there is no RGO in the polymer layers), h_g = 0 (there is only one agglomerate that is continuous throughout each sample), and with a hopping rate within the agglomerate h = $3.6 \cdot 10^{-18}$. Such small h can be explained by the contact resistance between the edges of the films and the electrodes. What is interesting to note is that the electrical percolation of these nanocomposites is as low as 0.008 vol.%, which is really close to the value found by Wang *et al.* [163] for graphene foam/epoxy nanocomposites, despite the GO in our nanocomposites has been reduced with a mild thermal treatment.

5.4 Conclusion

This chapter has shown from a theoretical perspective how the distribution of graphene, as defined in the previous chapter, could be beneficial for the electrical properties of nanocomposites when the aspect-ratios of the agglomerates are higher than the aspect-ratio of graphene. This conductivity model for nanocomposites affected by graphene agglomeration (Equation 4.15 with Equation 5.1) has been validated in the second part of this chapter, where it has been experimentally proved that agglomerates with high aspect-ratios containing highly packed graphene sheets can dramatically decrease the percolation threshold and increase the conductivity of nanocomposites.

Chapter 6.

Effect of nanofiller dispersion and distribution on the mechanical and electrical properties of LLDPE + 4.8 vol.% GNP nanocomposites prepared by Pressing-and-Folding

6.1 Introduction

In this chapter we will present other direct experimental evidences of the effect of nanofiller agglomeration on nanocomposite properties. We have prepared a series of samples of LLDPE containing a fixed amount of GNP (4.8 vol.%), but with very different agglomeration states ranging from highly inhomogeneous distributions with bad dispersions to homogeneous distributions and optimum dispersions. We would expect to observe any nanocomposite property, P, to change with the nanofiller dispersion level (*D*-factor, Equation 4.1) as follow:

$$P(D) \approx P_0 + (P_{th} - P_0) \cdot D \qquad \textit{Equation 6.1}$$

where P_0 is the property at $D = 0$ and P_{th} the expected value of the property when the nanofiller is perfectly dispersed ($D = 1$). As both the dispersion and the distribution of the platelets are improving in this series of samples, we could replace *D* inside Equation 6.1 with the difference 1-*g*, i.e. the percentage of platelets that is not agglomerated but well distributed inside the graphene-poor region. We highlight that Equation 6.1 is valid when the agglomeration state of the nanofiller is the only parameter changing in the nanocomposites, and other factors, such as the nanofiller orientation, remain the same. We will show that this is the case for these nanocomposites prepared with the P&F technique, as their microstructures present always aligned GNPs with well-defined distribution and dispersion levels ranging from $D \approx 0$ to $D \approx 1$. Each sample has been prepared with a defined number *n* of P&F cycles. Because P&F is a melt-blending technique, the number *n* could be converted into dispersion level *D* using Equation 4.9 where *t* is replaced by *n*. As illustrated by Figure 4.2b, if a nanofiller has a too high aspect-ratio, then it would never be perfectly distributed if its amount is above V_f^c. Therefore, to be sure that we could prepare nanocomposites with *D* up to 100%, we have used GNP from expanded graphite ~30 nm thick (see next section and appendix 11.1) because thick particles usually have $\xi << 1000$ and a relatively high V_f^c.

6.2 GNP characterisation

Figure 6.1 shows the SEM and AFM observations of the as received EG powder. The particles appeared to be irregularly shaped (Figure 6.1a), probably resulting from the aggregation of smaller sub-particles, as suggested by the observation in Figure 6.1b.

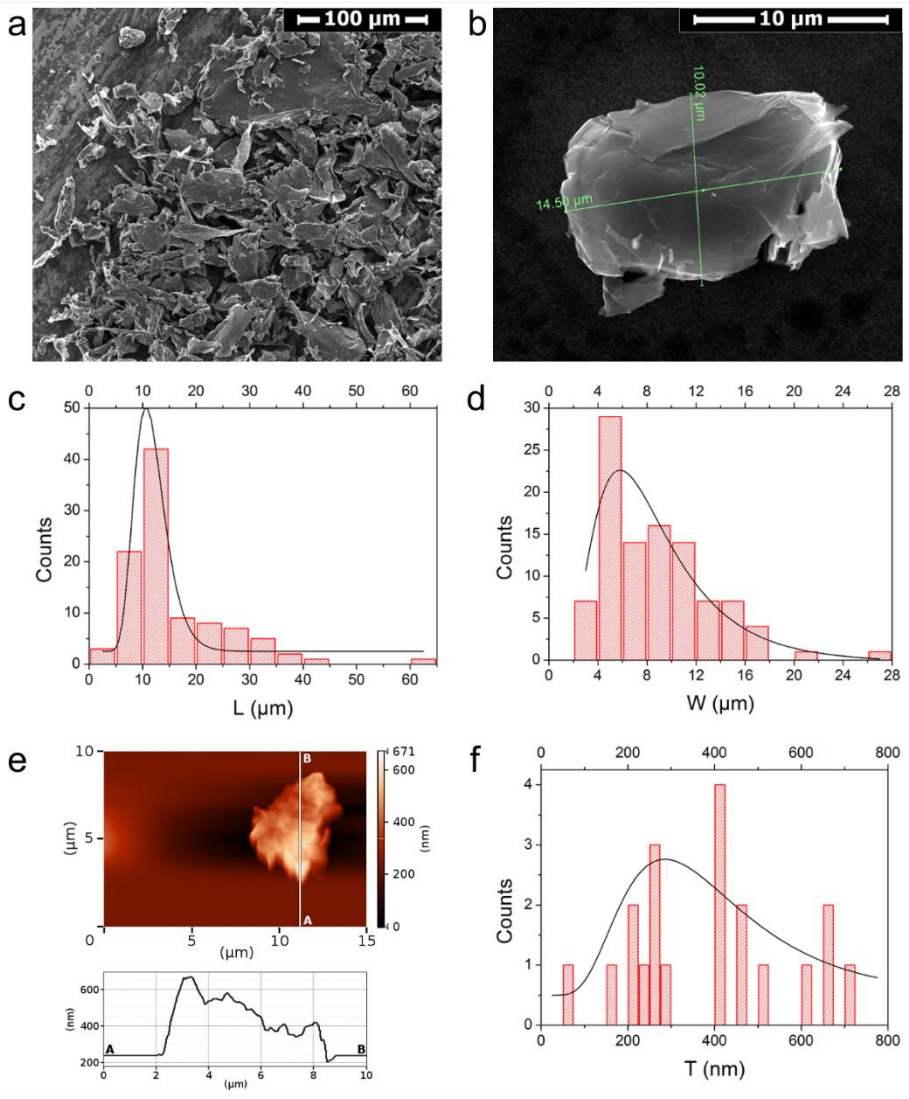

*Figure 6.1 Characterisation of the GNP used to prepare the P&F nanocomposites. (**a**-**b**) SEM images of EG powder. (**c**-**d**) Size distributions of the longest and shortest sides obtained from SEM measurements of 100 EG powder particles. (**e**) AFM image of an EG powder particle with the thickness profile of the highlighted AB line. (**f**) Thickness distribution obtained from AFM measurements of 20 EG powder particles.*

Parts c and d of Figure 6.1 show the size distributions of the longest (L) and shortest (W) sides of 100 EG powder particles. These distributions were fitted with a log-normal function [164], obtaining the following geometric mean values (that is, the median of each distribution) and geometric standard deviations (GSD): $\overline{L}$ = 11.4 µm with GSD_L = 1.3, and $\overline{W}$ = 7.8 µm with GSD_W = 1.7. Note that the geometric coefficient of variation is 30% for

L, and 72% for W, meaning that the distribution of the shortest particle side is more broadened. Since most of the measured particles (63%) have a W/L ratio greater than 0.5, the EG powder particles can be approximated to disc-like particles with a mean diameter $\overline{D} = \sqrt{\overline{LW}}$ = 9.4 µm. The thickness distribution of the EG powder particles is shown in Figure 6.1f, and was fitted with a log-normal function, obtaining the following values: $\overline{T}$ = 364 nm, GSD_T = 1.6. The geometric coefficient of variation of T is high: 64%, mainly because of the low number of measurements (20), and the irregular thickness of each particle (see the thickness profile of the particle in Figure 6.1e), probably due to some folded sides, or different numbers of agglomerated sub-particles, as suggested before.

The density of these EG powder particles cannot be measured, so the volume fractions occupied by these EG powder particles inside the nanocomposites cannot be calculated. However, the density of pure graphite, d_G = 2.2 g/cm^3 [165] can be attributed approximately. In this way, by using d_G and the above-mentioned values of $\overline{D}$ and $\overline{T}$, it is possible to calculate a specific surface area of $\frac{\pi\bar{D}^2/2+\pi\bar{D}\bar{T}}{d_G\pi\bar{D}^2\bar{T}/4}$ = 2.7 m^2/g for EG, which is much lower than the reported BET surface area (25 m^2/g). This confirms the initial hypothesis that the observed EG powder particles are made of agglomerated sub-particles (graphite nanoplatelets, GNP).

The density and thickness of these sub-particles can be deduced from the XRD pattern of EG powder (Figure 11.1) [166]. The graphite (002) peak centred on 26.6° 2θ (see Table 11.1 for details of the XRD pattern) corresponds to an interlayer spacing of 0.335 nm. This value is in good agreement with the *d*-spacing of bulk graphite [167–169], thus the density is the same one as for pure graphite. From the (002) peak, a thickness $\overline{t}$ of ~27 nm can also be calculated, which can be confirmed by the BET specific surface area (assuming that the lateral area of each particle is negligible because the particle diameter is much larger than the particle thickness): $\overline{t} \approx 2/(d_G \cdot S_{BET})$ = 36 nm. This is a clear evidence of the presence of GNP, and the GNP volume fractions inside nanocomposites can be certainly converted from the weight fractions by using the density of pure graphite, d_G.

It is possible to calculate the maximum effective Young's modulus of the filler, E_{GNP}^{eff}, from the value of the crystallographic thickness of GNP as suggested by Gong *et al.* (Equation 2.6) obtaining a value of ~65 GPa. This is reasonable if compared to the results of Krzesinska *et al.* [165], who studied the elastic modulus of expanded graphite powders with different porosities using ultrasound measurements, and found that the maximum

elastic modulus of completely compressed expanded graphite (without any porosity) is about 30 GPa.

6.3 Microstructural observations

Figure 6.2 shows a macroscopic visualisation of the effect of the P&F technique on the distribution of GNP throughout the specimen for a series of samples containing 4.8 vol.% of GNP. The first P&F cycles break down initial large agglomerates. Because of the relatively high GNP loading, the colour of the samples appears homogeneous to the eye after only 20-30 P&F cycles. Indeed, Figure 11.2a in appendix shows how the samples becomes darker and darker up to 500 P&F cycles if they contain a low GNP concentration of 0.21 vol.%.

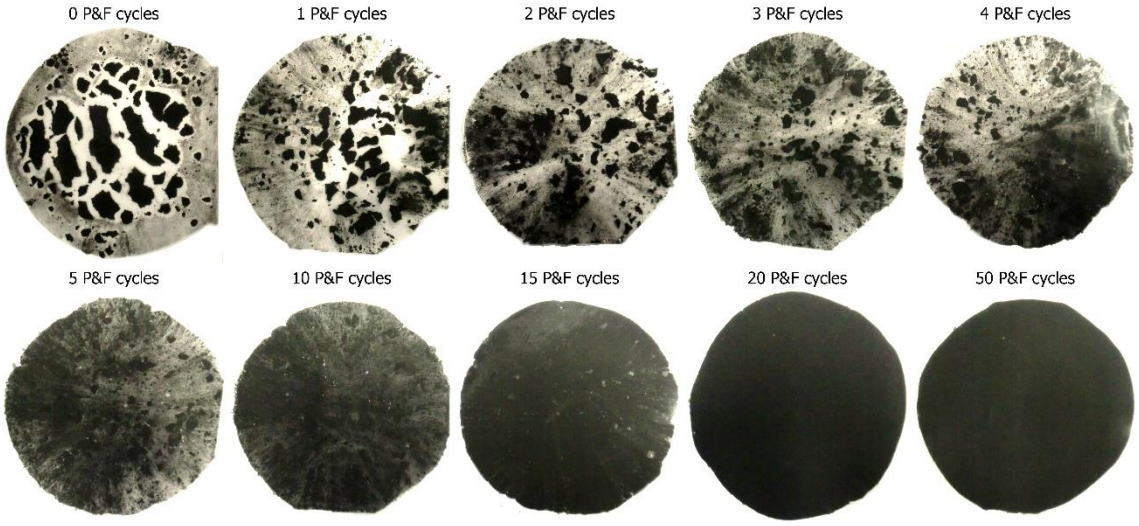

Figure 6.2 Pictures of LLDPE + 4.8 vol.% GNP samples at different P&F cycles. Samples were about 8 cm in diameter, and 300 µm thick.

Figure 6.3 shows how the microstructure of the same nanocomposites changes as a function of P&F cycles. At 10 P&F cycles, there are large GNP agglomerates with thicknesses close to those of the disk samples, with particles inside these agglomerates appearing to be mainly oriented parallel to the plane of the samples. These agglomerates decrease in thickness and width as the P&F cycles increase. Between 50 and 200 P&F cycles, it is difficult to find GNP agglomerates, and many dispersed particles appear throughout the matrix volume. Eventually, the microstructure at 500 P&F cycles results clearly well-ordered with homogeneously distributed and well dispersed particles oriented parallel to the plane of the samples.

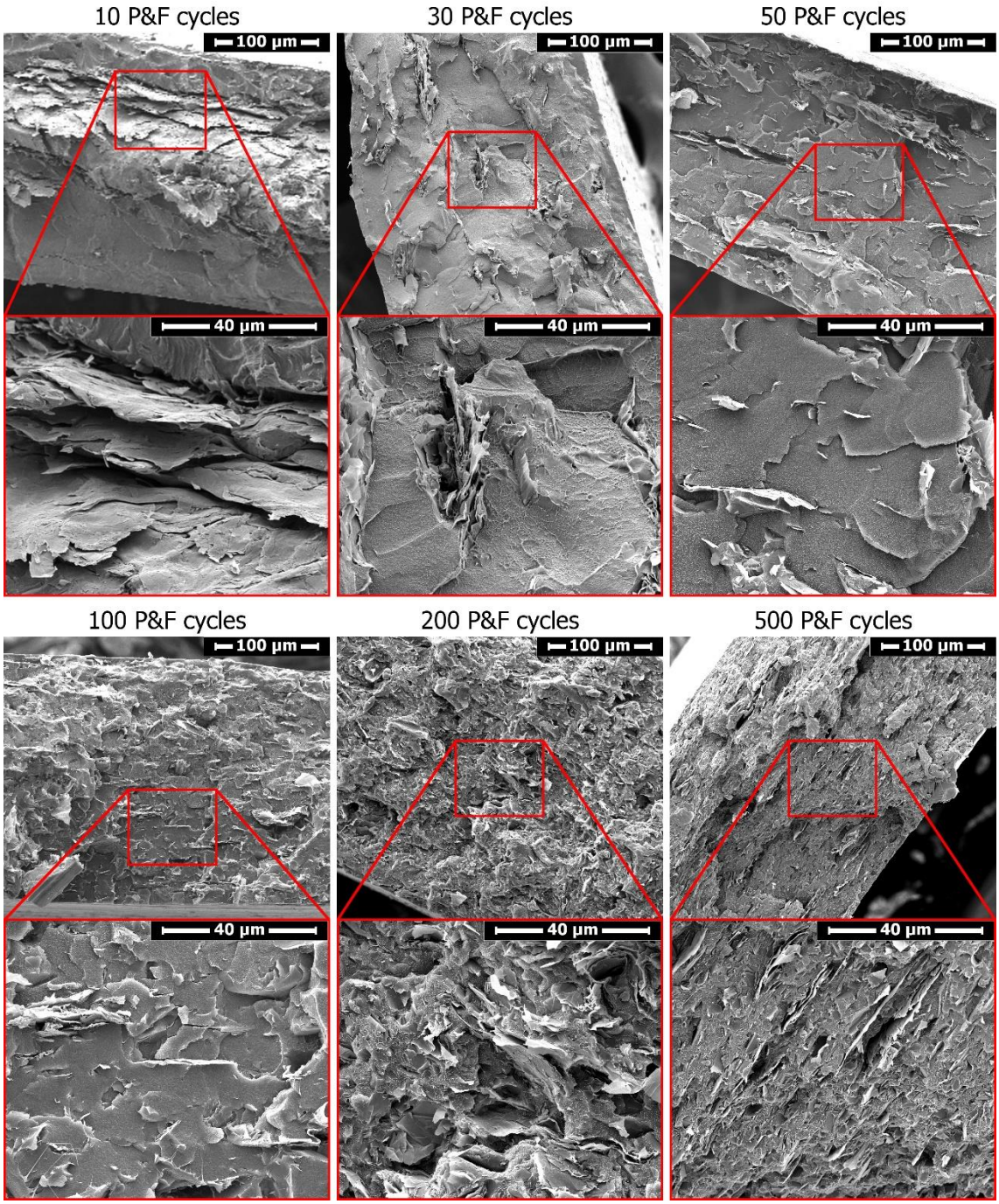

Figure 6.3 SEM images of the cross-sections of LLDPE + 4.8 vol.% GNP samples prepared at different P&F cycles.

The GNP agglomerates found in these microstructures have been studied in terms of their size. Parts a, b and c of Figure 6.4 show the statistical distributions of diameter, thickness, and aspect-ratio of the agglomerates at different P&F cycles. The geometrical means (GM) of these distributions are reported in Table 6.1 together with their geometrical standard deviations, and displayed in Figure 6.4d. The mean diameter and thickness decrease drastically up to ~ 50 P&F cycles, and further reduce to one tenth of their original dimensions after 500 P&F cycles, where they approach the size of individual

particles. Conversely, the aspect-ratio of the agglomerates does not change significantly with the P&F cycles as diameter and thickness do, and it only doubles its initial value after 500 P&F cycles. The GM of diameter, thickness and aspect-ratio of the agglomerates can be described by Equation 6.1 (see fitting lines in Figure 6.4d) as we would expect. From these fittings we find an estimation of the distribution rate: I = 0.02. The top axis of Figure 6.4d reports the converted values of n P&F cycles into dispersion level D.

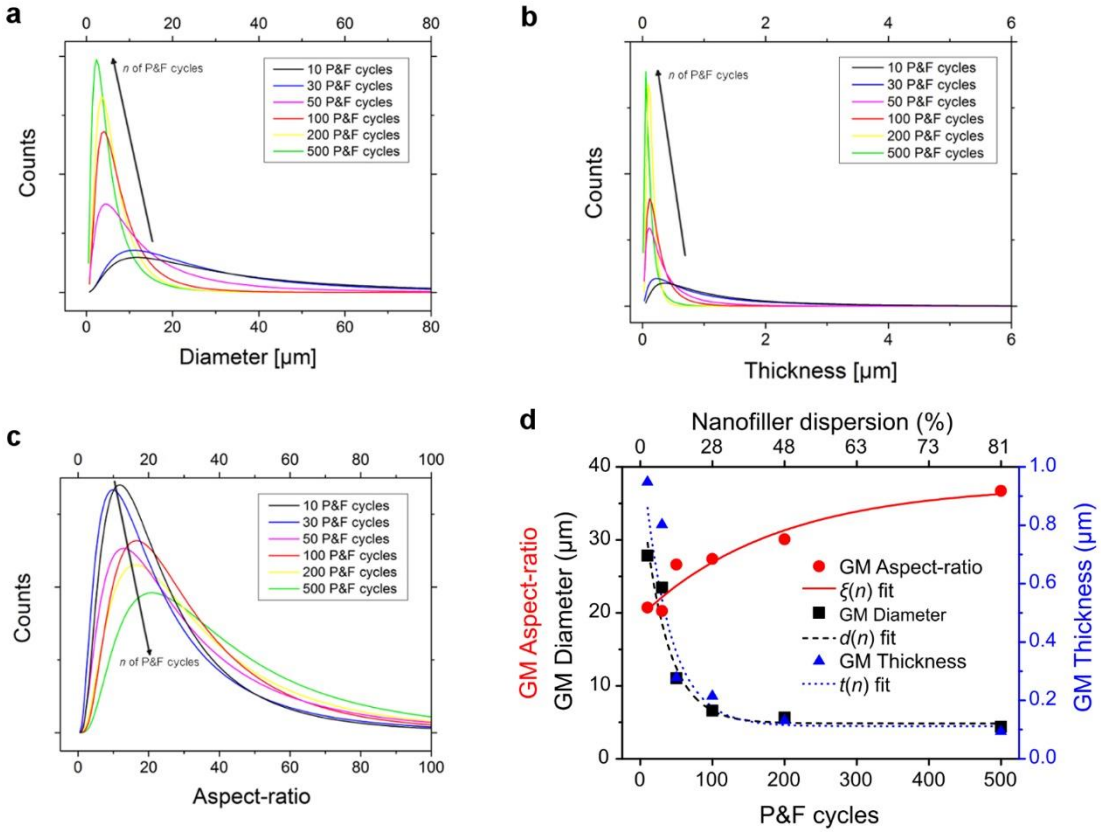

*Figure 6.4 Statistical analysis of agglomerates' size. Statistical distributions of (**a**) diameter, (**b**) thickness, and (**c**) aspect-ratio of filler agglomerates contained in nanocomposites of LLDPE + 4.8 vol.% GNP at different P&F cycles. (**d**) Geometrical mean values of filler agglomerates' aspect-ratio, diameter and thickness as a function of P&F cycles fitted with Equation 6.1 using the D-factor of Equation 4.9.*

Table 6.1 Geometrical means (GM) and geometrical standard deviations (GSD) related to the distributions of Figure 6.4.

P&F cycles	Diameter		Thickness		Aspect-ratio	
	GM (µm)	GSD	GM (µm)	GSD	GM	GSD
10	27.9	2.54	0.948	2.70	20.7	2.12
30	23.5	2.39	0.803	3.06	20.2	2.33
50	11.0	2.58	0.278	2.64	26.6	2.34
100	6.60	2.02	0.214	2.15	27.4	2.04
200	5.64	1.96	0.131	1.66	30.1	2.18
500	4.37	2.21	0.093	2.36	36.7	2.11

6.3.1 Nanocomposite of LLDPE + 4.8 vol.% GNP prepared by melt-blending

By comparison, the microstructure of a LLDPE nanocomposite containing the same amount of GNP but prepared by twin-screw melt-blending appears more 3D randomly oriented (Figure 6.5). But no large agglomerates are present, as in samples prepared above 200 P&F cycles, meaning that also a traditional melt-blending process can well disperse this type of GNP.

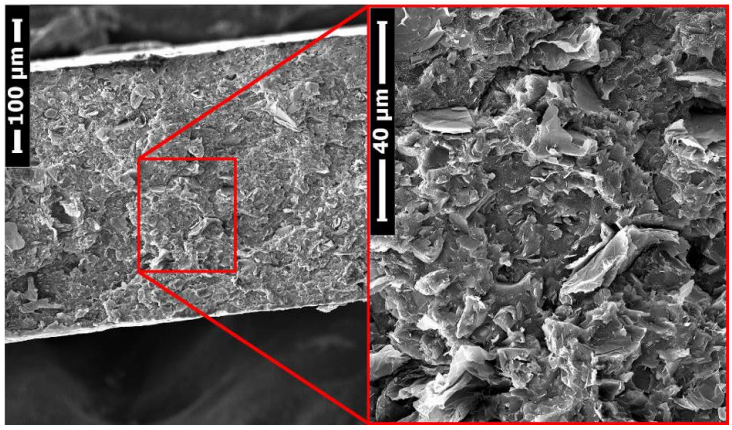

Figure 6.5 Cryogenic fracture surfaces of a LLDPE + 4.8 vol.% GNP sample prepared by melt-blending and compression moulding.

6.4 Micromechanical investigation of the P&F dispersion mechanism

Following the microstructural observations of the previous section, we wonder what the mechanism of P&F dispersion is. Could it bring any significant advantage compared to a traditional melt-blending technique, beside the possibility to align the particles?

To answer this question, we need to estimate the shear rate produced at each P&F cycle, compare it with the yield stress of the GNP agglomerates, and establish whether re-agglomeration occur. We can initially investigate these aspects by looking at the rheological data of the samples.

The following figures show the viscosity of the P&F samples containing 4.8 vol.% GNP at 120 °C, 140 °C, and 180 °C. The P&F technique was performed at a temperature (120 °C) really close to the melting point of the polymer (116 °C), differently from melt-blending techniques that use temperatures around 190 °C for LLDPE. This has a consequence on the viscosity of the samples, which results much higher than what it should be if the samples were processed at higher temperatures. Indeed, we observe that the viscosity of neat LLDPE decreases from ~4.000 Pa·s at 120 °C to ~350 Pa·s at 180 °C.

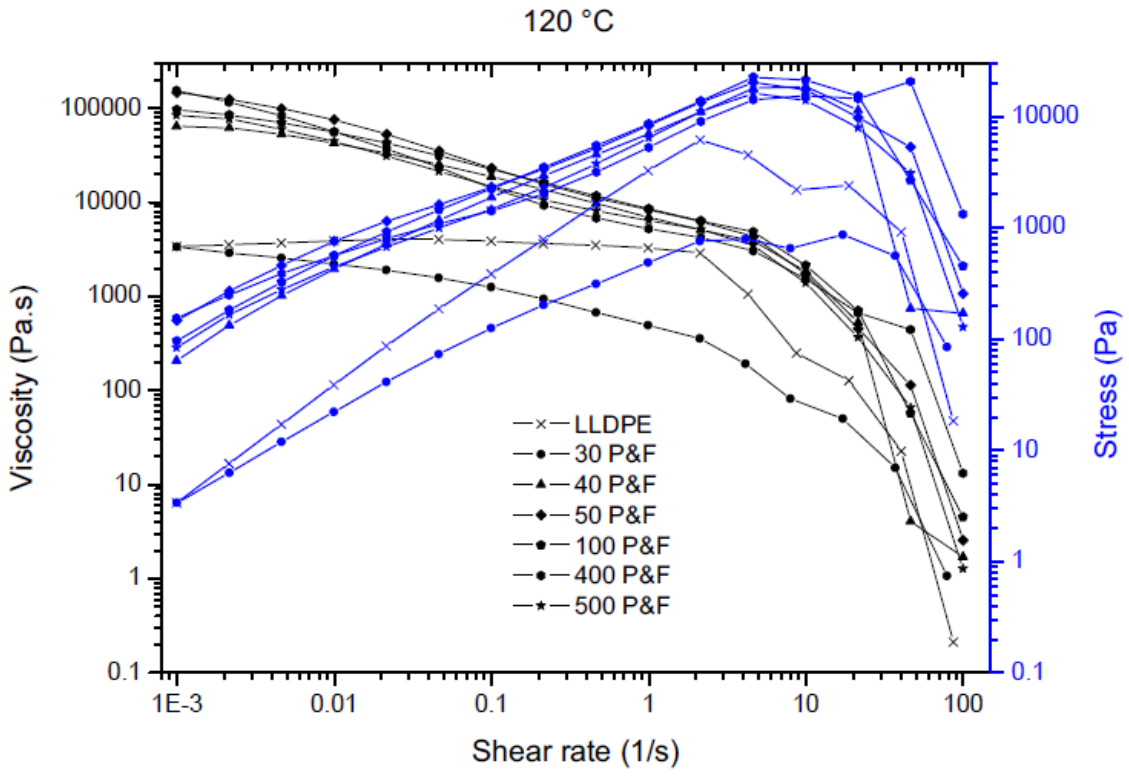

Figure 6.6 Viscosity and shear stress at 120 °C of LLDPE + 4.8 vol.% GNP nanocomposites prepared at different P&F cycles.

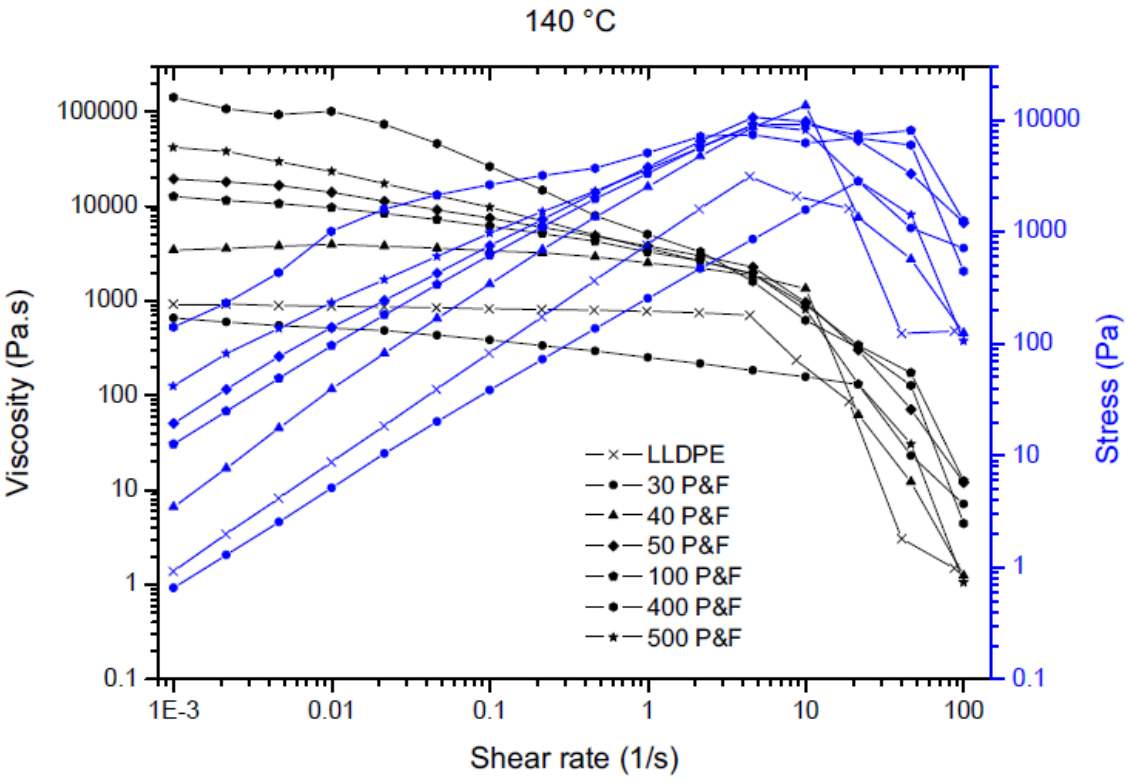

Figure 6.7 Viscosity and shear stress at 140 °C of LLDPE + 4.8 vol.% GNP nanocomposites prepared at different P&F cycles.

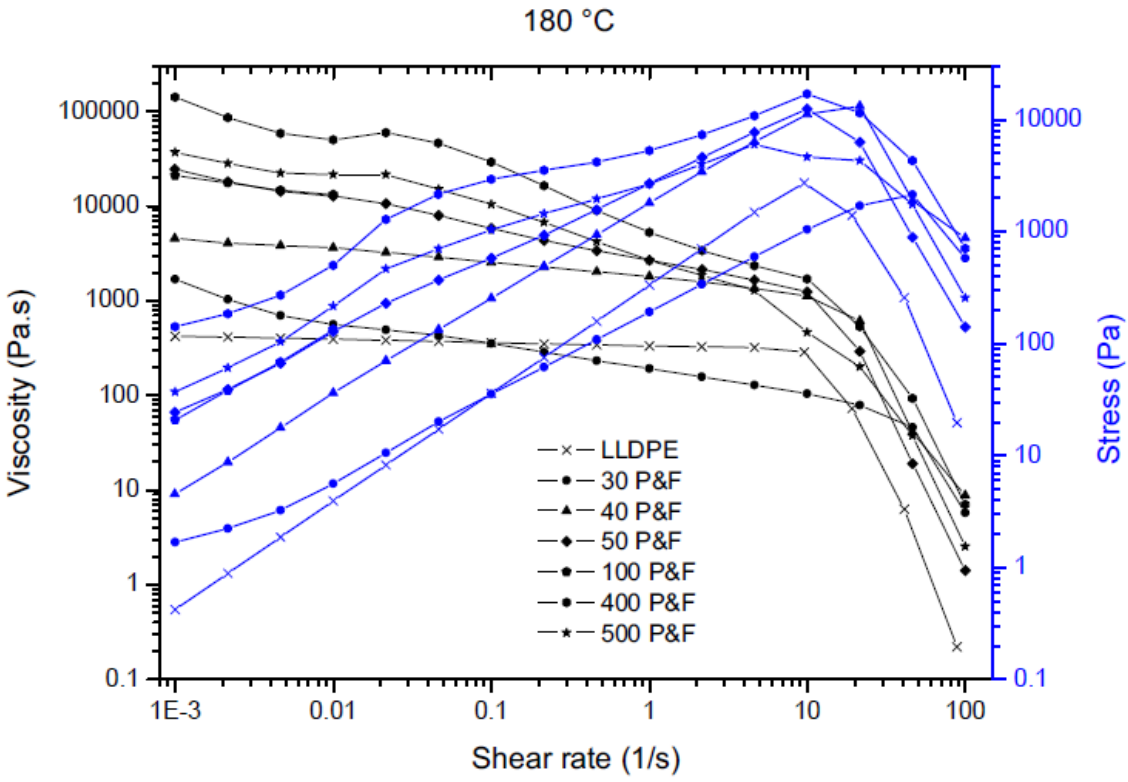

Figure 6.8 Viscosity and shear stress at 180 °C of LLDPE + 4.8 vol.% GNP nanocomposites prepared at different P&F cycles.

A common feature of the samples tested at different temperatures is the decrease of the shear stress over a range of shear rates in which also the viscosity decreases. This might be due to slippery on the walls of the rheometer. It is interesting to note that, for all the considered temperatures, the viscosity of the samples prepared with less than 40 P&F cycles is lower than the viscosity of neat LLDPE. Considering that the microstructure of nanocomposites prepared with less than 50 P&F cycles presents agglomerates that are bigger than the dimensions of the initial GNP powder macro particles (Figure 6.4d) and that these samples also lost some GNP powder from their tensile fracture surfaces (which will be discuss later), it is fair to infer that such agglomerates act as a lubricant to the molten LLDPE matrix, lowering the viscosity of sample compared to that of neat LLDPE. Samples prepared with more than 40 P&F cycles show increasing viscosity with the number of P&F cycles. When analysed at 120 °C, however, these samples do not show a remarkable increase of the viscosity with the number of P&F cycles as when they were analysed at higher temperatures do.

We can now examine the shear rate and stress that these samples undergo during the hot-pressing step of each P&F cycle.

The flow has a dominant extensional component that orients the particles with their flat faces perpendicular to the pressing direction. We approximate this flow as an axis-symmetric squeeze flow between two parallel plates located at a distance 2*h*. *R* denotes the radius of the sample when the gap height is 2*h*. In a cylindrical coordinate system with origin located at the midpoint between the plates, the radial velocity profile corresponding to a power-law fluid with constitutive equation $\tau_{rz} = m\left(-\frac{\partial v_r}{\partial r}\right)^n$ squeezed between two no-slip surfaces is [170]:

$$v_r = \left(\frac{-\dot{h}r}{h}\right) B_n \left[1 - \left(\frac{z}{h}\right)^{1+1/n}\right] \qquad \textit{Equation 6.2}$$

where $B_n = \frac{2n+1}{2n+2}$ (note: here *n* does not indicate the number of P&F cycles). The local shear rate is

$$\dot{\gamma} = \frac{\partial v_r}{\partial z} = \left(\frac{-\dot{h}r}{h^2}\right) B_n (1 + 1/n) \left(\frac{z}{h}\right)^{1/n} \qquad \textit{Equation 6.3}$$

and the volume-averaged shear rate magnitude over the sample is

$$\langle\dot{\gamma}\rangle = \frac{1}{\pi R^2 h} \int_{r=0}^{R} \int_{z=0}^{h} |\dot{\gamma}|\, 2\pi r dr dz = \frac{2}{3} B_n \frac{\dot{h}R}{h^2} \qquad \textit{Equation 6.4}$$

For $n > 0$, B_n varies weakly with n (for a shear thinning fluid, it varies from $B_n = ¾$ for $n = 1$ to $B_n = ½$ for $n = 0$). In terms of orders of magnitude, we can thus write

$$\langle\dot{\gamma}\rangle = c_n \frac{\dot{h}R}{h^2} \qquad \textit{Equation 6.5}$$

where c_n is a constant of order 1. In the case of slip surfaces, the flow is a uniform biaxial extensional flow and the average generalised shear rate is $\langle\dot{\gamma}\rangle = \sqrt{3}\frac{\dot{h}}{h}$ [171]. Because R/h >> 1, the average shear rate in the perfect slip case can be orders of magnitude smaller than in the no-slip case.

In our experiment, $|\dot{\gamma}| \approx 1.8$ mm/s, h varies from 1 mm to 0.25 mm, and the radius of the sample varies from 4 to 8 cm. In the case of slip surfaces, the average shear rate thus varies from 3 to 12 s^{-1} during compression. In the case of no-slip surfaces, the average shear rate varies from 72 to 2304 s^{-1}, where we have taken $c_n = 1$ for simplicity. The experimental case will likely be between the no-slip and the perfect slip case. We take $\langle\dot{\gamma}\rangle \sim 10$ s^{-1} and $\langle\dot{\gamma}\rangle \sim 1000$ s^{-1} as values representative of the initial and final stages of compression. Therefore, the squeeze flow in the thin gap between the plates produces large shear rates.

Fitting the LLDPE + 4.8 vol.% GNP samples data at 120 °C (Figure 6.6), we obtain a power-law for the viscous stress $\tau = k\langle\dot{\gamma}\rangle^n$, where $k \approx 500$ (in SI units) and $n \approx 0.75$. Thus, the average stress is estimated to vary roughly between 3 KPa and 90 KPa during compression, depending on the adhesion of the polymer to the confining walls.

To evaluate whether breakage of agglomerates and dispersion of GNP can take place, we need to compare the flow-induced stresses to the yield stress of the agglomerates σ_y. For percolating graphene suspensions, the following model has been recently proposed [151] that seems to fit well experimental data:

$$\sigma_y \cong \frac{4}{3}\frac{\Gamma}{D_p}{V_f^c}^2 f\left(\frac{V_f}{V_f^c}\right) \qquad \textit{Equation 6.6}$$

where V_f is the graphene volume fraction, V_f^c is the volume fraction at the percolation threshold (Equation 4.3), $\Gamma \approx 70$ mN/m is the graphene-graphene surface energy, D_p is the platelet diameter, and $f = \frac{\left(V_f/V_f^c - 1\right)^{2.5}}{\left(V_f/V_f^c + 1\right)^{0.5}}$. For $\xi \approx 26$ close to the initial aspect-ratio of the microparticles embedded into the polymer, we get $V_f^c \approx 5.7$ vol.%. For $D_p \approx 9.4$ µm, $\frac{\Gamma}{D_p}{V_f^c}^2 \approx 2.4$ Pa. Accounting for the f factor, even assuming that the local volume fraction within a macro aggregate is 10 times V_f^c, the aggregate yield stress is roughly $\sigma_y \approx 0.24$

KPa, much less than the applied viscous stress. This means that the high viscosity of the polymer (we are working just above the melting temperature) during each P&F cycle induces viscous stresses large enough to break the GNP agglomerates.

The formula above is probably not very accurate for dense macro agglomerates for which V_f is close to 1. In this case, using basic fracture mechanics arguments, one may write the order of magnitude of the force required to break the contact between each platelet in the macro agglomerate as ΓD_p. The force acts over an area D_p^2, so the corresponding stress is of the order of $\sigma_y \sim \Gamma D_p$, which is about 0.74 KPa. Also this estimate gives a yield stress value much smaller than the applied viscous stress.

The controlled flow in P&F has a further crucial benefit. With conventional processing methods, characterised by complex flow streamlines, the flow can promote re-agglomeration rather than dispersion if converging streamlines are present that force the particles to encounter each other. In contrast, in the P&F approach, the dominant extensional flow increases the particle separation at each cycle by "stretching" the fluid containing the suspended platelets. A key aspect of the method is that after the pressing step has ended, the shear rate goes practically to zero. As a consequence, the sample viscosity increases dramatically, "freezing" the microstructure (for samples at 120 °C containing 4.8 vol.% GNP, the viscosity increases from $\eta \cong 10$ Pa·s for $\dot{\gamma} \cong 10\ s^{-1}$ to $\eta \cong 10^5$ Pa·s for $\dot{\gamma} \cong 10^{-3}\ s^{-1}$). Moreover, the samples are cooled down to room temperature to perform the folding step of each P&F cycle, so re-agglomeration cannot occur at all (instead, cutting and overlapping steps always happen in the molten state in conventional multi-layer coextrusion). Hence, once dispersed, the platelets remain dispersed until the next pressing step.

6.5 Effect of GNP dispersion on nanocomposite properties

To study the nanocomposite properties as a function of nanofiller dispersion, we want to make sure that other factors do not have any influence on our samples with the P&F cycles, such as polymer degradation, polymer crystallinity change, and so forth. Sections 11.3 and 11.4 in appendix suggest that any variation in the properties of our LLDPE + 4.8 vol.% GNP nanocomposites is indeed only caused by improved GNP dispersion/distribution, and not by any change in the intrinsic properties of LLDPE and GNP.

6.5.1 Mechanical properties as a function of GNP dispersion

Figure 6.5a shows representative stress-strain curves for samples at different P&F cycles, containing 4.8 vol.% GNP. The mechanical reinforcement (*R*: the ratio between the elastic moduli of a composite, E_c, and its matrix, E_m; for LLDPE E_m = 140 ± 5 MPa), stress at yield (*Y*), and stress at break (*B*) are improved by nanofiller dispersion (Figure 6.9b), in agreement with studies reported in the scientific literature [149,172].

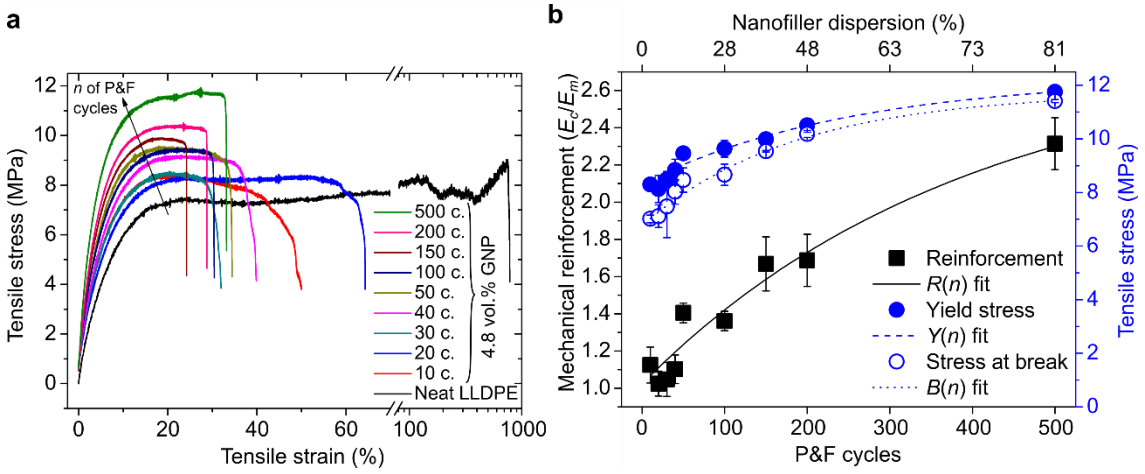

*Figure 6.9 Effect of nanofiller dispersion on the mechanical properties of LLDPE + 4.8 vol.% GNP nanocomposites. (**a**) Representative stress-strain curves. (**b**) Mechanical reinforcement (R(n)), stress at yield (Y(n)), and stress at break (B(n)) data, with best fits using Equation 6.1 with the D-factor of Equation 4.9.*

Since the yield stress depends also on the nanofiller specific surface area [17], its improvement compared with neat LLDPE (7.85 ± 0.27 MPa) is consequently explained by an increasing nanofiller-matrix interfacial area with P&F cycles. The stress at break overtakes the value of neat LLDPE (9.5 ± 0.7 MPa) only after 150 P&F cycles, when failure initiation due to stress concentrations generated by GNP agglomerates is overcome (Figure 6.10).

Figure 6.10 shows the tensile fractures of the samples. At low number of P&F cycles, the fractures have GNP agglomerates almost as thick as the samples (Figure 6.10a). Such large agglomerates are not visible in cryogenically broken specimen. This can be explained with the fact that the tensile specimen brake in correspondence of the widest agglomerates because of stress concentrations in the polymer matrix (the agglomerates cannot carry the applied load, since they are not a continuum body). In fact, samples prepared below 50 P&F cycles have lost some GNP powder from their breakage surfaces, indicating that in these samples the GNP are not fully wetted by the polymer. The consequence is that the stress at break results lower than that of pure LLDPE, as

pointed out earlier. For example, the sample prepared at 10 P&F cycles contains some wide agglomerates up to ~ 1/4 of the breakage surface area, and its stress at break is 7 MPa (whereas *B* of pure LLDPE is 9.5 MPa). If the cross-section relative to LLDPE is used for the calculation of the stress at break, then *B* results ~ 7 MPa / (1–1/4) = 9.3 MPa, which is the stress at break of pure LLDPE. Samples prepared above 150 P&F cycles do not present any GNP agglomerates in their fracture surfaces, so *B* of these samples is higher than that of neat LLDPE. Moreover, the profile of the fracture of these last samples appears linear and regular with short LLDPE fibrils disposed in layers (Figure 6.10b). On the contrary, samples prepared at low P&F cycles presents irregularly shaped fractures, with wide and long strained LLDPE fibrils, which are similar to those observed in neat LLDPE.

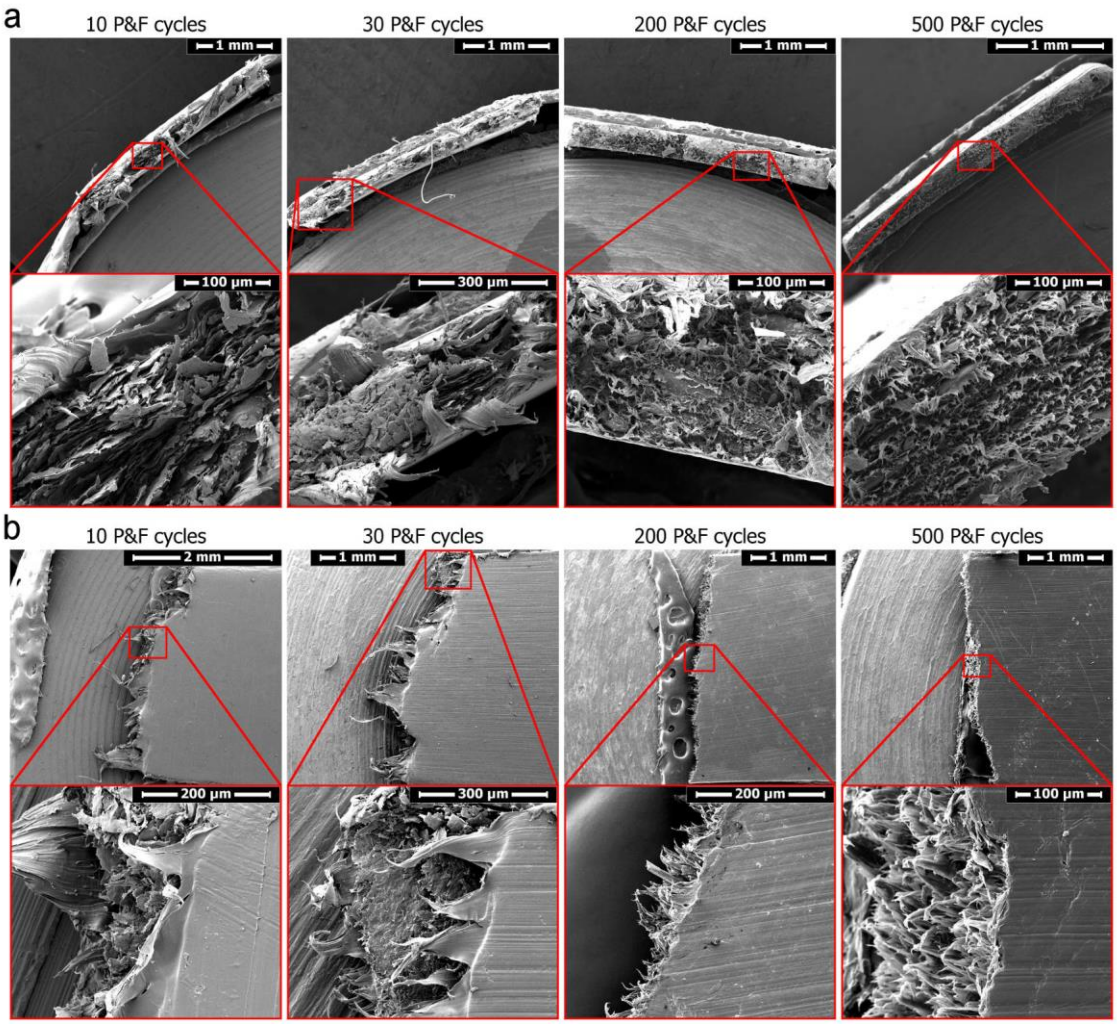

*Figure 6.10 Tensile fracture surfaces of LLDPE + 4.8 vol.% GNP nanocomposites with increasing GNP dispersions. (**a**) Front view; (**b**) side view.*

6.5.1.1 Reference properties of nanocomposites prepared by twin-screw extrusion

For comparison, the reference sample prepared by melt-blending followed by compression-moulding and containing 4.8 vol.% GNP has been tensile tested as well. The mechanical properties (Table 6.2) appear to be as low as those of P&F samples prepared between 100 and 150 P&F cycles. This is believed to be mainly due to the reduced in-plane alignment of the GNP nanoparticles inside this sample.

Table 6.2 Reference mechanical properties of LLDPE + 4.8 vol.% GNP prepared by melt compounding and compression moulding.

	Young's modulus (MPa)	Reinforcement (E_c/E_m)	Stress at yield (MPa)	Strain at yield (%)	Stress at break (MPa)	Strain at break (%)
Melt blending / compression moulding	200 ± 40	1.4 ± 0.3	9.9 ± 0.9	35 ± 4	9.4 ± 1.1	51 ± 8

The morphology of the tensile fracture (Figure 6.11) is straight as it happens for P&F samples above 100 P&F cycles. Additionally, the LLDPE fibrils after failure have a morphology similar to that observed in the P&F sample prepared at 200 P&F cycles. Again, this means that the GNP dispersion in this nanocomposite is good.

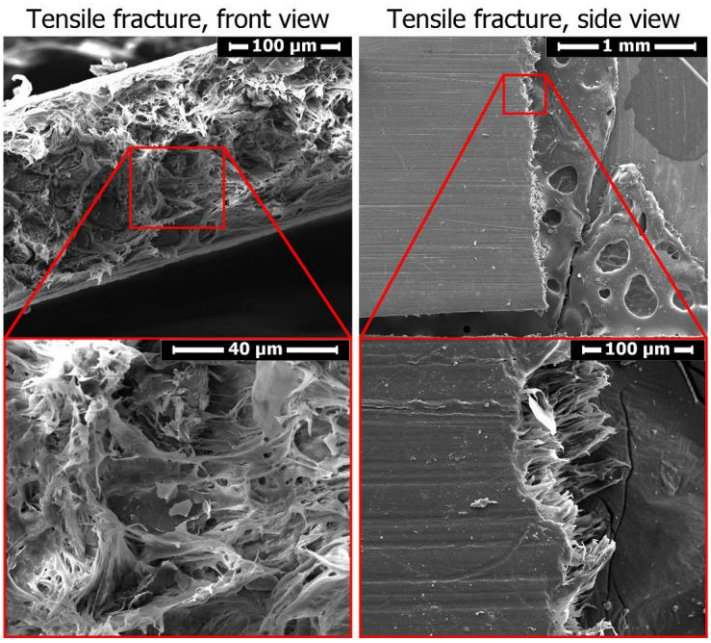

Figure 6.11 Tensile fracture surfaces of a LLDPE + 4.8 vol.% GNP sample prepared by melt-blending and compression moulding.

6.5.2 Electrical conductivity as a function of GNP dispersion

The in-plane and out-of-plane electrical conductivities of the nanocomposite films (Figure 6.12) have been measured using a two-point-probe setup. The anisotropic microstructure observed by SEM is reflected in the electrical properties: in-plane conductivity is ~4 orders of magnitude higher than that of out-of-plane. The conductivities of samples prepared with less than 40 P&F cycles are too small to be measured, suggesting well-isolated GNP agglomerates inside the matrix. Between 50 and 150 P&F cycles, the electrical conductivities reach a maximum, as particles become sufficiently dispersed/distributed to develop an optimal conductive network. This conductivity rise with nanofiller dispersion agrees with some observations reported in the literature [149,173,174]. The electrical conductivities then decrease at higher P&F cycles, suggesting an effective distributive mixing of nanoparticles thereby deteriorating the conductive network. This agrees with the studies of Tkalya *et al.* [71], who have reported increased percolation thresholds in nanocomposites with better graphene dispersions. The reduction in electrical conductivity can also be explained by a partial fragmentation of GNP. This effect, however, should be less dominant than the nanofiller dispersion/distribution effect, as there is no evidence of a reduction of mechanical properties with P&F cycles. Notably, the reference sample prepared by melt-blending/compression-moulding (also containing 4.8 vol.% GNP) is not electrically conductive, probably because of a combination of 3D random orientation and good dispersion of GNP.

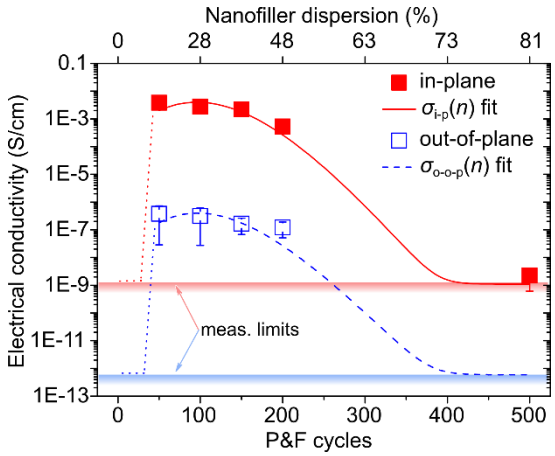

Figure 6.12 Effect of nanofiller dispersion on the electrical properties of LLDPE + 4.8 vol.% GNP nanocomposites. The horizontal shades areas indicate the lower measurement limits for in-plane (red) and out-of-plane (blue) electrical conductivity. The measurement limits are due to the apparatus employed that could measure a minimum conductance of $2 \cdot 10^{-11}$ S, combined with the geometries of the samples used (1.5/(0.8×0.03) cm^{-1} for in-plane measurements, and 0.03/(1×1) cm^{-1} for out-of-plane). The dotted lines are only a guide for the eye. The continuous and dashed lines are best fits of Equation 6.7 keeping the parameters σ_{th} and σ_M constant (σ_{th} to the measurable conductivity threshold, and σ_M to the maximum experimental value) to minimize the number of free variables.

6.6 Model fitting of P&F data

The nanocomposite properties reported in Figure 6.5, Figure 6.9 and Figure 6.12 could be fitted by our nanofiller dispersion model, so the number of P&F cycles could have been converted into percentage of nanofiller dispersion level, as shown on the top axes of these figures. This is because other factors influencing the mechanical properties of nanocomposites, such as the nanofiller orientation state or the nanofiller exfoliation state or the properties of the matrix, do not change during the P&F process, as shown in section 6.3 and in appendices 11.1, 11.3 and 11.4.

However, the electrical conductivity in Figure 6.12 clearly does not present the behaviour expected by Equation 6.1, and it has been fitted using another formula. Indeed, this property presents a percolation behaviour that is highly affected by the inter-particle distance, which is controlled also by the GNP dispersion state, besides its concentration. We expect the variation of the electrical conductivity with GNP dispersion to depend on the following aspects:

- Dimension of the considered interval of nanofiller dispersion, ΔD;
- a, which is a constant that describes the velocity of the conductivity change with the inter-particle distance;
- Critical nanofiller dispersion, D_c, at which there is a quick change in electrical conductivity (for instance, from insulator to conductor), namely by the difference $D - D_c$;
- Asymptotic conductivity, σ_{th}, that is the theoretical conductivity when the nanofiller is perfectly dispersed (D = 1) or when there is a drop-down of the percolation network due to inter-particle distances greater than the critical distance for electron tunnelling between particles. This corresponds to the difference $\sigma_{th} - \sigma$.

These aspects can be translated into a differential equation that can be solved to give the following relationship between conductivity σ and nanofiller dispersion D:

$$\sigma(D) = \sigma_{th} + (\sigma_M - \sigma_{th}) \cdot e^{-a(D-D_c)^2} \qquad \textit{Equation 6.7}$$

where σ_M is the maximum conductivity reached at the critical nanofiller dispersion level D_c, and D is given by Equation 4.9. We believe that Equation 6.7 provides a more realistic description of the electrical conductivity than Equation 6.1.

Table 6.3 reports the fitting parameters for each property of Figure 6.5, Figure 6.9 and Figure 6.12. The *I*-factor of the P&F process results to be independent of the analysed

property. However, we decided to calculate and use for the conversion of n in D a mean distribution-rate I of $(3.3 \pm 1.4)\cdot10^{-3}$ from the mechanical and electrical properties only, because the GNP agglomerate measurements could have been affected by some obvious problems of images resolution and operator-related errors.

Table 6.3 Fitting parameters of the properties of LLDPE + 4.8 vol.% GNP nanocomposites for our nanofiller dispersion model.

Observable property, P	P&F-related dispersion model (Equation 4.9 where t is substituted by n)	Predictive model of Equation 6.1		Predictive model of Equation 6.7		Adjusted R^2 of the fit
	I-factor	P_0	P_{th}	n_c *	a	
GM aspect-ratio, ξ	$5\cdot10^{-3}$	19.5	38	-	-	0.86
GM diameter, d	$29\cdot10^{-3}$	38 µm	4.9 µm	-	-	0.89
GM thickness, t	$27\cdot10^{-3}$	1.1 µm	112 nm	-	-	0.74
Reinforcement, R	$2.5\cdot10^{-3}$	1.02	2.8	-	-	0.79
Yield stress, Y	$3.9\cdot10^{-3}$	8.32 MPa	12.3 MPa	-	-	0.98
Stress at break, B	$5.5\cdot10^{-3}$	6.76 MPa	11.7 MPa	-	-	0.997
In-plane electrical conductivity, $\sigma_{i\text{-}p}$	$2.0\cdot10^{-3}$	-	-	96	114	0.80
Out-of-plane electrical conductivity, $\sigma_{o\text{-}o\text{-}p}$	$2.5\cdot10^{-3}$	-	-	97	84	0.64

* n_c is the critical number of P&F cycles, which is related to the critical nanofiller dispersion level D_c through Equation 4.9.

Consequently, our nanocomposites can be divided in three categories according to the nanofiller dispersion state: 1) nanocomposites with D < 15% containing inhomogeneous GNP distribution and isolated GNP agglomerates that cannot form an electrically conductive network, resulting also in mechanical properties close or worse than those of neat LLDPE. 2) Nanocomposites with 15% < D < 50% containing homogeneously distributed, well dispersed, and aligned GNP, showing high and anisotropic conductivities and mechanical reinforcement effects. 3) Nanocomposites with D > 50%

presenting highly dispersed, distributed, and aligned GNP, which reflects in enhanced mechanical properties, but poor electrical conductivity.

6.7 Conclusion

This chapter has experimentally demonstrated how the properties of nanocomposites change with the nanofiller dispersion level. The mechanical properties always improve with increasing GNP dispersion, accordingly to Equation 6.1. This fact experimentally proves the theoretical background on which the effective volume fraction (Equation 4.1) is based. Indeed, Equation 6.1 is the general expression of any composite theory (such as the Halpin-Tsai equations for the elastic modulus and the Pukanszky model for the yield stress) that has been expanded in a first-order McLaurin series, considering V_f^{eff} (Equation 4.1) as the independent variable.

However, the electrical conductivity is not a monotonic function of the GNP dispersion. If the aspect-ratio of the GNP agglomerates is high enough, we can observe a conductivity enhancement, with values much higher than what theoretically expected by the classical percolation theory for homogeneously distributed GNP. This proves once again the distribution-conductivity model based on Equation 4.15 and Equation 5.1. For simplicity, we express the conductivity enhancement observed in our P&F samples with Equation 6.7.

Chapter 7.

Further investigations of the P&F technique

7.1 Introduction

In this chapter we will attempt to understand whether we could estimate the P&F distribution rate for any polymer-nanofiller system without analysing the nanocomposite properties or microstructure. We also want to understand how we could speed up the nanofiller distribution, and how the process differs from the traditional multi-layer co-extrusion, as this technique is also based on the baker's transformation.

7.2 Another approach to estimate the distribution rates

The rate of a nanofiller distribution inside a certain matrix during the P&F dispersion process can be quickly calculated by using the initial nanofiller/matrix contact area (A_0), and the contact area after n P&F cycles (A_n):

$$I = \frac{1}{n} ln\left(\frac{A_p - A_0}{A_p - A_n}\right) \qquad \textit{Equation 7.1}$$

The total nanofiller surface area (A_p) can be calculated using the specific surface area (S), and the amount m of nanofiller introduced inside a sample:

$$A_p = S \cdot m \qquad \textit{Equation 7.2}$$

Both A_0 and A_n could be estimated by measuring the percentage, $C\%$, of sample area covered by nanofiller from the optical pictures of the sample:

$$A_{0,n} = 2 \cdot sample\ area \cdot C\% \qquad \textit{Equation 7.3}$$

Figure 7.1 shows the method used to calculate the sample area and $C\%$ from the optical pictures. A_n is more accurate if $C\%$ is measured at low (<5) P&F cycles, i.e. when the probability of having an overlapping of nanofiller agglomerates is low, thus A_n will not result underestimated.

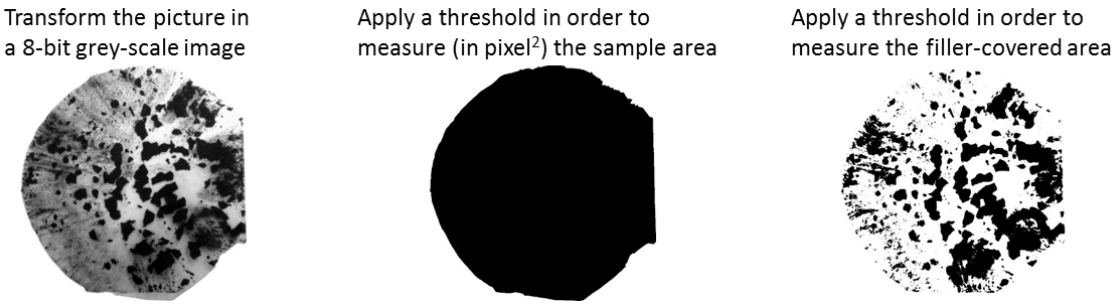

Figure 7.1 Method used to calculate the area of a sample, and its fraction covered by nanofiller.

With this method, we can calculate a distribution-rate of $(3.5 \pm 2.0)\cdot10^{-3}$ for GNP in LLDPE, by analysing the pictures taken during the first four P&F cycles. Despite this method may not be accurate, it still gives a good estimation of the distribution-rate. Indeed, the distribution-rate found from the fitting of the mechanical and electrical properties results quite similar and equal to $(3.3 \pm 1.4)\cdot10^{-3}$ (see section 6.6).

As the distribution-rate is important for the determination of the dispersion level of a nanofiller, in Table 7.1 we report the distribution rates of different nanofiller/matrix systems.

Table 7.1 *Distribution-rates for different nanofiller/matrix systems.*

Filler \ Matrix	LLDPE	HDPE	Phenoxy	PC	TPU
C-Therm 002 S = 25 m^2/g	$(3.5 \pm 2.0)\cdot10^{-3}$	$(9.3 \pm 1.5)\cdot10^{-3}$	$(7.4 \pm 1.0)\cdot10^{-3}$	$(2.3 \pm 1.0)\cdot10^{-3}$	$(5.43 \pm 0.23)\cdot10^{-3}$
xGnP 750 S = 100 m^2/g *	$(2.6 \pm 0.4)\cdot10^{-3}$	$(2.58 \pm 0.11)\cdot10^{-3}$	$(3.9 \pm 1.7)\cdot10^{-3}$	$(1.6 \pm 0.3)\cdot10^{-3}$	$(1.63 \pm 0.14)\cdot10^{-3}$
MMT (Cloisite 20A) $S \approx$ 800 m^2/g	$\geq7\cdot10^{-2}$	$\geq10\cdot10^{-2}$	$\geq2\cdot10^{-2}$		$\geq3\cdot10^{-2}$

* S calculated from XRD thickness: $S \approx 2/(d \cdot t_{XRD})$, where d is the density of graphite

Note that for the case of montmorillonite (MMT) nanocomposites, the MMT agglomerates disappear during the dispersion process, leaving the samples transparent. Therefore, we have recorded the number n of P&F cycles needed to obtain a sample transparent to the naked eye and free of white agglomerates. We believe that when a sample does not show MMT agglomerates anymore, then the dispersion-factor must be at least 50%. Therefore, we can estimate the distribution-rate with the following equation:

$$I = \frac{1}{n} ln\left(\frac{A_p - A_0}{0.5A_p}\right)$$ *Equation 7.4*

The distribution-rates of MMT results to be much higher than GNP powders, and this might be due to the functionalisation of the MMT used, or to a better nanofiller/matrix interaction that aid the dispersion process.

7.3 Increasing the number of folding to increase the distribution rate

To investigate whether the number of folding could speed up the dispersion process, we have prepared three series of LLDPE + 5 vol.% xGnP750 samples by folding them twice, three times and four times at each P&F cycle. xGnP750 contains GNP ~ 9 nm thick, and their surface area is much higher than that of the GNP used in the previous chapter. Therefore, we should expect better nanocomposite properties, provided this type of GNP can be dispersed adequately. And if we can accelerate the dispersion process, we should see an enhancement of properties at lower P&F cycles.

To avoid any misleading interpretation of the results, we have checked whether polymer degradation, polymer crystallinity and graphene exfoliation occur during the process, and we have found that we can exclude these effects. Therefore, any difference in the properties between these three series of samples must be due to only to a faster GNP distribution.

We can use the method presented in the previous section to have a rough idea of the distribution rates for each series of samples. Figure 7.2 shows the photographs of the series prepared < 5 P&F cycles. These samples contain a concentration of xGnP750 as low as 0.5 vol.% to be able to measure the samples' covered area more accurately. After analysing these pictures, we obtain $I = (2.6 \pm 0.4)\cdot10^{-3}$ for the series of samples folded twice at each P&F cycles, $I = (3.7 \pm 1.0)\cdot10^{-3}$ for the series folded three times per cycle, and $I = (7.8 \pm 1.2)\cdot10^{-3}$ for the series folded four times per cycle. This means that for every increment in the number of folds, the distribution rate results improved by a factor of ~1.5, i.e. we can speed up the process by increasing the number of folds.

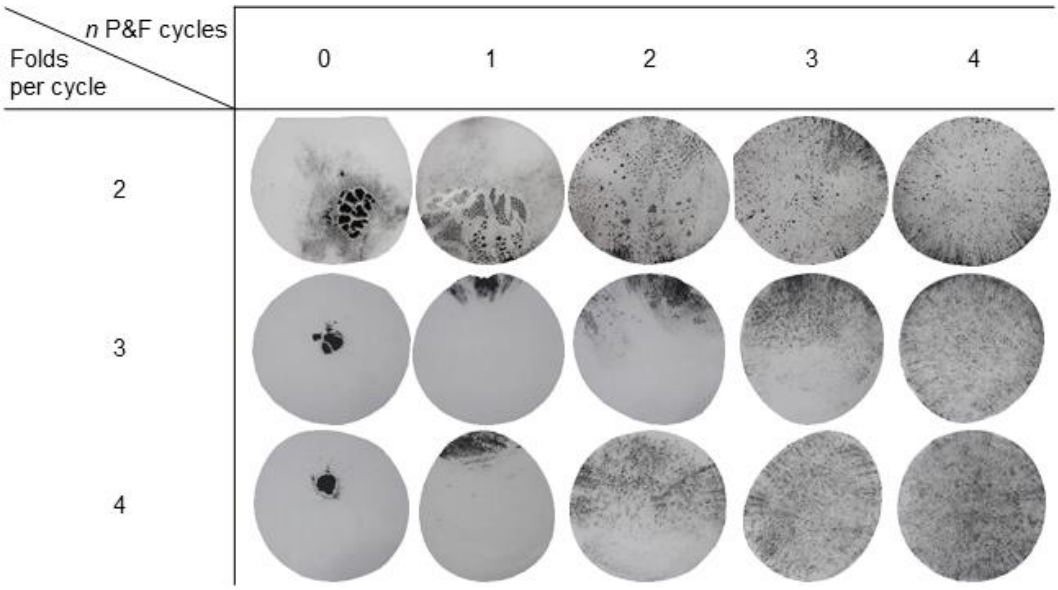

Figure 7.2 Optical pictures of LLDPE + 0.5 vol.% xGnP750 nanocomposites prepared at different P&F cycles and number of folds per cycle.

Figure 7.3 reports typical tensile curves at different P&F cycles for series of samples of LLDPE + 4.8 vol.% xGnP750 prepared with two, three and four folds per P&F cycle. For the latter series, we have prepared only one sample with 10 P&F cycles because it is hard to fold the films four times and keep them folded before the hot-pressing step.

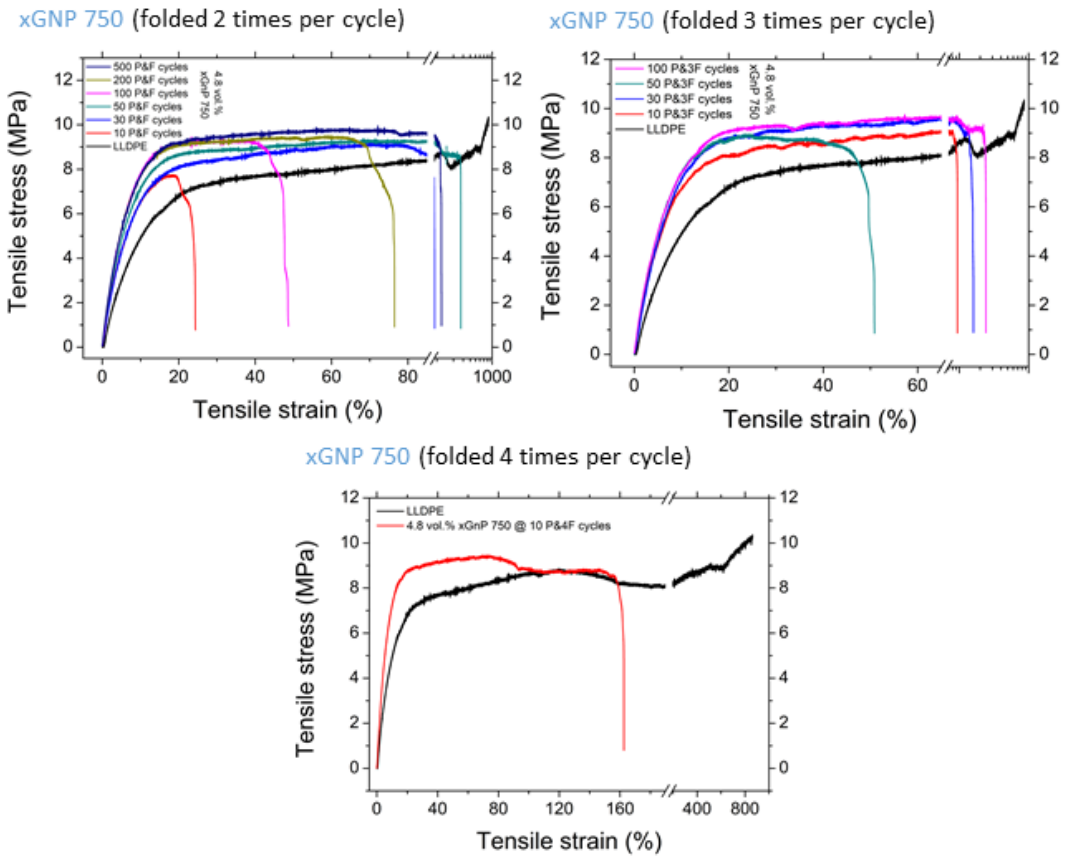

Figure 7.3 Tensile curves of LLDPE + 4.8 vol.% xGnP750 nanocomposites prepared at different P&F cycles and number of folds per cycles.

The mechanical properties that we obtain from the stress-strain curves of Figure 7.3 are presented in Figure 7.4. All properties improve quicker with P&F cycles when the samples are folded more times per cycle. Fitting these data with Equation 6.1 using *D* defined by Equation 4.9, we find a distribution rate $I = 27 \cdot 10^{-3}$ for the series of samples folded twice per cycle, and $I = 70 \cdot 10^{-3}$ for the series folded three times per cycle. This proves again that folding the samples a higher number of times per cycle speeds up the dispersion process. However, the distribution rates are higher than those estimated previously, and the properties plateau at values that are smaller than the nanocomposites of the previous chapter. the theoretical background of Equation 4.10 explains these differences: as xGnP750 contain thinner particles with higher aspect-ratios, the maximum achievable nanofiller-polymer contact area (A_{max}) is lower than the total nanofiller surface area. Consequently, the distribution rates are quicker, and the maximum achievable mechanical properties are smaller.

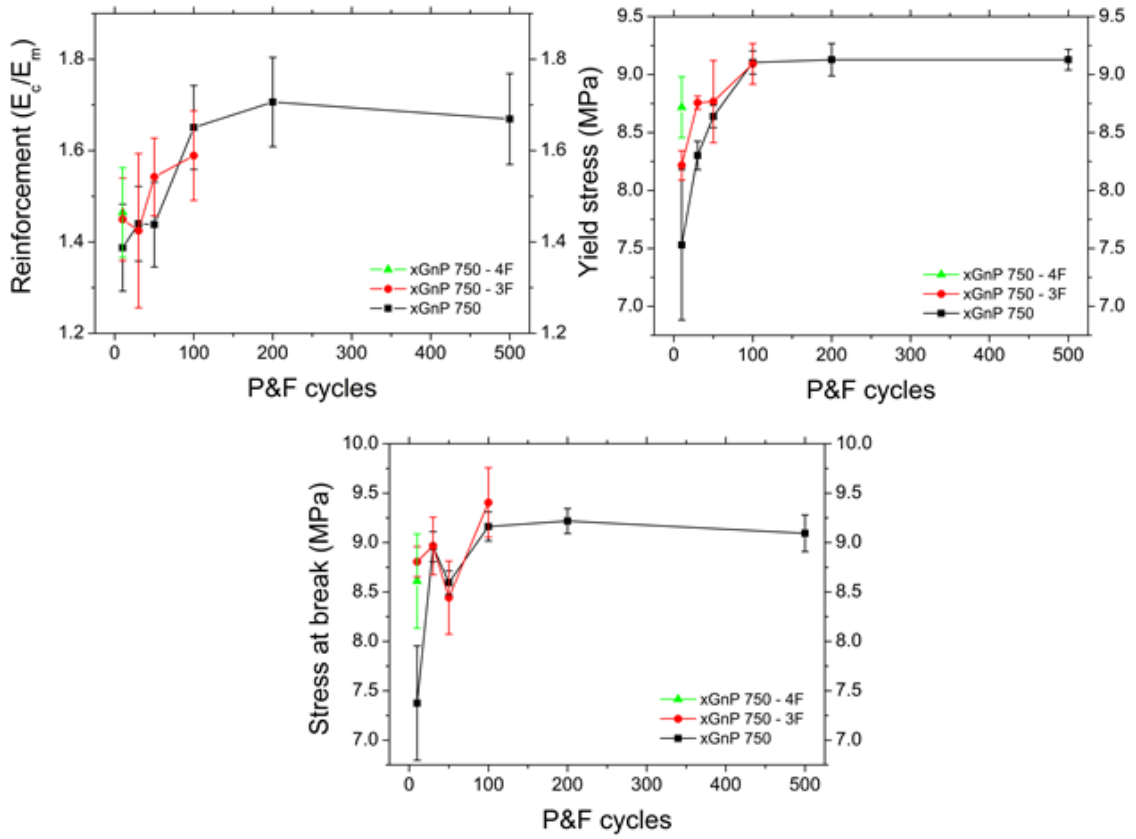

Figure 7.4 Mechanical properties of LLDPE + 4.8 vol.% xGnP750 nanocomposites as a function of P&F cycles. The series of samples folded twice at each P&F cycle is indicated as "xGnP750" in the legend, the one folded three times per cycle as "xGnP750 – 3F", and the one folded four times as "xGnP750 – 4F".

The series of nanocomposites folded twice per cycle does not have any electrical conductivity for any P&F cycle. The series of samples folded three times per cycle, instead, presents a conductivity enhancement around 50 P&F cycles, as shown in Figure

7.5. The sample prepared with 10 P&F cycles and folded four times has a conductivity of $(1.1 \pm 0.5) \cdot 10^{-8}$ S/cm. Also these results indicate that the distribution rate improves with number of folds per cycle. Moreover, it seems that both the distribution rate and the time that the samples remain in the molten state have an influence on the percolative network of nanofiller agglomerates throughout the matrix, as the series of samples folded twice do not present any conductivity.

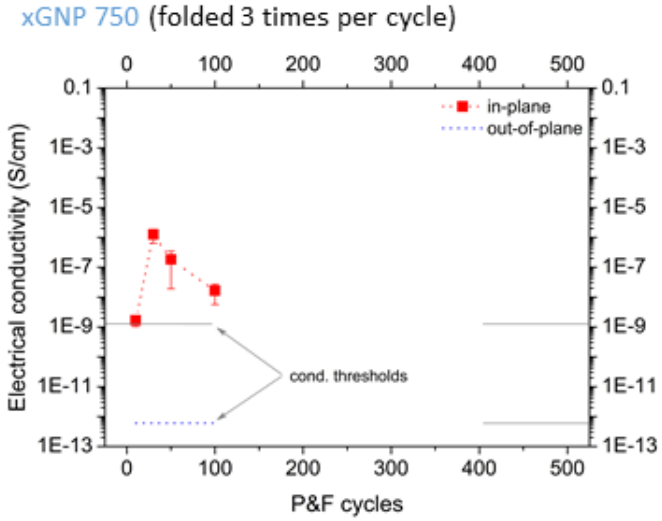

Figure 7.5 Electrical conductivity as a function of P&F cycles of LLDPE + 4.8 vol.% xGnP750 nanocomposites folded three times per P&F cycle.

7.4 Comparison of P&F technique with multi-layer coextrusion

Multi-layer coextrusion is a technique with the potential to disperse and mix two different materials with a small number of fixed elements ad the end of two converging extrusion lines. These elements apply the baker's transformation to the molten materials, so that the dispersion can occur even at the nanoscale. The other advantage of this technique is that the materials are prepared with a layered structure, and the nanofillers result aligned along the machine's extrusion direction.

We have prepared three series of nanocomposites of HDPE + 2 wt.% xGnP750 using 1, 6 and 8 multi-layer elements. Therefore, their microstructures should present 2, 64 and 256 layers, and the mechanical properties should considerably improve as the alignment of nanofiller and the breakdown of agglomerates should significantly increase with the number of multi-layer elements.

Figure 7.6 presents the tensile curves for these materials tested along and transversely to the extrusion direction. Surprisingly, there is no evident change in the mechanical properties (Figure 7.7) with the number of ML-elements.

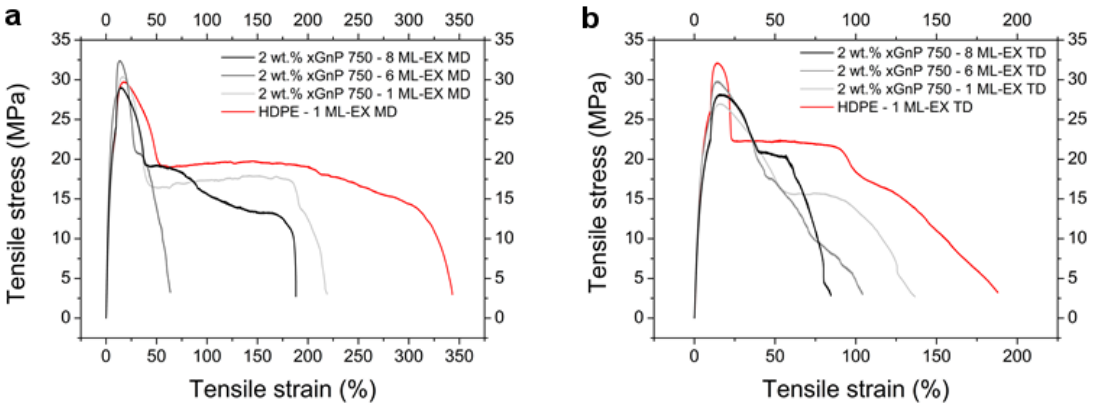

*Figure 7.6 Tensile tests of HDPE + 2 wt.% xGnP750 nanocomposites prepared by multi-layer coextrusion. (**a**) Specimen cut out along the machine direction. (**b**) Specimen cut out transversely to the machine direction.*

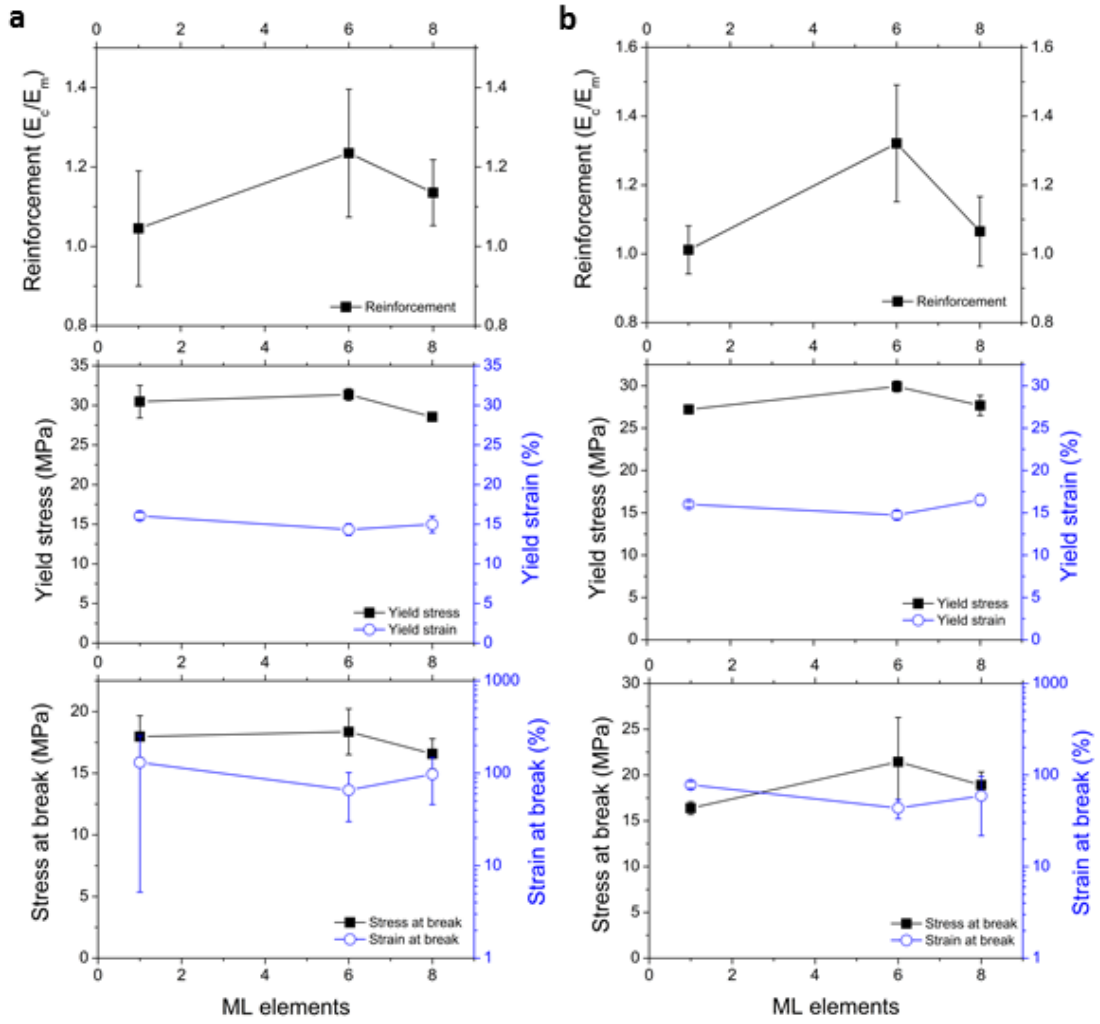

*Figure 7.7 Mechanical properties of HDPE + 2 wt.% xGnP750 nanocomposites prepared by multi-layer coextrusion. (**a**) Specimen cut out along the machine direction. (**b**) Specimen cut out transversely to the machine direction.*

Moreover, there is no mechanical improvement compared to the properties of neat HDPE. These two observations could be explained considering that xGnP750 and HDPE were already blended together before multi-layer coextrusion with a maximum reachable contact area that is lower than the surface area of xGnP750. We have processed the same starting pellets also with the P&F technique, and no mechanical improvement has been found in the resulting nanocomposites. This means that, for this type of materials, there is no evident advantage of using the P&F technique in addition to avoiding thermal degradation of the polymer.

7.5 Conclusion

The dispersion process of the P&F technique can be speeded up by folding the samples a higher number of times per cycle. However, when the nanofillers have a high specific surface area, it does not matter how fast the dispersion process is: the maximum dispersion level may not further improve after a certain limit. This is a critical aspect for demanding applications, where high quality nanofillers in terms of specific surface area and aspect-ratio should impart significant properties enhancements but cannot be properly dispersed and the nanocomposites result bad performing. Lastly, we have found that multi-layer coextrusion cannot guarantee a dispersion efficiency better than the P&F technique.

Chapter 8.

Toward efficient and highly loaded nanocomposites using the P&F technique

8.1 Introduction

Poor performing nanocomposites are a common issue often originated from low nanofiller dispersions, which usually occur when traditional techniques like solution-mixing and melt-blending process high nanofiller loadings. For example, to assess the reinforcing efficiency of different layered nanocomposites of LLDPE and GNP/graphene, Figure 8.1 compares reinforcement values found in literature [144,173,175–178] with theoretical predictions using the Halpin-Tsai model. None of the scientific literature data follows the linear behaviour predicted by the Halpin-Tsai model. Therefore, these nanocomposites show the typical reduction in reinforcing efficiency with nanofiller loading, commonly attributed to decreasing nanofiller dispersions.

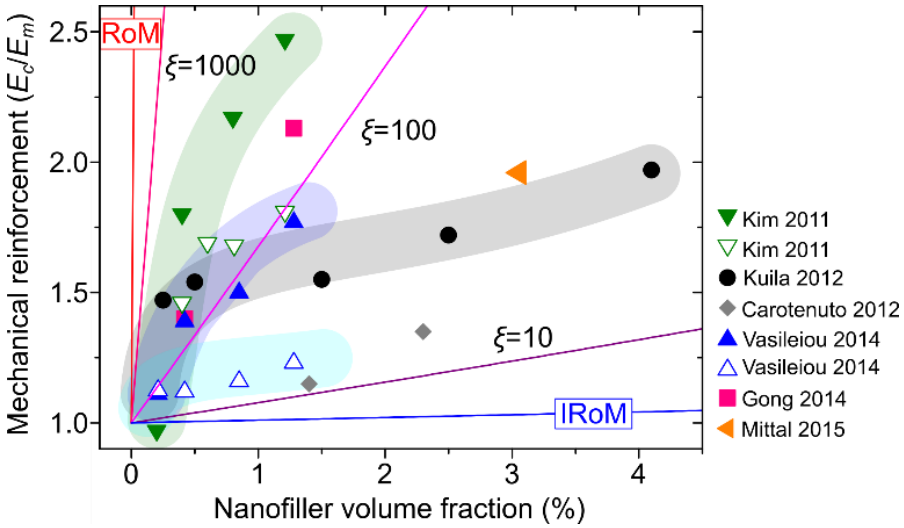

Figure 8.1 Assessment of the mechanical reinforcement of GNP-LLDPE nanocomposites from literature, together with prediction lines of the Halpin-Tsai model at different aspect-ratios (ξ) of mono-layer graphene. The shadowed areas are only a guide for the eye to highlight the decrease of reinforcing efficiency with nanofiller loading. In some cases, there are two data-sets per reference, corresponding to nanocomposites prepared by different techniques or with different matrix/nanofiller functionalisation: these aspects influence the nanofiller dispersion/orientation state or the nanofiller-matrix interface [179] and consequently the mechanical properties.

As high aspect-ratio nanofillers may be difficult to be efficiently dispersed, here we show that nanofillers with $\xi << 1000$ such as GNP (obtained from EG) and MMT could be efficiently disperse with the P&F technique in high concentrations. This would hardly be possible with traditional melt-blending techniques because the viscosities of the processed materials would be too high. The resulting nanocomposites are well performing and present a uniform dispersion level.

8.2 Highly loaded GNP nanocomposites without any reinforcing efficiency loss

Below, we will study LLDPE nanocomposites containing different GNP loadings, but with a constant dispersion level of ~50%, which corresponds approximately to agglomerates made of only two nanoparticles (according to the definition of the *D*-factor, and in agreement with the microstructural observations of chapter Chapter 6). Indeed, the best compromise between mechanical and electrical properties occurs around this dispersion level (see Figure 6.9b and Figure 6.12). We should be able to predict properties at different nanofiller loadings using the Halpin-Tsai and Pukanszky models modified by Equation 4.1 with a *D*-factor of ~50%, provided that the dispersion efficiency of the P&F process does not decrease at high amounts of this low aspect-ratio GNP. Section 11.5 in appendix demonstrates that any variation in the nanocomposite properties must be caused only by the GNP amount contained in the samples, and not by any change in the intrinsic properties of LLDPE and GNP.

Representative stress-strain curves of these nanocomposites prepared with 200 P&F cycles are shown in Figure 8.2a. It is clear that the strain at break abruptly decreases with the amount of GNP in the samples. The stress at break is fairly close to the yield stress of these samples, and increases with GNP concentration, but it exceeds the value of neat LLDPE (9.5 MPa) only for samples with a GNP concentration greater than 2.1 vol.%.

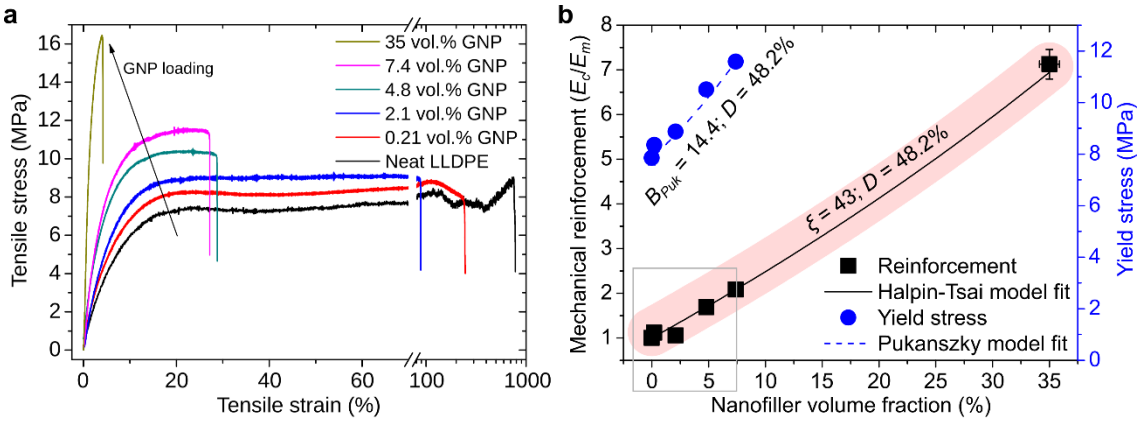

*Figure 8.2 Mechanical properties of LLDPE nanocomposites with different GNP loadings but similar dispersion levels (48.2%). (**a**) Representative stress-strain curves. (**b**) Mechanical reinforcement and yield stress together with fitting lines of the Halpin-Tsai and Pukanszky models.*

Interestingly, the mechanical reinforcement and yield stress data (Figure 8.2b) are fitted by the Halpin-Tsai and Pukanszky models using V_f^{eff} with D = 48.2%, which proves the

theoretical validity of the effective volume fraction, V_f^{eff}. The fits give a nanofiller aspect-ratio of 43 (in agreement with the theoretical one, ξ_{th} = 38, from the fit in Figure 6.4d), and an interaction parameter B_{Puk} (an estimation of nanofiller-matrix interaction) of 14.4, similar to values reported for clay nanocomposites [180]. The latter is a surprisingly high result considering that no compatibilizer was used, suggesting a fairly good GNP-LLDPE interaction.

These results demonstrate that the dispersion efficiency of the P&F technique does not decrease at high nanofiller amounts, and subsequently neither does the reinforcing efficiency. The frame at low volume fractions in Figure 8.2b indicates the region where literature data typically fall and lose their reinforcing efficiency (Figure 8.1).

The in-plane conductivity is again four orders of magnitude higher than the out-of-plane conductivity (Figure 8.3a). This reflects the anisotropic layered microstructures.

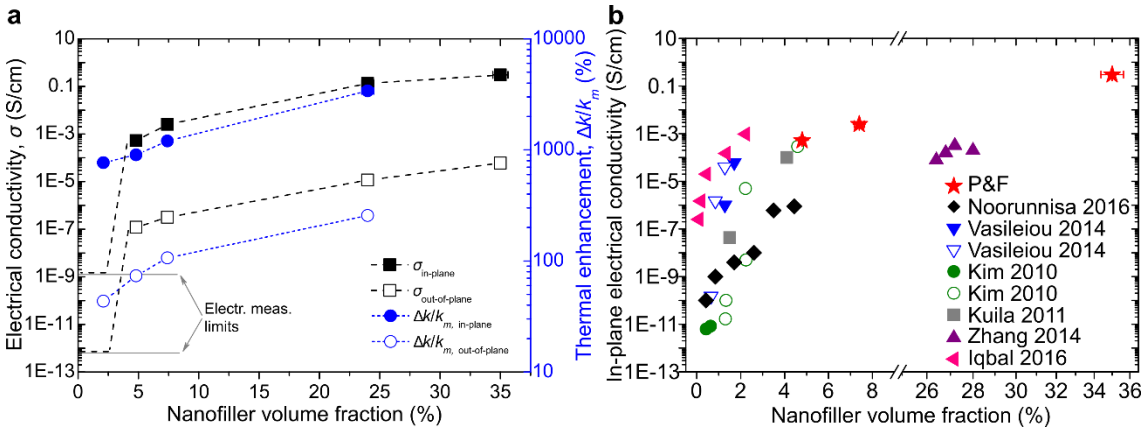

*Figure 8.3 Electrical and thermal conductivities of LLDPE nanocomposites with different GNP loadings but similar dispersion levels (48.2%). (**a**) Electrical conductivity (the lines are only a guide for the eye), and thermal conductivity enhancement respect to LLDPE thermal conductivity (k_m). (**b**) Assessment of the in-plane conductivity for LLDPE-GNP nanocomposites. Note the high in-plane conductivity of 0.3 S/cm of our P&F sample containing 35 vol.% GNP.*

Considering the aspect-ratio of the GNP used (~40) and referring to the work of Li and Kim [70], we should expect a percolation threshold around 15 vol.%, if GNP were perfectly dispersed and distributed. However, the percolation threshold lies somewhere between 2.1 and 4.8 vol.% (Figure 8.3a). This range is theoretically expected for perfectly dispersed nanoplatelets with aspect-ratios of 150 – 250. Therefore, the non-homogeneous, imperfect GNP dispersion ($D \approx 50\%$) in our nanocomposites increases the electrical conductivity (as depicted in Figure 6.12), hence lowering the percolation threshold to values theoretically expected for higher aspect-ratio fillers. This corroborates our conductivity model (Equation 6.7). Note that these high electrical conductivities come with massive in-plane thermal conductivity enhancements (>10 W/m·K, which is >3000%

higher than LLDPE thermal conductivity), while the out-of-plane conductivity increases up to ~1 W/m·K. To the best of our knowledge, this is the highest combination of thermal conductivity enhancement and thermal anisotropy ever reported.

Finally, a comparison of the in-plane conductivity data with the values found in the literature [174,176,181–184] for layered nanocomposites of LLDPE with GNP/graphene shows how our samples are among the highest conductive nanocomposites (Figure 8.3b). Note that the conductivity of our samples is predicted to be even higher for a *D*-factor close to $D_c \approx 25\%$, where the agglomerates should have a higher aspect-ratio.

8.3 Highly loaded MMT nanocomposites

Nanocomposites of LLDPE and montmorillonite have been prepared with only 50 P&F cycles, because at this number of cycles should correspond a MMT dispersion of ~ 99%. Indeed, the distribution-rate for MMT in LLDPE is ~ $7 \cdot 10^{-2}$, much higher than ~$3 \cdot 10^{-3}$ for GNP (see Table 7.1). Thermal gravimetric analysis reveals a MMT content of ~74 wt.%. Despite this ultrahigh filler content, the sample appears transparent (Figure 8.4a) because of the good MMT dispersion and alignment (Figure 8.4b).

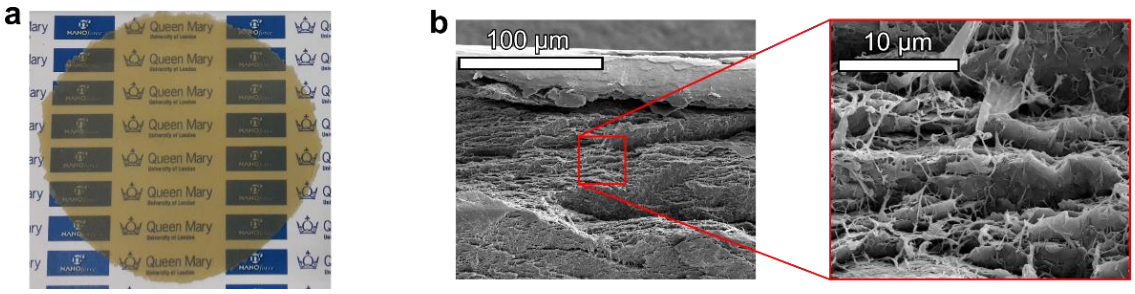

*Figure 8.4 Pictures of LLDPE + 74 wt.% MMT. (**a**) Optical picture (sample ~10 cm wide, and ~400 µm thick). (**b**) SEM micrographs of the microstructure.*

The nanocomposite has a Young's modulus of ~1.8 GPa, ~13 times higher than the pure polymer (E_c/E_m ~13), which is a record-breaking value for a nanocomposite based on a commodity or engineering plastic prepared by a top-down technique. However, the strength is only ~12.5 MPa, and the strain at break is ~1%.

To assess our nanocomposite, Figure 8.5 reports the mechanical reinforcement found in literature (see Table 11.2 in appendix) for MMT nanocomposites with non-elastomeric matrices. Our P&F sample is the highest loaded and reinforced sample ever reported for

nanocomposites prepared by a top-down method. Only bottom-up techniques, such as solution processing and layer-by-layer, can reach the same loading and mechanical reinforcement of our P&F sample.

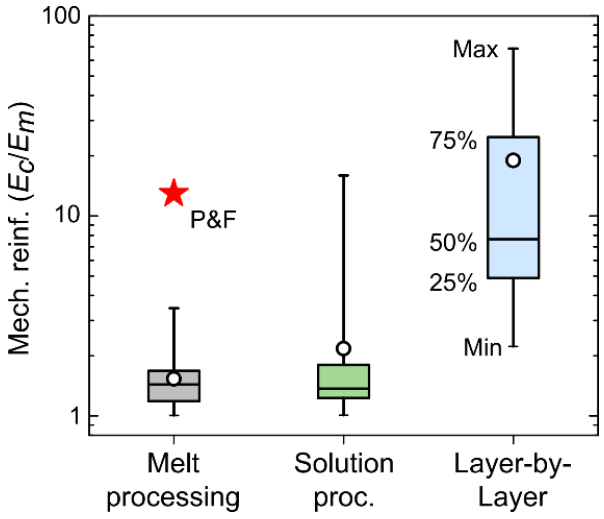

Figure 8.5 Assessment of the mechanical reinforcement of MMT nanocomposites, grouped by the processing method.

8.4 Conclusion

With the P&F technique, it is possible to disperse high amounts of relative low aspect-ratios nanofillers without losing reinforcing efficiency. This seems to be the only way to increase the nanocomposite mechanical properties avoiding agglomeration problems that affect high aspect-ratio nanofillers.

Chapter 9.

Future work: design of multifunctional properties enhancement in nanocomposites with tailored microstructures

9.1 Introduction

The theoretical framework presented in chapters 4, 5 and 6 advances the possibility of doing material design with nanoparticles, addressing the optimization of nanocomposite microstructures to fulfil particular technological applications of interest. For example, a layered microstructure with perfectly dispersed nanoparticles is needed for mechanical properties, or gas-barrier films for food packaging and flexible electronics [185,186]. The same applies also to thermal conductivity of heat dissipating devices [187]. For example, we measured the thermal conductivity of LLDPE nanocomposites with 4.8 vol.% GNP after 400 P&F cycles. Unexpectedly, thermal conductivities were ~3 W/m·K in-plane (~900% higher than neat LLDPE thermal conductivity) and ~0.3 W/ m·K out-of-plane, while being electrically insulating in all directions (average inter-particle distance longer than electron mean-free path [188]). The combination of high thermal conductivity and low electrical conductivity makes these nanocomposites promising for anisotropic thermal interface management of modern electronic, optoelectronic and photonic devices [188].

The ability of tailoring the microstructure demonstrated for the P&F process is a crucial factor for imparting nanocomposites with other multi-functionalities, such as self-heating, strain sensing, energy management, and mechanical enhancement due to nacre-like hierarchical microstructure, as described hereinafter.

9.2 Multifunctional properties of LLDPE/GNP nanocomposites prepared by P&F

The samples of LLDPE + GNP presented in chapters Chapter 6 and Chapter 8 can be used as microstructural references for nanocomposites with Joule-heating, strain-sensing and energy management functionalities enhanced by particular nanofiller dispersion states.

9.2.1 Joule-heating

Joule-heating materials are important, for example, in de-icing [189] or safety self-limiting power devices [190,191]. They require high electrical conductivities, which could be obtained with microstructures containing nanofiller dispersions close to the critical level D_c of Equation 6.7, where the aspect-ratio of the agglomerates is higher than that of individual nanoparticles.

Figure 9.1 shows the self-heating of LLDPE+GNP nanocomposites due to Joule effect when different electrical potentials are applied to the extremities of the samples. The inset pictures of the samples (Figure 9.1a, b, and c) were taken with a thermal camera, and show good thermal homogeneity reflecting an optimal microstructure. The sample containing 7.4 vol.% GNP with a dispersion level of 48.2% (Figure 9.1b) heats up less than the sample containing 4.8 vol.% GNP (Figure 9.1a) because its nanofiller dispersion state is grater, so less conductive paths are available for Joule heating (see the comparison graph of the samples' self-heating effects in Figure 9.1e).

When the nanofiller concentration is high, the theoretical conductivity at high dispersion states (σ_{th}) should not be very different from that at the critical dispersion level (σ_M). Therefore, one should find good electrical properties even if the nanofiller dispersion is greater than D_c. This is the case for nanocomposites containing 24 vol.% GNP with a dispersion level of 48.2% (Figure 9.1c,d), which appear to be simultaneously promising for self-heating devices triggered by low voltages (Figure 9.1e), mechanical properties (because $D > D_c$), and strain-sensing for health monitoring.

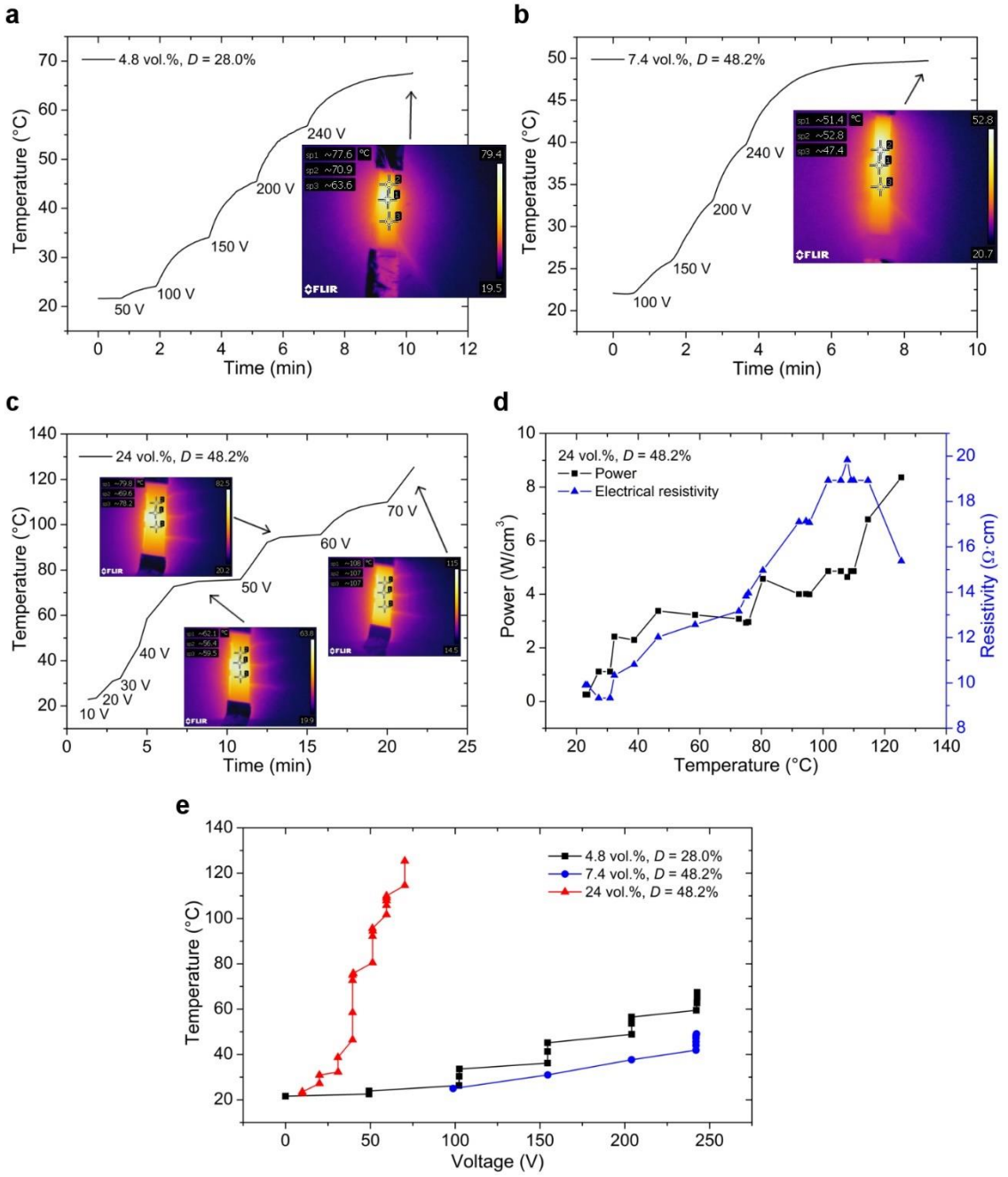

*Figure 9.1 Self-heating tests of LLDPE nanocomposites with different GNP loadings and dispersion levels. (**a**) Sample containing 4.8 vol.% GNP with a dispersion level of 28% reaches a temperature of ~70 °C when 240 V of AC electrical potential difference is applied to its extremities. (**b**) Sample containing 7.4 vol.% GNP with a dispersion level of 48.2% reaches only a temperature of ~50 °C after 240 V. (**c**) Sample containing 24 vol.% GNP with a dispersion level of 48.2%. (**d**) Power supplied to sample (c) and sample resistivity correlation with measured temperature. (**e**) Comparison of the self-heating behaviour of the tested samples as a function of the applied AC electrical potential difference.*

9.2.2 Strain sensing

Resistive sensor materials can find applications in smart textiles and structural health monitoring applications [20,192]. The sensitivity of these materials to strain is typically

the highest when the microstructures contain a graphene concentration close to the critical volume fraction for electrical percolation, or when the aspect-ratio of the agglomerates is slightly higher than that of individual nanoplatelets, i.e. when $\sigma(D)$ approaches σ_{th} (see Equation 6.7), which happens when $D_c << D < 1$.

Strain sensing during extension of nanocomposites (Figure 9.2a) reveals that the variation of electrical resistance is much more evident for samples containing low amounts of GNP. The sample containing 4.8 vol.% GNP with a dispersion level of 28% (close to the critical dispersion level D_c) presents a resistance variation similar to the sample of same composition but higher dispersion level (48.2%) only at high strains, when its conductivity approaches the theoretical one, σ_{th}. All nanocomposites present several orders of magnitude variation in resistance before yielding (which occurs around 15% of strain), demonstrating their suitability for structural health monitoring applications.

Figure 9.2b shows the resistance variation of the same nanocomposites when undergo a cyclic strain. The small peaks at the minima of strain are due to the bending of the samples. High nanofiller dispersions give high resistance variations (gauge factor of ~30) because the nanocomposite conductivity approaches the theoretical value σ_{th} quicker with the strain (see sample containing 4.8 vol.% GNP with D = 48.2%). However, dispersions closer to the critical level, D_c, provide better electrical signals (see sample containing 4.8 vol.% GNP with D = 28%, which has a low initial resistance of ~140 kΩ). The resistance variation becomes less evident for increasing amounts of GNP because the difference between σ_M and σ_{th} becomes ever smaller.

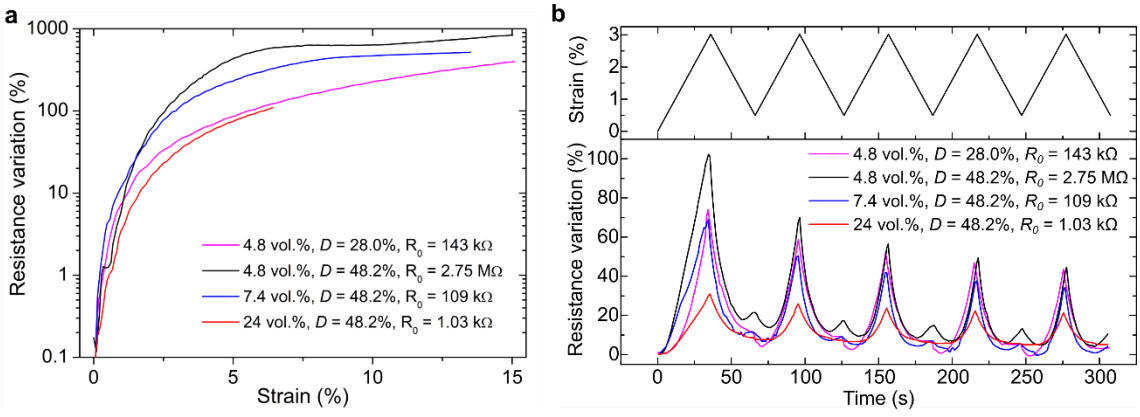

*Figure 9.2 Strain-sensing of LLDPE nanocomposites containing different GNP loadings and GNP dispersion states. (**a**) Variation of electrical resistance as a function of tensile strain. (**b**) Variation of electrical resistance during time when a cyclic strain is applied to the nanocomposites.*

9.2.3 Energy management

Materials for energy-management devices [193,194] must have high nanofiller dispersion levels, provided the electrical conductivity (σ_{th} in Equation 6.7) is small enough to allow huge polarization effects inside the layered microstructures, so that the materials can show high dielectric constant (high-k) and small dielectric loss. Polymer nanocomposites with such microstructures could be employed, for example, as gate dielectrics, energy storage devices or electroactive materials [193]. Nanocarbon-polymer composites satisfy the synergistic requirements of high-k and limited loss just before reaching the percolation threshold. Above this point there is a huge increase in the dielectric loss, due to the ohmic electrical conduction of the percolated network.

Figure 9.3 shows the admittance magnitude of LLDPE nanocomposites containing 4.8 vol.% GNP with different nanofiller dispersion states. Admittance (Y), which is inversely proportional to impedance [195], has been plotted to facilitate the relationship of AC-properties with DC-conductivity measurements. First, the pristine polymer that initially exhibits a purely capacitive behaviour (linear frequency-dependence, Figure 9.3a) is transformed into a conductive material (non-frequency dependant) when containing GNP agglomerated states (*D*-factor of 28% and 48.2%). The different trends of |Y| along frequency support our previous observations of the electrical conductivity as a function of nanofiller dispersion (Figure 6.12), hence it is in accordance with the behaviour expected by Equation 6.7. Indeed, a slight agglomeration of nanofiller allows a conductive percolation network inside the material (admittance is predominantly real, Ohmic conduction), especially when is close to the critical dispersion level D_c (which corresponds to 25% for our nanocomposites containing 4.8 vol.% GNP). In such case, the resistive equivalent circuit shown in Figure 9.3b (R_1 and R_2) may represent the nanocomposites. However, when the nanofiller dispersion increases, the nanocomposite conductivity decreases from high values (the highest is σ_M when $D = D_c$) to lower values (approaching the theoretical conductivity σ_{th} expected by Equation 6.7 at high nanofiller dispersion states), because the percolation network becomes “disconnected” in many points. These “dead-ends” contribute to the formation of micro-capacitors at those conductive/dielectric/conductive regions of well-dispersed platelets with non-negligible interparticle gaps. Nanocomposites with such a microstructure containing highly dispersed GNP can be represented by a parallel R-C equivalent circuit, as depicted in Figure 9.3b (R_3 and C_3), and a frequency-dependent admittance is observed (see sample with D = 80.6% in Figure 9.3a). Contrary to the common believe, this absence of percolation in nanocarbon/polymer nanocomposites can be also exploited for

technological applications where dielectric materials with a high dielectric constant (real permittivity, ε') and a low dielectric loss (imaginary permittivity, ε'') are needed.

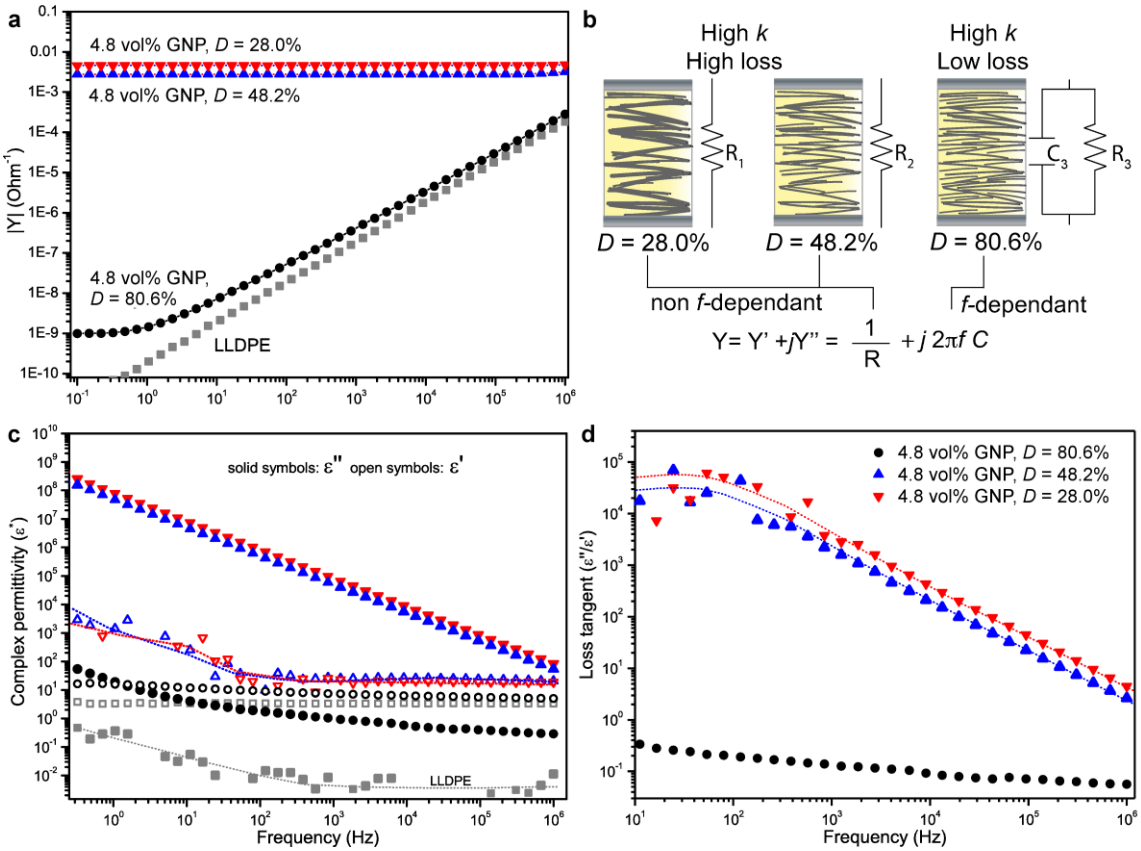

*Figure 9.3 Impedance spectroscopy of LLDPE + 4.8 vol.% GNP nanocomposites with different GNP dispersion states. Frequency sweep of: (**a**) admittance modulus (|Y|), (**c**) complex permittivity, and (**d**) loss tangent. (**b**) Draw that summarises the observed behaviours: while a nanofiller dispersion close to the critical dispersion level Dc (≈ 25% for these samples) of Equation 6.7 makes the nanocomposites conductive (resistive, R1 and R2), high dielectric constant (ε', high-k) and low loss tangent (ε''/ε') nanocomposites can be addressed only if the nanofiller dispersion state is optimized (D close to 100%).*

The real component of permittivity for dielectric/conductor nanocomposites is a measure of the migration and accumulation of charges at the dielectric/conductor interfaces (Maxwell–Wagner–Sillars polarization) [196], while the imaginary part is related to dielectric and conduction losses, associated to the material's ohmic resistance and the induced polarisation, respectively. As seen from Figure 9.3c, the imaginary permittivity of the resistive samples (*D* = 28% and 48.2%) is as high as 10^8 at low frequencies and decreases to 10^2 at 1 MHz. The sample with a high nanofiller dispersion of 80.6% has an imaginary permittivity that remains notably low, between 100 and 0.1 throughout the entire frequency window. Furthermore, this last sample shows a loss tangent (ε''/ε') as low as ~0.1 (Figure 9.3d), in comparison with values above 10 for samples with lower nanofiller dispersions (*D* = 28% and 48.2%). These results confirm that the electrical properties of GNP-polymer nanocomposites can be tailored by the nanofiller dispersion

state, exploiting the needs of a wide variety of conductive or insulating (capacitive) applications.

Figure 9.4 summarises these findings and illustrates how nanofiller agglomeration reflects in conductive nanocomposites that are mainly resistive: the imaginary (Z'') *vs.* real impedance (Z') Nyquist plots of the samples show very small values of Z'' for a constant value of Z' (diverging slightly only at high frequencies due to contact resistance). Higher dispersion levels and distributions of aligned GNP inside the dielectric LLDPE matrix result in nanocomposites with a capacitive behaviour (sample containing 4.8 vol.% GNP with a dispersion level 80.6%, see the C_3 || R_3 equivalent circuit, shown also in Figure 9.3b). This is due to the build-up of electrostatic charges at the interfaces between conductive and dielectric domains (in accordance with the small percolation conductivity σ_{th} expected by Equation 6.7), which is important for energy-management applications.

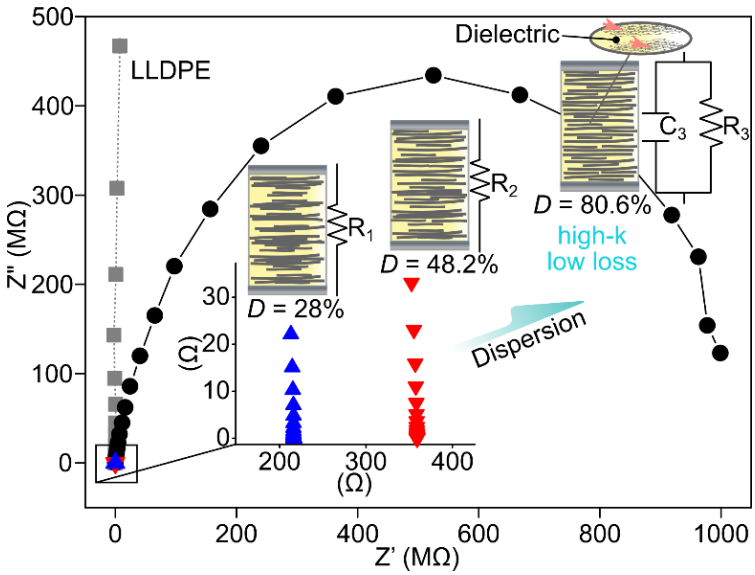

Figure 9.4 Imaginary (Z'') vs. real impedance (Z') obtained from impedance spectroscopy of LLDPE containing 4.8 vol.% GNP in different dispersion states.

9.3 Mimicry of nacre 2-level hierarchical structure in (PDMS/MMT)/TPU nanocomposites

The microstructural controlling capability of the P&F technique can be exploited also to mimic natural structures that are known to possess high mechanical performances. Nacre, for example, is made mainly of calcium carbonate that is a brittle material as mentioned previously (Figure 2.10). However, because of its 2-level hierarchical and

layered structure (Figure 9.5), nacre exhibits good mechanical properties and high toughness.

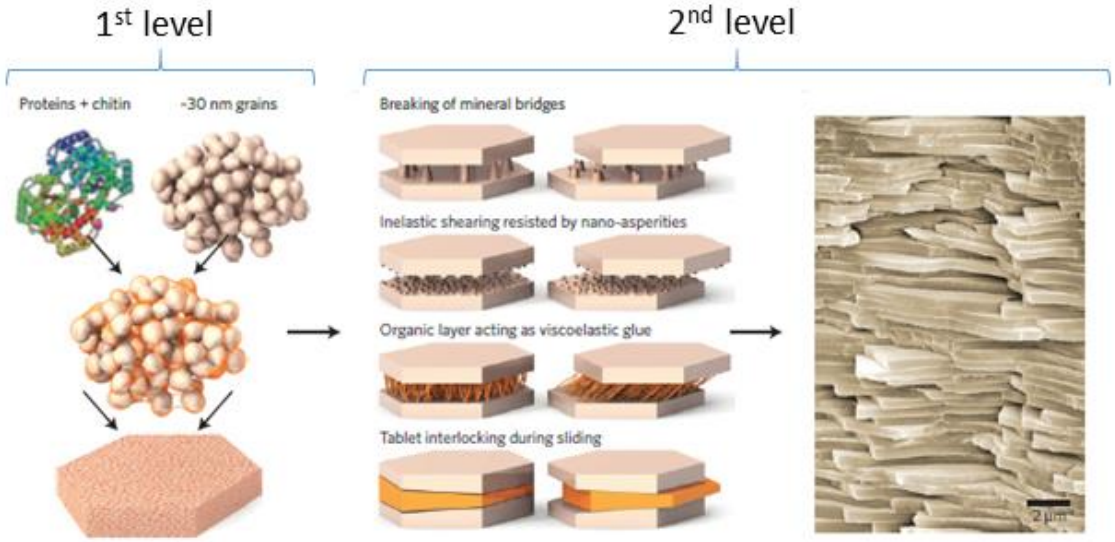

Figure 9.5 Illustration of the hierarchical structure of nacre. Figure adapted from ref. [49].

It would be useful to prepare materials with nacre-like structure, for example, for biomedical applications. For this purpose, blends of thermoplastic polyurethane (TPU) and polydimethylsiloxane rubber (PDMS) are believed to bring several advantages [197]: mechanical strength/toughness from TPU, and inertness from PDMS; biocompatibility (useful, for example, in scaffolds for tissue engineering, membranes for guided tissue regeneration, cartilage replacements, etc.); processing with conventional plastic techniques (extruders); and no need for crosslinking the PDMS component (which avoids the migration of curing chemicals to the surrounding tissues during the long term implantation period of the material).

However, the main obstacle in blending TPU with PDMS is the formation of an immiscible blend, which will lead to phase separation. To partially mitigate this problem, these polymers are usually compatibilized in several ways. We could investigate whether TPU and PDMS can be blended together without functionalisation using the P&F technique and, with the aid of nanofillers such as MMT arranged in nacre-like 2-level hierarchical structure, increase their mechanical properties.

9.3.1 Preparation of nacre-like PDMS/MMT nanocomposites and (PDMS/MMT)/TPU nanocomposites

We have prepared nanocomposite of PDMS + 80 wt.% MMT to mimic the first-level hierarchical structure of nacre. These two materials cannot be directly blended by P&F because the amount of MMT is too high, and the viscosity of PDMS too low (Figure 9.6). Thus, PDMS have been initially mixed with a MMT concentration of ~30 wt.%. Then, little amounts of MMT have been repetitively added and mixed with the initial putty by P&F at room temperature. After the complete addition of MMT, the sample has been further processed with 20 P&F cycles at room temperature to ensure a good dispersion and alignment of MMT.

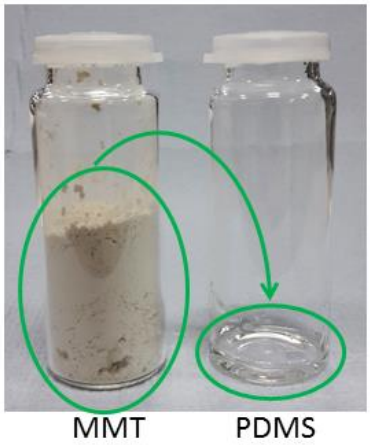

Figure 9.6 Starting materials used to prepare PDMS/MMT nanocomposites.

Note that, when containing >50 wt.% MMT, the sample easily crumbles because the amount of MMT is too high for the PDMS to keep all the particles stuck together. The sample becomes consistent again after few P&F cycles, when the MMT particles are sufficiently bounded by PDMS. Moreover, the final concentration of 81 wt.% MMT corresponds to ~74 vol.% MMT, which means that we are approaching the theoretical limit of space that can be occupied by MMT. Above this limit, the sample should always be crumbled because there is no enough polymer to keep the platelets of MMT stuck together.

Eventually, ketoxime has been added as a cross-linking agent for the PDMS matrix and mixed with 10 P&F cycles (drops added during the first 3 P&F cycles). The sample was left to cross-link for 1 day.

To mimic and study the effect of the second hierarchical level of nacre's structure, a range of samples has been prepared by adding 1 – 20 wt.% TPU to the previous

nanocomposite material. Each sample has obtained by sandwiching a certain amount of PDMS/MMT nanocomposite between two TPU films previously weighted, and then blending with 10 P&F cycles at 180 °C for 20 seconds and 50 bars. A reference PDMS/MMT sample has also been processed with 10 P&F cycles at 180 °C for 20 seconds and 50 bars.

9.3.2 Microstructural observations

Figure 9.7 shows SEM pictures of the microstructures of PDMS + 81 wt.% MMT nanocomposites. The MMT appear aligned in-plane of the films, and the thermal treatment at 180 °C with 10 P&F cycles does not have any significant impact on the microstructure.

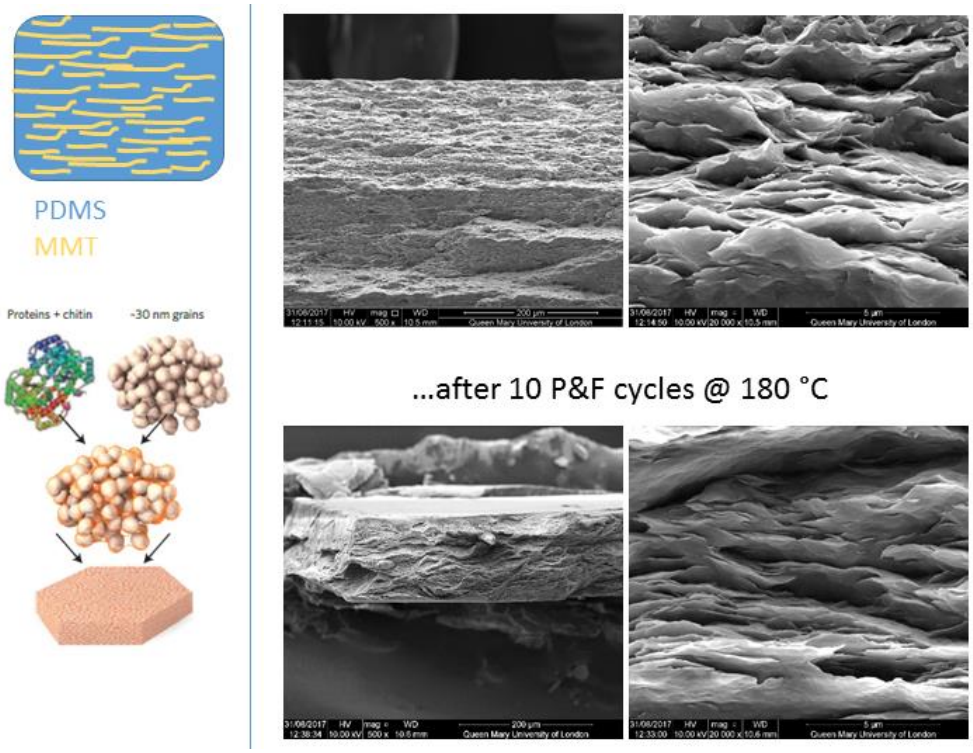

Figure 9.7 SEM observations of PDMS + 80 wt.% MMT nanocomposites miming the first level of hierarchical structure of nacre.

Figure 9.8 presents the microstructure of the same nanocomposites after defined amounts of TPU have been added and mixed with 10 P&F cycles at 180 °C. The MMT appear still aligned, but there is no evidence of the brick and mortar structure (“mortar” TPU separating “bricks” of PDMS/MMT) at the studied magnification. Indeed, the initial

TPU layers were ~ 50 µm thick, so after 10 P&F cycles they should be thin ~ 50 nm, i.e. hardly notable.

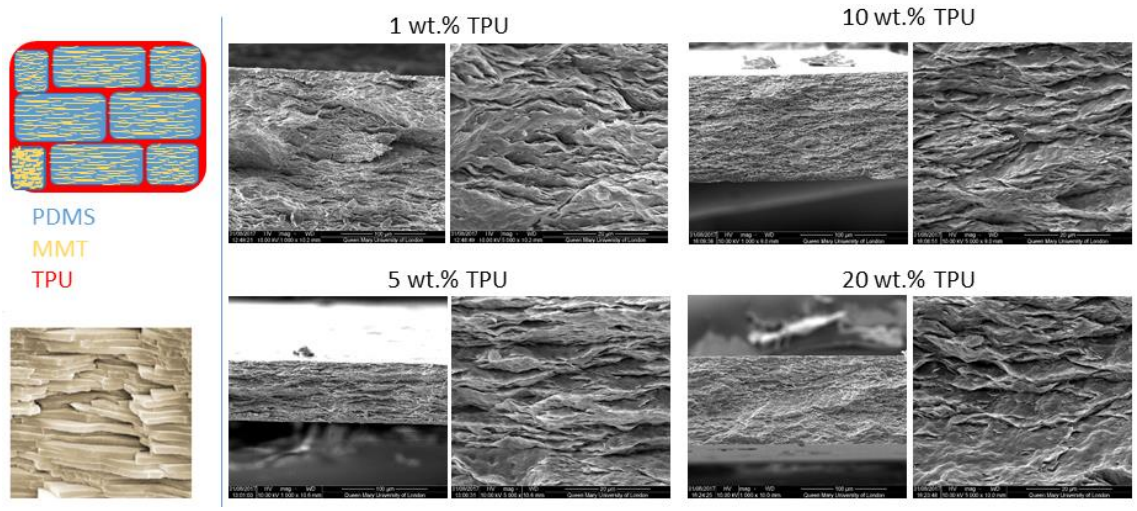

Figure 9.8 SEM observations of the microstructures of PDMS/MMT nanocomposites after adding TPU to simulate the second level of hierarchical structure of nacre.

9.3.3 Mechanical properties

Figure 9.9 reports the mechanical properties of PDMS/MMT nanocomposites, together with those of neat PDMS. The presence of MMT clearly increases the properties of PDMS but decreases the toughness. The cross-linking degree of PDMS increases with time, making the nanocomposite even stiffer and stronger, but less tough.

The nanocomposite processed with 10 P&F cycles at 180 °C (reference for next samples with TPU) are less stiff/strong, and much more brittle.

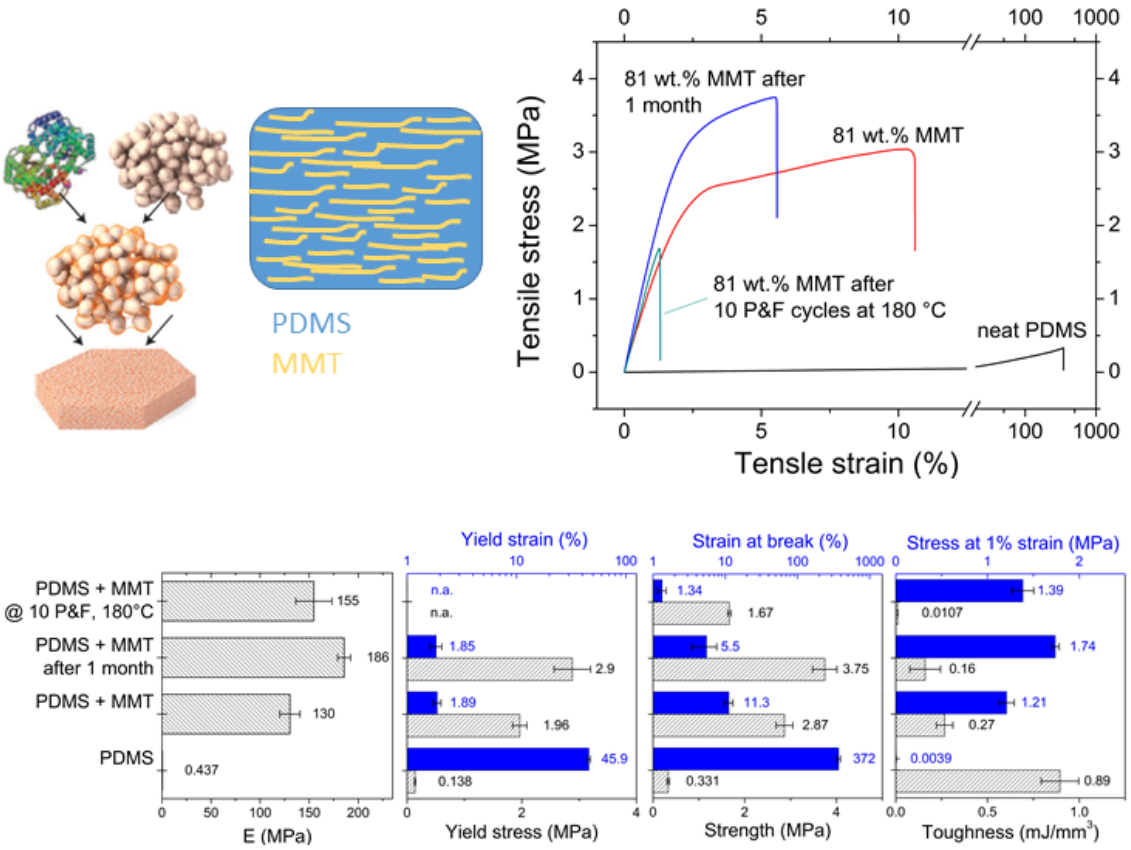

Figure 9.9 Mechanical properties of PDMS + 80 wt.% MMT nanocomposites miming the first level of hierarchical structure of nacre.

Figure 9.10 shows the effect on the mechanical properties of PDMS/MMT nanocomposites when different amounts of TPU have been added. Surprisingly, there is an ideal concentration of TPU (ca. 2.5 wt.%) that gives an enhancement in stiffness, strength, and toughness. As TPU has mechanical properties (Table 9.1) that are much lower than those of PDMS/MMT nanocomposites, the mechanical enhancement observed after an addition of 2.5 wt.% TPU must be due to an optimised microstructure. At this TPU concentration, the “bricks” of PDMS/MMT must have reached an optimal size within the “mortar” TPU network, resulting in a “nacre-effect” that has enhanced the mechanical properties.

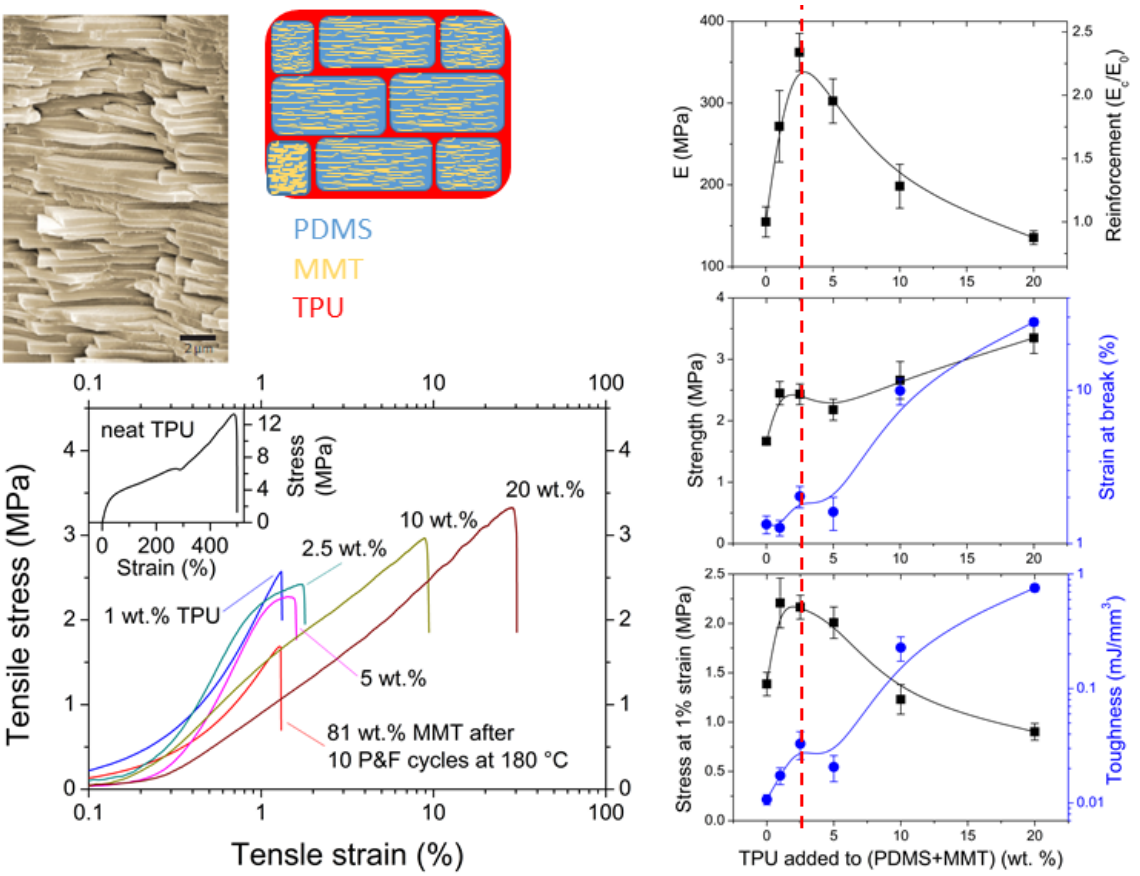

Figure 9.10 Mechanical properties of the microstructures of PDMS/MMT nanocomposites after adding TPU to simulate the second hierarchical level of nacre's structure.

Table 9.1 Mechanical properties of neat TPU.

Modulus (MPa)	Stress at 1% strain (MPa)	Strength (MPa)	Strain at break (%)	Toughness (mJ/mm^3)
18.3 ± 1.0	0.167 ± 0.027	13.1 ± 1.1	492 ± 11	33.4 ± 1.3

9.4 Conclusion

The microstructural control allowed by the P&F technique allows the preparation of nanocomposites with defined dispersion levels of nanofiller and with hierarchical microstructures. In particular, we have shown that high dispersion levels of nanofiller (i.e. $D \rightarrow 1$) are reached, then the energy-management functions of nanocomposites are optimized, whereas the strain-sensing functionalities are increased with a slightly lower nanofiller dispersion, and the Joule-heating effect is increased by dispersion levels close to D_c. Eventually, we have demonstrated that blends of PDMS/TPU can be obtained by P&F without any coupling agents and that these blends present enhanced mechanical properties when TPU organises PDMS-MMT blocks in a way that mimic the effect of the second hierarchical level of nacre's structure.

Chapter 10.

Conclusions

Graphene is an ideal nanofiller because can improve the performance of composites, making them stiffer, stronger and lighter. These aspects seem to be the most appealing for many industries. However, the mechanical potential of graphene-based nanocomposites has not been fully exploited yet, and this might not be easily reached in the near future. Several issues must be resolved first, before a large and effective use of graphene as a mechanical reinforcement can be adopted. The dispersion and distribution of graphene inside polymers is still the main concern, especially at high loadings and when graphene has high aspect-ratios. Nanocomposites containing agglomerates of graphene present bad properties and could even perform worse than neat polymers. A production technique that allows controlling the dispersion of high graphene amounts, together with the spatial orientation of the graphene sheets for achieving anisotropic nanocomposites, is therefore needed. Nevertheless, some of the properties of graphene-based nanocomposites are already exploitable, as they are less affected by graphene dispersion problems than the mechanical properties are.

In this study, we have unravelled the relationship between nanocomposite properties and nanofiller dispersions and distributions, both experimentally and theoretically. Our theoretical framework can be used either to back-calculate an unknown nanofiller dispersion level, or to optimize microstructures to exploit nanocomposite multifunctional properties for desired technological applications.

Thanks to the spray-assisted LbL technique, we have prepared nanocomposites with enhanced electrical conductivities, consequence of a tailored graphene agglomeration. The sa-LbL technique could be automatized to prepare large-area nanocomposite films or coatings with extremely low electrical percolation thresholds.

To increase our control over nanofiller dispersion and alignment, and to prepare nanocomposites with high nanofiller loadings, we have developed the pressing-and-folding technique that seems to be promising at least for relatively low aspect-ratio nanofillers. With the P&F we have experimentally demonstrated the effect of nanofiller dispersion on nanocomposite properties, and that mechanical reinforcements close to maximum theoretical predictions and independent on nanofiller loading could be achieved. We have also shown some nanocomposites with optimised microstructures that present enhanced multifunctionalities such as strain-sensing, self-heating, energy management, and mechanical reinforcement due to a “nacre-effect”.

P&F is a scalable processing method that has the advantage to operate at relatively low temperatures, avoiding re-agglomeration of nanofillers. It may be possible to prepare

nanocomposites also with high nanofiller loadings and aspect-ratios if this technique was scaled up and automatized.

Chapter 11.

Appendices

11.1 X-ray diffraction (XRD) observations

Figure 11.1 shows the XRD patterns of expanded graphite (EG) powder, neat linear low density polyethylene (LLDPE) at different pressing and folding (P&F) cycles, nanocomposites of LLDPE + 0.21 vol.% of graphite nanoplatelets (GNP) at different P&F cycles, nanocomposites of LLDPE + 4.8 vol.% of GNP at different P&F cycles, and a nanocomposite of LLDPE + 35 vol.% of GNP at 200 P&F cycles. All the details of these XRD patterns are presented in Table 11.1.

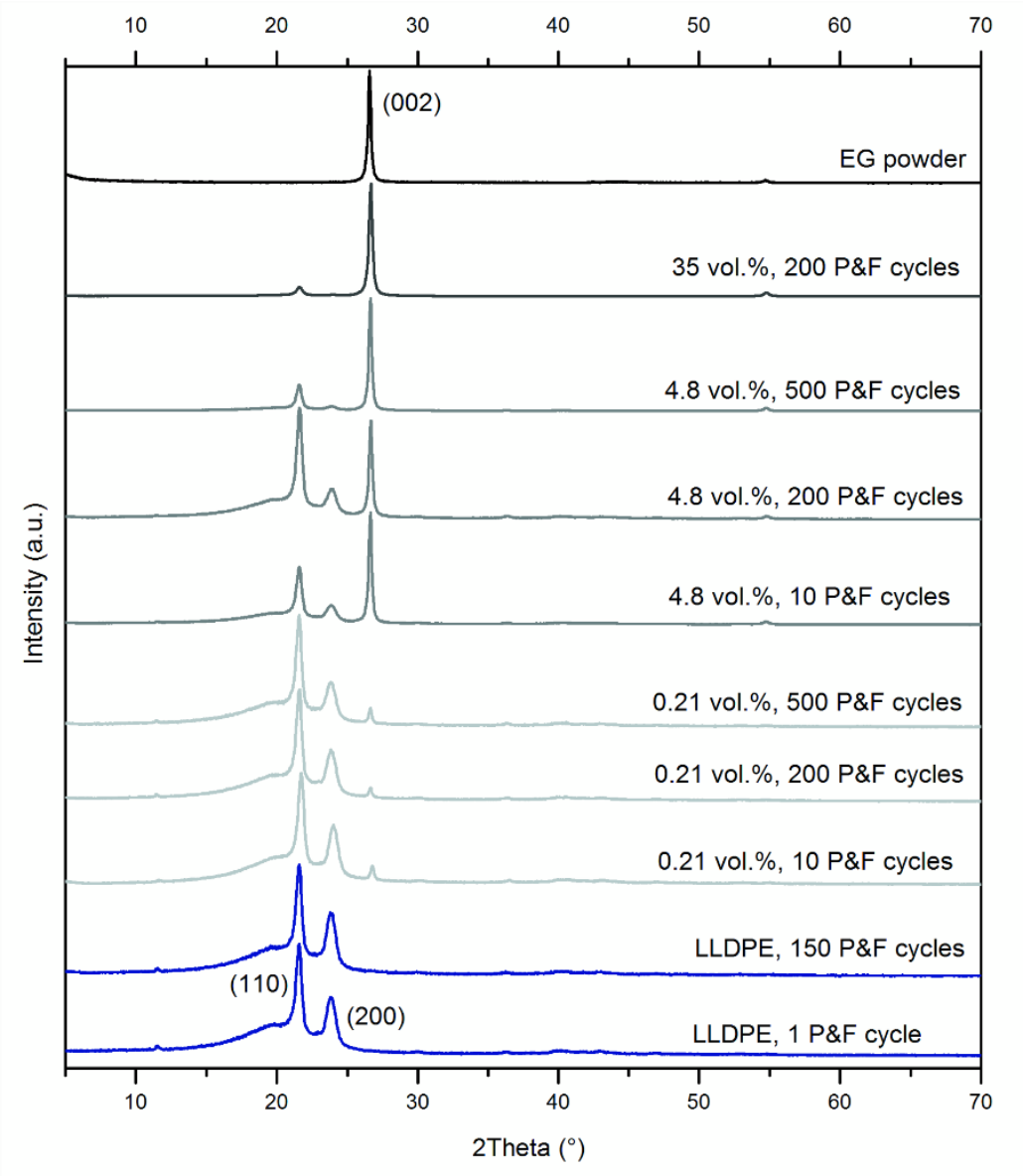

Figure 11.1 XRD patterns of EG powder, neat LLDPE, and LLDPE nanocomposites containing specified GNP loadings.

Table 11.1 Values found or calculated from all the XRD patterns of Figure 11.1.

Sample	P&F cycles	GNP (002) peak (° 2θ)	$\overline{t}$ of GNP (nm)	LLDPE crystallite size from (110) peak (nm)	LLDPE crystallite size from (200) peak (nm)	LLDPE crystallinity, X_c (%)
EG powder		26.57	27			
LLDPE	1			16.6	11.1	32.4 ± 0.6
	150			16.9	11.2	33.4 ± 0.4
LLDPE + 0.21 vol.% GNP	10	26.77	26	16.5	11.1	32.5 ± 0.4
	200	26.63	33	17.3	11.1	31.5 ± 0.4
	500	26.63	31	17.3	11.0	33.1 ± 0.5
LLDPE + 4.8 vol.% GNP	10	26.62	28	17.4	11.6	34.0 ± 0.6
	200	26.66	26	17.5	11.3	36.6 ± 0.6
	500	26.63	28	18.1	12.5	36.7 ± 1.3
LLDPE + 35 vol.% GNP	200	26.66	27	15.0	11.0	40 ± 4

11.2 Nanocomposites of LLDPE + 0.21 vol.% GNP at different P&F cycles: nanofiller distribution and microstructures

Figure 11.2a shows a macroscopic visualisation of the effect of the P&F technique on the distribution of GNP throughout the specimen of a series of samples containing 0.21 vol.% of GNP. The colour of these samples became darker with P&F cycles because of better nanofiller dispersion and distribution. Figure 11.2b shows the microstructures of these nanocomposites at different P&F cycles. At low P&F cycles, the microstructures show large EG agglomerates with a thickness nearly the same as the film sample, which decreased in thickness and width with P&F cycles. Eventually, at 500 P&F the particles were well distributed, dispersed and oriented parallel to the plane of the film samples.

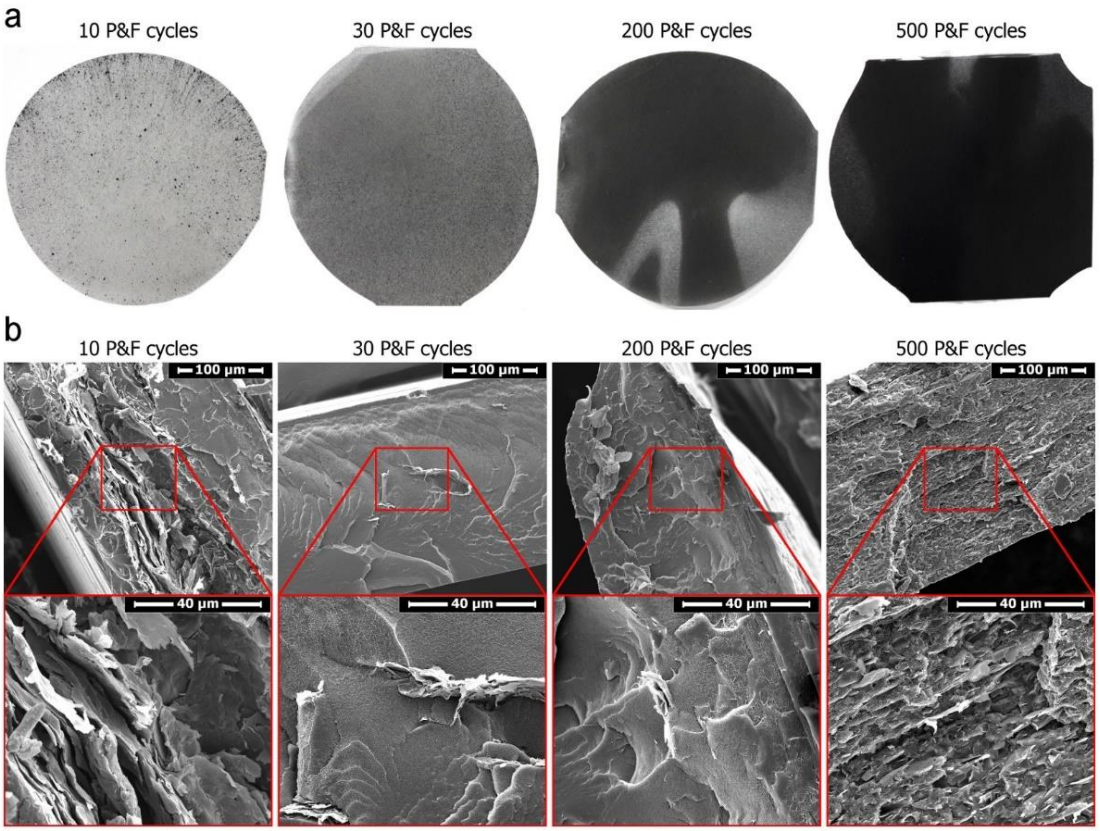

*Figure 11.2 Pictures (**a**) and SEM images (**b**) of the cross-sections of LLDPE + 0.21 vol.% GNP samples at different P&F cycles.*

11.3 Influence of P&F cycles on the properties of neat LLDPE

The P&F technique consists of pressing a thermoplastic polymer with a nanofiller at a temperature slightly above the polymer's melting point, thus the polymer should recover its initial properties after cooling down to ambient temperature. It is worth noting that the P&F was performed in air, and to assess any effect of thermal degradation on the alteration of polymer properties, samples of pure LLDPE were prepared at 1, 50, 100, and 150 P&F cycles. Tensile tests revealed that the properties (Young's modulus, yield stress, and ultimate tensile stress) of pure LLDPE at different numbers of P&F cycles were relatively unaffected by the P&F technique up to 150 P&F cycles (Figure 11.3). Therefore, the sample prepared at the first P&F cycle was used as reference sample for comparison with nanocomposite properties.

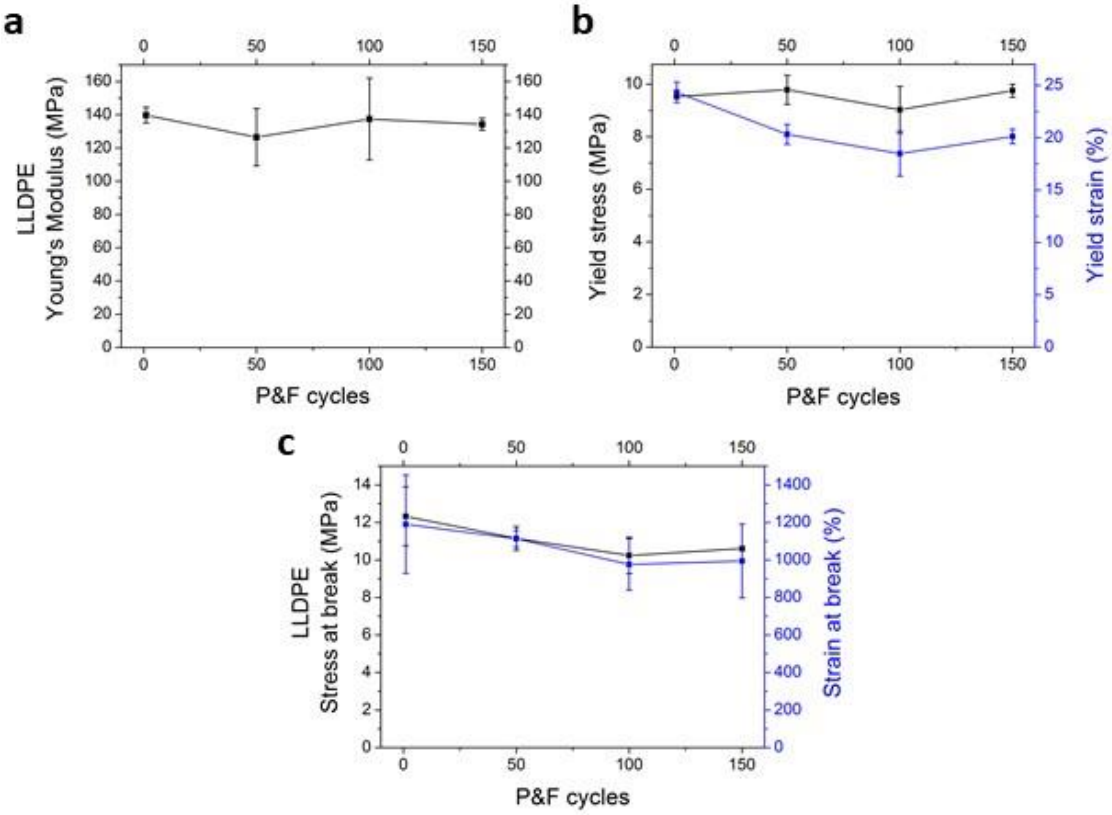

Figure 11.3 Young's modulus (**a**), yield (**b**), and break point (**c**) of neat LLDPE samples prepared at different P&F cycles.

The XRD pattern of pure LLDPE (Figure 11.1) shows two diffraction peaks around 21.6° 2θ and 23.8° 2θ due to the (110) and (200) reflections superimposed to an amorphous halo [198,199]. The crystallinity was ~33% for both samples prepared at one and 150 P&F cycles (Table 11.1). The crystallites size calculated from the (110) and (200) peaks were of 17 nm and 11 nm, for both samples. These findings suggest that the P&F

technique up to 150 P&F cycles has little effect on the properties of neat LLDPE. Moreover, Table 11.1 shows that a sample of LLDPE containing a small amount of GNP (0.21 vol.%) did not change its crystallinity up to 500 P&F cycles, confirming that the properties of LLDPE are not significantly influenced by the P&F technique.

11.4 Influence of P&F cycles on the properties of LLDPE and GNP inside nanocomposites

It was shown above how the P&F technique itself does not significantly influence the properties of neat LLDPE, however, the presence of GNP together with the effect of the pressing and folding cycles could change its crystallinity. This is important because LLDPE of higher crystallinity has an increased Young's modulus and yield stress, but lower tensile strength and elongation at break [145].

Nanocomposites containing 4.8 vol.% of GNP showed that the LLDPE crystallite sizes and crystallinity increased slightly with the number of P&F cycles (Table 11.1). However, referring to the findings of Kundu *et al.* [145], a relative increase of ~8% in crystallinity found for the sample at 500 P&F is too low to significantly alter the mechanical properties of LLDPE. Therefore, an eventual improvement of the nanocomposite's mechanical properties should be attributed mainly to an improved reinforcing efficiency of the nanofiller as a result of an improvement in nanofiller distribution and dispersion rather than an increase of polymer crystallinity.

Regarding the GNP characteristics, the graphite diffraction peak did not change its position with the number of P&F cycles, meaning that the crystalline interlayer spacing, and the density of GNP was unaffected by the P&F cycles. Likewise, since the (002) peak did not shift to lower 2θ values as it happens for graphite oxide [169,173,176,200,201], no oxidation of GNP is expected to take place during the P&F process. Furthermore, the thickness of GNP remained the same with P&F cycles, meaning that there was no exfoliation of GNP during the process, thus any variation in the properties of the nanocomposites with P&F cycles must be caused only by improved distribution and dispersion of the nanofiller, rather than an increase in aspect-ratio.

All the above observations are confirmed by the samples of LLDPE containing 0.21 vol.% of GNP. No relevant changes in LLDPE crystallite sizes and crystallinity with the number of P&F cycles was present (Table 11.1), that is, the matrix properties are not influenced

by the P&F technique. The graphite diffraction peak did not modify its position with the number of P&F cycles, meaning that the density of GNP was unaffected by the P&F cycles, and that GNP did not oxidize during the hot-pressing steps. Furthermore, the thickness of GNP remained the same with P&F cycles, viz. there was no exfoliation of GNP during the process.

11.5 Influence of GNP loading on the properties of GNP and LLDPE inside nanocomposites prepared at 200 P&F cycles

As reported in Table 11.1, the LLDPE crystallite sizes remained almost the same for samples prepared at 200 P&F cycles containing three different amounts of GNP (0.21, 4.8, and 35 vol.%): there was only a small decrease from 17 nm to 15 nm for the crystallite size related to the (110) peak of the sample containing 35 vol.% of GNP. The LLDPE crystallinity increased with the amount of GNP. These findings are in contrast with what is reported in literature: the addition of nanofiller slightly increased the LLDPE crystallite sizes [144], and decreased the degree of crystallinity [144,198], because of a random interface between nanofiller and matrix, which “inhibited the ordered crystalline structure of the polymer chains” [144]. Other studies indicated that the LLDPE crystallinity calculated from differential scanning calorimetry (DSC) measurements did not change with the amount of GNP [175], or with the amount of graphene [173]. Therefore, the P&F technique might help the LLDPE polymer chains to arrange themselves in a crystalline structure among graphite nanoparticles. However, referring to the findings of Kundu *et al.* [145], a relative increase of ~22% in crystallinity compared with pure LLDPE was found for the sample containing 35 vol.% of GNP is too low to significantly alter the mechanical properties of LLDPE.

Eventually, the position of the graphite (002) peak and the thickness of GNP remained the same as a function of the amount of GNP in the samples, meaning that there was no change in the intrinsic properties of GNP during the processing of these nanocomposites.

11.6 Mechanical reinforcement of MMT nanocomposite found in literature

Table 11.2 Mechanical reinforcement found in literature for MMT nanocomposites prepared by melt processing, solution processing, or layer-by-layer.

Processing technique	Matrix	MMT content (wt.%)	Mechanical reinforcement (E_c/E_m)	Reference
Melt blending	PVC	0.5 1 3 5	1.01 1.01 1.06 1.04	[202]
Solution processing	PLA	2 4 6 8	1.22 1.36 1.33 1.31	[203]
Melt blending	PA6	1.5 2.9 4.6 6.6	1.26 1.53 1.69 1.85	[204]
Melt blending	PA6	2 4 6.5	1.30 1.50 1.73	[204]
Solution processing	PET	1 2 3	1.30 1.49 1.85	[205]
Solution processing	PVA	2 4 6 10	1.80 3.10 2.75 3.40	[206]
Solution processing	PS	3.6 5.6 7.6	1.15 1.31 1.59	[207]
Melt blending	PBS	1.5 2.5 4 5.5	1.19 1.42 1.80 3.46	[208]
Melt blending	LLDPE	0.8	1.39	[209]

		2.5 4.6 6.9	1.80 2.52 2.99	
Melt blending	PLA	1.2 3 4	1.46 1.49 1.65	[210]
Solution processing	PS	5 10 20 30	1.07 1.57 2.18 1.51	[211]
Solution processing	Chitosan	2.5 5 10	1.09 1.16 1.26	[212]
Solution processing	Polyester	3 5 7 10	1.12 1.22 1.18 1.32	[213]
Melt blending	PLA	2.5 5 7.5	1.17 1.32 1.50	[214]
Solution processing	PLA	2 4 6 8	1.22 1.37 1.32 1.31	[215]
Solution processing	PLA	2 4 6 8	1.21 1.29 1.49 3.04	[215]
Melt blending	LDPE	3 6	1.02 1.03	[216]
Melt blending	PA6	2.7 4.9	1.45 1.66	[217]
Solution processing	Cellulose	1 5 10 25 50	1.01 1.56 1.55 1.69 1.67	[218]

Solution processing	PEO	76 85	6.25 15.9	[219]
Solution processing	Cellulose	60 83	3.70 5.80	[219]
LbL	PVA	70	7.64	[220]
LbL	PVA-GA	70	53.0	[220]
LbL	PDDA	80	68.7	[221]
LbL	Chitosan	80	3.21	[222]
LbL	PVA	70 70 70	7.64 24.1 34.1	[223]
LbL	PAA	70	6.14	[224]
LbL	PVA	55	5.89	[225]
LbL	PVA	96 97 98 99	2.22 4.88 24.8 18.8	[226]
LbL	PVP	95	3.80	[227]

Chapter 12.

References

1. Alcoutlabi, M.; McKenna, G.B. Effects of confinement on material behaviour at the nanometre size scale. *J. Phys.: Condens. Matter* **2005**, *17*, R461, doi:10.1088/0953-8984/17/15/R01.
2. Pugno, N.M. A general shape/size-effect law for nanoindentation. *Acta Materialia* **2007**, *55*, 1947–1953, doi:10.1016/j.actamat.2006.10.053.
3. Piggott, M.R. 8 - Reinforcement with Platelets. In *Load-Bearing Fibre Composites*; International Series on the Strength and Fracture of Materials and Structures; Pergamon, 1980; pp. 141–154 ISBN 978-0-08-024231-6.
4. Griffith, A.A. The Phenomena of Rupture and Flow in Solids. *Philosophical Transactions of the Royal Society of London A: Mathematical, Physical and Engineering Sciences* **1921**, *221*, 163–198, doi:10.1098/rsta.1921.0006.
5. Weibull, W.; Sweden, S. A statistical distribution function of wide applicability. *Journal of Applied Mechanics* **1951**, 293–297.
6. Pugno, N.M.; Ruoff, R.S. Quantized fracture mechanics. *Philos. Mag.* **2004**, *84*, 2829–2845, doi:10.1080/14786430412331280382.
7. Geim, A.K.; Novoselov, K.S. The rise of graphene. *Nat Mater* **2007**, *6*, 183–191, doi:10.1038/nmat1849.
8. Lee, C.; Wei, X.; Kysar, J.W.; Hone, J. Measurement of the Elastic Properties and Intrinsic Strength of Monolayer Graphene. *Science* **2008**, *321*, 385–388, doi:10.1126/science.1157996.
9. Schuller, J.A.; Barnard, E.S.; Cai, W.; Jun, Y.C.; White, J.S.; Brongersma, M.L. Plasmonics for extreme light concentration and manipulation. *Nat Mater* **2010**, *9*, 193–204, doi:10.1038/nmat2630.
10. Evanoff, D.D.; Chumanov, G. Synthesis and optical properties of silver nanoparticles and arrays. *ChemPhysChem* **2005**, *6*, 1221–1231, doi:10.1002/cphc.200500113.
11. Daniel, M.-C.; Astruc, D. Gold Nanoparticles: Assembly, Supramolecular Chemistry, Quantum-Size-Related Properties, and Applications toward Biology, Catalysis, and Nanotechnology. *Chem. Rev.* **2004**, *104*, 293–346, doi:10.1021/cr030698+.
12. Eichhorn, S.J.; Dufresne, A.; Aranguren, M.; Marcovich, N.E.; Capadona, J.R.; Rowan, S.J.; Weder, C.; Thielemans, W.; Roman, M.; Renneckar, S.; et al. Review: current international research into cellulose nanofibres and nanocomposites. *J Mater Sci* **2010**, *45*, 1, doi:10.1007/s10853-009-3874-0.
13. Huang, X.; Yin, Z.; Wu, S.; Qi, X.; He, Q.; Zhang, Q.; Yan, Q.; Boey, F.; Zhang, H. Graphene-Based Materials: Synthesis, Characterization, Properties, and Applications. *Small* **2011**, *7*, 1876–1902, doi:10.1002/smll.201002009.
14. Bunch, J.S.; Verbridge, S.S.; Alden, J.S.; van der Zande, A.M.; Parpia, J.M.; Craighead, H.G.; McEuen, P.L. Impermeable Atomic Membranes from Graphene Sheets. *Nano Lett.* **2008**, *8*, 2458–2462, doi:10.1021/nl801457b.
15. Novoselov, K.S.; Geim, A.K.; Morozov, S.V.; Jiang, D.; Zhang, Y.; Dubonos, S.V.; Grigorieva, I.V.; Firsov, A.A. Electric Field Effect in Atomically Thin Carbon Films. *Science* **2004**, *306*, 666–669, doi:10.1126/science.1102896.
16. Balandin, A.A.; Ghosh, S.; Bao, W.; Calizo, I.; Teweldebrhan, D.; Miao, F.; Lau, C.N. Superior Thermal Conductivity of Single-Layer Graphene. *Nano Lett.* **2008**, *8*, 902–907, doi:10.1021/nl0731872.
17. Keledi, G.; Hári, J.; Pukánszky, B. Polymer nanocomposites: structure, interaction, and functionality. *Nanoscale* **2012**, *4*, 1919, doi:10.1039/c2nr11442a.
18. Peigney, A.; Laurent, C.; Flahaut, E.; Bacsa, R.R.; Rousset, A. Specific surface area of carbon nanotubes and bundles of carbon nanotubes. *Carbon* **2001**, *39*, 507–514, doi:10.1016/S0008-6223(00)00155-X.

19. Young, R.J.; Kinloch, I.A.; Gong, L.; Novoselov, K.S. The mechanics of graphene nanocomposites: A review. *Composites Science and Technology* **2012**, *72*, 1459–1476, doi:10.1016/j.compscitech.2012.05.005.
20. Luo, S.; Liu, T. Graphite Nanoplatelet Enabled Embeddable Fiber Sensor for in Situ Curing Monitoring and Structural Health Monitoring of Polymeric Composites. *ACS Appl. Mater. Interfaces* **2014**, *6*, 9314–9320, doi:10.1021/am5017039.
21. Li, X.; Yang, T.; Yang, Y.; Zhu, J.; Li, L.; Alam, F.E.; Li, X.; Wang, K.; Cheng, H.; Lin, C.-T.; et al. Large-Area Ultrathin Graphene Films by Single-Step Marangoni Self-Assembly for Highly Sensitive Strain Sensing Application. *Adv. Funct. Mater.* **2016**, *26*, 1322–1329, doi:10.1002/adfm.201504717.
22. Singh, V.; Joung, D.; Zhai, L.; Das, S.; Khondaker, S.I.; Seal, S. Graphene based materials: Past, present and future. *Progress in Materials Science* **2011**, *56*, 1178–1271, doi:10.1016/j.pmatsci.2011.03.003.
23. Zhu, Y.; Murali, S.; Cai, W.; Li, X.; Suk, J.W.; Potts, J.R.; Ruoff, R.S. Graphene and Graphene Oxide: Synthesis, Properties, and Applications. *Adv. Mater.* **2010**, *22*, 3906–3924, doi:10.1002/adma.201001068.
24. Arora, A.; Padua, G. w. Review: Nanocomposites in Food Packaging. *Journal of Food Science* **2010**, *75*, R43–R49, doi:10.1111/j.1750-3841.2009.01456.x.
25. Jones, W.E.; Chiguma, J.; Johnson, E.; Pachamuthu, A.; Santos, D. Electrically and Thermally Conducting Nanocomposites for Electronic Applications. *Materials* **2010**, *3*, 1478–1496, doi:10.3390/ma3021478.
26. Samorì, P.; Kinloch, I.A.; Feng, X.; Palermo, V. Graphene-based nanocomposites for structural and functional applications: using 2-dimensional materials in a 3-dimensional world. *2D Materials* **2015**, *2*, 030205, doi:10.1088/2053-1583/2/3/030205.
27. Naskar, A.K.; Keum, J.K.; Boeman, R.G. Polymer matrix nanocomposites for automotive structural components. *Nature Nanotechnology* **2016**, *11*, 1026–1030, doi:10.1038/nnano.2016.262.
28. Liu, Y.; Kumar, S. Recent Progress in Fabrication, Structure, and Properties of Carbon Fibers. *Polymer Reviews* **2012**, *52*, 234–258, doi:10.1080/15583724.2012.705410.
29. Newcomb, B.A. Processing, structure, and properties of carbon fibers. *Composites Part A: Applied Science and Manufacturing* **2016**, *91*, *Part 1*, 262–282, doi:10.1016/j.compositesa.2016.10.018.
30. Gong, L.; Kinloch, I.A.; Young, R.J.; Riaz, I.; Jalil, R.; Novoselov, K.S. Interfacial Stress Transfer in a Graphene Monolayer Nanocomposite. *Adv. Mater.* **2010**, *22*, 2694–2697, doi:10.1002/adma.200904264.
31. Vlassiouk, I.; Polizos, G.; Cooper, R.; Ivanov, I.; Keum, J.K.; Paulauskas, F.; Datskos, P.; Smirnov, S. Strong and Electrically Conductive Graphene-Based Composite Fibers and Laminates. *ACS Applied Materials & Interfaces* **2015**, *7*, 10702–10709, doi:10.1021/acsami.5b01367.
32. Liu, P.; Jin, Z.; Katsukis, G.; Drahushuk, L.W.; Shimizu, S.; Shih, C.-J.; Wetzel, E.D.; Taggart-Scarff, J.K.; Qing, B.; Vliet, K.J.V.; et al. Layered and scrolled nanocomposites with aligned semi-infinite graphene inclusions at the platelet limit. *Science* **2016**, *353*, 364–367, doi:10.1126/science.aaf4362.
33. Cox, H.L. The elasticity and strength of paper and other fibrous materials. *Br. J. Appl. Phys.* **1952**, *3*, 72, doi:10.1088/0508-3443/3/3/302.
34. May, P.; Khan, U.; O'Neill, A.; Coleman, J.N. Approaching the theoretical limit for reinforcing polymers with graphene. *J. Mater. Chem.* **2011**, *22*, 1278–1282, doi:10.1039/C1JM15467B.
35. Kalaitzidou, K.; Fukushima, H.; Drzal, L.T. Mechanical properties and morphological characterization of exfoliated graphite–polypropylene nanocomposites. *Composites Part A: Applied Science and Manufacturing* **2007**, *38*, 1675–1682, doi:10.1016/j.compositesa.2007.02.003.

36. Morimune, S.; Nishino, T.; Goto, T. Poly(vinyl alcohol)/graphene oxide nanocomposites prepared by a simple eco-process. *Polym J* **2012**, *44*, 1056–1063, doi:10.1038/pj.2012.58.
37. Bagri, A.; Mattevi, C.; Acik, M.; Chabal, Y.J.; Chhowalla, M.; Shenoy, V.B. Structural evolution during the reduction of chemically derived graphene oxide. *Nat Chem* **2010**, *2*, 581–587, doi:10.1038/nchem.686.
38. Kouroupis-Agalou, K.; Liscio, A.; Treossi, E.; Ortolani, L.; Morandi, V.; Pugno, N.M.; Palermo, V. Fragmentation and exfoliation of 2-dimensional materials: a statistical approach. *Nanoscale* **2014**, *6*, 5926, doi:10.1039/c3nr06919b.
39. Gong, L.; Young, R.J.; Kinloch, I.A.; Riaz, I.; Jalil, R.; Novoselov, K.S. Optimizing the Reinforcement of Polymer-Based Nanocomposites by Graphene. *ACS Nano* **2012**, *6*, 2086–2095, doi:10.1021/nn203917d.
40. Zalamea, L.; Kim, H.; Pipes, R.B. Stress transfer in multi-walled carbon nanotubes. *Composites Science and Technology* **2007**, *67*, 3425–3433, doi:10.1016/j.compscitech.2007.03.011.
41. Weir, M.P.; Johnson, D.W.; Boothroyd, S.C.; Savage, R.C.; Thompson, R.L.; Parnell, S.R.; Parnell, A.J.; King, S.M.; Rogers, S.E.; Coleman, K.S.; et al. Extrinsic Wrinkling and Single Exfoliated Sheets of Graphene Oxide in Polymer Composites. *Chemistry of Materials* **2016**, *28*, 1698–1704, doi:10.1021/acs.chemmater.5b04502.
42. Potts, J.R.; Dreyer, D.R.; Bielawski, C.W.; Ruoff, R.S. Graphene-based polymer nanocomposites. *Polymer* **2011**, *52*, 5–25, doi:10.1016/j.polymer.2010.11.042.
43. Compton, O.C.; Kim, S.; Pierre, C.; Torkelson, J.M.; Nguyen, S.T. Crumpled Graphene Nanosheets as Highly Effective Barrier Property Enhancers. *Adv. Mater.* **2010**, *22*, 4759–4763, doi:10.1002/adma.201000960.
44. Li, Z.; Young, R.J.; Wilson, N.R.; Kinloch, I.A.; Vallés, C.; Li, Z. Effect of the orientation of graphene-based nanoplatelets upon the Young's modulus of nanocomposites. *Composites Science and Technology* **2016**, *123*, 125–133, doi:10.1016/j.compscitech.2015.12.005.
45. Coleman, J.N.; Khan, U.; Blau, W.J.; Gun'ko, Y.K. Small but strong: A review of the mechanical properties of carbon nanotube–polymer composites. *Carbon* **2006**, *44*, 1624–1652, doi:10.1016/j.carbon.2006.02.038.
46. Domun, N.; Hadavinia, H.; Zhang, T.; Sainsbury, T.; Liaghat, G.H.; Vahid, S. Improving the fracture toughness and the strength of epoxy using nanomaterials – a review of the current status. *Nanoscale* **2015**, *7*, 10294–10329, doi:10.1039/C5NR01354B.
47. Turcsányi, B.; Pukánszky, B.; Tüdõs, F. Composition dependence of tensile yield stress in filled polymers. *J Mater Sci Lett* **1988**, *7*, 160–162, doi:10.1007/BF01730605.
48. Sun, J.; Bhushan, B. Hierarchical structure and mechanical properties of nacre: a review. *RSC Adv.* **2012**, *2*, 7617–7632, doi:10.1039/C2RA20218B.
49. Wegst, U.G.K.; Bai, H.; Saiz, E.; Tomsia, A.P.; Ritchie, R.O. Bioinspired structural materials. *Nat Mater* **2015**, *14*, 23–36, doi:10.1038/nmat4089.
50. Gong, S.; Ni, H.; Jiang, L.; Cheng, Q. Learning from nature: constructing high performance graphene-based nanocomposites. *Materials Today* **2016**, doi:10.1016/j.mattod.2016.11.002.
51. Li, Y.-Q.; Yu, T.; Yang, T.-Y.; Zheng, L.-X.; Liao, K. Bio-Inspired Nacre-like Composite Films Based on Graphene with Superior Mechanical, Electrical, and Biocompatible Properties. *Adv. Mater.* **2012**, *24*, 3426–3431, doi:10.1002/adma.201200452.
52. Hu, X.; Xu, Z.; Gao, C. Multifunctional, supramolecular, continuous artificial nacre fibres. *Scientific Reports* **2012**, *2*, doi:10.1038/srep00767.
53. Cheng, Q.; Wu, M.; Li, M.; Jiang, L.; Tang, Z. Ultratough Artificial Nacre Based on Conjugated Cross-linked Graphene Oxide. *Angewandte Chemie International Edition* **2013**, *52*, 3750–3755, doi:10.1002/anie.201210166.

54. Cui, W.; Li, M.; Liu, J.; Wang, B.; Zhang, C.; Jiang, L.; Cheng, Q. A Strong Integrated Strength and Toughness Artificial Nacre Based on Dopamine Cross-Linked Graphene Oxide. *ACS Nano* **2014**, *8*, 9511–9517, doi:10.1021/nn503755c.
55. Wan, S.; Hu, H.; Peng, J.; Li, Y.; Fan, Y.; Jiang, L.; Cheng, Q. Nacre-inspired integrated strong and tough reduced graphene oxide–poly(acrylic acid) nanocomposites. *Nanoscale* **2016**, *8*, 5649–5656, doi:10.1039/C6NR00562D.
56. Atif, R.; Shyha, I.; Inam, F. Mechanical, Thermal, and Electrical Properties of Graphene-Epoxy Nanocomposites—A Review. *Polymers* **2016**, *8*, 281, doi:10.3390/polym8080281.
57. Cui, Y.; Kundalwal, S.I.; Kumar, S. Gas barrier performance of graphene/polymer nanocomposites. *Carbon* **2016**, *98*, 313–333, doi:10.1016/j.carbon.2015.11.018.
58. Kim, H.; Miura, Y.; Macosko, C.W. Graphene/Polyurethane Nanocomposites for Improved Gas Barrier and Electrical Conductivity. *Chem. Mater.* **2010**, *22*, 3441–3450, doi:10.1021/cm100477v.
59. Paul, D.R.; Robeson, L.M. Polymer nanotechnology: Nanocomposites. *Polymer* **2008**, *49*, 3187–3204, doi:10.1016/j.polymer.2008.04.017.
60. Nielsen, L.E. Models for the Permeability of Filled Polymer Systems. *Journal of Macromolecular Science: Part A - Chemistry* **1967**, *1*, 929–942, doi:10.1080/10601326708053745.
61. Lape, N.K.; Nuxoll, E.E.; Cussler, E.L. Polydisperse flakes in barrier films. *Journal of Membrane Science* **2004**, *236*, 29–37, doi:10.1016/j.memsci.2003.12.026.
62. Carbon Clinchers—Are They Ready for Prime Time? | RKP Available online: http://redkiteprayer.com/2012/07/carbon-clinchers-are-they-ready-for-prime-time/ (accessed on May 24, 2017).
63. Yu, A.; Ramesh, P.; Itkis, M.E.; Bekyarova, E.; Haddon, R.C. Graphite Nanoplatelet−Epoxy Composite Thermal Interface Materials. *J. Phys. Chem. C* **2007**, *111*, 7565–7569, doi:10.1021/jp071761s.
64. Kuilla, T.; Bhadra, S.; Yao, D.; Kim, N.H.; Bose, S.; Lee, J.H. Recent advances in graphene based polymer composites. *Progress in Polymer Science* **2010**, *35*, 1350–1375, doi:10.1016/j.progpolymsci.2010.07.005.
65. Ganguli, S.; Roy, A.K.; Anderson, D.P. Improved thermal conductivity for chemically functionalized exfoliated graphite/epoxy composites. *Carbon* **2008**, *46*, 806–817, doi:10.1016/j.carbon.2008.02.008.
66. Wei, J.; Vo, T.; Inam, F. Epoxy/graphene nanocomposites – processing and properties: a review. *RSC Advances* **2015**, *5*, 73510–73524, doi:10.1039/C5RA13897C.
67. Mazzocchetti, L.; Benelli, T.; D'Angelo, E.; Ligi, S.; Minak, G.; Poodts, E.; Tarterini, F.; Palermo, V.; Giorgini, L. Managing heat phenomena in epoxy composites production via graphenic derivatives: synthesis, properties and industrial production simulation of graphene and graphene oxide containing composites. *2D Materials* **2016**, *4*, 015020, doi:10.1088/2053-1583/4/1/015020.
68. Ram, R.; Rahaman, M.; Aldalbahi, A.; Khastgir, D. Determination of percolation threshold and electrical conductivity of polyvinylidene fluoride (PVDF)/short carbon fiber (SCF) composites: effect of SCF aspect ratio. *Polym. Int.* **2017**, *66*, 573–582, doi:10.1002/pi.5294.
69. Verdejo, R.; Bernal, M.M.; Romasanta, L.J.; Lopez-Manchado, M.A. Graphene filled polymer nanocomposites. *J. Mater. Chem.* **2011**, *21*, 3301–3310, doi:10.1039/C0JM02708A.
70. Li, J.; Kim, J.-K. Percolation threshold of conducting polymer composites containing 3D randomly distributed graphite nanoplatelets. *Composites Science and Technology* **2007**, *67*, 2114–2120, doi:10.1016/j.compscitech.2006.11.010.
71. Tkalya, E.; Ghislandi, M.; Otten, R.; Lotya, M.; Alekseev, A.; van der Schoot, P.; Coleman, J.; de With, G.; Koning, C. Experimental and Theoretical Study of the Influence of the State of Dispersion of Graphene on the Percolation Threshold of

Conductive Graphene/Polystyrene Nanocomposites. *ACS Applied Materials & Interfaces* **2014**, *6*, 15113–15121, doi:10.1021/am503238z.
72. Wang, Y.; Shan, J.W.; Weng, G.J. Percolation threshold and electrical conductivity of graphene-based nanocomposites with filler agglomeration and interfacial tunneling. *Journal of Applied Physics* **2015**, *118*, 065101, doi:10.1063/1.4928293.
73. Boland, C.S.; Khan, U.; Backes, C.; O'Neill, A.; McCauley, J.; Duane, S.; Shanker, R.; Liu, Y.; Jurewicz, I.; Dalton, A.B.; et al. Sensitive, High-Strain, High-Rate Bodily Motion Sensors Based on Graphene–Rubber Composites. *ACS Nano* **2014**, *8*, 8819–8830, doi:10.1021/nn503454h.
74. Boland, C.S.; Khan, U.; Ryan, G.; Barwich, S.; Charifou, R.; Harvey, A.; Backes, C.; Li, Z.; Ferreira, M.S.; Möbius, M.E.; et al. Sensitive electromechanical sensors using viscoelastic graphene-polymer nanocomposites. *Science* **2016**, *354*, 1257–1260.
75. Huang, Y.; Sutter, E.; Shi, N.N.; Zheng, J.; Yang, T.; Englund, D.; Gao, H.-J.; Sutter, P. Reliable Exfoliation of Large-Area High-Quality Flakes of Graphene and Other Two-Dimensional Materials. *ACS Nano* **2015**, *9*, 10612–10620, doi:10.1021/acsnano.5b04258.
76. Chen, J.; Duan, M.; Chen, G. Continuous mechanical exfoliation of graphene sheets via three-roll mill. *J. Mater. Chem.* **2012**, *22*, 19625–19628, doi:10.1039/C2JM33740A.
77. Fim, F. de C.; Guterres, J.M.; Basso, N.R.S.; Galland, G.B. Polyethylene/graphite nanocomposites obtained by in situ polymerization. *J. Polym. Sci. A Polym. Chem.* **2010**, *48*, 692–698, doi:10.1002/pola.23822.
78. Hernandez, Y.; Nicolosi, V.; Lotya, M.; Blighe, F.M.; Sun, Z.; De, S.; McGovern, I.T.; Holland, B.; Byrne, M.; Gun'Ko, Y.K.; et al. High-yield production of graphene by liquid-phase exfoliation of graphite. *Nature Nanotechnology* **2008**, *3*, 563–568, doi:10.1038/nnano.2008.215.
79. Paton, K.R.; Varrla, E.; Backes, C.; Smith, R.J.; Khan, U.; O'Neill, A.; Boland, C.; Lotya, M.; Istrate, O.M.; King, P.; et al. Scalable production of large quantities of defect-free few-layer graphene by shear exfoliation in liquids. *Nature Materials* **2014**, *13*, 624–630, doi:10.1038/nmat3944.
80. Yi, M.; Shen, Z. A review on mechanical exfoliation for the scalable production of graphene. *Journal of Materials Chemistry A* **2015**, *3*, 11700–11715, doi:10.1039/C5TA00252D.
81. Liu, L.; Shen, Z.; Yi, M.; Zhang, X.; Ma, S. A green, rapid and size-controlled production of high-quality graphene sheets by hydrodynamic forces. *RSC Advances* **2014**, *4*, 36464–36470, doi:10.1039/C4RA05635C.
82. M. Abdelkader, A.; J. Cooper, A.; W. Dryfe, R.A.; A. Kinloch, I. How to get between the sheets: a review of recent works on the electrochemical exfoliation of graphene materials from bulk graphite. *Nanoscale* **2015**, *7*, 6944–6956, doi:10.1039/C4NR06942K.
83. Low, C.T.J.; Walsh, F.C.; Chakrabarti, M.H.; Hashim, M.A.; Hussain, M.A. Electrochemical approaches to the production of graphene flakes and their potential applications. *Carbon* **2013**, *54*, 1–21, doi:10.1016/j.carbon.2012.11.030.
84. Liu, N.; Luo, F.; Wu, H.; Liu, Y.; Zhang, C.; Chen, J. One-Step Ionic-Liquid-Assisted Electrochemical Synthesis of Ionic-Liquid-Functionalized Graphene Sheets Directly from Graphite. *Adv. Funct. Mater.* **2008**, *18*, 1518–1525, doi:10.1002/adfm.200700797.
85. Chen, X.; Zhang, L.; Chen, S. Large area CVD growth of graphene. *Synthetic Metals* **2015**, *210*, 95–108, doi:10.1016/j.synthmet.2015.07.005.
86. Levchenko, I.; Ostrikov, K. (Ken); Zheng, J.; Li, X.; Keidar, M.; B. K. Teo, K. Scalable graphene production: perspectives and challenges of plasma applications. *Nanoscale* **2016**, *8*, 10511–10527, doi:10.1039/C5NR06537B.
87. Tiwari, A.; Raman, R.K.S. Multilayer Graphene on Copper for Corrosion Mitigation. In; Brisbane, 2013.

88. V. Zaretski, A.; J. Lipomi, D. Processes for non-destructive transfer of graphene: widening the bottleneck for industrial scale production. *Nanoscale* **2015**, *7*, 9963–9969, doi:10.1039/C5NR01777G.
89. Norimatsu, W.; Kusunoki, M. Epitaxial graphene on SiC{0001}: advances and perspectives. *Physical Chemistry Chemical Physics* **2014**, *16*, 3501–3511, doi:10.1039/C3CP54523G.
90. Understanding Particle Size Distribution Calculations - HORIBA Available online: http://www.horiba.com/scientific/products/particle-characterization/education/general-information/data-interpretation/understanding-particle-size-distribution-calculations/ (accessed on Jul 31, 2017).
91. Vallés, C.; Beckert, F.; Burk, L.; Mülhaupt, R.; Young, R.J.; Kinloch, I.A. Effect of the C/O ratio in graphene oxide materials on the reinforcement of epoxy-based nanocomposites. *J. Polym. Sci. Part B: Polym. Phys.* **2016**, *54*, 281–291, doi:10.1002/polb.23925.
92. López-Polín, G.; Gómez-Navarro, C.; Parente, V.; Guinea, F.; Katsnelson, M.I.; Pérez-Murano, F.; Gómez-Herrero, J. Increasing the elastic modulus of graphene by controlled defect creation. *Nat Phys* **2015**, *11*, 26–31, doi:10.1038/nphys3183.
93. Gómez-Navarro, C.; Burghard, M.; Kern, K. Elastic Properties of Chemically Derived Single Graphene Sheets. *Nano Lett.* **2008**, *8*, 2045–2049, doi:10.1021/nl801384y.
94. Khan, U.; O'Neill, A.; Lotya, M.; De, S.; Coleman, J.N. High-Concentration Solvent Exfoliation of Graphene. *Small* **2010**, *6*, 864–871, doi:10.1002/smll.200902066.
95. Ferrari, A.C.; Meyer, J.C.; Scardaci, V.; Casiraghi, C.; Lazzeri, M.; Mauri, F.; Piscanec, S.; Jiang, D.; Novoselov, K.S.; Roth, S.; et al. Raman Spectrum of Graphene and Graphene Layers. *Phys. Rev. Lett.* **2006**, *97*, 187401, doi:10.1103/PhysRevLett.97.187401.
96. Loh, K.P.; Bao, Q.; Ang, P.K.; Yang, J. The chemistry of graphene. *Journal of Materials Chemistry* **2010**, *20*, 2277, doi:10.1039/b920539j.
97. Kuila, T.; Bose, S.; Mishra, A.K.; Khanra, P.; Kim, N.H.; Lee, J.H. Chemical functionalization of graphene and its applications. *Progress in Materials Science* **2012**, *57*, 1061–1105, doi:10.1016/j.pmatsci.2012.03.002.
98. Georgakilas, V.; Otyepka, M.; Bourlinos, A.B.; Chandra, V.; Kim, N.; Kemp, K.C.; Hobza, P.; Zboril, R.; Kim, K.S. Functionalization of Graphene: Covalent and Non-Covalent Approaches, Derivatives and Applications. *Chemical Reviews* **2012**, *112*, 6156–6214, doi:10.1021/cr3000412.
99. Layek, R.K.; Nandi, A.K. A review on synthesis and properties of polymer functionalized graphene. *Polymer* **2013**, *54*, 5087–5103, doi:10.1016/j.polymer.2013.06.027.
100. Saravanan, N.; Rajasekar, R.; Mahalakshmi, S.; Sathishkumar, T.; Sasikumar, K.; Sahoo, S. Graphene and modified graphene-based polymer nanocomposites – A review. *Journal of Reinforced Plastics and Composites* **2014**, *33*, 1158–1170, doi:10.1177/0731684414524847.
101. Nadiv, R.; Shtein, M.; Buzaglo, M.; Peretz-Damari, S.; Kovalchuk, A.; Wang, T.; Tour, J.M.; Regev, O. Graphene nanoribbon – Polymer composites: The critical role of edge functionalization. *Carbon* **2016**, *99*, 444–450, doi:10.1016/j.carbon.2015.12.039.
102. Terrones, M.; Martín, O.; González, M.; Pozuelo, J.; Serrano, B.; Cabanelas, J.C.; Vega-Díaz, S.M.; Baselga, J. Interphases in Graphene Polymer-based Nanocomposites: Achievements and Challenges. *Advanced Materials* **2011**, *23*, 5302–5310, doi:10.1002/adma.201102036.
103. Xu, Z.; Gao, C. Graphene fiber: a new trend in carbon fibers. *Materials Today* **2015**, *18*, 480–492, doi:10.1016/j.mattod.2015.06.009.
104. Zhu, W.; Lu, C.-H.; Chang, F.-C.; Kuo, S.-W. Supramolecular ionic strength-modulating microstructures and properties of nacre-like biomimetic

nanocomposites containing high loading clay. *RSC Adv.* **2012**, *2*, 6295–6305, doi:10.1039/C2RA20523H.
105. Unalan, I.U.; Cerri, G.; Marcuzzo, E.; Cozzolino, C.A.; Farris, S. Nanocomposite films and coatings using inorganic nanobuilding blocks (NBB): current applications and future opportunities in the food packaging sector. *RSC Adv.* **2014**, *4*, 29393–29428, doi:10.1039/C4RA01778A.
106. Huang, Y.; Qin, Y.; Zhou, Y.; Niu, H.; Yu, Z.-Z.; Dong, J.-Y. Polypropylene/Graphene Oxide Nanocomposites Prepared by In Situ Ziegler−Natta Polymerization. *Chem. Mater.* **2010**, *22*, 4096–4102, doi:10.1021/cm100998e.
107. N. Tripathi, S.; Srinivasa Rao, G.S.; B. Mathur, A.; Jasra, R. Polyolefin/graphene nanocomposites: a review. *RSC Advances* **2017**, *7*, 23615–23632, doi:10.1039/C6RA28392F.
108. Zhao, X.; Zhang, Q.; Hao, Y.; Li, Y.; Fang, Y.; Chen, D. Alternate Multilayer Films of Poly(vinyl alcohol) and Exfoliated Graphene Oxide Fabricated via a Facial Layer-by-Layer Assembly. *Macromolecules* **2010**, *43*, 9411–9416, doi:10.1021/ma101456y.
109. Yang, M.; Hou, Y.; Kotov, N.A. Graphene-based multilayers: Critical evaluation of materials assembly techniques. *Nano Today* **2012**, *7*, 430–447, doi:10.1016/j.nantod.2012.08.006.
110. Ahn, E.; Lee, T.; Gu, M.; Park, M.; Min, S.H.; Kim, B.-S. Layer-by-Layer Assembly for Graphene-Based Multilayer Nanocomposites: The Field Manual. *Chemistry of Materials* **2017**, *29*, 69–79, doi:10.1021/acs.chemmater.6b02688.
111. Lee, T.; Min, S.H.; Gu, M.; Jung, Y.K.; Lee, W.; Lee, J.U.; Seong, D.G.; Kim, B.-S. Layer-by-Layer Assembly for Graphene-Based Multilayer Nanocomposites: Synthesis and Applications. *Chemistry of Materials* **2015**, *27*, 3785–3796, doi:10.1021/acs.chemmater.5b00491.
112. Sellam, C.; Zhai, Z.; Zahabi, H.; Picot, O.T.; Deng, H.; Fu, Q.; Bilotti, E.; Peijs, T. High mechanical reinforcing efficiency of layered poly(vinyl alcohol) – graphene oxide nanocomposites. *Nanocomposites* **2015**, *1*, 89–95, doi:10.1179/2055033215Y.0000000001.
113. Li, P.; Huang, T.-C.; L. White, K.; Hawkins, S.; Kotaki, M.; Nishimura, R.; Sue, H.-J. Spray-coated epoxy barrier films containing high aspect ratio functionalized graphene nanosheets. *RSC Advances* **2015**, *5*, 102633–102642, doi:10.1039/C5RA15363H.
114. Kim, H.; Kobayashi, S.; AbdurRahim, M.A.; Zhang, M.J.; Khusainova, A.; Hillmyer, M.A.; Abdala, A.A.; Macosko, C.W. Graphene/polyethylene nanocomposites: Effect of polyethylene functionalization and blending methods. *Polymer* **2011**, *52*, 1837–1846, doi:10.1016/j.polymer.2011.02.017.
115. Hot Melt Extrusion - Drug Manufacturing | Twin Screw Extruders Available online: http://www.particlesciences.com/news/technical-briefs/2011/hot-melt-extrusion.html (accessed on Aug 2, 2017).
116. Xu, S.; Wen, M.; Li, J.; Guo, S.; Wang, M.; Du, Q.; Shen, J.; Zhang, Y.; Jiang, S. Structure and properties of electrically conducting composites consisting of alternating layers of pure polypropylene and polypropylene with a carbon black filler. *Polymer* **2008**, *49*, 4861–4870, doi:10.1016/j.polymer.2008.08.056.
117. Li, X.; McKenna, G.B.; Miquelard-Garnier, G.; Guinault, A.; Sollogoub, C.; Regnier, G.; Rozanski, A. Forced assembly by multilayer coextrusion to create oriented graphene reinforced polymer nanocomposites. *Polymer* **2014**, *55*, 248–257, doi:10.1016/j.polymer.2013.11.025.
118. Ghanem, A.; Lemenand, T.; Della Valle, D.; Peerhossaini, H. Static mixers: Mechanisms, applications, and characterization methods – A review. *Chemical Engineering Research and Design* **2014**, *92*, 205–228, doi:10.1016/j.cherd.2013.07.013.

119. Luan, C. Baker's transformation and its irreversibility. *Physics Letters A* **1991**, *152*, 6–10, doi:10.1016/0375-9601(91)90618-I.
120. Gao, Y.; Picot, O.T.; Tu, W.; Bilotti, E.; Peijs, T. Multilayer coextrusion of graphene polymer nanocomposites with enhanced structural organization and properties. *Journal of Applied Polymer Science* **2018**, *135*, 46041, doi:10.1002/app.46041.
121. Shen, J.; Li, J.; Guo, S. The distribution and morphological evolution of dispersed phase in laminating-multiplying elements during extrusion. *Polymer Composites* **2012**, *33*, 693–699, doi:10.1002/pc.22193.
122. Wen, M.; Sun, X.; Su, L.; Shen, J.; Li, J.; Guo, S. The electrical conductivity of carbon nanotube/carbon black/polypropylene composites prepared through multistage stretching extrusion. *Polymer* **2012**, *53*, 1602–1610, doi:10.1016/j.polymer.2012.02.003.
123. Miquelard-Garnier, G.; Guinault, A.; Fromonteil, D.; Delalande, S.; Sollogoub, C. Dispersion of carbon nanotubes in polypropylene via multilayer coextrusion: Influence on the mechanical properties. *Polymer* **2013**, *54*, 4290–4297, doi:10.1016/j.polymer.2013.06.007.
124. Decker, J.J.; Meyers, K.P.; Paul, D.R.; Schiraldi, D.A.; Hiltner, A.; Nazarenko, S. Polyethylene-based nanocomposites containing organoclay: A new approach to enhance gas barrier via multilayer coextrusion and interdiffusion. *Polymer* **2015**, *61*, 42–54, doi:10.1016/j.polymer.2015.01.061.
125. Ribbe, A.E.; Hashimoto, T. Homogenization Mechanism of Spinodally Decomposed Polymer Blends via Baker's Transformation. *Macromolecules* **2000**, *33*, 7827–7834, doi:10.1021/ma000752d.
126. Jarus, D.; Hiltner, A.; Baer, E. Microlayer coextrusion as a route to innovative blend structures. *Polymer Engineering & Science* **2001**, *41*, 2162–2171, doi:10.1002/pen.10911.
127. l'Abee, R.M.A.; Vissers, A.M.J.T.; Goossens, J.G.P.; Spoelstra, A.B.; van Duin, M. Characterization of the morphology of co-extruded, thermoplastic/rubber multi-layer tapes. *Analytica Chimica Acta* **2009**, *654*, 11–19, doi:10.1016/j.aca.2009.06.036.
128. Throckmorton, J.; Palmese, G. Direct Preparation of Few Layer Graphene Epoxy Nanocomposites from Untreated Flake Graphite. *ACS Applied Materials & Interfaces* **2015**, *7*, 14870–14877, doi:10.1021/acsami.5b03465.
129. Li, Y.; Zhang, H.; Crespo, M.; Porwal, H.; Picot, O.; Santagiuliana, G.; Huang, Z.; Barbieri, E.; Pugno, N.M.; Peijs, T.; et al. In Situ Exfoliation of Graphene in Epoxy Resins: A Facile Strategy to Efficient and Large Scale Graphene Nanocomposites. *ACS Appl. Mater. Interfaces* **2016**, *8*, 24112–24122, doi:10.1021/acsami.6b07492.
130. Research and development Available online: https://www.exakt.de/en/products/three-roll-mills/research-and-development.html (accessed on Aug 2, 2017).
131. Tang, Z.; Liu, X.; Hu, Y.; Zhang, X.; Guo, B. A slurry compounding route to disperse graphene oxide in rubber. *Materials Letters* **2017**, *191*, 93–96, doi:10.1016/j.matlet.2017.01.054.
132. Potts, J.R.; Shankar, O.; Murali, S.; Du, L.; Ruoff, R.S. Latex and two-roll mill processing of thermally-exfoliated graphite oxide/natural rubber nanocomposites. *Composites Science and Technology* **2013**, *74*, 166–172, doi:10.1016/j.compscitech.2012.11.008.
133. Wan, Y.-J.; Yu, S.-H.; Yang, W.-H.; Zhu, P.-L.; Sun, R.; Wong, C.-P.; Liao, W.-H. Tuneable cellular-structured 3D graphene aerogel and its effect on electromagnetic interference shielding performance and mechanical properties of epoxy composites. *RSC Advances* **2016**, *6*, 56589–56598, doi:10.1039/C6RA09459G.
134. Jia, J.; Sun, X.; Lin, X.; Shen, X.; Mai, Y.-W.; Kim, J.-K. Exceptional Electrical Conductivity and Fracture Resistance of 3D Interconnected Graphene

Foam/Epoxy Composites. *ACS Nano* **2014**, *8*, 5774–5783, doi:10.1021/nn500590g.
135. Qiu, L.; Liu, J.Z.; Chang, S.L.Y.; Wu, Y.; Li, D. Biomimetic superelastic graphene-based cellular monoliths. *Nature Communications* **2012**, *3*, ncomms2251, doi:10.1038/ncomms2251.
136. D'Elia, E.; Barg, S.; Ni, N.; Rocha, V.G.; Saiz, E. Self-Healing Graphene-Based Composites with Sensing Capabilities. *Adv. Mater.* **2015**, *27*, 4788–4794, doi:10.1002/adma.201501653.
137. Tang, G.; Jiang, Z.-G.; Li, X.; Zhang, H.-B.; Dasari, A.; Yu, Z.-Z. Three dimensional graphene aerogels and their electrically conductive composites. *Carbon* **2014**, *77*, 592–599, doi:10.1016/j.carbon.2014.05.063.
138. Li, X.-H.; Li, X.; Liao, K.-N.; Min, P.; Liu, T.; Dasari, A.; Yu, Z.-Z. Thermally Annealed Anisotropic Graphene Aerogels and Their Electrically Conductive Epoxy Composites with Excellent Electromagnetic Interference Shielding Efficiencies. *ACS Appl. Mater. Interfaces* **2016**, *8*, 33230–33239, doi:10.1021/acsami.6b12295.
139. Deville, S. Ice-templating, freeze casting: Beyond materials processing. *Journal of Materials Research* **2013**, *28*, 2202–2219, doi:10.1557/jmr.2013.105.
140. Tegou, E.; Pseiropoulos, G.; Filippidou, M.K.; Chatzandroulis, S. Low-temperature thermal reduction of graphene oxide films in ambient atmosphere: Infra-red spectroscopic studies and gas sensing applications. *Microelectronic Engineering* **2016**, *159*, 146–150, doi:10.1016/j.mee.2016.03.030.
141. Zumbrunnen, D.A.; Inamdar, S.; Kwon, O.; Verma, P. Chaotic Advection as a Means to Develop Nanoscale Structures in Viscous Melts. *Nano Lett.* **2002**, *2*, 1143–1148, doi:10.1021/nl0256558.
142. Ottino, J.M. *The Kinematics of Mixing: Stretching, Chaos, and Transport*; Cambridge University Press, 1989; ISBN 978-0-521-36878-0.
143. Li, X.; McKenna, G.B.; Miquelard-Garnier, G.; Guinault, A.; Sollogoub, C.; Regnier, G.; Rozanski, A. Forced assembly by multilayer coextrusion to create oriented graphene reinforced polymer nanocomposites. *Polymer* **2014**, *55*, 248–257, doi:10.1016/j.polymer.2013.11.025.
144. Kuila, T.; Bose, S.; Mishra, A.K.; Khanra, P.; Kim, N.H.; Lee, J.H. Effect of functionalized graphene on the physical properties of linear low density polyethylene nanocomposites. *Polymer Testing* **2012**, *31*, 31–38, doi:10.1016/j.polymertesting.2011.09.007.
145. Kundu, P.P.; Biswas, J.; Kim, H.; Choe, S. Influence of film preparation procedures on the crystallinity, morphology and mechanical properties of LLDPE films. *European Polymer Journal* **2003**, *39*, 1585–1593, doi:10.1016/S0014-3057(03)00056-9.
146. Hermans, P.H.; Weidinger, A. On the determination of the crystalline fraction of polyethylenes from X-ray diffraction. *Makromol. Chem.* **1961**, *44*, 24–36, doi:10.1002/macp.1961.020440103.
147. Oskouyi, A.B.; Sundararaj, U.; Mertiny, P. Current-voltage characteristics of nanoplatelet-based conductive nanocomposites. *Nanoscale research letters* **2014**, *9*, 1–8.
148. Nezakati, T.; Tan, A.; Seifalian, A.M. Enhancing the electrical conductivity of a hybrid POSS–PCL/graphene nanocomposite polymer. *Journal of Colloid and Interface Science* **2014**, *435*, 145–155, doi:10.1016/j.jcis.2014.08.020.
149. Šupová, M.; Martynková, G.S.; Barabaszová, K. Effect of Nanofillers Dispersion in Polymer Matrices: A Review. *Science of Advanced Materials* **2011**, *3*, 1–25, doi:10.1166/sam.2011.1136.
150. Fornes, T.D.; Paul, D.R. Modeling properties of nylon 6/clay nanocomposites using composite theories. *Polymer* **2003**, *44*, 4993–5013, doi:10.1016/S0032-3861(03)00471-3.

151. Barwich, S.; Coleman, J.N.; Möbius, M.E. Yielding and flow of highly concentrated, few-layer graphene suspensions. *Soft Matter* **2015**, *11*, 3159–3164, doi:10.1039/C4SM02855D.
152. Halpin, J.C.; Thomas, R.L. Ribbon Reinforcement of Composites. *Journal of Composite Materials* **1968**, *2*, 488–497, doi:10.1177/002199836800200409.
153. Affdl, J.C.H.; Kardos, J.L. The Halpin-Tsai equations: A review. *Polym Eng Sci* **1976**, *16*, 344–352, doi:10.1002/pen.760160512.
154. Van Es, M.A.; Van Turnhout, J. Polymer-clay nanocomposites: the importance of particle dimensions. Ph.D. Thesis, Delft University of Technology, 2001.
155. Khan, U.; May, P.; O'Neill, A.; Bell, A.P.; Boussac, E.; Martin, A.; Semple, J.; Coleman, J.N. Polymer reinforcement using liquid-exfoliated boron nitride nanosheets. *Nanoscale* **2012**, *5*, 581–587, doi:10.1039/C2NR33049K.
156. Duclaux, L.; Nysten, B.; Issi, J.-P.; Moore, A.W. Structure and low-temperature thermal conductivity of pyrolytic boron nitride. *Phys. Rev. B* **1992**, *46*, 3362–3367, doi:10.1103/PhysRevB.46.3362.
157. Li, J.; Ma, P.C.; Chow, W.S.; To, C.K.; Tang, B.Z.; Kim, J.-K. Correlations between Percolation Threshold, Dispersion State, and Aspect Ratio of Carbon Nanotubes. *Adv. Funct. Mater.* **2007**, *17*, 3207–3215, doi:10.1002/adfm.200700065.
158. Otten, R.H.J.; van der Schoot, P. Connectivity percolation of polydisperse anisotropic nanofillers. *J Chem Phys* **2011**, *134*, 094902, doi:10.1063/1.3559004.
159. Ploehn, H.J.; Liu, C. Quantitative Analysis of Montmorillonite Platelet Size by Atomic Force Microscopy. *Ind. Eng. Chem. Res.* **2006**, *45*, 7025–7034, doi:10.1021/ie051392r.
160. Deng, H.; Skipa, T.; Bilotti, E.; Zhang, R.; Lellinger, D.; Mezzo, L.; Fu, Q.; Alig, I.; Peijs, T. Preparation of High-Performance Conductive Polymer Fibers through Morphological Control of Networks Formed by Nanofillers. *Adv. Funct. Mater.* **2010**, *20*, 1424–1432, doi:10.1002/adfm.200902207.
161. Zhang, S.; Lin, L.; Deng, H.; Gao, X.; Bilotti, E.; Peijs, T.; Zhang, Q.; Fu, Q. Dynamic percolation in highly oriented conductive networks formed with different carbon nanofillers. *Colloid Polym Sci* **2012**, *290*, 1393–1401, doi:10.1007/s00396-012-2661-7.
162. Zhang, H.; Bilotti, E.; Tu, W.; Lew, C.Y.; Peijs, T. Static and dynamic percolation of phenoxy/carbon nanotube nanocomposites. *European Polymer Journal* **2015**, *68*, 128–138, doi:10.1016/j.eurpolymj.2015.04.022.
163. Wang, Z.; Shen, X.; Han, N.M.; Liu, X.; Wu, Y.; Ye, W.; Kim, J.-K. Ultralow Electrical Percolation in Graphene Aerogel/Epoxy Composites. *Chem. Mater.* **2016**, *28*, 6731–6741, doi:10.1021/acs.chemmater.6b03206.
164. Kouroupis-Agalou, K.; Liscio, A.; Treossi, E.; Ortolani, L.; Morandi, V.; Pugno, N.M.; Palermo, V. Fragmentation and exfoliation of 2-dimensional materials: a statistical approach. *Nanoscale* **2014**, *6*, 5926, doi:10.1039/c3nr06919b.
165. Krzesińska, M.; Celzard, A.; Marêché, J.F.; Puricelli, S. Elastic properties of anisotropic monolithic samples of compressed expanded graphite studied with ultrasounds. *Journal of Materials Research* **2001**, *16*, 606–614.
166. Sun, G.; Li, X.; Qu, Y.; Wang, X.; Yan, H.; Zhang, Y. Preparation and characterization of graphite nanosheets from detonation technique. *Materials Letters* **2008**, *62*, 703–706, doi:10.1016/j.matlet.2007.06.035.
167. Howe, J.Y.; Cavin, B.O.; Drakeford, A.E.; Peascoe, R.A.; Zontek, T.L.; Miller, D.J. Influence of Bulk Graphite Thickness on the Accuracy of X-Ray Diffraction Measurement. In *Carbon 2007*; Seattle, Washington, USA, 2007.
168. Chung, D.D.L. Review graphite. *Journal of materials science* **2002**, *37*, 1475–1489.
169. Blanton, T.N.; Majumdar, D. X-ray diffraction characterization of polymer intercalated graphite oxide. *Powder Diffraction* **2012**, *27*, 104–107, doi:10.1017/S0885715612000292.
170. Leider, P.J.; Bird, R.B. Squeezing Flow between Parallel Disks. I. Theoretical Analysis. *Ind. Eng. Chem. Fund.* **1974**, *13*, 336–341, doi:10.1021/i160052a007.

171. Engmann, J.; Servais, C.; Burbidge, A.S. Squeeze flow theory and applications to rheometry: A review. *Journal of Non-Newtonian Fluid Mechanics* **2005**, *132*, 1–27, doi:10.1016/j.jnnfm.2005.08.007.
172. Wu, T.-L.; Lo, T.-S.; Kuo, W.-S. Effect of dispersion on graphite nanosheet composites. *Polymer Composites* **2009**, *31*, 292–298, doi:10.1002/pc.20802.
173. Kim, H.; Kobayashi, S.; AbdurRahim, M.A.; Zhang, M.J.; Khusainova, A.; Hillmyer, M.A.; Abdala, A.A.; Macosko, C.W. Graphene/polyethylene nanocomposites: Effect of polyethylene functionalization and blending methods. *Polymer* **2011**, *52*, 1837–1846, doi:10.1016/j.polymer.2011.02.017.
174. Noorunnisa Khanam, P.; AlMaadeed, M.A.; Ouederni, M.; Harkin-Jones, E.; Mayoral, B.; Hamilton, A.; Sun, D. Melt processing and properties of linear low density polyethylene-graphene nanoplatelet composites. *Vacuum* **2016**, *130*, 63–71, doi:10.1016/j.vacuum.2016.04.022.
175. Carotenuto, G.; De Nicola, S.; Palomba, M.; Pullini, D.; Horsewell, A.; Hansen, T.W.; Nicolais, L. Mechanical properties of low-density polyethylene filled by graphite nanoplatelets. *Nanotechnology* **2012**, *23*, 485705, doi:10.1088/0957-4484/23/48/485705.
176. Vasileiou, A.A.; Kontopoulou, M.; Docoslis, A. A Noncovalent Compatibilization Approach to Improve the Filler Dispersion and Properties of Polyethylene/Graphene Composites. *ACS Appl. Mater. Interfaces* **2014**, *6*, 1916–1925, doi:10.1021/am404979g.
177. Gong, J.; Niu, R.; Liu, J.; Chen, X.; Wen, X.; Mijowska, E.; Sun, Z.; Tang, T. Simultaneously improving the thermal stability, flame retardancy and mechanical properties of polyethylene by the combination of graphene with carbon black. *RSC Adv.* **2014**, *4*, 33776–33784, doi:10.1039/C4RA04623D.
178. Mittal, V.; Chaudhry, A.U. Polymer - graphene nanocomposites: effect of polymer matrix and filler amount on properties: Polymer - Graphene Nanocomposites: Effect of Polymer Matrix and Filler Amount on Properties. *Macromolecular Materials and Engineering* **2015**, *300*, 510–521, doi:10.1002/mame.201400392.
179. Layek, R.K.; Nandi, A.K. A review on synthesis and properties of polymer functionalized graphene. *Polymer* **2013**, *54*, 5087–5103, doi:10.1016/j.polymer.2013.06.027.
180. Bilotti, E.; Zhang, R.; Deng, H.; Quero, F.; Fischer, H.R.; Peijs, T. Sepiolite needle-like clay for PA6 nanocomposites: An alternative to layered silicates? *Composites Science and Technology* **2009**, *69*, 2587–2595, doi:10.1016/j.compscitech.2009.07.016.
181. Kim, S.; Seo, J.; Drzal, L.T. Improvement of electric conductivity of LLDPE based nanocomposite by paraffin coating on exfoliated graphite nanoplatelets. *Composites Part A: Applied Science and Manufacturing* **2010**, *41*, 581–587, doi:10.1016/j.compositesa.2009.05.002.
182. Kuila, T.; Bose, S.; Hong, C.E.; Uddin, M.E.; Khanra, P.; Kim, N.H.; Lee, J.H. Preparation of functionalized graphene/linear low density polyethylene composites by a solution mixing method. *Carbon* **2011**, *49*, 1033–1037, doi:10.1016/j.carbon.2010.10.031.
183. Zhang, P.; Cao, D.; Cui, S. Resistivity-temperature behavior and morphology of low density polyethylene/graphite powder/graphene composites. *Polymer Composites* **2014**, *35*, 1453–1459, doi:10.1002/pc.22798.
184. Iqbal, M.Z.; Abdala, A.A.; Mittal, V.; Seifert, S.; Herring, A.M.; Liberatore, M.W. Processable conductive graphene/polyethylene nanocomposites: Effects of graphene dispersion and polyethylene blending with oxidized polyethylene on rheology and microstructure. *Polymer* **2016**, *98*, 143–155, doi:10.1016/j.polymer.2016.06.021.
185. Arora, A.; Padua, G. w. Review: Nanocomposites in Food Packaging. *Journal of Food Science* **2010**, *75*, R43–R49, doi:10.1111/j.1750-3841.2009.01456.x.

186. Priolo, M.A.; Holder, K.M.; Greenlee, S.M.; Grunlan, J.C. Transparency, Gas Barrier, and Moisture Resistance of Large-Aspect-Ratio Vermiculite Nanobrick Wall Thin Films. *ACS Appl. Mater. Interfaces* **2012**, *4*, 5529–5533, doi:10.1021/am3014289.
187. Jones, W.E.; Chiguma, J.; Johnson, E.; Pachamuthu, A.; Santos, D. Electrically and Thermally Conducting Nanocomposites for Electronic Applications. *Materials* **2010**, *3*, 1478–1496, doi:10.3390/ma3021478.
188. Shahil, K.M.F.; Balandin, A.A. Graphene–Multilayer Graphene Nanocomposites as Highly Efficient Thermal Interface Materials. *Nano Lett.* **2012**, *12*, 861–867, doi:10.1021/nl203906r.
189. Enríquez, E.; Fernández, J.F.; De Frutos, J.; De la Rubia, M.A. Tailoring of the electrical properties of carbon black–silica coatings for de-icing applications. *Ceramics International* **2015**, *41*, 2735–2743, doi:10.1016/j.ceramint.2014.10.088.
190. Rybak, A.; Boiteux, G.; Melis, F.; Seytre, G. Conductive polymer composites based on metallic nanofiller as smart materials for current limiting devices. *Composites Science and Technology* **2010**, *70*, 410–416, doi:10.1016/j.compscitech.2009.11.019.
191. Yi, X.-S.; Wu, G.; Pan, Y. Properties and applications of filled conductive polymer composites. *Polym. Int.* **1997**, *44*, 117–124, doi:10.1002/(SICI)1097-0126(199710)44:2<117::AID-PI811>3.0.CO;2-L.
192. Thostenson, E.T.; Chou, T.-W. Real-time in situ sensing of damage evolution in advanced fiber composites using carbon nanotube networks. *Nanotechnology* **2008**, *19*, 215713, doi:10.1088/0957-4484/19/21/215713.
193. Yuan, J.; Luna, A.; Neri, W.; Zakri, C.; Schilling, T.; Colin, A.; Poulin, P. Graphene liquid crystal retarded percolation for new high-k materials. *Nature Communications* **2015**, *6*, 8700, doi:10.1038/ncomms9700.
194. Raccichini, R.; Varzi, A.; Passerini, S.; Scrosati, B. The role of graphene for electrochemical energy storage. *Nat Mater* **2015**, *14*, 271–279, doi:10.1038/nmat4170.
195. Sandler, J.; Shaffer, M.S.P.; Prasse, T.; Bauhofer, W.; Schulte, K.; Windle, A.H. Development of a dispersion process for carbon nanotubes in an epoxy matrix and the resulting electrical properties. *Polymer* **1999**, *40*, 5967–5971, doi:10.1016/S0032-3861(99)00166-4.
196. Dang, Z.-M.; Yuan, J.-K.; Yao, S.-H.; Liao, R.-J. Flexible Nanodielectric Materials with High Permittivity for Power Energy Storage. *Adv. Mater.* **2013**, *25*, 6334–6365, doi:10.1002/adma.201301752.
197. Rajan, K.P.; Al-Ghamdi, A.; Parameswar, R.; Nando, G.B. Blends of Thermoplastic Polyurethane and Polydimethylsiloxane Rubber: Assessment of Biocompatibility and Suture Holding Strength of Membranes Available online: https://www.hindawi.com/journals/ijbm/2013/240631/ (accessed on Feb 27, 2018).
198. Chen, W.; Qu, B. LLDPE/ZnAl LDH-exfoliated nanocomposites: effects of nanolayers on thermal and mechanical properties. *Journal of Materials Chemistry* **2004**, *14*, 1705, doi:10.1039/b401790k.
199. Wirsén, A.; Lindberg, K.T.; Albertsson, A.-C. Graft polymerization of acrylamide onto linear low-density polyethylene film by electron beam pre-irradiation in air or argon: 3. Morphology. *Polymer* **1996**, *37*, 761–769, doi:10.1016/0032-3861(96)87251-X.
200. Zhang, K.; Zhang, Y.; Wang, S. Enhancing thermoelectric properties of organic composites through hierarchical nanostructures. *Scientific Reports* **2013**, *3*, doi:10.1038/srep03448.
201. Seung Hun, H.; Hae-Mi, J.; Sung-Ho, C. X-ray Diffraction Patterns of Thermally-reduced Graphenes. *Journal of the Korean Physical Society* **2010**, *57*, 1649, doi:10.3938/jkps.57.1649.

202. Wan, C.; Qiao, X.; Zhang, Y.; Zhang, Y. Effect of different clay treatment on morphology and mechanical properties of PVC-clay nanocomposites. *Polymer Testing* **2003**, *22*, 453–461, doi:10.1016/S0142-9418(02)00126-5.
203. Chang, J.-H.; An, Y.U.; Sur, G.S. Poly(lactic acid) nanocomposites with various organoclays. I. Thermomechanical properties, morphology, and gas permeability. *J. Polym. Sci. B Polym. Phys.* **2003**, *41*, 94–103, doi:10.1002/polb.10349.
204. Shah, R.K.; Paul, D.R. Nylon 6 nanocomposites prepared by a melt mixing masterbatch process. *Polymer* **2004**, *45*, 2991–3000, doi:10.1016/j.polymer.2004.02.058.
205. Chang, J.-H.; Kim, S.J.; Joo, Y.L.; Im, S. Poly(ethylene terephthalate) nanocomposites by in situ interlayer polymerization: the thermo-mechanical properties and morphology of the hybrid fibers. *Polymer* **2004**, *45*, 919–926, doi:10.1016/j.polymer.2003.11.037.
206. Strawhecker, K.E.; Manias, E. Structure and Properties of Poly(vinyl alcohol)/Na^+ Montmorillonite Nanocomposites. *Chemistry of Materials* **2000**, *12*, 2943–2949, doi:10.1021/cm000506g.
207. Fu, X.; Qutubuddin, S. Polymer–clay nanocomposites: exfoliation of organophilic montmorillonite nanolayers in polystyrene. *Polymer* **2001**, *42*, 807–813.
208. Sinha Ray, S.; Okamoto, K.; Okamoto, M. Structure−Property Relationship in Biodegradable Poly(butylene succinate)/Layered Silicate Nanocomposites. *Macromolecules* **2003**, *36*, 2355–2367, doi:10.1021/ma021728y.
209. Hotta, S.; Paul, D.R. Nanocomposites formed from linear low density polyethylene and organoclays. *Polymer* **2004**, *45*, 7639–7654, doi:10.1016/j.polymer.2004.08.059.
210. Maiti, P.; Yamada, K.; Okamoto, M.; Ueda, K.; Okamoto, K. New Polylactide/Layered Silicate Nanocomposites: Role of Organoclays. *Chemistry of Materials* **2002**, *14*, 4654–4661, doi:10.1021/cm020391b.
211. Noh, M.W.; Lee, D.C. Synthesis and characterization of PS-clay nanocomposite by emulsion polymerization. *Polymer Bulletin* **1999**, *42*, 619–626.
212. Wang, S.F.; Shen, L.; Tong, Y.J.; Chen, L.; Phang, I.Y.; Lim, P.Q.; Liu, T.X. Biopolymer chitosan/montmorillonite nanocomposites: Preparation and characterization. *Polymer Degradation and Stability* **2005**, *90*, 123–131, doi:10.1016/j.polymdegradstab.2005.03.001.
213. Kornmann, X.; Berglund, L.A.; Sterte, J.; Giannelis, E.P. Nanocomposites based on montmorillonite and unsaturated polyester. *Polymer Engineering & Science* **1998**, *38*, 1351–1358.
214. Jiang, L.; Zhang, J.; Wolcott, M.P. Comparison of polylactide/nano-sized calcium carbonate and polylactide/montmorillonite composites: Reinforcing effects and toughening mechanisms. *Polymer* **2007**, *48*, 7632–7644, doi:10.1016/j.polymer.2007.11.001.
215. Chang, J.-H.; An, Y.U.; Cho, D.; Giannelis, E.P. Poly(lactic acid) nanocomposites: comparison of their properties with montmorillonite and synthetic mica (II). *Polymer* **2003**, *44*, 3715–3720, doi:10.1016/S0032-3861(03)00276-3.
216. Morawiec, J.; Pawlak, A.; Slouf, M.; Galeski, A.; Piorkowska, E.; Krasnikowa, N. Preparation and properties of compatibilized LDPE/organo-modified montmorillonite nanocomposites. *European Polymer Journal* **2005**, *41*, 1115–1122, doi:10.1016/j.eurpolymj.2004.11.011.
217. Chavarria, F.; Paul, D.R. Comparison of nanocomposites based on nylon 6 and nylon 66. *Polymer* **2004**, *45*, 8501–8515, doi:10.1016/j.polymer.2004.09.074.
218. Wu, C.-N.; Saito, T.; Fujisawa, S.; Fukuzumi, H.; Isogai, A. Ultrastrong and High Gas-Barrier Nanocellulose/Clay-Layered Composites. *Biomacromolecules* **2012**, *13*, 1927–1932, doi:10.1021/bm300465d.
219. Sehaqui, H.; Kochumalayil, J.; Liu, A.; Zimmermann, T.; Berglund, L.A. Multifunctional Nanoclay Hybrids of High Toughness, Thermal, and Barrier

Performances. *ACS Applied Materials & Interfaces* **2013**, *5*, 7613–7620, doi:10.1021/am401928d.
220. Podsiadlo, P.; Kaushik, A.K.; Arruda, E.M.; Waas, A.M.; Shim, B.S.; Xu, J.; Nandivada, H.; Pumplin, B.G.; Lahann, J.; Ramamoorthy, A.; et al. Ultrastrong and Stiff Layered Polymer Nanocomposites. *Science* **2007**, *318*, 80–83, doi:10.1126/science.1143176.
221. Tang, Z.; Kotov, N.A.; Magonov, S.; Ozturk, B. Nanostructured artificial nacre. *Nature Materials* **2003**, *2*, 413–418, doi:10.1038/nmat906.
222. Podsiadlo, P.; Tang, Z.; Shim, B.S.; Kotov, N.A. Counterintuitive Effect of Molecular Strength and Role of Molecular Rigidity on Mechanical Properties of Layer-by-Layer Assembled Nanocomposites. *Nano Letters* **2007**, *7*, 1224–1231, doi:10.1021/nl0700649.
223. Podsiadlo, P.; Kaushik, A.K.; Shim, B.S.; Agarwal, A.; Tang, Z.; Waas, A.M.; Arruda, E.M.; Kotov, N.A. Can Nature's Design be Improved Upon? High Strength, Transparent Nacre-Like Nanocomposites with Double Network of Sacrificial Cross Links †. *The Journal of Physical Chemistry B* **2008**, *112*, 14359–14363, doi:10.1021/jp801492n.
224. Huang, G.; Ge, C.; He, B. Preparation, characterization and properties of amino-functionalized montmorillonite and composite layer-by-layer assembly with inorganic nanosheets. *Applied Surface Science* **2011**, *257*, 7123–7128, doi:10.1016/j.apsusc.2011.03.066.
225. Gaidukov, S.; Danilenko, I.; Gaidukova, G. Characterization of Strong and Crystalline Polyvinyl Alcohol/Montmorillonite Films Prepared by Layer-by-Layer Deposition Method. *International Journal of Polymer Science* **2015**, *2015*, 1–8, doi:10.1155/2015/123469.
226. Shu, Y.; Yin, P.; Liang, B.; Wang, H.; Guo, L. Bioinspired Design and Assembly of Layered Double Hydroxide/Poly(vinyl alcohol) Film with High Mechanical Performance. *ACS Applied Materials & Interfaces* **2014**, 140825162306007, doi:10.1021/am503273a.
227. Finnemore, A.; Cunha, P.; Shean, T.; Vignolini, S.; Guldin, S.; Oyen, M.; Steiner, U. Biomimetic layer-by-layer assembly of artificial nacre. *Nature Communications* **2012**, *3*, 966, doi:10.1038/ncomms1970.